AD-A284 398

DTIC
SELECTED
SEP 1 4 1994
F

INVESTIGATION OF THE FRACTURE BEHAVIOR OF SCALED HY-130 WELDMENTS
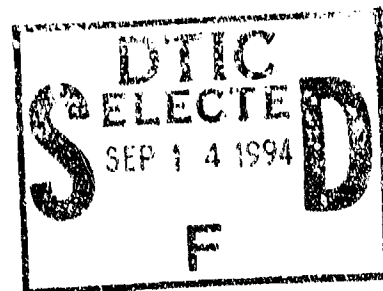
BY J. H. GIOVANOLA, R. W. KLOPP, J. W. SIMONS, AND A. H. MARCHAND
(POULTER LABORATORY/SRI INTERNATIONAL)

FOR   NAVAL SURFACE WARFARE CENTER
      RESEARCH AND TECHNOLOGY DEPARTMENT

JUNE 1990

94-29790

NAVAL SURFACE WARFARE CENTER

Dahlgren, Virginia 22448-5000 • Silver Spring, Maryland 20903-5000

DTIC QUALITY INSPECTED 3

94 9 13 001

INVESTIGATION OF THE FRACTURE BEHAVIOR OF SCALED HY-130 STEEL WELDMENTS

BY J. H. GIOVANOLA, R. W. KLOPP, J. W. SIMONS, AND A. H. MARCHAND
POULTER LABORATORY/SRI INTERNATIONAL

FOR NAVAL SURFACE WARFARE CENTER
(RESEARCH AND TECHNOLOGY DEPARTMENT)

JUNE 1990

Accesion For		
NTIS CRA&I	☑	
DTIC TAB	☐	
U..announced	☐	
Justification		
By		
Distribution /		
Availability Codes		
Dist	Avail and / or Special	
A-1		

Approved for public release; distribution is unlimited.

DTIC QUALITY INSPECTED 3

NAVAL SURFACE WARFARE CENTER

Dahlgren, Virginia 22448-5000 • Silver Spring, Maryland 20903-5000

FOREWORD

This report was prepared by SRI International under Naval Surface Warfare Center (NAVSWC) contract N60921-86-C-0253 in support of the Submarine Damage Mechanisms Task of the Undersea Warheads and Explosives Block Program sponsored by the Office of Naval Technology. The contract technical monitor was Mr. William W. McDonald, NAVSWC Code R14.

The document presents an experimental and analytical study of the fracture properties of HY-130 steel test specimens performed by SRI International under the above contract. SRI International conducted tests of similar designs of stiffened flat plate test specimens under both quasi-static and explosive test conditions. The principal objective of the work was to determine the dependence of specimen baseplate fractures upon scale under dynamic conditions. To provide a theoretical understanding of the empirically derived scaling rule, and to provide a tool for extending the rule to untested scales and other structure designs, SRI also developed a finite element fracture model based on a semi-empirically derived local fracture criterion.

The Submarine Mechanisms Task is an effort to develop an empirically based methodology for predicting the fracture of submarine pressure hulls in response to the loadings of underwater explosions. The work in this report was funded in

recognition of the key importance to this Task of the issue known in the engineering community as the fracture size effect that is exhibited by many structural materials.

Approved by:

WILLIAM H. BOHLI, Head
Energetic Materials Division

CONTENTS

ILLUSTRATIONS

ILLUSTRATIONS (Cont.)

ILLUSTRATIONS (Cont.)

ILLUSTRATIONS (Cont.)

ILLUSTRATIONS (Cont.)

ILLUSTRATIONS (Cont.)

ILLUSTRATIONS (Cont.)

ILLUSTRATIONS (Cont.)

TABLES

Tables (Cont.)

INTRODUCTION

SRI International is engaged in an experimental program to assist the Naval Surface Warfare Center (NAVSWC) in developing a capability for predicting failures of welded naval structures. This technical report presents the results of the first part of the program and covers the development of experimental techniques and analytical models and the derivation of scaling rules for the fracture of HY-130 steel weldments. In the second part of the program, we apply the methodology developed for HY-130 steel weldments to titanium alloys weldments. The results of the work on titanium weldments will be presented in a separate report.

BACKGROUND AND PROGRAM OBJECTIVES

NAVSWC is developing a statistical model to predict the fracture probability of welded, ring-stiffened naval structures subjected to dynamic loads such as result from an underwater explosive charge. Figure 1a illustrates the pertinent configuration. Several issues must be resolved for the successful development of the statistical model.

The first issue arises from the following practical considerations. A statistically significant fracture data base must be available to aid in selecting the proper fracture distribution function for the NAVSWC statistical model. For economic reasons, full-scale tests cannot be performed on ring-stiffened naval structures, so small-scale model tests must be performed on similar structures. The question then is, how can the fracture behavior of welds observed in small-scale tests be extrapolated to welds in full-scale structures?

Establishing the fracture scaling behavior of welds represents an intricate problem, because fracture generally does not follow geometric scaling and the welding process itself cannot easily be scaled. Although linear elastic and elastoplastic fracture mechanics provide scaling rules when fracture begins at a preexisting macroscopic sharp crack, little if any well-established methodology exists for deriving scaling rules when fracture begins in the absence of an existing crack or at blunt stress concentrations. Furthermore, because the specific heat input and number of passes can never be reproduced exactly when welded scale models are manufactured, large- and small-scale welds may have different geometries, microstructures, and properties.
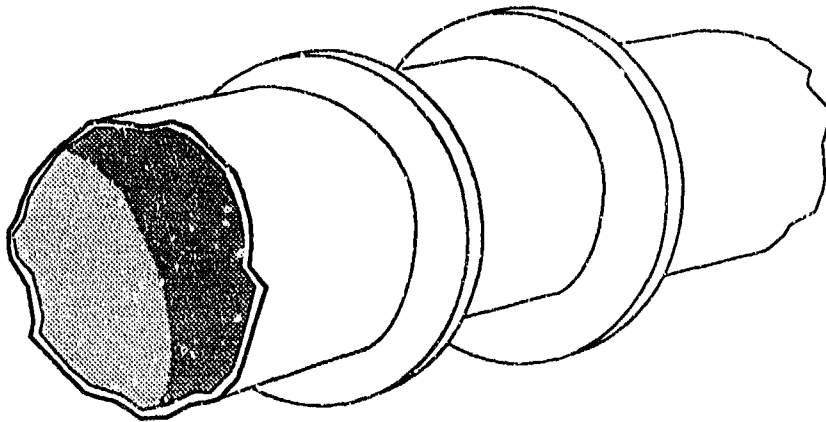
(a) Actual configuration

$$\frac{t}{H} = 0.5$$
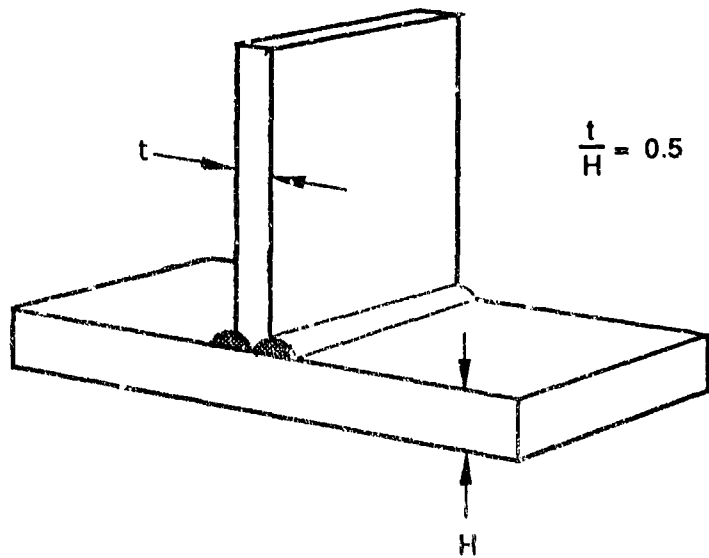
(b) Model configuration

RA-M-2612-96

Figure 1.   Weldment configuration of interest.

The second issue in developing a statistical fracture model for welded, ring-stiffened naval structures involves defining what constitutes a fracture event in the welded stiffener-plate assembly under consideration. In contrast to fracture beginning from preexisting macroscopic cracks, in which the onset of macrocrack extension can provide an unequivocal definition, a fracture event in materials containing only microdefects is more difficult to define and model.

The third issue is the correlation of fracture event and test variables. In an explosively loaded, ring-stiffened structure, loading depends on many parameters such as charge weight, charge standoff, pressure pulse duration, and structure configuration. Although conceivable, a direct multivariable regression model that includes all the loading parameters may prove practically intractable. Therefore, we want to incorporate the effects of all the variables in a single "measure of severity" that would characterize the critical loading needed to cause fracture of the welded joint. An example of such a measure of severity applicable to structures with macrocracks is the stress-intensity factor, the fundamental parameter of linear elastic fracture mechanics. If possible, an analogous parameter should be found that characterizes fracture of the welded joint in ring-stiffened structures and that can serve as a measure of severity in the NAVSWC statistical model.

Finally, as mentioned above, a small-scale dynamic test involving a geometry simpler than that of a ring-stiffened structure, yet promoting weld fracture under equivalent conditions, is desirable for developing statistical dynamic failure models. Moreover, because small-scale welds are difficult and costly to produce, it would be advantageous to avoid welding small-scale model structures and instead to machine the stiffeners from a thicker piece of material. The problem then becomes the design of the stiffener-base plate connection so that fracture will begin at the same location and under the same loading conditions as in the actual weldment.

SRI's research project addresses the four issues discussed above. To simplify the problem, we consider the stiffened plate geometry illustrated in Figure 1b. The pertinent materials of interest for the plate and stiffener are HY-130 steel, in the first phase of the program, and Ti-6Al-4V and Ti-4Al-2V, in the second phase of the program. The specific objectives of the SRI research program are to:

1. Establish scaling laws for predicting the fracture of plates with welded stiffeners in models of different sizes.

2. Define simple parameters that will quantify and correlate the fracture damage produced in the experiments and that can be used in the statistical model developed by NAVSWC.

3. Determine how, for a given model size and for the same loading parameters, fracture of plates with welded stiffeners relates to fracture of plates with machined stiffeners.

4. Propose methods of enforcing the same fracture behavior in plates with welded or machined stiffeners.

TECHNICAL APPROACH

To achieve these objectives, SRI followed the complementary empirical and experimental approach illustrated in Figure 2. We first derived deterministic empirical scaling rules on the basis of simple fracture experiments. Then we interpreted the results by developing and applying a weldment model combined with a local fracture model.

The empirical part of the approach began with characterizing the geometry and microstructure of a family of weldments of various scales to establish in what respects these weldments differ. This information later served as input for developing the weldment model. Next, we investigated the fracture behavior of 1/2-, 1/4-, and 1/8-scale weldments by performing simple static fracture experiments, which allowed convenient monitoring of the test parameters and detailed observations of the fracture events. Properly normalized results of these experiments provided the basis for deriving an empirical fracture scaling rule. We then checked the validity of this rule under dynamic loading by performing a series of explosively loaded experiments on 1/4- and 1/8-scale weldments.

To provide a theoretical basis for the empirical scaling rules, we developed a weldment fracture model in parallel with the experimental work. In a finite element code, we combined a weldment model, which includes the main geometric and strength features of the weldment regions [weld metal, heat-affected zone (HAZ), and base metal], with a local fracture criterion capable of predicting fracture that begins in the absence of a preexisting crack. In particular, the fracture model contains a nonscaling length characteristic of the material.

The model can be used to rationalize the fracture behavior of weldments of various sizes, to safely extrapolate the empirical scaling law to full-scale weldments not investigated in the present program, to assess the effect of different welding processes on fracture behavior, and to guide the choice of an appropriate severity parameter for the NAVSWC statistical fracture model. Finally, we suggest using the model to design machined small-scale specimens that fail under the same loading conditions as welded specimens and that adequately simulate the full-scale ring-stiffened cylindrical structures.
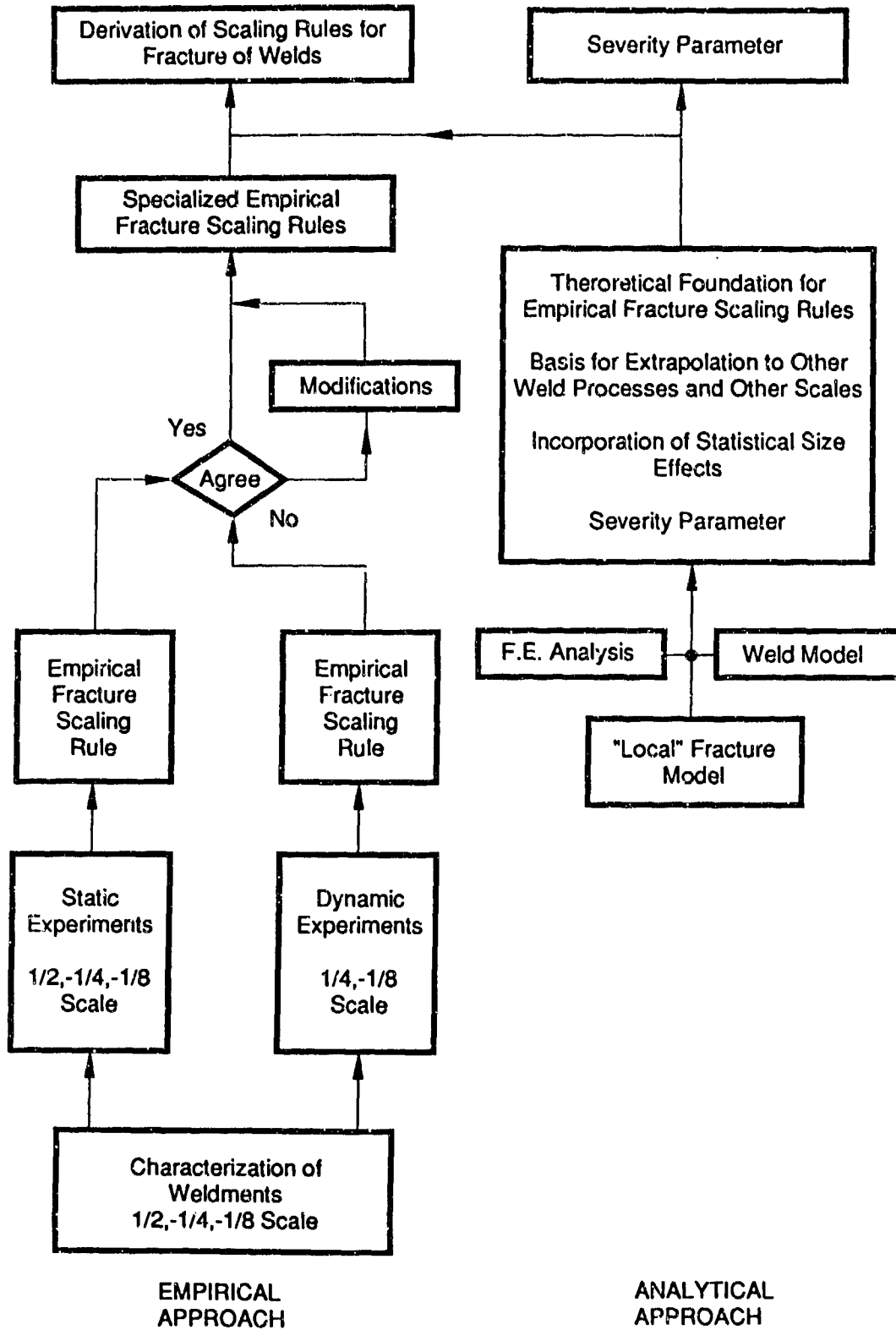
Figure 2. Technical approach to weldment fracture scaling problem.

RM-2612-64

The approach to characterizing T-weldment fracture and deriving scaling rules was first ried with HY-130 steel weldments. This report discusses the development of the necessary perimental and analytical techniques and the results of the investigation of HY-130 steel weldments. Application of the approach to two titanium alloys and the results of that investigation will be presented in another report.

The next four sections of this report summarize the methods used and the results obtained for the main objectives of the research; a detailed discussion of each of these topics can be found in the appendices. The main topics and the corresponding appendices are

- Characterizing HY-130 steel weldments (Appendix A)

- Static fracture experiments (Appendix B)

- Dynamic fracture experiments (Appendix C)

- Modeling experiments and weldment fracture (Appendix D)

The report concludes by stating the fracture scaling rules derived from this research and by making recommendations for future research.

STEEL AND WELD CHARACTERIZATION

CHARACTERIZATION METHOD

We first reviewed the literature to gather a data base on HY-130 steel and weldments, focusing on the strength, ductility, and fracture properties and on the variations in microstructure and gradient of mechanical properties in the weld regions. We complemented this data base by performing smooth and notched round bar tensile tests on selected batches of the HY-130 steel plates used in our investigation. We then fabricated 1/2-, 1/4-, and 1/8-scale welded T-joints from HY-130 steel plates using the gas tungsten arc welding (GTAW) process and 100S weld wire (undermatched welds).

For each scale we measured the weld beads and the heat-affected zone, then produced microhardness maps of the welded joints to obtain an approximate map of the strength variation throughout the joints.

RESULTS

The literature survey demonstrated that in the whole temperature range pertinent to the full-scale ring-stiffened cylindrical structures (0°C and above), fracture of HY-130 steel and most likely the weld metals occurs on the upper shelf of the fracture-temperature transition curve. Therefore, the fracture data we generated at room temperature during the present investigation are also relevant for the actual full-scale structures in service. Moreover, scanning electron microscopy observations have established that on the upper shelf, fracture of HY-130 steel occurs by the nucleation and growth of ductile voids. This observation justifies using a strain-based local fracture criterion when modeling the weldment fracture.

Through selected smooth and notched tensile tests, we verified that published constitutive data and failure envelopes that can be used in conjunction with a strain-based local fracture model for HY-130 steel are relevant for the base material we tested.
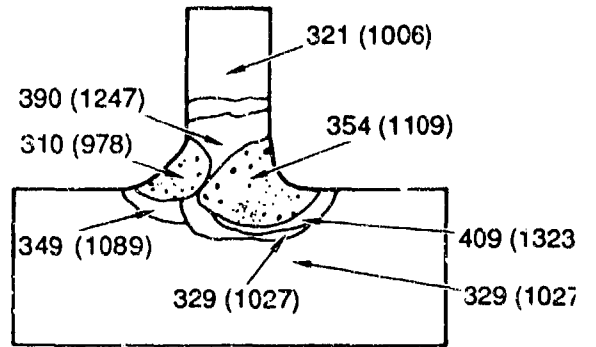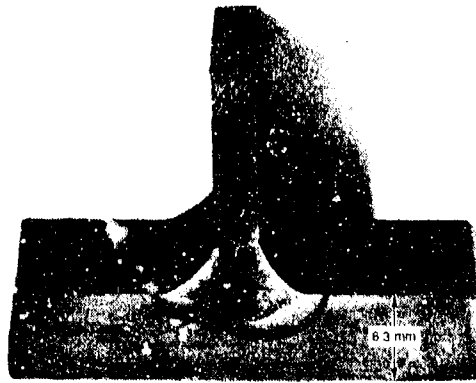
1/8-Scale
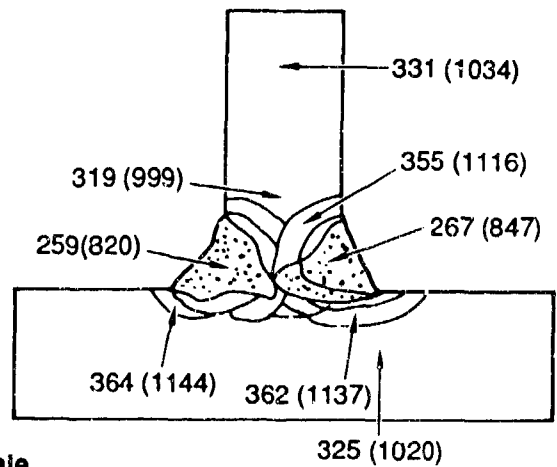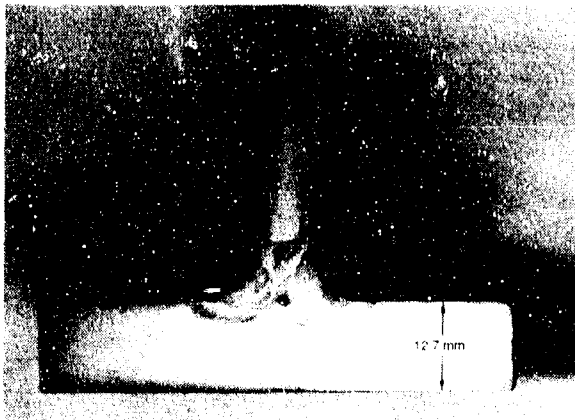
1/4-Scale
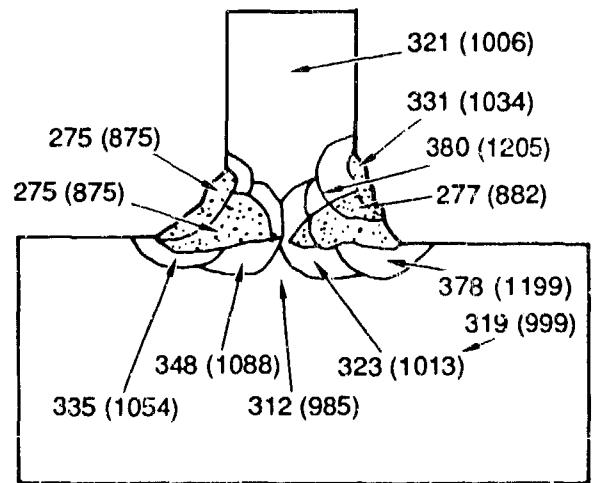
1/2-Scale

RP-2612-34

Figure 3.   Macrographs and 300g diamond pyramid hardness maps for three scales of HY-130 steel/HY-100 GTAW weldments investigated.

8

Macrographs of the cross sections of 1/2-, 1/4-, and 1/8-scale GTAW weldments fabricated at SRI are shown in Figure 3 with hardness maps of the weldment. We made two significant observations during the weld characterization:

1. The dimensions of the various parts of the weldment--weld metal and heat-affected zones--do not scale. In particular, the HAZ width remains approximately the same at all scales.

2. The region of the heat-affected zone at the toe of the weld near the plate surface has the greatest hardness. Although some variability is observed from scale to scale, weldments of the three scales have similar HAZ properties.

These two observations are significant for modeling the weldments and for understanding what factors control where fracture begins.

STATIC FRACTURE EXPERIMENTS

The objective of the static fracture experiments was to derive empirical scaling rules for the range of scales from 1/2 to 1/8. We focused primarily on the conditions controlling the initiation of a macrocrack at the root of the stiffener, although we also made some qualitative observations of macrocrack propagation into the specimen plate.

EXPERIMENTAL METHOD

The configuration for the static bend tests is illustrated in Figure 4. A T-shaped specimen is gripped rigidly at the top of the stiffener and loaded in bending by loads applied symmetrically at the two extremities of the plate.

Two 1/2-, four 1/4-, and eight 1/8-scale specimens were manufactured from HY-130 steel plates and tested under displacement-controlled conditions in a 500-kN servohydraulic machine. The dimensions of the 1/4-scale specimen are indicated in Figure 4. Dimensions for the other two specimen sizes are scaled geometrically, except for the widths, which are tabulated in Figure 4.

During the experiments, we recorded the load applied to the stiffener and the displacement of the plate extremities. We monitored the acoustic emission from the specimen to detect fracture initiation. Posttest measurements of the specimen deformation, with kinematic considerations, provided another method—termed the plastic hinge method—of identifying conditions at fracture initiation (see Appendix B for more details).

The acoustic emission and plastic hinge methods are complementary; the former detects the onset of microscopic fracture (formation of microvoids), whereas the latter indicates the formation of a macroscopic crack that significantly influences the specimen's deformation response. Because we are interested in structural rather than microstructural failure, we adopted the plastic hinge displacement definition of crack initiation.

To compare the results of the static fracture experiments for specimens of different scales, we normalized the displacement by dividing by the specimen plate thickness H, and we normalized the load by multiplying by the factor
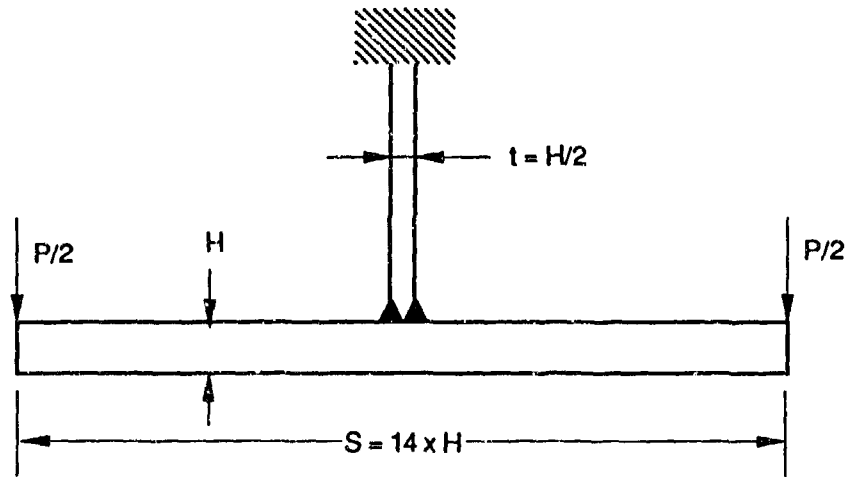
Scale	H (mm)	Width B (mm)
1/8	6.35	50.8
1/4	12.7	88.9
1/2	25.4	152.4

RM-2612-13A

Figure 4.   Configuration for static fracture experiments.

$$\alpha_{load} = \frac{S}{\sigma_Y B H^2}$$

where σ_Y is the yield stress and B and H are the plate width and thickness, respectively.

RESULTS

We observed the same fracture morphology in all static fracture experiments. As illustrated in Figure 5, a crack initiated in the heat-affected zone of the specimen plate at the toe of the weld and propagated through the HAZ or along the HAZ/base metal boundary, then abruptly changed direction to propagate across the specimen plate. We established that the change in propagation direction is associated with an arrest and blunting of the initial crack. In all but one experiment, crack propagation through the plate was stable.

The results of the bend experiments are summarized in Figure 6, which plots the normalized load-deflection curve of the specimens with the largest and smallest energy absorption for each of the three scales investigated. The two 1/2-scale experiments produced almost identical results. Also plotted in Figure 6 are the ranges of displacement at which macroscopic crack extension began.

Figure 6 indicates that although the fully plastic load for the 1/8- and 1/4-scale specimens is essentially the same, that for the 1/2-scale specimens is about 10 percent smaller. A systematic evaluation of all the factors that could affect the fully plastic load suggests (see Appendix B) that the observed difference probably arises mainly from scale-to-scale variations in geometry and relative sizes, and in yield and flow strength gradients in the weldment region. This conclusion will need confirmation by more detailed geometric characterization and hardness mapping of selected weldments.

Figure 6 also shows significant scatter in the static test results, particularly in terms of the displacement at the initiation of macroscopic crack growth. However, if average values of the displacement values at initiation are considered, the static test results indicate that the beginning of macroscopic crack extension at the toe of the weld occurs at approximately the same scaled displacement.

The static fracture experiments demonstrate that, within the scattered data and provided that strength differences in the weldment region are accounted for in the normalization process, fracture initiation in the weldments follows replica scaling.
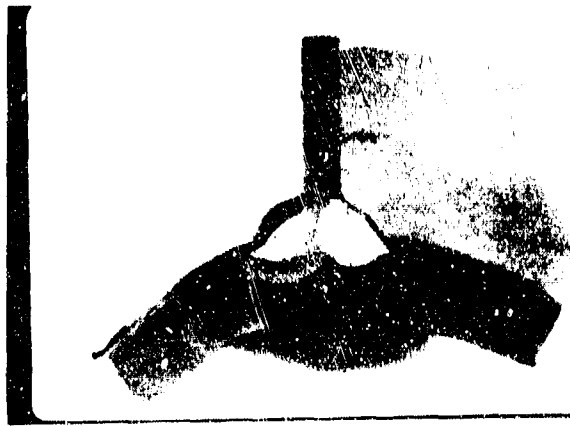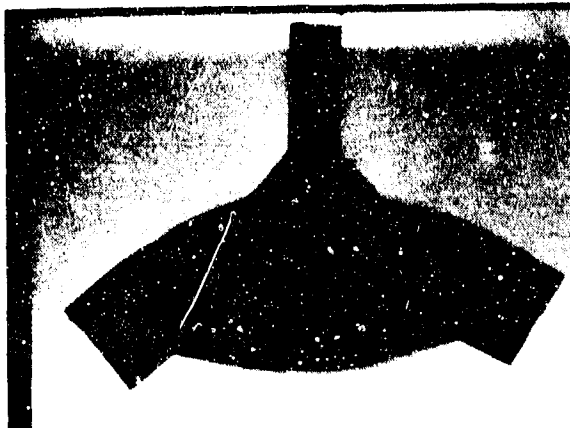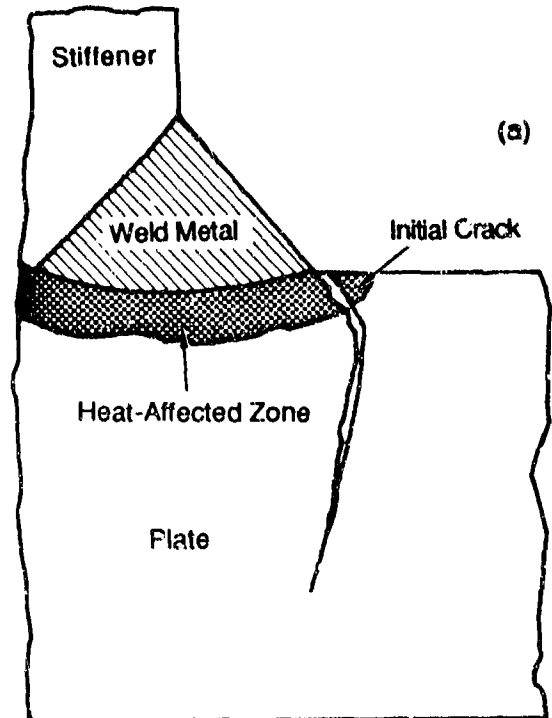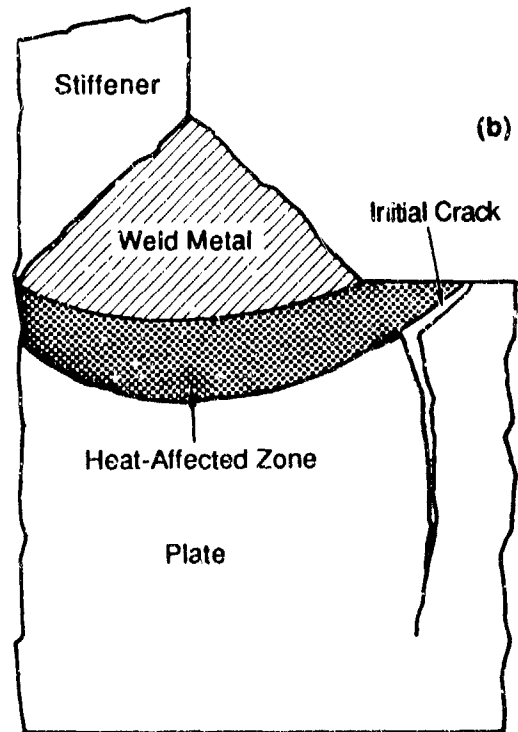
Figure 5.   Cross section of statically fractured specimens showing crack path.
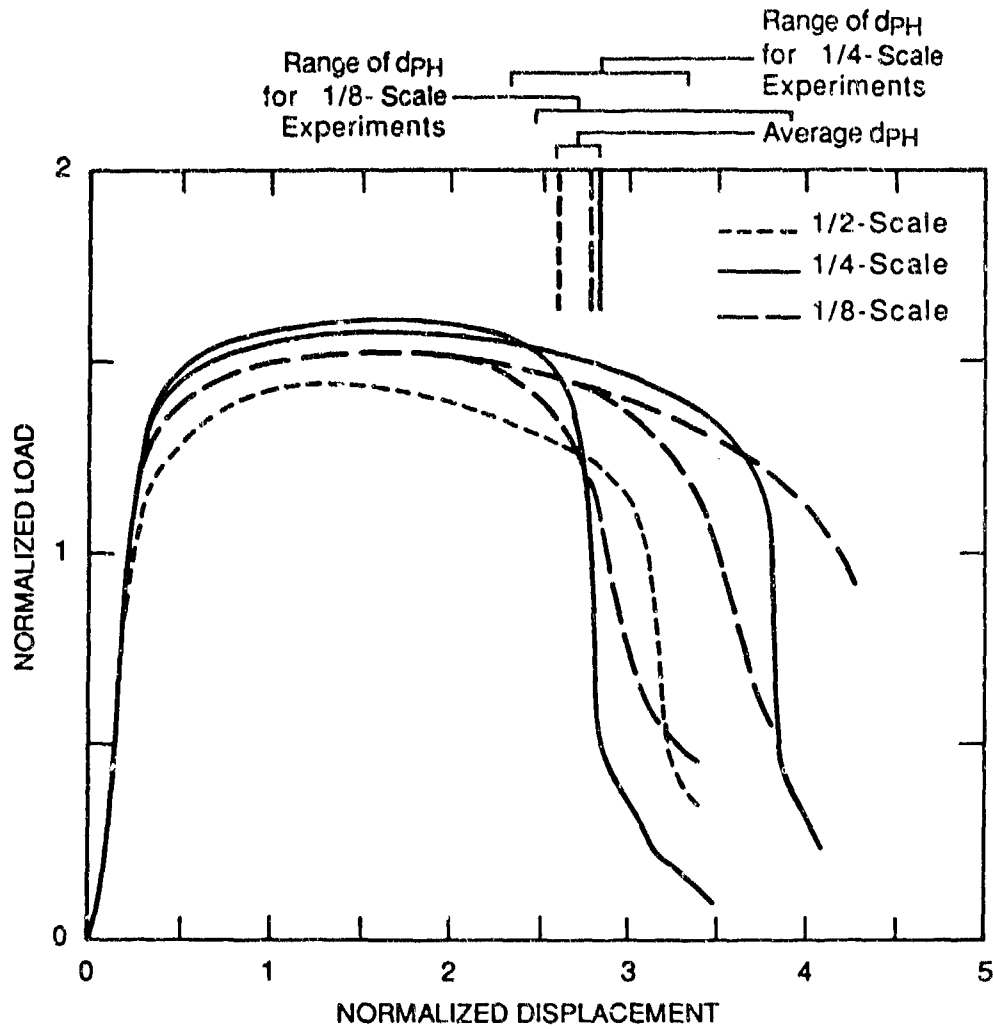
Figure 6. Summary and comparison of results of the static fracture experiments.

RA-m-2612-16A

This conclusion is significant for extrapolating small-scale experimental data to large-scale welded structures and is consistent with predictions based on local fracture models.

Estimates based on the experimental load-displacement curves of the plastic energy dissipated during the crack initiation and propagation phases of fracture indicate that the energy expended to propagate the crack through about 70 percent of the plate thickness is only about 20-25 percent of the total energy dissipated during the test. Therefore, although theoretical considerations suggest that there will always be non-replica scaling effects in the crack extension phase of fracture, the influence of those effects on the total energy dissipated in the fracture process is slight compared with the scatter in the experimental data. We confirmed this conclusion with a J-based elastoplastic analysis of crack growth in HY-130 steel (see Appendix D).

The scatter in the experimental fracture data is not due to experimental uncertainties, nor to the effect of residual stresses in the weldment, because the large plastic strains redistribute and wipe out those residual stresses long before the onset of fracture. Rather, we believe the scatter in data is due to the intrinsic scatter in geometric and material properties of the weldments, as suggested by finite element simulations. More work will be needed to establish the origin of the scatter with any certainty .

In summary, the static fracture of 1/8-, 1/4-, and 1/2-scale weldments tested in this investigation followed replica scaling. We suggest two approaches to account for the observed small differences in load limits: (1) The fully plastic load for each scale could be measured directly, because the required experiments would be relatively easy to perform, even for full-scale weldments; and (2) the load limits could be determined by estimating relative size differences and strength gradients in each scale of weldment using macrographs of cross sections and detailed hardness maps, than by using these geometric and strength distribution data in numerical simulations of the weldments to calculate the fully plastic load.

DYNAMIC FRACTURE EXPERIMENTS

EXPERIMENTAL PROCEDURE

We performed dynamic fracture experiments using an explosive loading technique to produce loading rates comparable to those achieved in structures loaded by underwater explosions. The specimen for the dynamic fracture experiments consisted of a slotted base plate with two symmetrically positioned stiffeners, as shown in Figure 7. Figure 7a shows the 1/4-scale specimen, whereas Figure 7b shows the specimen dimensions. The schematic of the loading arrangement is shown in Figure 8a; the actual fixture is shown in Figure 8b.

Each stiffener is rigidly bolted to an independent E-shaped yoke; the specimen plate is bolted to a steel die, which, in turn, is rigidly attached to a base plate. The center of the specimen plate between the two slots is loaded with strips of sheet explosives backed by blocks of polymethylmethacrylate (PMMA), which increase the impulse delivered to the plate for a given explosive sheet thickness. With this test arrangement, only the center of the specimen plate is significantly deformed during the experiments, whereas the portion supported by the die acts as a reaction frame, inducing membrane stresses in the plate. We constructed fixtures to load specimens corresponding to 1/4- and 1/8-scale of the full scale structural element.

We tested six 1/4- and four 1/8-scale specimens; only two 1/8-scale specimens yielded valid fracture results. The specimens were instrumented with contact pins to measure the deflection velocity of the plate's center line. More pins were placed beneath the plate at the weldment location to detect the instant of complete fracture. We also instrumented selected 1/4-scale experiments with strain gages. The center line velocity measurements characterized the impulse delivered to the specimen and were used as input for numerical simulations of the experiments.

In performing the explosive experiments, we varied the explosive thickness and hence the total impulse imparted to the specimen, and bracketed the conditions for starting a crack in the weldment region and for completely propagating it through the specimen plate. Fracture conditions were assessed in terms of the explosive thickness needed and the specimen center deflection at the instant of crack initiation or complete propagation through the plate. We first bracketed the

(a) 1/4-Scale specimen

Through-the-
Thickness
Saw Cuts

177.8

12.7

6.35

12.7

76.2

101.6

114.3

31.7

304.8

127

25.4

12.7

25.4

12.7

330.2
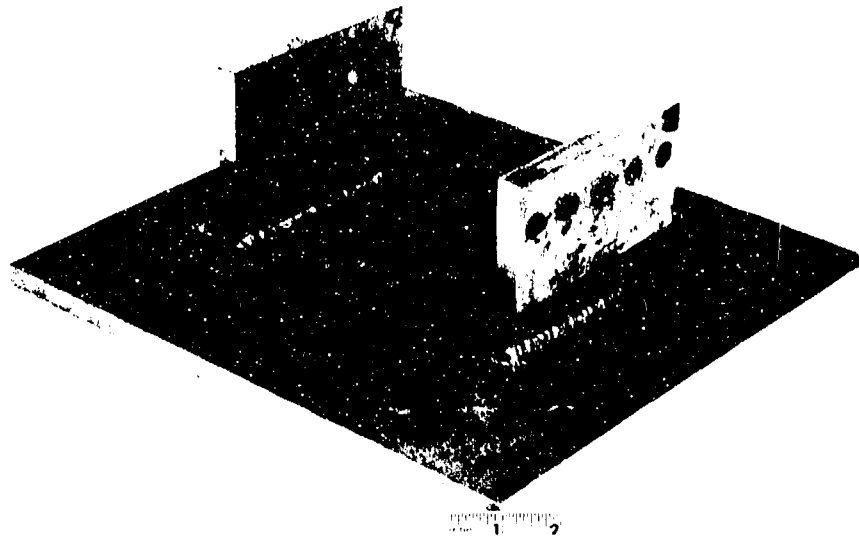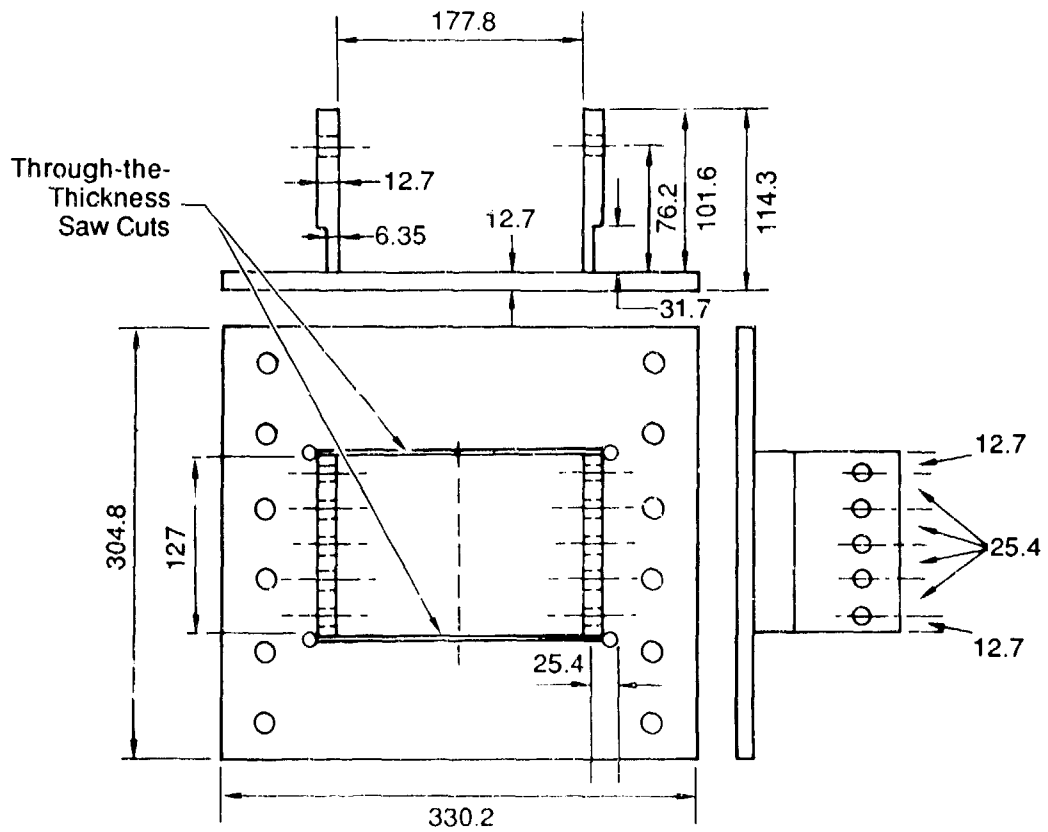
(b) Dimensions (in mm) of 1/4-scale specimen

RP-2612-7A

Figure 7.   Specimen for dynamic fracture experiments.
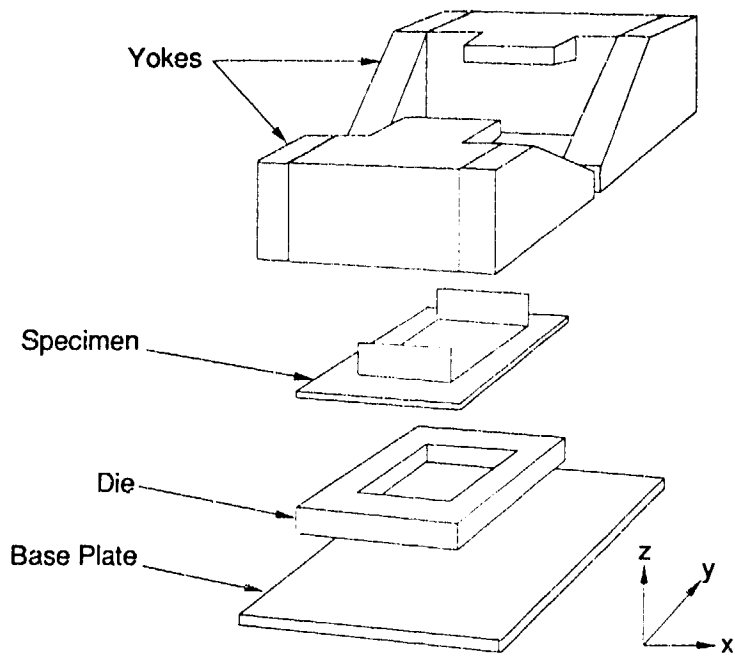
18

(a) Schematic of fixture
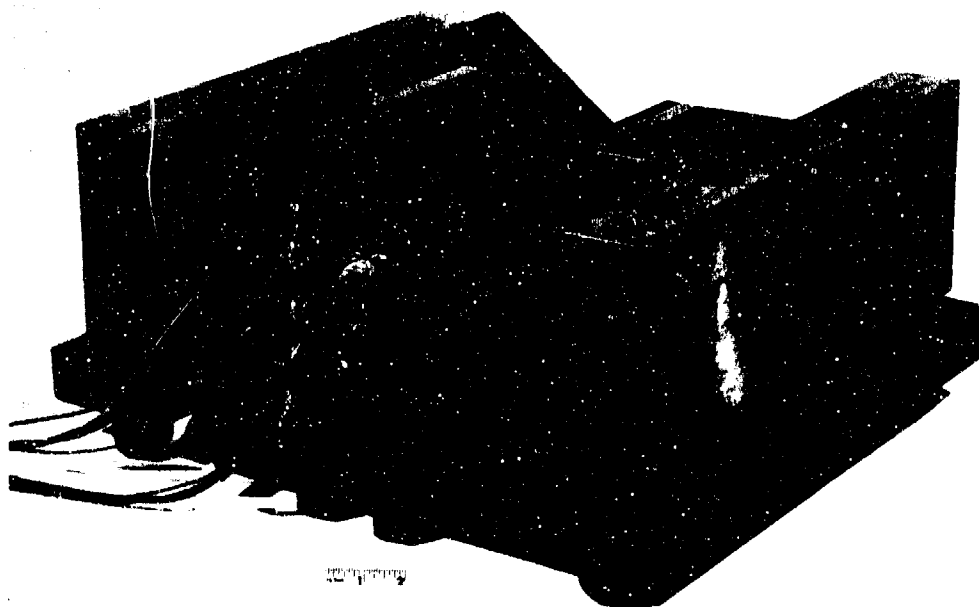
(b) Specimen-fixture assembly for 1/4-scale experiments

RP-2612-8A

Figure 8.   Loading fixture for dynamic fracture experiments.

explosive thicknesses that produced incipient and complete fracture in the 1/4-scale specimens; then we scaled those conditions geometrically for the 1/8-scale experiments.

RESULTS

The results of the explosive fracture experiments are summarized in Figures 9 and 10 and Table 1. Figure 9 plots the normalized deflection history for all 12 specimens tested and represents their structural responses. The normalization procedure is detailed in Appendix C and accounts for differences in specimen scale, material properties, explosive thickness, and specific energy. Figure 10 plots the normalized deflection of the specimens reconstructed from posttest measurements as a function of normalized explosive thickness. Both quantities were normalized by the specimen plate thickness. Figure 10 also indicates domains of partial or complete fracture and thus can be regarded as a failure map.

TABLE 1. RESULTS OF DYNAMIC FRACTURE EXPERIMENTS

HY-130 EXPERIMENT NO.	EXPLOSIVE THICKNESS (MM)	EXPLOSIVE TYPE	INITIAL VELOCITY (M/S)	NORMALIZED PLATE CENTER DEFLECTION "AT FRACTURE"	COMMENTS
WE4-1	2.87	D	226	1.90	Fracture through one side
	3.05	C			only; stiffener broke on other side
WE4-2	1.08	C	115	-	No fracture
WE4-3	1.63	C	142	-	No fracture
WE4-4	2.54	C	187	1.90	Partial fracture
WE4-5	2.54	C	192	1.85	Partial fracture
WE4-6	2.98	C	216	2.24	Fracture through both sides
WE8-1	1.36	C	211	-	No fracture; abnormal plate anchoring bolt deformation
WE8-2	1.65	C	235	-	Incipient fracture, plate anchoring bolt fracture
WE8-3	1.65	C	234	2.25	Complete fracture
WE8-4	1.36	C	227	1.98	Partial fracture

Figure 9 shows that the responses of specimens of different scales are appropriately normalized because they reduce to the same curve for identical initial velocities. Figure 9 also suggests that during early times the structural response of the specimen is the same for all initial velocities and scales. At later times there appear to be at least two response modes, one for low (< 150 m/s) and one for high (> 150 m/s) initial velocities. More work is needed to establish the details of the specimen structural response.
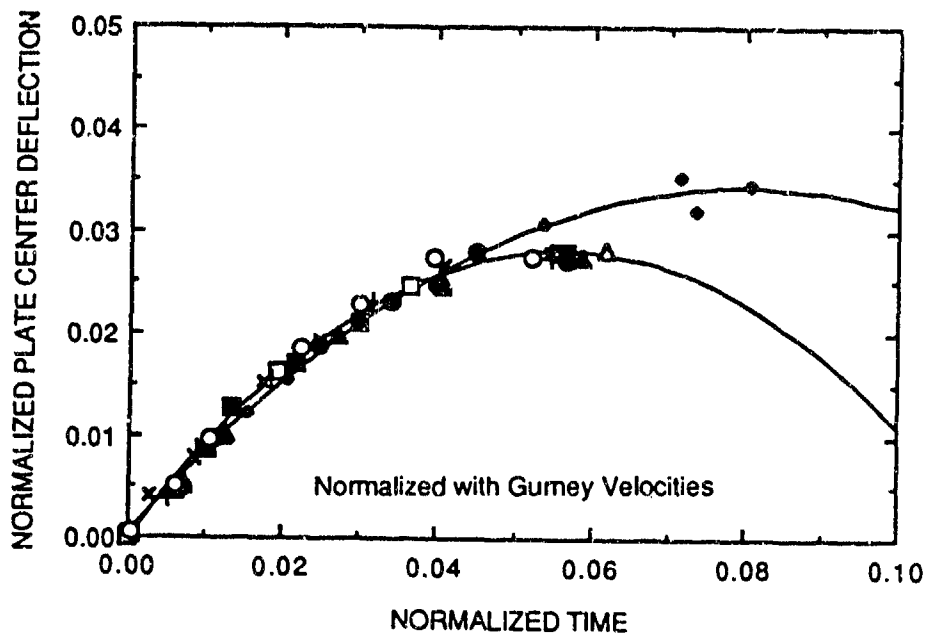
Figure 9. Normalized plate center deflection histories for dynamic fracture experiments.

Finite element simulations show good agreement between the experimental and the calculated specimen deflections, thus demonstrating that the measurements performed provide enough information for faithful simulations of the experiments. The simulations also indicate strain rates in the weldment region on the order of several thousands per second.

In all the specimens in which fracture was induced, the morphology of fracture and the fracture path were similar to those observed in the static fracture experiments. This observation, along with the insensitivity of the stress-strain curve to the loading rate (see Appendix A) and the estimates of the strains to failure obtained from finite element simulations, indicates that weldment failure is not overly rate-sensitive for the range of strain rates investigated and that the same local fracture model might be used for both static and dynamic fracture experiments. The 1/8-scale experiments, in which the data from two specimens were invalidated because clamping bolts yielded extensively or fractured prematurely, showed that the clamping arrangement has a profound effect on fracture behavior.

As can be seen in Figure 10, the center plate deflection at which incipient fracture was induced, normalized by the plate thickness of the specimen, is essentially the same in the 1/4- and the 1/8-scale specimens. A similar result holds true for the normalized center plate deflection needed to induce complete plate fracture. Moreover, the explosive thickness needed to produce these deflections also scales geometrically, as we anticipated from dynamics considerations.

On the basis of the preceding (limited) results, we conclude that in first approximation, fracture of explosively loaded HY-130 steel weldments follows replica scaling, as did fracture under quasi-static loading conditions. However, more research would be desirable to confirm this conclusion, because these experiments indicate a certain degree of scatter.
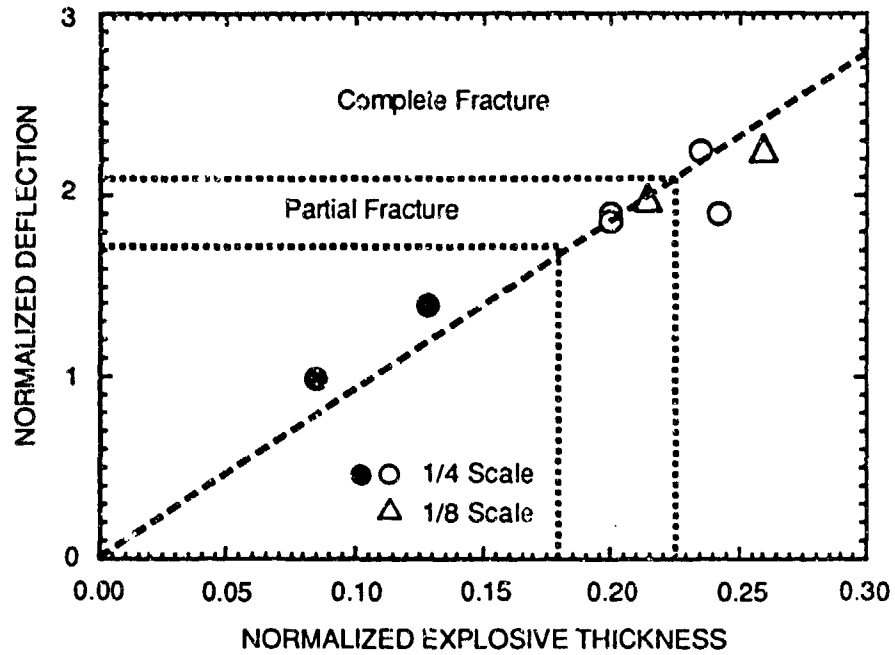
Figure 10. Fracture envelope for HY-130 steel weldments established on the basis of the dynamic fracture experiments.

(Dashed straight line represents predicted maximum deflection in the absence of fracture.)

MODELING WELDMENT FRACTURE

OBJECTIVES AND MODELING APPROACH

The objective of the modeling task was to provide both an understanding of the specimen structural response in the static and dynamic fracture experiments and an analytical foundation for the empirical scaling rules derived from the experimental results.

Our approach in the modeling task was to perform finite element simulations of the static and dynamic experiments and to develop a fracture model for the weldment combining the main geometric and strength features of the weldment in a finite element formulation with a strain based local fracture criterion. The model allows the prediction of fracture initiation in weldments without a preexisting crack and natural crack propagation without prescribing *a priori* the crack path. The model also contains a constant characteristic material length that introduces nonscaling effects. We complemented this modeling work by performing an elastoplastic analysis of crack growth in HY-130 steel bend specimens to estimate nonscaling effects associated with crack growth.

RESULTS

Finite Element Simulations of Static Fracture Experiments

The finite element simulations of the static fracture experiments showed that geometric softening, associated with large specimen deformations, dominates most deformation of the HY-130 static fracture specimens. This geometric softening should not be confused with softening introduced by macrocrack nucleation, which occurred only in the last phase of the experiments.

The finite element simulations also showed that, as we anticipated on the basis of the experimental observations, the most severe straining of the weldment—and, for that matter, of the specimen—occurs at the toe of the weld metal bead, in the HAZ. Both the equivalent plastic strain and the stress triaxiality are maximal at that location.

The parametric study, in which we varied the weldment geometry and the strength gradients across the weldment, revealed that variations of these parameters consistent with the results of the weldment characterization task can result in significant differences of 25 percent or

more in specimen displacement at the beginning of fracture. This result provides a possible explanation for the large scatter in the data from the static fracture experiments.

Finally, good agreement of the calculated and experimental load-deflection curves demonstrates that a two-dimensional plane strain simulation of the experiments is appropriate.

Finite Element Simulations of Dynamic Fracture Experiments

Analyzing the dynamic fracture experiments demonstrated that the simulation method gives a good approximation of the actual specimen behavior and that measuring the plate center velocity history provides adequate experimental input for the simulations. The observed differences in the calculated and measured final deformed shape may be due to differences in the boundary conditions of the simulations and the experiments. These differences could be minimized by introducing more compliant boundary conditions at the edge of the plate in the calculations to better simulate the actual clamping conditions.

The strain rates at the base of the stiffener calculated in the simulations are high, on the order of several thousands per second. The calculated stress and strain fields indicate that in spite of the difference in loading mode and strain rate, fracture in the dynamic experiments occurs at strain and triaxiality levels consistent with those in the static experiments, suggesting that a strain-based ductile fracture model appropriate for the static fracture experiments may also be applicable to the dynamic experiments.

Weldment Fracture Model

The weldment fracture model consists of three components, as illustrated in Figure 11: (1) a geometric and strength model of the weldment, based on metallographic observations and hardness measurements; and (2) a strain-based fracture criterion, both implemented in (3) a finite element formulation. The fracture criterion is the simplest form of a ductile fracture criterion. It assumes that failure of a material element of characteristic size R_{MIC} occurs once the element has accumulated a critical plastic strain, a function of the state of stress experienced by the element during straining. Mathematically, fracture of the element occurs when

$$D = \int \frac{d\varepsilon_{eq}^P}{\varepsilon_c(\sigma_{mean}/\sigma_{eq})} = 1 \quad \text{over RMIC}$$

where D can be regarded as a normalized damage parameter, ε_{eq}^P is the equivalent plastic strain, and $\varepsilon_c(\sigma_{mean}/\sigma_{eq})$ is the critical failure strain for a given strain triaxiality $\sigma_{mean}/\sigma_{eq}$.

(a) Local Fracture Model

$$D = \int \frac{d\varepsilon_p}{\varepsilon_c(\sigma_m/\sigma_{eq})} = 1 \text{ over } R_{MIC}$$

ε_c = Critical fracture strain, depends on the state of stress

R_{MIC} = Characteristic microstructural dimension

(b) Geometric Model

(c) Finite Element Model
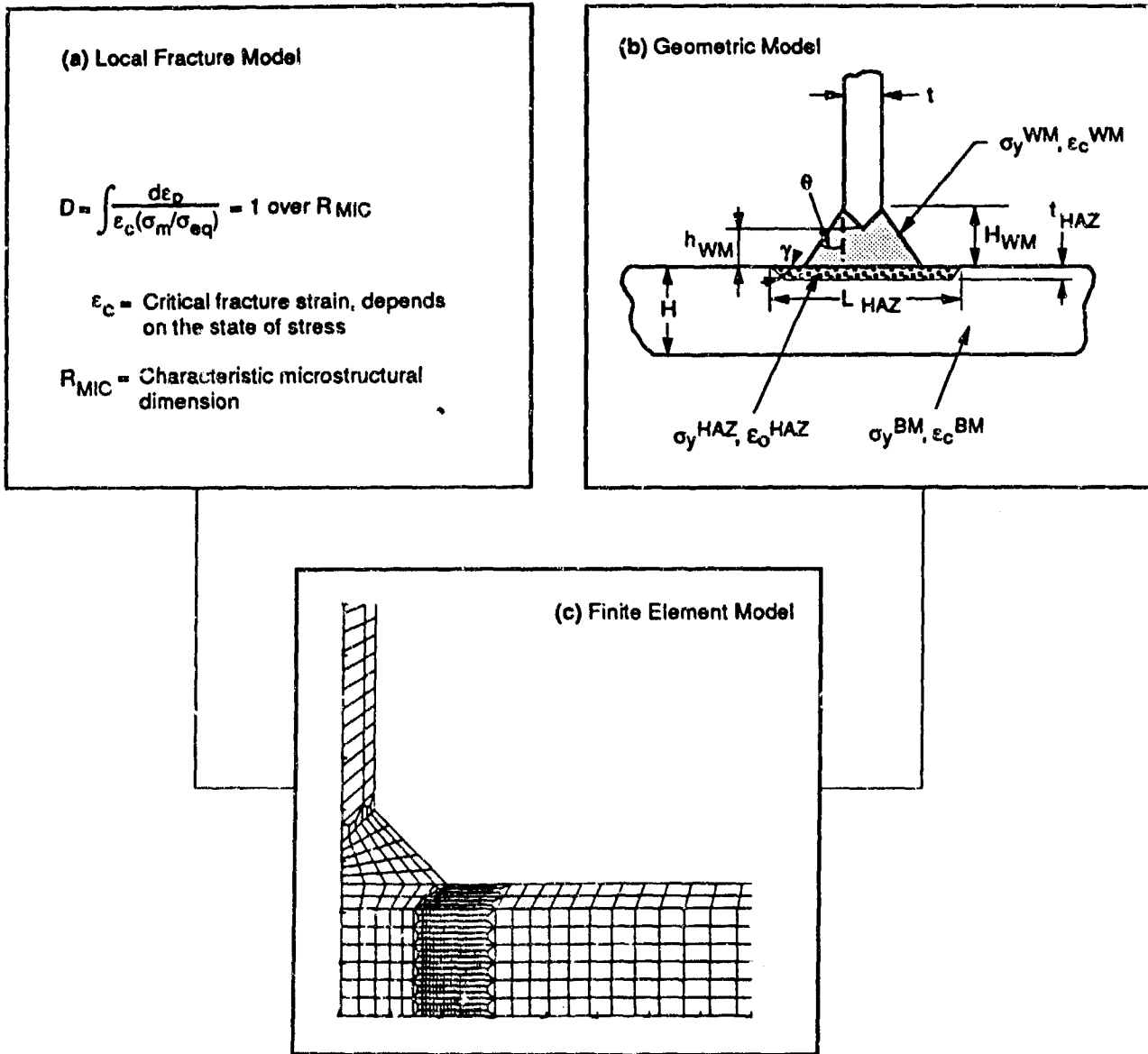
RM-2612-144

Figure 11.   Elements of the HY-130 weldment fracture model.

27

Two key features of the local fracture criterion are that (1) the critical failure strain is a function of the stress triaxiality that can be measured experimentally, and (2) the criterion contains a non-scaling material parameter R_{MIC} and hence implies non-replica scaling effects for fracture.

We implemented the weldment model and the local fracture criterion in the NIKE2D finite element code and performed preliminary simulations of a 1/4-scale static fracture experiment. Figure 12a shows contours of the elements that fully cracked at an applied normalized displacement of 4, whereas Figure 12b compares the calculated and measured load-displacement curves. The results of the simulation show good qualitative agreement with the experiment. The weldment fracture model correctly predicts the location of crack initiation. The overall crack path in the specimen is also predicted correctly, although details are somewhat different in the experiment and the simulation (compare Figures 5 and 12a).

We think the differences in the crack path prediction are caused by the somewhat coarse mesh used in the simulation and by the difference in boundary conditions in the simulation and in the experiments once crack extension occurs. The model predicts a displacement at which the HAZ is completely penetrated by the crack, which agrees well with d_{PH}, the experimental value of the displacement at the initiation of a macrocrack. On the other hand, the model overpredicts the fracture resistance of the weldment, and the final load drop-off occurs later in the simulation than in the experiment. We believe the difference is due to the limited experimental failure data used to calibrate the model. In particular, values of the failure strain for high stress triaxiality (>1.5) are desirable. The mesh size used in the simulation also influenced the results by artificially broadening the damage zone.

After minor modifications to the failure envelope and the mesh size, the model will be ready for a detailed investigation of fracture in specimens of different scales. By varying the boundary and geometric conditions, as well as introducing different mechanical and fracture properties for the weldment regions in the finite element simulations, we can evaluate the effects of experimental conditions, geometric imperfections, and material variability on fracture behavior. By simulating the fracture of weldments of different scales with the weldment fracture model, we can establish fracture scaling rules and compare them with the experimentally derived rules. We can then use the model to make fracture predictions for scales not experimentally investigated, and we can provide a theoretical rationale for the empirical scaling rules.
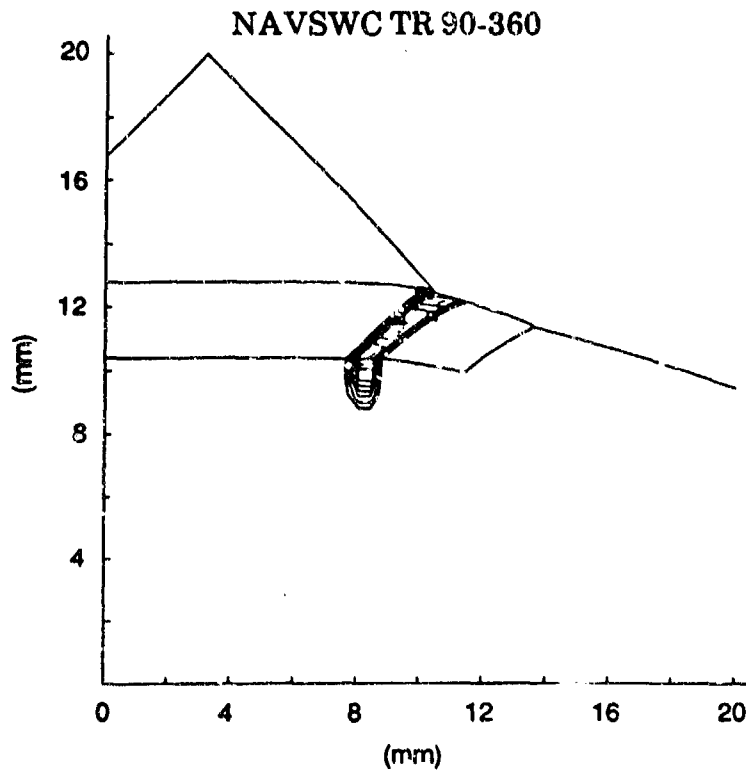
(a) Contours of damage greater than 1 at $d_{NORM} = 4$
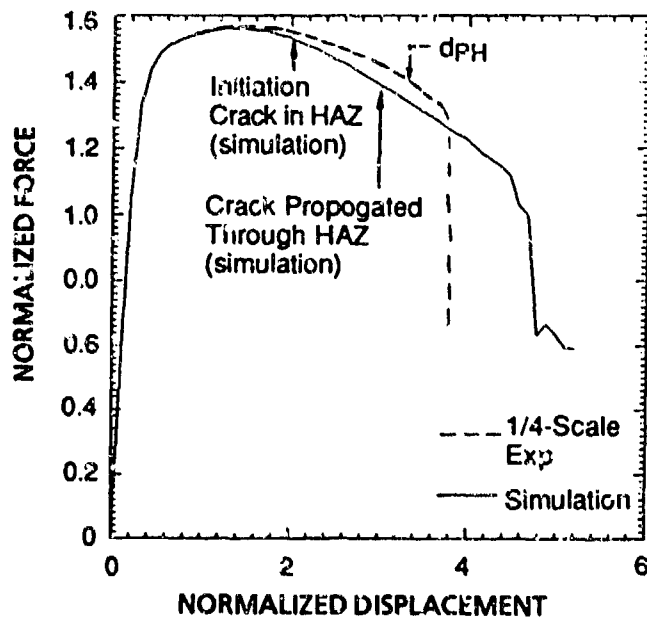
(b) Comparison of simulated and experimental
load-displacement curves

RA-2612-145

Figure 12.   Results of simulation of 1/4-Scale static fracture experiment
using HY-130 steel weldment fracture model.

To investigate the effect of different welding processes, we can vary the weld geometry in the finite element mesh and the material properties in the local fracture model. Finally, using the model in simulations of various structural configurations, we can relate structure deformation to the fracture processes in the weldment to define a suitable severity parameter for use in the statistical model being developed by NAVSWC.

ELASTOPLASTIC FRACTURE ANALYSIS

The elastoplastic fracture analysis of crack extension in HY-130 steel three-point-bend specimens showed that although non-replica scaling effects arise during crack extension, the differences in energy dissipation caused by the nonscaling are only a percentage point or so of the total fracture energy. Similarly, the differences in displacement are also only a few percentage points of the total needed to begin and grow the crack. These differences are always small compared with the scatter in data, and hence they can be ignored.

CONCLUSIONS AND RECOMMENDATIONS

The present investigation has laid the groundwork for reaching the program objectives stated in the introduction to this report. In particular, the investigation yielded the following results and conclusions:

- We established a reliable experimental and analytical approach to evaluating the fracture of welded structures of different sizes and extrapolating results from small-scale experiments to large-scale welded structures. This approach now stands ready for application to weldments in other metallic alloys, such as titanium alloys.

- HY-130 steel undermatched (100S weld wire) welded T-joints of 1/8-, 1/4-, and 1/2-scale have the same fracture morphologies when loaded statically. Dynamic loading of 1/8- and 1/4-scale specimens also produces the same fracture morphology at both scales, similar to those seen with static loading.

- In first approximation and given the scatter in the experimental results, crack initiation and propagation in undermatched HY-130 steel welded T-joints follow replica scaling for both static and dynamic loading.

- Experimental results suggest that differences in relative size and in strength gradients in weldments of different sizes could introduce nonreplica scaling of the fully plastic load for the weldment. The small resulting differences can be accounted for by detailed mapping of the weldment geometry and of the strength gradient (by means of macrographs and of hardness measurements) or by direct measurement of the fully plastic loads for simple loading configurations.

- Analyzing of the crack extension phase of fracture in HY-130 steel indicates that crack extension does not strictly follow replica scaling, but the resulting scale-to-scale differences in fracture energy are slight compared with the total energy expended to fracture the weldment and with the scatter in experimental data.

- For a given scale, weldment-to-weldment variations in weld bead geometry can induce significant differences in weldment deformation at the onset of fracture and may account for some of the scatter in the experimental data.

- A weldment fracture model, including a stress-modified strain-based fracture criterion, allows reliable simulations of static crack initiation and propagation in HY-130 steel welded T-joints. The model can be used to extrapolate scaling rules to weldment sizes not tested in the program, to assess the effect of geometric and strength variability on weldment fracture, and to define simple parameters for characterizing fracture in the analysis of ring-stiffened welded structures.

To provide more support and verification for the results and conclusions of this study, we recommend that further research be conducted on the fracture scaling of HY-130 steel weldments. The objectives of this research should be to provide reliable extrapolation of the empirical scaling rules to larger scale weldments and to estimate more accurately the magnitude of non-replica scaling effects. We recommend that the following specific tasks be undertaken:

- Analyze a full-scale HY-130 steel field weldment to establish the geometry of the various weldment regions and to map out the strength gradients. These data will then be compared with those generated in the present investigation and will serve as input in the model of the full-scale weldment.

- Using the weldment model developed under the current program, simulate the fracture of HY-130 steel weldments of various scales to extrapolate the empirical scaling rules to larger scales and to provide quantitative estimates of non-replica scaling effects associated with crack extension.

- Perform other dynamic fracture experiments on 1/8- and possibly 1/2-scale specimens to augment the dynamic fracture data base and to define more precisely the conditions for fracture at various scales.

- Evaluate the suitability of the weldment fracture model for predicting fracture under dynamic loading and introduce necessary modifications to account for possible loading rate effects.

The experimental tools and analytical methods described in this report have applicability beyond the scope of the fracture scaling behavior of welded HY-130 steel T-joints. In particular, we believe the weldment fracture model could be useful in optimizing new weld designs and welding procedures for advanced high-strength, low-alloy (HSLA) steels now under consideration by the United States Navy.

APPENDIX A: MATERIAL PROPERTIES OF HY-130 STEEL AND ITS WELDMENTS

CONTENTS

APPENDIX A

MATERIAL PROPERTIES OF HY-130 STEEL AND ITS WELDMENTS

INTRODUCTION

In this section we report on the properties of HY-130 steel and its weldments, as well as some of the characteristics of the welds tested in this investigation. The properties of HY-130 steel were obtained from a survey of the literature, specification sheets provided by the Naval Surface Warfare Center (NAVSWC), and experiments performed in the course of the investigation.

The objective of the literature search was to gather information on the stress-strain and fracture behavior of HY-130 steel as a function of the loading rate and temperature in support of the experiments and the modeling work to be performed in the investigation. We also sought information about the microstructural, mechanical, and fracture behavior of HY-130 steel weldments to guide the design and interpretation of our experiments.

MATERIAL PROCUREMENT

The material for this research program was supplied to SRI by NAVSWC in the following form:

- Six HY-130 steel plates, 203 by 406 by 41 mm (8 by 16 by 1.63 in.) each.

- Six HY-130 steel plates, 406 by 762 by 12.7 mm (16 by 30 by 0.5 in.) each.

- Two HY-130 steel plates, 381 by 381 by 6.4 mm (15 by 15 by 0.25 in.) each.

The origin, heat treatment, and specifications for these steel plates are not available, but we assume they meet specifications for HY-130 steel and the standard Mil-S-23471A.

NAVSWC also sent SRI one 30-lb. spool of 0.062-in. 100S weld wire and one 10-lb. spool of 0.030-in. 100S weld wire for preparing specimens for investigating welded T-joints, and two plates of HY-130 steel, 381 by 762 by 50.8 mm (15 by 30 by 2 in.) produced by Lukens Steel Co. were transferred from Mare Island Naval Shipyard to SRI. The chemical composition of these plates is given in Table A-1, and their mechanical properties are summarized in Table A-2.

TABLE A-1. COMPOSITION OF HY-130 STEEL PLATES PROCURED FROM LUKENS STEEL CO. (MELT C6161, SLAB 4C) AND SUPPLIED BY MARE ISLAND SHIPYARDS

C	Mn	P	S	Cu	Ni	Cr	Mo	V	Ti
0.1	0.73	0.008	0.003	0.13	0.32	4.97	0.40	0.081	0.002

TABLE A-2. MECHANICAL PROPERTIES OF HY-130 STEEL PLATES PROCURED FROM LUKENS STEEL CO. (MELT C6161, SLAB 4C) AND SUPPLIED BY MARE ISLAND SHIPYARDS

Orientation	Yield Strength (MPa)	Tensile Strength (MPa)	Elongation (% in 50 mm)	Reduction of Area (%)	21°C CVN (J)	-18°C CVN (J)
TX	992	1016	16.0	66.1	124	118
BX	986	1022	16.0	64.8	132	126

The data in these tables were assembled from the Lukens Test Certificate Sheets and excerpts from a report forwarded by Mare Island.

MECHANICAL PROPERTIES OF HY-130 STEEL

In this section we compile mechanical properties data obtained from the literature and from limited testing at SRI. For most of the references reviewed, the chemical composition of the material tested differed only marginally from the composition listed in Table A-1. However, the heat treatment was mentioned in only three reports,[A-1–A-3] The first two list the following heat treatment:

1. Heat to 982°C; water-quench.

2. Temper 1 hr at 566°C; water-quench.

This heat treatment results in a Rockwell-C hardness of 31 and a tempered martensite microstructure with a prior austenite average grain size of 12.5 μm. On the other hand, Joyce and Gudas[A-3] quote a different heat treatment:

1. Hold 1.5 hr at 830°C; water-quench.

2. Temper 1.5 hr at 630°C; water-quench.

More information on heat-treatment schedules is most likely available from the literature, but no specific search was undertaken for the metallurgical characteristics of HY-130 steel. As a

guide to evaluating the effects of variations in heat-treatment schedules, the isothermal transformation diagram obtained from U S. Steel data sheets[A-4] is reproduced in Figure A-1.

Data from Literature Review

Tensile Data. A summary of static tensile data compiled from the literature review is shown in Table A-3. The results for temperatures ranging from -192°C to 148°C are included. Typical nominal and true static stress-strain curves, excerpted from U.S. Steel data sheets,[A-5] are shown in Figure A-2.

The static data indicate only a mild hardening for HY-130 steel but a strong dependence of the yield and flow strength on temperature. Furthermore, it appears that, up to 50 mm, plate thickness has little influence on achievable strength levels and ductilities.

Dynamic tensile data for HY-130 steel have been reported by others.[A-6,A-7] From Lindholm and Hargreaves,[A-6] the results of tensile experiments performed with a servohydraulic machine at strain rates of 0.03, 0.3, 2.5, and 15 s^{-1} are shown in Figure A-3. The data demonstrate that within this strain rate range, HY-130 steel displays essentially no strain rate sensitivity.

TABLE A-3. TENSILE DATA FOR HY-130 STEEL COMPILED FROM THE LITERATURE

Yield Strength (MPa)	Ultimate Strength (MPa)	Elongation (%)	Reduction of Area (%)	Temperature (°C)	Plate Thickness (mm)	Orientation[a]	Reference
1241	1307	25.7	51.0	-192	25.0	-	1, 2
1040	1121	22.0	58.1	-120	25.0	-	1, 2
982	1044	21.1	60.1	-80	25.0	-	1, 2
956	1012	21.3	64.7	-35	25.0	-	1, 2
898	940	27.0	64.7	20	25.0	-	1, 2
852	910	-	-	148	25.0	-	1, 2
937	978	21.0	55.0	20	25.0	-	3
972	1034	19.0	64.0	20	25.0	-	3
896-1034	-	14.0	-	20	9.5-14.3	-	5
896-999	-	15.0	50.0	20	15.9-102	-	5
957	1025	20.3	67.8	20	50.8	L	13
959	1026	19.9	66.4	20	50.8	LT	13
885	-	-	-	20	-	LT	8, 14
885	-	-	-	20	-	ST	8, 14
965	1089	-	-	20	-	-	6
909	1240	25.0	69.0	20	25.0	L	7
978	1047	19.0	65.0	20	50.8	L	9

[a] L = Longitudinal, rolling direction.
LT = Long transverse, perpendicular to rolling direction and thickness direction.
ST = Short transverse, through thickness direction.
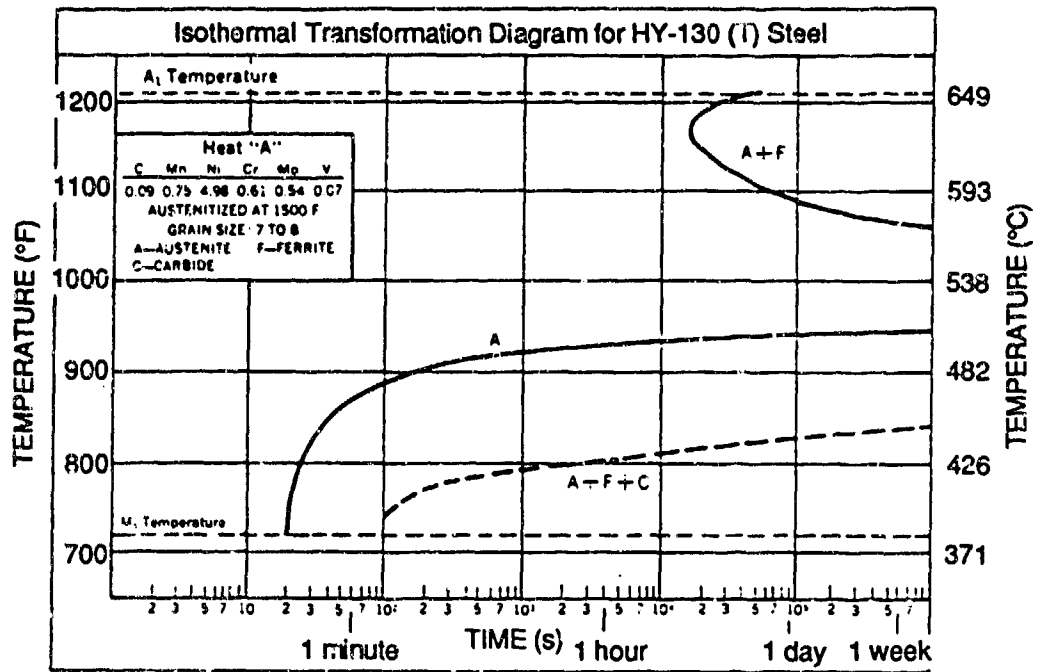
Figure A-1. Isothermal transformation diagram for HY-130 steel.
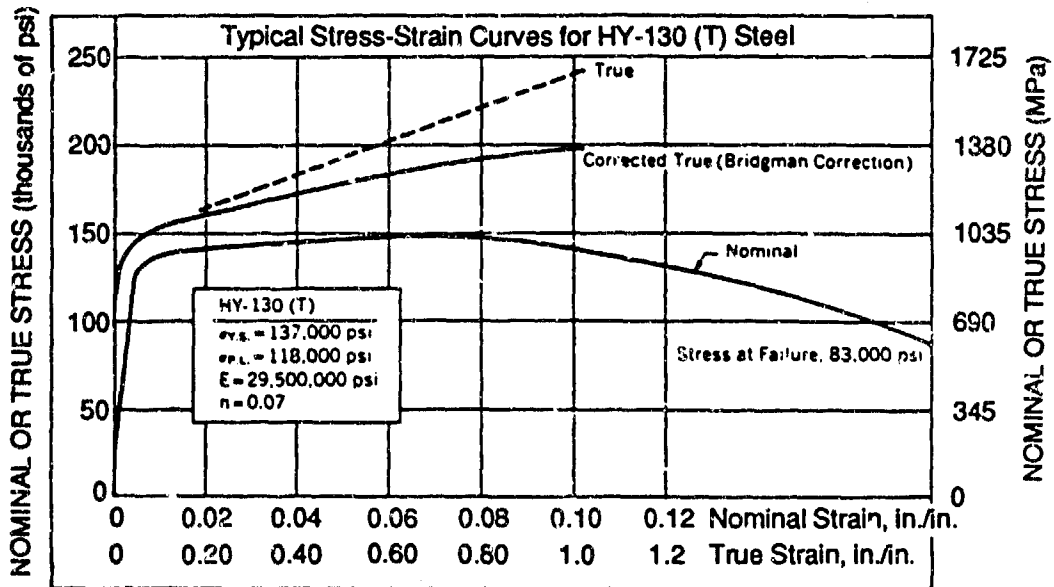
Figure A-2. Typical nominal and true static stress-strain curves for HY-130 steel.

Figure A-3. Effect of strain rate on the nominal tensile stress-strain curve for HY-130 steel.

Conn et al.[A-7] present tensile test results at strain rates ranging from 10^{-3} to 10^3 s^{-1}. These results are summarized in Figure A-4. Conn et al. comment that the dip in the data at a strain rate of 10 is an artifact associated with the testing and data reduction procedure. Figure A-4 demonstrates that the stress-strain behavior of HY-130 steel is not sensitive to the loading rate, at least up to a strain rate of 10^3 s^{-1}.

Notched Tensile Test Data. Notched tensile data are pertinent to the present investigation because the notched tensile test allows us to investigate the dependence on stress triaxiality of the effective plastic strain at fracture. Knowledge of this dependence is a key element of the local fracture model used to simulate the fracture tests on HY-130 steel welded T-joints (see Appendix D).

Mackenzie et al.[A-8] experimentally determined the variation of the effective plastic strain at fracture with stress triaxiality for HY-130 steel specimens oriented in the long transverse, or LT, and the short transverse, or ST directions. Their results are presented in Figures A-5 and A-6. Figure A-5 plots the average stress in the cross section as a function of the effective strain and notch geometry, for specimens in the LT and ST directions. Figure A-6 show ow the effective plastic strain at fracture measured in the experiments varies with the ratio of mean to effective stress, which is a measure of stress triaxiality. The data presented in Figure A-6 were obtained by applying Bridgman's analysis[A-9] of the notched bar to the experimental results.

Figures A-5 and A-6 clearly illustrate the strong dependence of the effective plastic strain at fracture on the mean stress. The data also show that, for HY-130 steel, there is a marked orientation dependence of the fracture behavior.

Fracture Data. The lowest assumed service temperature for HY-130 steel is 0°C. At that temperature, HY-130 steel fractures only after showing significant plastic deformation. Therefore, toughness measurements, which are useful for fracture analysis, must be performed using elastoplastic fracture testing techniques and must be expressed in terms of J_{Ic} (a measure of resistance to crack initiation) and the J-R curve (a measure of the resistance to crack extension).

Before the advent of elastoplastic fracture mechanics, a large body of fracture data was developed using the Charpy impact test [Charpy impact energy (CVN)] and the dynamic tear test [dynamic tear energy (DTE)]. Although these tests do not yield data directly applicable to fracture mechanics analysis, they allow determination of the ductile brittle transition temperature and are used in establishing material specification. Empirical correlations have also been established to relate CVN and DTE to the fracture toughness K_{Ic} or J_{Ic}.
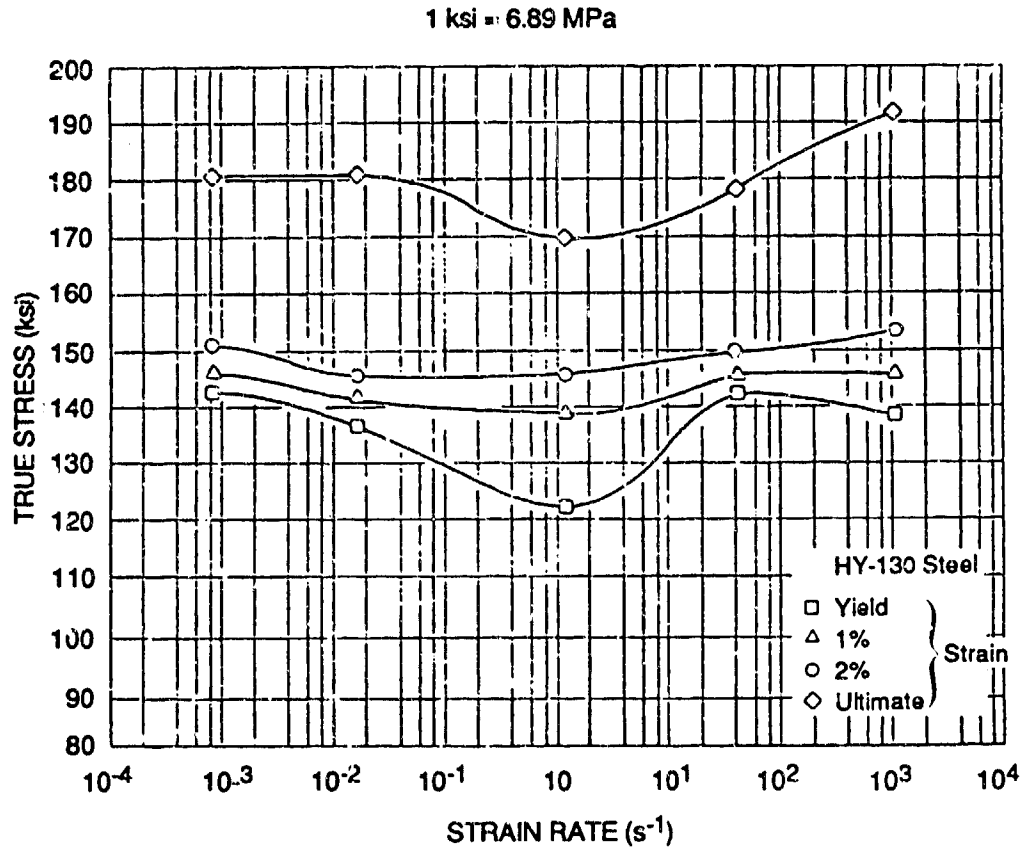
Figure A-4. Effect of strain rate on the true flow stress for HY-130 steel.

(a) Long transverse orientation

(b) Short transverse orientation
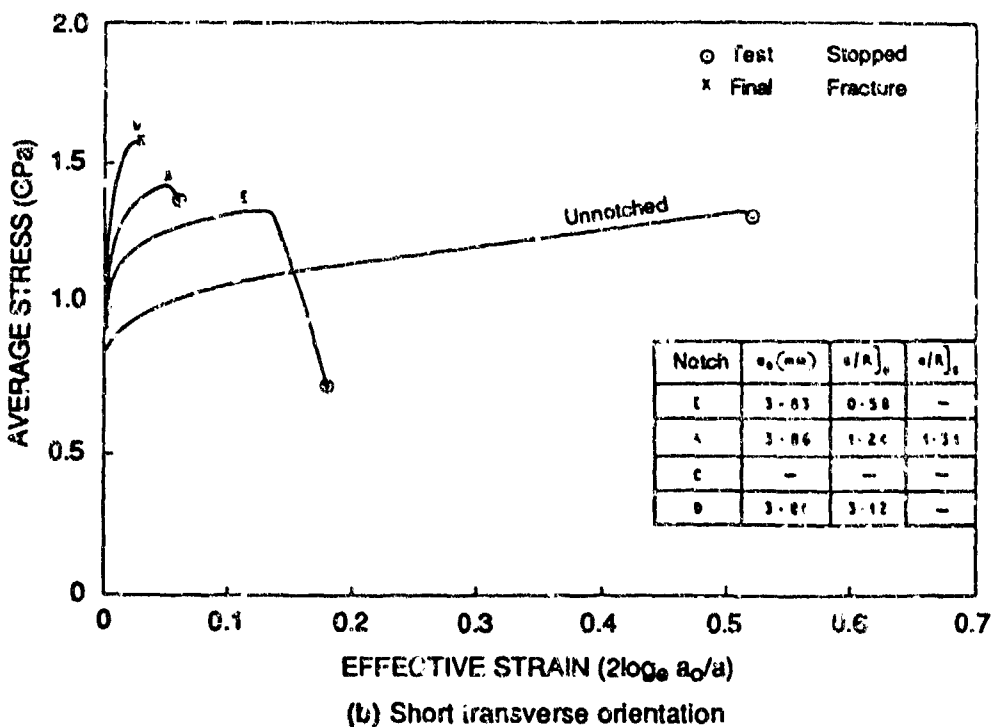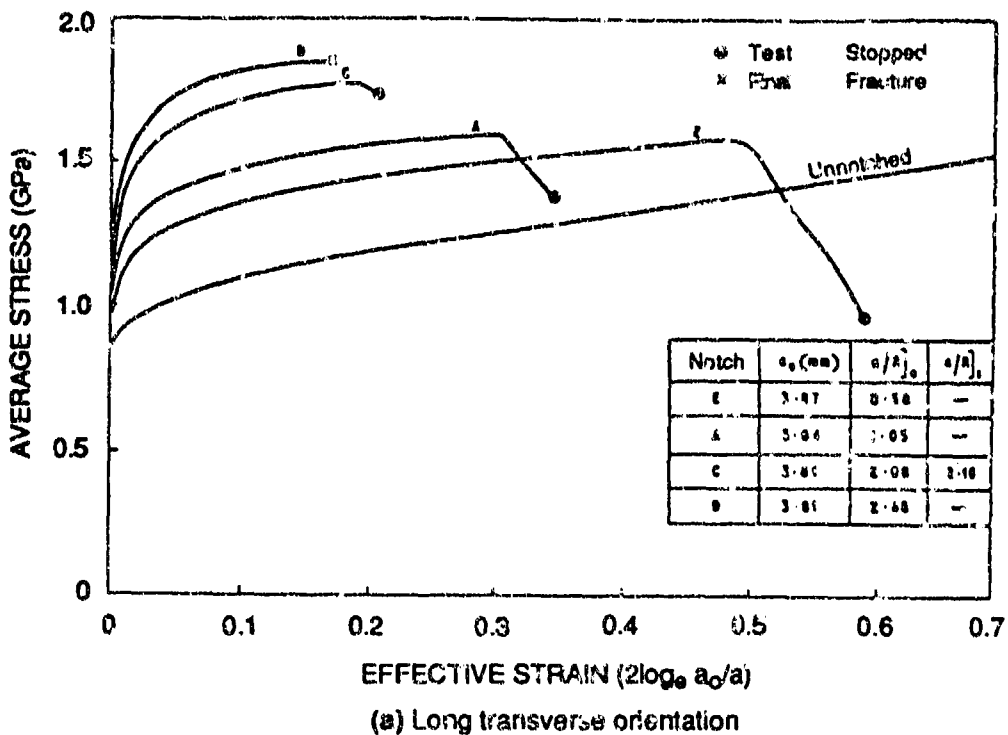
SOURCE: Mackenzie et al. (1977).   RA-2612-70

Figure A-5.   Effect of notch acuity on the stress-strain curve of HY-130 steel.
R = notch root radius; a = net section radius.

Figure A-6.   Failure strain as a function of triaxiality ratio (mean stress over effective stress ratio) for HY-130 steel.

Hasson and Joyce[A-1,A-2] determined the variation in J_{Ic} for HY-130 steel as a function of temperature at both quasi-static and rapid-loading rates (loading time to crack initiation on the order of several milliseconds). The results are shown in Figure A-7 demonstrating that the fast loading rate elevates the upper shelf of HY-130 steel and tends to sharpen the ductile-brittle temperature transition. In terms of J_{Ic}, HY-130 steel is well on the upper shelf at 0°C. The transition temperature is around -100°C, compared with approximately -75°C for the CVN transition temperature.

The room-temperature J-R curve for HY-130 steel was measured extensively in a round-robin program organized by the American Society for Testing and Materials (ASTM).[A-10] Representative results for tests performed with compact tension specimens are plotted in Figure A-8. The J value needed to produce a 4-mm crack extension is about three times the J_{Ic} value. Room-temperature J-R curves as well as those at -80°, -35°, and 150°C are also available from Joyce and Hasson.[A-1] No important difference is observed in the J-R curves at temperatures between -80° and 25°C, whereas heating to 150°C lowers J_{Ic} significantly and the tearing modulus slightly.

The influence of the notch root acuity on ductile crack initiation and extension is revealed by the J-R curve data obtained by Joyce and Gudas,[A-3] shown in Figure A-9. Increasing the notch radius from a fatigue crack to 0.05 mm increases the initiation value of J by a factor of more than 4. Further increasing the root radius to 0.08 mm increases J only slightly. In contrast, the tearing resistance of the fatigue precracked specimens is higher than that of the specimens with blunt notches, perhaps because the crack when it extends from a blunt notch, propagates into a material that has seen more extensive plastic deformation over a larger region and hence has exhausted more of its ductility.

Barsom and Pellegrino[A-11] have characterized the toughness of HY-130 steel in the temperature range between -200° and -100°C in terms of the plane strain fracture toughness K_{Ic}. In this range, K_{Ic} varies monotonically from 44 to 121 MPa√m. The same investigators also report measurements of the plane strain ductility of HY-130 steel.

Hahn and Kanninen[A-12] published a compilation of dynamic fracture toughness parameters for HY-130 steel that include data for K_{Id} (dynamic crack initiation toughness), K_{Im} (minimum dynamic crack propagation toughness), K_{Ia} (crack arrest toughness), CVN, and DTE data. Typical and lower limit values for these parameters at 0°C were extracted from the compiled data and are listed in Table A-4. None of the K-based toughness values is lower than 148 MPa√m. However, most of the K-based data were not measured directly but were estimated from CVN and DTE data, using empirical correlations not verified for HY-130 steel.
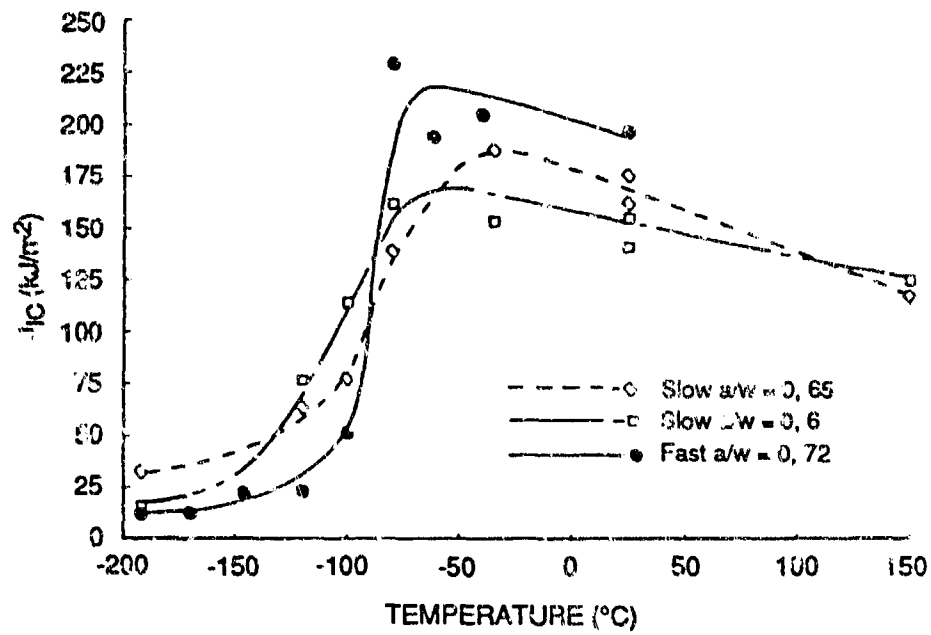
Figure A-7. J_{IC} as a function of temperature and loading rate for HY-130 steel. a = crack length; w = specimen width.
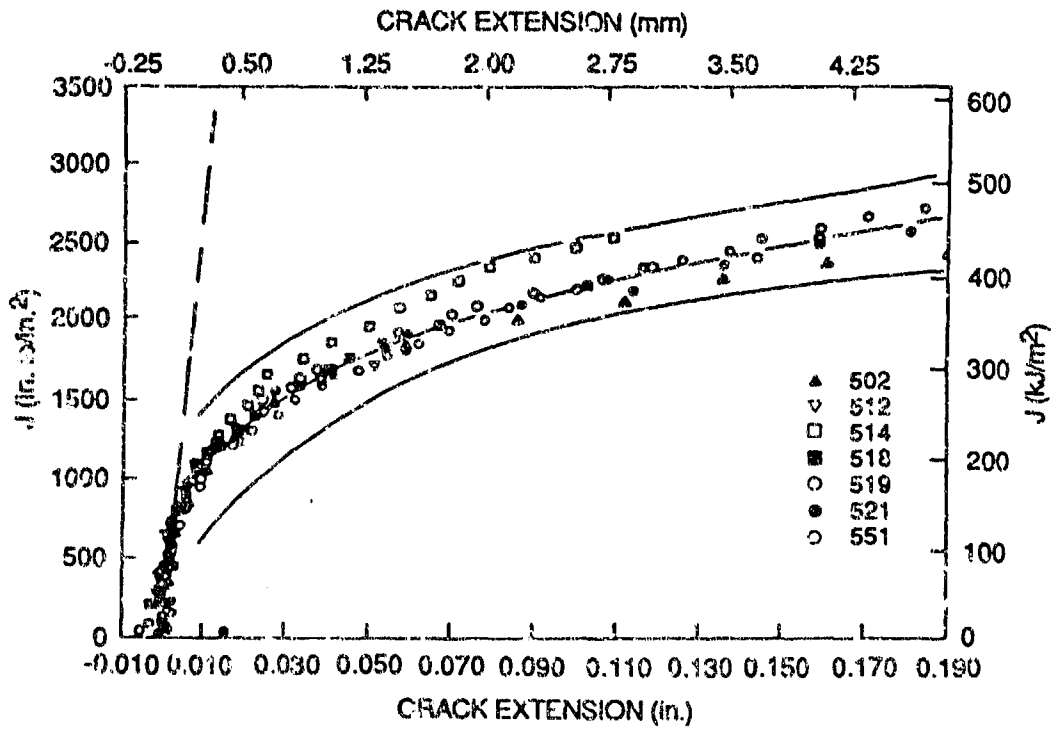
RA-2612-72

SOURCE: Gudas and Davis (1982).

RA-2612-73

Figure A-8. Representative J-resistance curves for HY-130 steel obtained with compact tension specimens.
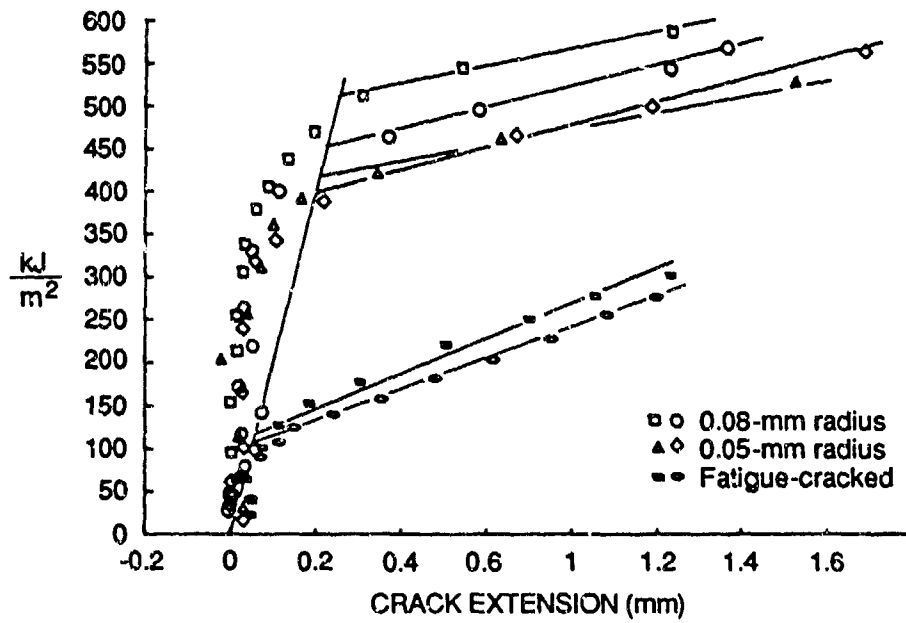
SOURCE: Joyce and Gudas (1979).   RA-2612-74

Figure A-9.   Effect of notch root radius on J-resistance curve of HY-130 steel.

TABLE A-4. FRACTURE PROPERTIES OF HY-130 STEEL
(AFTER HAHN AND KANNINEN[A-12])

Toughness Parameter	Typical Value	Lower Limit Estimate
Nil ductility temperature (°C)	-84	-51
Charpy V-notch, (J)	108	81
5/8 in. Dynamic tear energy (J)	746	447
K_{Ic}, based on DTE (MPa $\sqrt{m}^{1/2}$)	203	149
K_{Id}, based on DTE (MPa $\sqrt{m}^{1/2}$)	203	≥149
K_{Im} (MPa $\sqrt{m}^{1/2}$)	252	191

Sovak[A-13] compared the CVN toughness of HY-130 steel measured in slow bend and impact experiments for longitudinal and transverse orientations. The results are shown in Figure A-10 and indicate that the CVN upper shelf is significantly higher for dynamic than for static loading. This is consistent with the J_{Ic}-transition curves of Figure A-7. The upper shelf values for the transverse orientation are significantly lower than those for the longitudinal orientation.

Fractographic Observations. Observations on the microscopic mechanisms of fracture HY-130 steel were reported by Barsom and Pellegrino[A-11] for a wide range of temperatures. Below -140°C, the fracture mechanism is primarily cleavage. Above -100°C, it is void nucleation growth and coalescence. In the transition temperature region, both mechanisms coexist and the proportion of each depends on the loading rate, temperature, and state of stress.

Hancock and Mackenzie[A-14] studied the mechanism of void nucleation, growth and coalescence for fracture planes normal to the long and the short transverse directions. In the long transverse direction, fracture occurs by nucleation of voids at relatively large inclusions (about 5 μm). These voids grow more or less uniformly, leading upon coalescence to a single size distribution of cusps, typically 10-20 μm, on the fracture surface.

On the other hand, in the short transverse direction, clusters of relatively large voids nucleate at inclusion stringers oriented parallel to the fracture plane by the rolling process and coalesce to form microcracks several hundreds of micrometers long and distributed on different parallel planes. The microcracks are then linked by shear walls produced by the nucleation and growth of much smaller voids (typically 2 μm in diameter).

TEMPERATURE °C

HY-130 Longitudinal

HY-130 Transverse

- - □ - - Static: from Manlabs Slow-Bend Machine
- ─○─ Dynamic: from Impact Machine

1 ft-lb = 1356 J

ENERGY ABSORPTION (ft lb)

TEMPERATURE (°F)
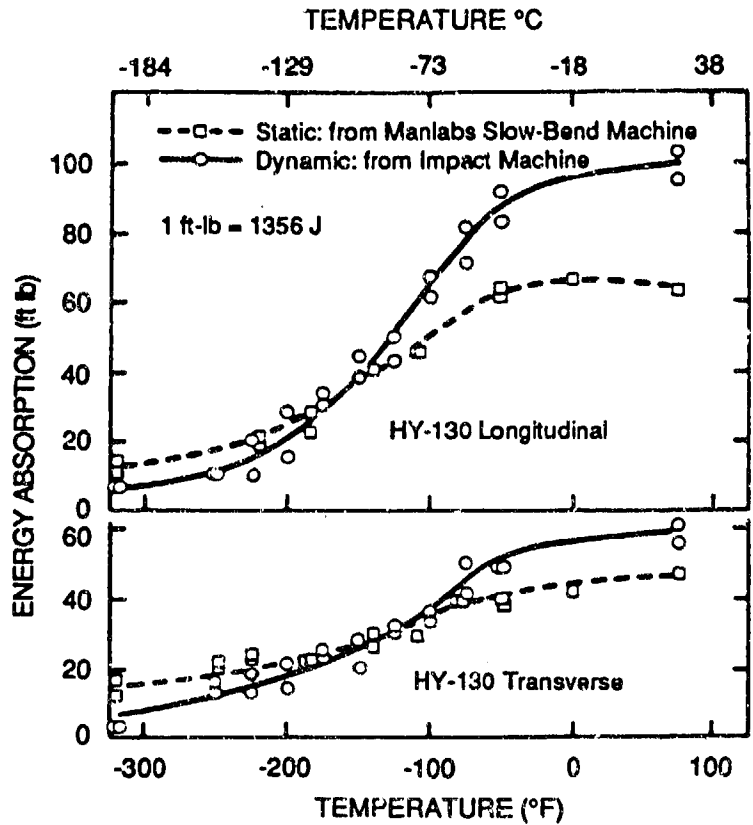
SOURCE: Sovak 1982).

RA-2612-75

Figure A-10.   Static and dynamic standard CVN energy results
for HY-130 steel.

These fractographic observations suggest that a deformation-based local fracture model, modified to account for the influence of the mean stress on void growth, may be appropriate in a first attempt to model the fracture behavior of HY-130 steel at temperatures above 0°C.

Characterization by SRI

To evaluate possible plate-to-plate differences in the mechanical properties of HY-130 steel and to verify that the mechanical properties data from the literature are also relevant for our material, we performed two unnotched round bar tensile tests each for material from a 12.7- and a 41.4-mm-thick plate. The original diameter of the specimens was 6.3 mm. During the experiments, the neck diameter was measured with a micrometer at regular displacement increments to obtain the true stress beyond the point of maximum load. The neck curvature was also estimated so that we could apply the Bridgman stress triaxiality correction to the stress data.

Besides the unnotched tensile bars, we also tested one notched round tensile bar for each of the plates investigated. The purpose of these tests was to verify that the fracture strain locus in Figure A-6 is applicable to the material tested in this investigation. The net diameter, 2a, of the notch was 4.8 mm, and the notch root radius, R, was 2.4 mm, yielding an a/R ratio of 1. As for the unnotched specimen, the reduction in the notch diameter was measured with a micrometer at regular displacement increments during the test.

The tensile test results are summarized in Table A-5 and Figure A-11. Table A-5 lists the engineering tensile data and the corresponding averages for each of the four unnotched specimens tested. The average yield stress, ultimate stress, total elongation and reduction of area are 930 and 988, and 22.1 and 70.1 percent, respectively. These values are in good agreement with the data listed in Table A-3.

The true stress-true strain curve obtained by averaging the results of the four unnotched tensile tests is shown in Figure A-11a (curve b). An estimate of the Bridgman correction was applied to the data, and, once corrected for triaxiality, the stress-strain curve for HY-130 steel shows little strain hardening (curve c in Figure A-11a). The influence of triaxiality in elevating the average stress is also illustrated by the results of the notched tensile tests (curve a in Figure A-11a), which show a 40 percent increase in the average yield stress over the unnotched test results. Conversely, the failure strain is greatly reduced, dropping from about 1.1 for the unnotched to about 0.3 for the notched specimens. The results of the notched tensile bar tests for the two plate thicknesses tested were identical to within the experimental uncertainty. The effective fracture strain measured in these two experiments is in good agreement with the results obtained by Mackenzie et al.[A-8] for the same notch geometry.
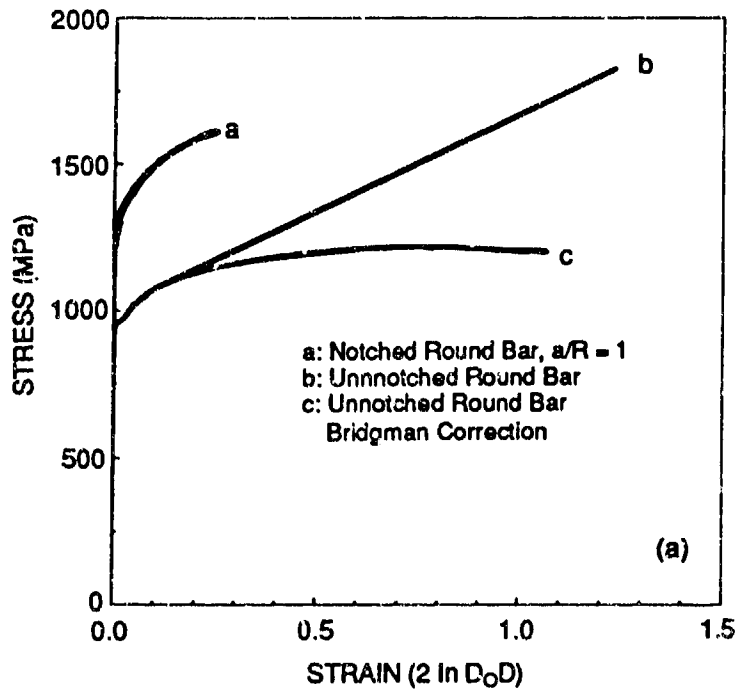
(a) Average stress-strain curve for notched and unnotched round bars
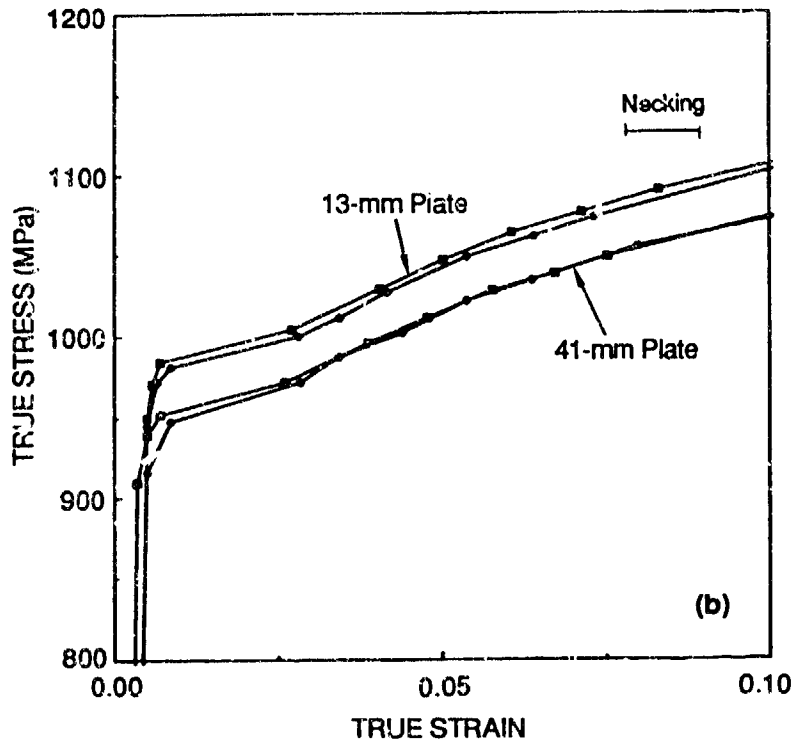
(b) Magnified part of individual stress-strain curves

RA-2612-19

Figure A-11.   Tensile test results for 13-and 41-mm HY-130 steel plates.

TABLE A-5, TENSILE PROPERTIES OF HY-130 STEEL MEASURED AT SRI

Specimen No.	Plate Thickness (mm)	Yield Strength (MPa)	Ultimate Strength (MPa)	Elongation (%)	Reduction Area (%)
1-1	41.4	916	975	21.7	72.0
1-2	41.4	909	973	-	70.0
1/2-1	12.7	949	1004	22.8	69.5
1/2-2	12.7	945	998	21.8	69.0
Average	-	930	988	22.1	70.1

Figure A-11 shows a magnified portion of the true stress-true strain curve up to the point of necking for all four specimens tested. Table A-5 and Figure A-11 show that, although the results are similar, the stress-strain curve for the 41.4-mm plate is about 3–4 percent lower than that for the 12.7-mm plate.

The good agreement between the tensile data obtained at SRI and those published in the literature demonstrates that the latter data can be used confidently in analyzing our fracture experiments. In particular, it is appropriate to incorporate the effective fracture strain locus of Figure A-6 in a local fracture model for the material investigated in this project and to assume that the flow properties for HY-130 steel are not rate-sensitive for strain rates up to 1000 s^{-1} or so.

PROPERTIES OF HY-130 STEEL WELDS

In this project, we tested welded T-joints between HY-130 steel plate and a HY-130 steel stiffener half as thick as the plate. The welds were undermatched (i.e., they were produced with weld wire of a lesser strength [100S weld wire, 690 MPa yield strength] than the base metal). In preparing for the fracture experiments, we surveyed the literature to obtain as much information as possible about welded HY-130 steel joints and their mechanical behavior. We also produced trial 1/8-, 1/4-, and 1/2-scale welds and characterized them in terms of their geometry and hardness. The results of the literature survey and the weld characterization investigation are presented below.

Data from Literature Review

No information was found in the literature on the mechanical properties and microstructures of undermatched HY-130 steel base metal HY-100 steel weld metal welded joints. However, papers on HY-130 and HY-100 weldments provided relevant data for the present investigation.

Stoop and Metzbower[A-15] investigated butt welds in 6.35- and 12.7-mm-thick HY-130 steel plates produced by four different welding processes: shielded metal arc welding (SMAW), gas metal arc welding (GMAW), electron beam welding (EBW), and laser beam welding (LBW). Their paper provides information about how welds produced by the same process are affected by the weld scale. Furthermore, for a given weldment size it indicates how the weld properties are affected by the welding process.

Common features are observed for all four weld processes and for both weld scales. Hardness profiles through the weld joint indicate that the hardness value is always greatest near the boundary between the heat-affected zone (HAZ) and the base metal (BM). The microstructure of the HAZ is also finer near the HAZ/BM boundary and becomes coarser toward the weld metal (WM)/HAZ interface.

The width of the HAZ is more or less constant for a given welding process, independent of the weldment scale. For SMAW and GMAW, the two processes most pertinent to our study, the HAZ width is on the order of 4–6 mm. The microstructure of the HAZ near the WM/HAZ interface is a coarse bainite microstructure for the SMAW weldment and a coarse bainite with some acicular ferrite for the GMAW weldment. Near the HAZ/BM interface, the HAZ microstructure is a fine autotempered martensite with some ferrite for both weldment types. For the 6.35-mm-thick weldments, the average hardness of the SMAW HAZ is 37.5 HRC, whereas for the GMAW HAZ, it is 40.5 HRC. For the 12.7-mm-thick weldments, the average HAZ hardness is somewhat less and equal to 33 HRC for both welding processes.

The fracture behavior of the weld joints was characterized by performing dynamic tear tests. When the dynamic tear energy values normalized by the two plate thicknesses are compared for SMAW and GMAW, it appears that the 6.35-mm-thick welds have a somewhat better fracture resistance than the 12.7-mm-thick welds.

More information on the effect of weldment thickness is provided by a study of 50-mm-thick GMAW weldments of HY-130 steel by Challenger et al.[A-16] They investigated the effect of heat cycling, which occurs in large multiple bead weldments, on the hardness and microstructure of the HAZ at several locations. For each location along the HAZ of the multipass weldment, two regions with distinctly different hardness values were found. The HAZ width at the interface between the BM and the weld bead was 3–5 mm. This observation, along with the data from Stoop and Metzbower,[A-15] demonstrates that the size of the HAZ does not scale but rather tends to remain constant in welds of different scales.

The characterization of the HAZ near the final weld pass on the joint surface is especially pertinent to this investigation. Two regions with different hardness values are found in the HAZ.

A region about 2 mm wide near the base metal shows the highest hardness value (410 HV). A softer region (390 HV) exists from the fusion line to about 2 mm into the HAZ. The HAZ immediately adjacent to the BM is very soft (270 HV). The hard region of the HAZ consists of fine lath martensite, whereas a mixture of coarse lath bainite and fine lath martensite dominates in the soft region. The fusion zone microstructure of SMAW and GMAW was also characterized by Chen et al.[A-17,A-18] They found that the microstructure was dependent on the welding process, bead size, heat input, preheat temperature, and base metal thickness.

Hasson et al.[A-19] have investigated the fracture behavior of HY-130 welds produced by the gas tungsten arc welding (GTAW) and the GMAW processes; they also investigated, for a given process, the influence of varying the welding heat input. The fracture resistance of the weld metal in 38-mm-thick weldments was characterized in terms of the J-R curve. The results of their experiments are summarized in Figure A-12. The welding process, as well as the heat input, significantly affects the fracture behavior of the weld metal. GTAW welds are much tougher than GMAW welds. Lowering the heat input increases the toughness of GTAW welds, whereas it reduces that of GMAW welds. J-R curves for HY-130 steel welds were also obtained by Read.[A-20] The results are shown in Figure A-13 and demonstrate the considerable scatter that may prevail when performing fracture tests on welds.

Hahn and Kanninen[A-12] give estimates of the dynamic fracture properties of HY-130 weldments. These estimates are listed in Table A-6. One important conclusion drawn from these estimates is that the transition temperature for weldments may be significantly higher than that for the base metal. On the basis of lower-limit 50-mm DT data, Hahn and Kanninen indicate that the lowest assumed service temperature of 0°C may be in the fracture transition range for HY-130 steel weldments.

TABLE A-6. FRACTURE PROPERTIES OF MIL-1405 GMA, HY-130 WELD METAL

Toughness Parameter	Typical Value	Lower Bound Estimate
Nil ductility temperature (°C)	-79	-51
5/8-in. Dynamic tear energy (J)	746	461
K_{Ic}, based on DTE (MPa $\sqrt{m}^{1/2}$)	192	154
K_{Id}, based on DTE (MPa $\sqrt{m}^{1/2}$)	192	154
K_{Im} (MPa $\sqrt{m}^{1/2}$)	242	191
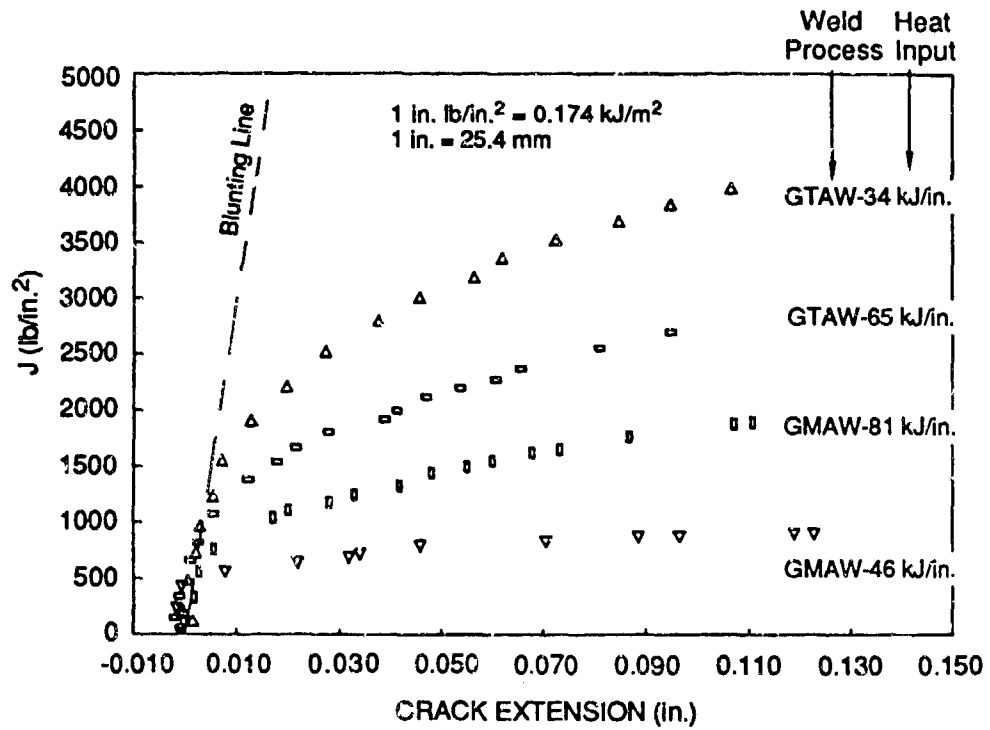
SOURCE: Hasson et al. (1984).   RA-2612-76

Figure A-12.   Dependence of HY-130 weld metal J-resistance curve on
welding process and heat input.
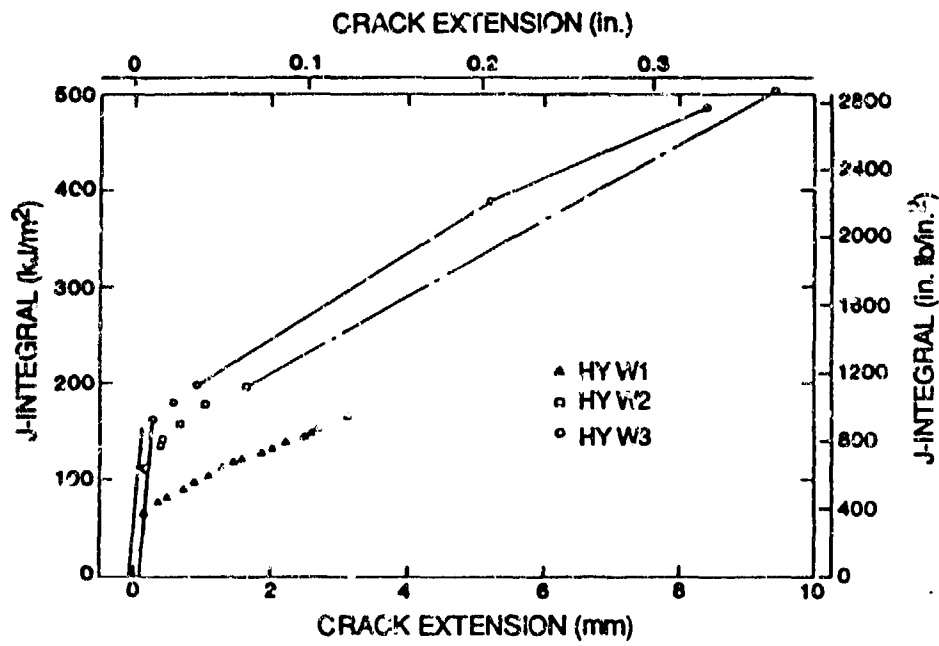
SOURCE: Reed (198-   RA-2612-77

Figure A-13.   Scatter in J resistance curve data for three nominally identical
               GMAW HY-130 weldments.

Finally, Deb et al.[A-21] investigated HY-100 weldments produced by the submerged arc welding (SAW) and the GMAW processes. Their study showed a significantly lower hardness value in the SAW than in the GMAW weldment. The CVN transition temperature of the SAW weldment was also about 50°C higher than that for the GMAW weldment, but both were on the CVN upper shelf at 0°C. The differences in properties in the SAW and GMAW processes were explained by differences in microstructure and inclusion content of the weld beads.

Characterizing Trial Welds at SRI

We undertook an investigation of the welding procedure and resulting weld properties for three sizes of T-welds, corresponding to 1/2-, 1/4-, and 1/8-scale welded models. The plate thicknesses were 6.35, 12.7, and 25.4 mm, whereas the stiffener thicknesses were 3.17, 6.35, and 12.7 mm for the 1/8-, 1/4-, and 1/2-scale welds, respectively. Trial welds were first produced using the GMAW process; however, for better control of the weld quality and geometry, we switched to the GTAW process for later trial welds and all the test specimen welds.

The welds were produced using 100S weld wire; Table A-7 lists the welding conditions for the trial welds.

TABLE A-7. WELDING CONDITIONS FOR TRIAL HY-130 STEEL WELDS (100S WELD WIRE) GTAW PROCESS

Specimen Scale	1/8	1/4	1/2
Weld wire diameter	0.75 mm	1.5 mm	1.5 mm
Amperage	100-120 A	100-120 A	100-120 A
Voltage	20-28 V	20-28 V	20-28 V
Protective environment	Argon	Argon	Argon
Preheat temperature	90-100°C	90-100°C	90-100°C
Interpass temperature	90-150°C	90-150°C	90-150°C
Number of passes	2 each side	3 each side	9 each side

Weld Geometry and Hardness Maps. Macrographs of the 1/8-, 1/4-, and 1/2-scale trial welds are shown in Figure A-14, with corresponding hardness maps. These macrographs clearly indicate the boundaries between base metal, heat-affected zone, and weld metal. It is apparent that the weldments are asymmetrical, with the side that was welded first displaying larger WM and heat-affected zones. The asymmetry decreases with increasing weldment scale. All the trial welds displayed some lack of penetration at the center. Sealer passes were later used to ensure full penetration when fracture specimens were welded. Figure A-14 also illustrates the important
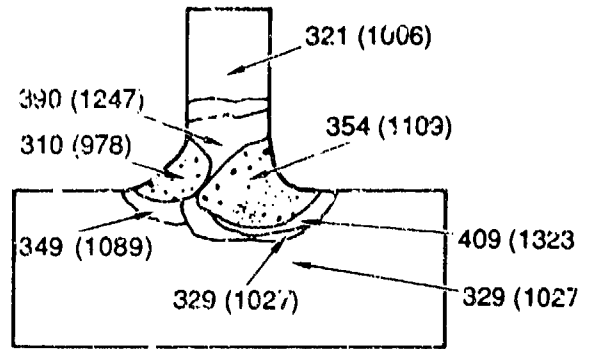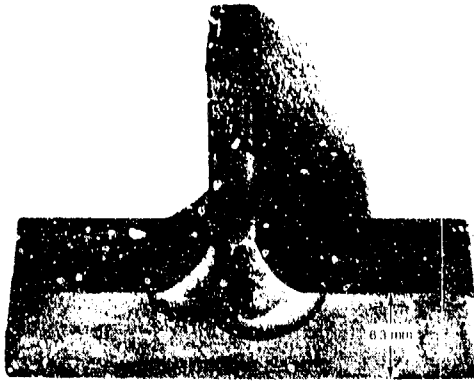
1/8-Scale
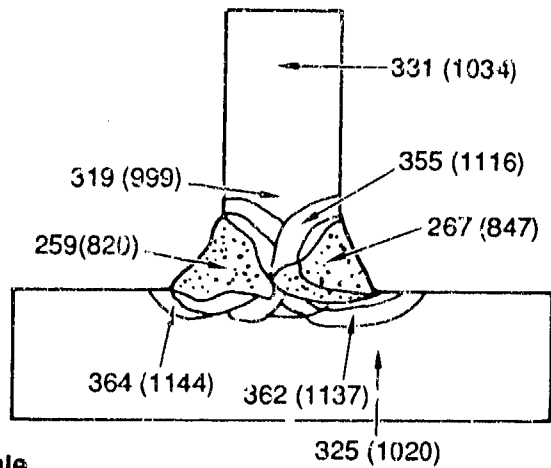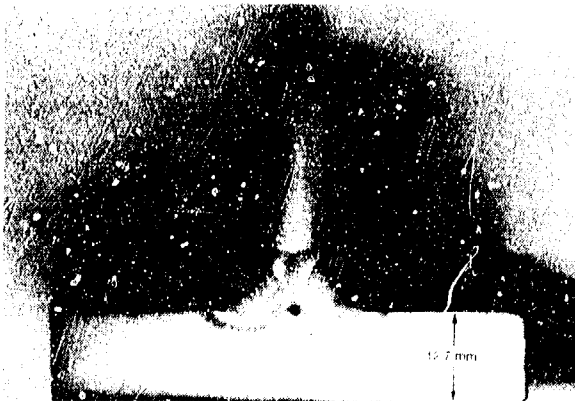
1/4-Scale
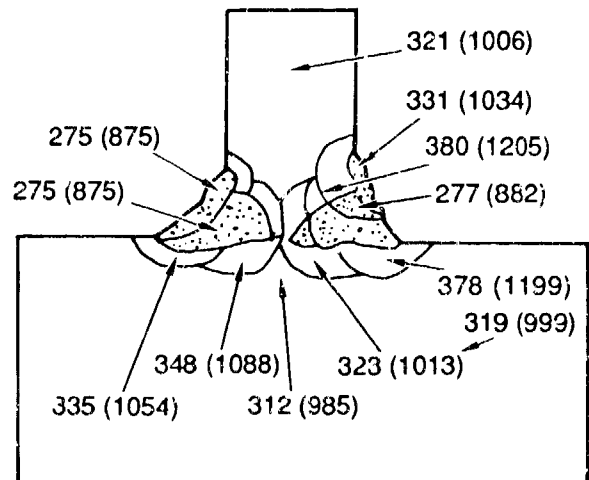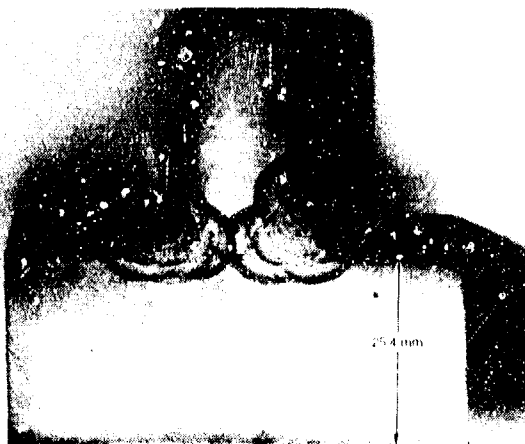
1/2-Scale

RP-2612-34

Figure A-14. Macrographs and 300g diamond pyramid hardness maps for three scales of HY-130 steel/HY-100 GTAW weldments investigated.

stiffener distortion that can result from the welding process; distortions are in turn associated with residual stresses that may affect the weldment's fracture behavior.

Hardness maps for the three trial weldments are shown in Figure A-14, whereas more detailed hardness profiles across the HAZ near the surface are shown in Figure A-15. The hardness numbers represent the 300-g diamond pyramid hardness number; in Figure A-14 the numbers in parenthesis are estimates of the yield stress obtained from the hardness reading.

Overall, the hardness maps are similar for all three weldment scales. In particular, the highest hardness value is always achieved in the plate HAZ. However, some differences can also be observed. The hardness map for the 1/8-scale weldment is asymmetrical, with the side welded first having higher hardness values (in corresponding zones) than the side welded second. In contrast, the hardness maps for the 1/4- and 1/2-scale weldments are essentially symmetrical. Furthermore, the hardness values for WM and HAZ are significantly higher in the 1/8-scale than in the other two weldments. These observations can be explained by the differences in thermal histories experienced by the weldments because of the difference in the number of weld beads for each scale.

The hardness profiles through the plate HAZ (Figure A-15) indicate that the hardness is maximal near the HAZ/BM interface, as previously noted in the literature. The 1/4-scale weldment is the exception and presents a more uniform hardness across the HAZ.

The micrographs in Figure A-15 provide an indication of the kind of geometric defect that may be encountered in the weldment (e.g., the ripples at the edge of the 1/4-scale weldment could become crack initiation sites). The geometry of the three welds was quantified, and the results are presented in Figure A-16. The measurements demonstrate that the overall size of the weldments does not scale; the 1/2-scale welded joint is proportionally smaller than the 1/8- and 1/4-scale joints. More important, the size of the HAZ does not scale but remains more or less constant. This observation agrees with the data gathered from the literature survey and is an important element in constructing a fracture model of the weldment.

Although it is possible to enlarge the 1/2-scale weldment to enforce scaling, we decided to maintain the sizes shown in Figure A-16 because a 1/8-scale weldment geometrically scaled to a 1/2-scale model would result in an unrealistically large weldment compared with actual field welds. This geometric difference will be implicitly reflected in the fracture scaling rule.
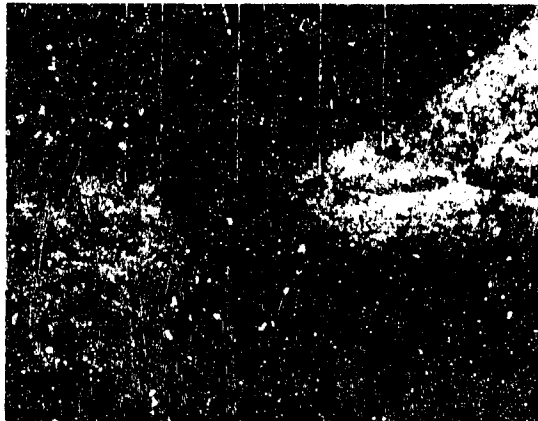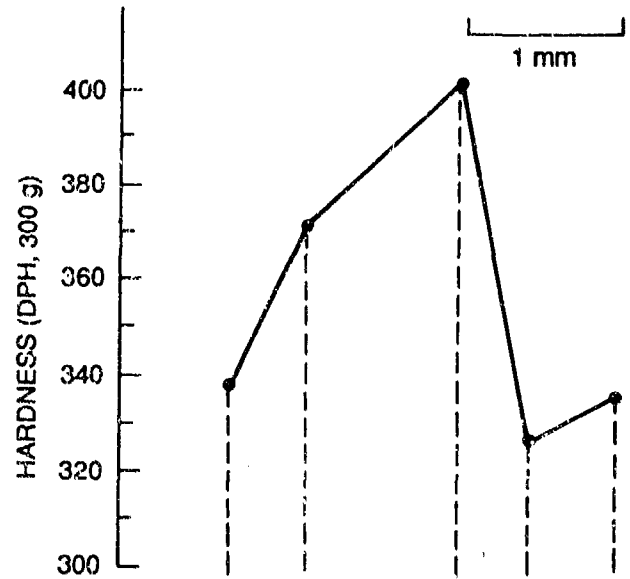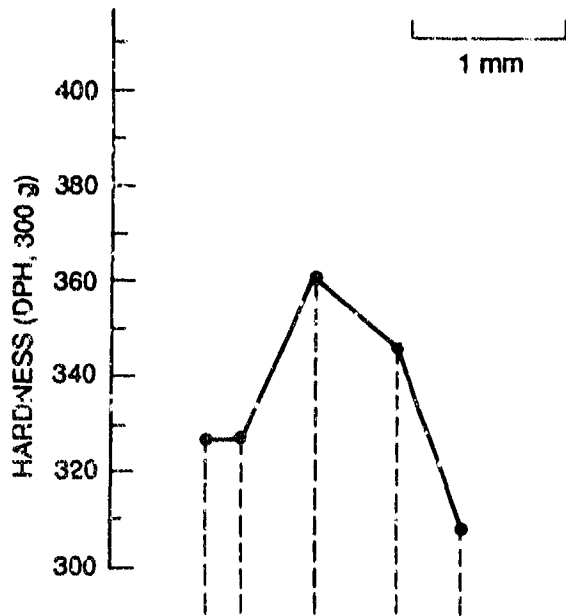
Second Side Welded
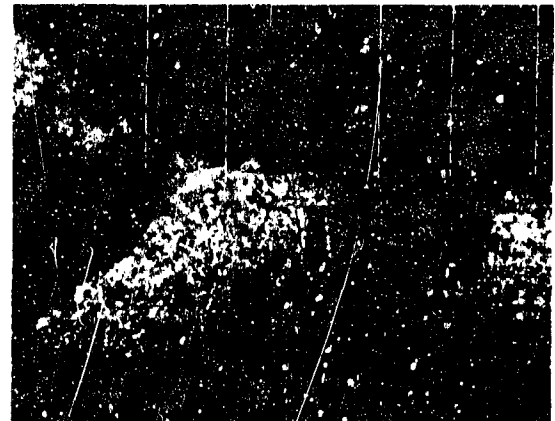
First Side Welded

(a) 1/8-Scale

RP-2612-78

Figure A-15. Details of the weldment microstructure and hardness profile near the plate surface for trial HY-130 steel/HY-100 GTAW weldments.
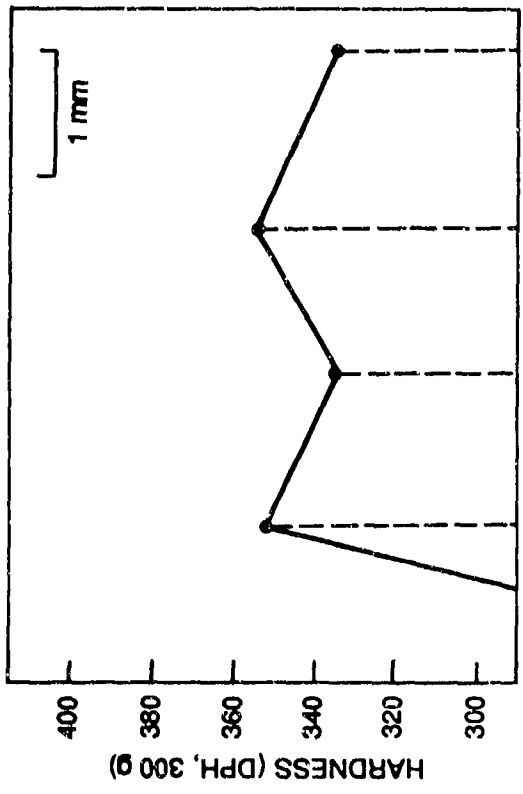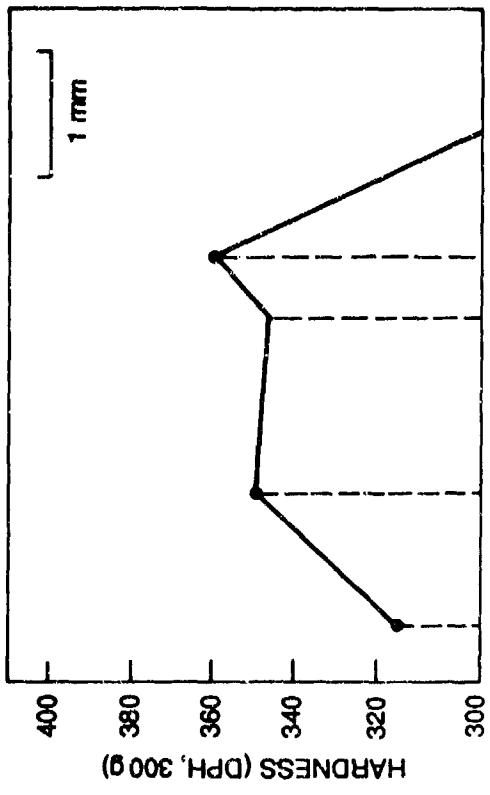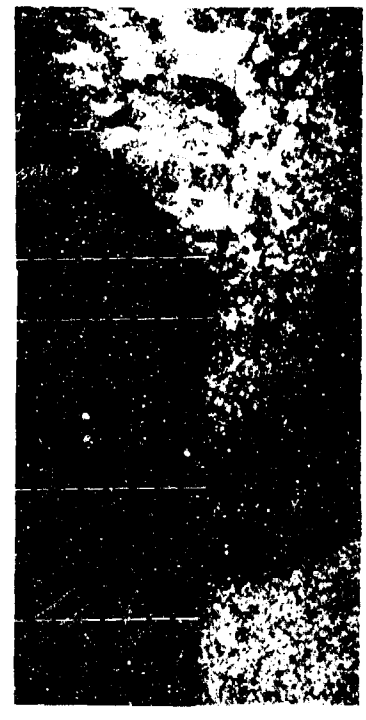
Figure A-15. Details of the weldment microstructure and hardness profile near the plate surface for trial HY-130 steel/HY-100 GTAW weldments (continued).

(b) 1/4-Scale
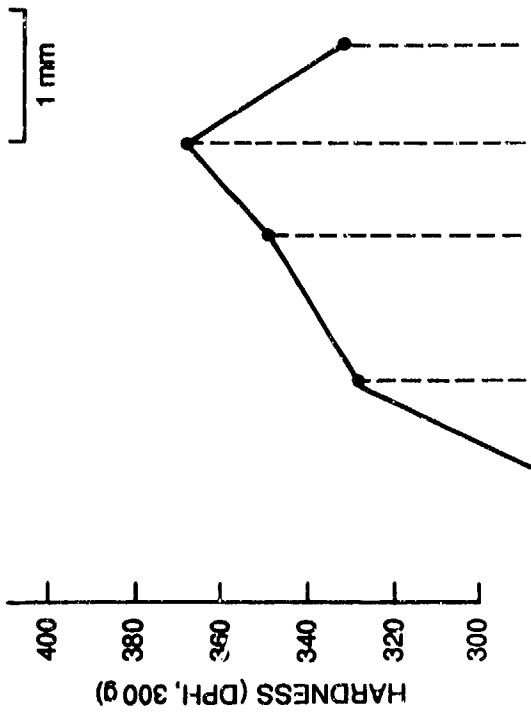
RP-2612-90

First Side Welded
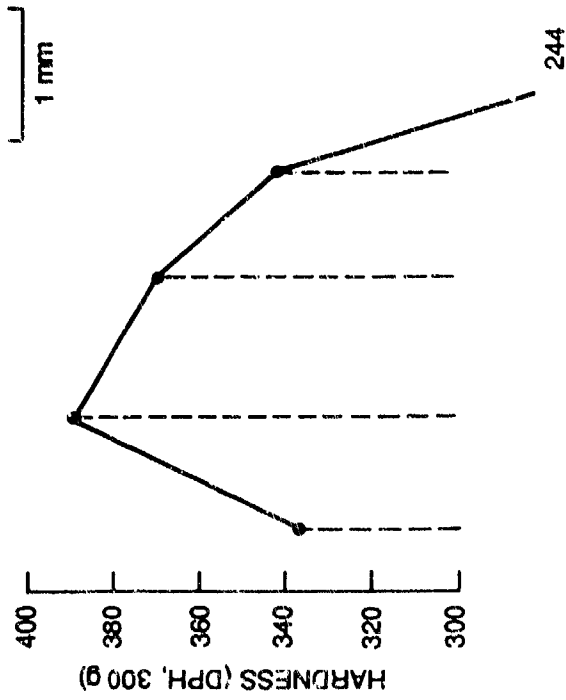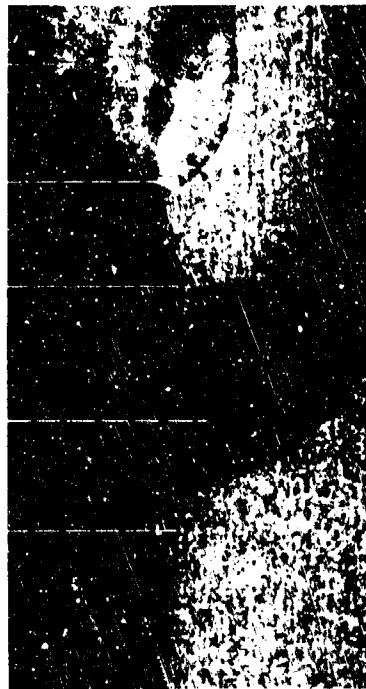
Second Side Welded

(c) 1/2-Scale

Figure A-15.   Details of the weldment microstructure and hardness profile near the plate surface for trial HY-130 steel/HY-100 GTAW weldments (concluded).
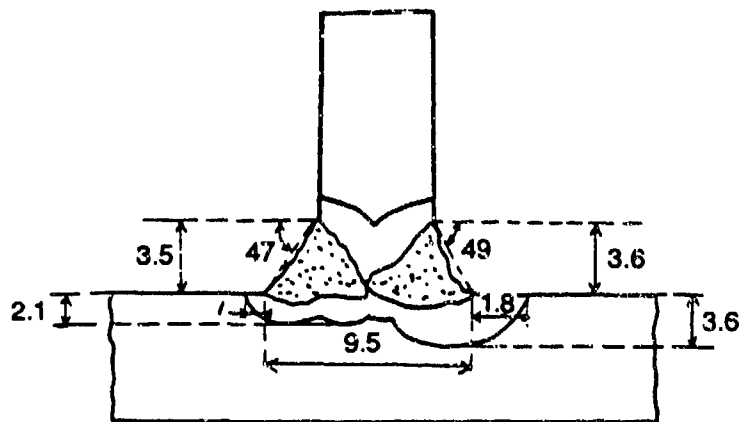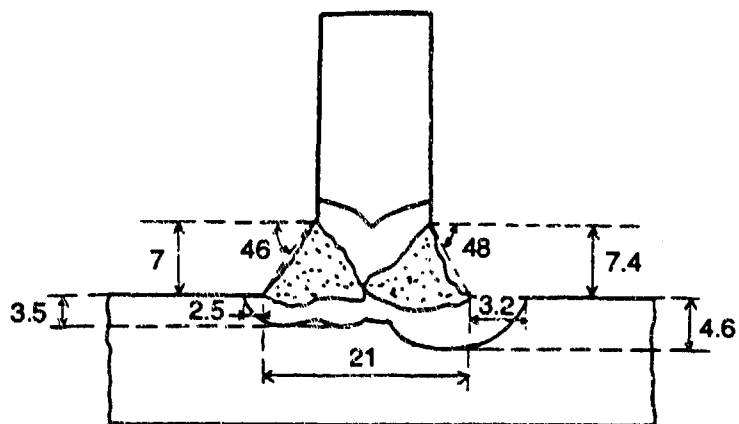
1/8-Scale Weldment

1/4-Scale Weldment
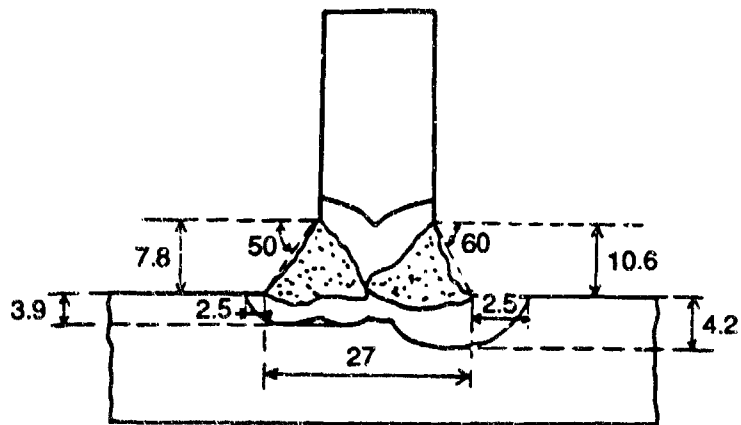
1/2-Scale Weldment

RA-2612-81

Figure A-16. Comparison of dimensions for three scales of trial HY-130 steel/HY-100 GTAW Weldments.

DISCUSSION AND CONCLUSIONS

The literature survey and the characterization at SRI of HY-130 steel weldments have provided a large body of information applicable to designing fracture experiments on those weldments, preparing welded fracture specimens, analyzing of fracture test results, deriving of scaling rules for fracture of welded T-joints, and modeling the joints.

From this information, we can draw the following conclusions:

- The tensile properties of HY-130 steel for a variety of plate thicknesses, orientations, and presumably heat treatments vary by no more than about 15 percent. Tensile properties for two plates used in this program are within 3 percent of each other and fall close to the average of the data published in the literature. Therefore, we feel justified in drawing from the literature data, when appropriate, for the present research.

- The failure strain data developed from notched tensile tests for two of the plates used in this program are consistent with a failure strain locus as a function of mean stress published in the literature. Therefore, this failure strain locus can be used confidently in modeling fracture of the welded T-joints.

- The dimensions of the various metallurgical regions of a weldment do not scale geometrically when plate and stiffener thicknesses are scaled. In particular, the size of the HAZ remains more or less constant, on the order of 2–4 mm.

- The hardness value of the weldment is highest in the HAZ, independent of the weldment scale. Within the HAZ, the hardness value is often highest near the HAZ/BM interface. This finding and the previous conclusion are significant because they suggest that for the loading conditions pertinent to this investigation, fracture will always begin in the HAZ. These findings further suggest that for purposes of fracture analysis, the weldment can be modeled as a brittle layer of constant thickness equal to that of the HAZ. This point is addressed in more detail in Appendix D.

- The welding process significantly affects the fracture toughness of the weld metal, as well as the microstructure and hardness of the HAZ. These influences will need to be taken into consideration when extrapolating the results of this investigation to large structures welded by different processes.

REFERENCES

A-1. Joyce, J. A. and Hasson, D. F., "Characterization of transition temperature behavior of HY-130 Steel by the J_{Ic} Fracture Toughness Parameter," *Engineering Fracture Mechanics*, Vol. 13, 1980, pp. 417-430.

A-2. Hasson, D. F. and Joyce, J. A., "The Effect of a Higher Loading Rate on the J_{Ic} Fracture Toughness Transition Temperature of HY Steels," *Journal of Engineering Material and Technology*, Vol. 103, Apr 1981, pp. 133-141.

A-3. Joyce, J. A. and Gudas, J. P., "Computer Interactive J_{Ic} Testing of Navy Alloys," in: *Elastic Plastic Fracture*, ASTM STP 668 (J. D. Landes et al., eds). American Society for Testing and Materials, 1979, pp. 451-468.

A-4. "HY-130 (T) and HY-140 (T), New Ultraservice Steels under Development," Interim Technical Data, US Steel Corp., Jul 1968.

A-5. "HY-130 Ultraservice Steel," US Properties Card, 1970.

A-6. Lindholm, U. S. and Hargreaves, C. R., "Dynamic Testing of High Strength Steels and Their Susceptibility to Inhomogeneous Shear," *Proceedings of the Second International Conference on Mechanical Behavior of Materials*, Boston, Aug 1976, pp. 1463-1467.

A-7. Conn, A. F.; Rudy, S. L.; and Howard, S. C., "The Strain Rate Dependence of Three High-Strength Naval Alloys," Technical Report 7111-1, prepared for Office of Naval Research under Contract No. N00014-71-C-0220 NR 064-521, Hydronautics, Inc., Laurel, MD, Jun 1974.

A-8. Mackenzie, A. C.; Hancock, J. W.; and Brown, D. K., "On the Influence of State of Stress on Ductile Failure Initiation in High-Strength Steels," *Engineering Fracture Mechanics*, Vol. 9, 1977, pp. 167-188.

A-9. Bridgman, P. W., "Studies in Large Flow and Fracture," McGraw-Hill, New York, 1952.

A-10. Gudas, J. P. and Davis, D. A., "Evaluation of the Tentative J_I-R Curve Testing Procedure by Round-Robin Tests of HY-130 Steel," *Journal of Testing and Evaluation*, Vol. 10, 1982, pp. 252-262.

A-11. Barsom, J. M. and Pellegrino, J. V., "Relationship Between K_{Ic} and Plane-Strain Tensile Ductility and Microscopic Mode of Fracture," *Engineering Fracture Mechanics*, Vol. 5, 1973, pp. 209-221.

REFERENCES (Cont.)

A-12. Hahn, G. T. and Kanninen, M. F., "Dynamic Fracture Toughness Parameters for HY-80 and HY-130 Steels and Their Weldments," *Engineering Fracture Mechanics*, Vol. 14, 1981, pp. 725-740.

A-13. Sovak, J. F., "Correlation of Data from Standard and Precracked Charpy Specimens with Fracture Toughness Data for HY-130, A517-F, and HY-80 Steel," *Journal of Testing and Evaluation*, Vol. 10, No. 3, 1982, pp. 102-114.

A-14. Hancock, J. W. and Mackenzie, A. C., "On the Mechanisms of Ductile Failure in High-Strength Steels Subjected to Multiaxial Stress States," *Journal of the Mechanics and Physics of Solids*, Vol. 24, 1976, pp. 147-169.

A-15. Stoop, J. and Metzbower, E. A., " A Metallurgical Characterization of HY-130 Steel Welds," *Welding Journal, Welding Research Supplement*, Nov 1978, pp. 345s-353s.

A-16. Challenger, K. D.; Brucker, R. B.; Elger, W. M.; and Sorek, M. J., "Microstructure-Thermal History Correlations for HY-130 Thick Section Weldments," *Welding Journal, Welding Research Supplement*, Aug 1984, pp. 254s-262s.

A-17. Chen, C.; Thompson, A. W.; and Bernstein, I. M., "The Correlation of Microstructure and Stress Corrosion Fracture of HY-130 Steel Weldments," *Metallurgical Transactions*, Vol. 11A, 1980, pp. 1723-1730.

A-18. Chen, C.; Thompson, A. W.; and Bernstein, I. M., "Microstructure of Stress Corrosion Cracking of Low-Carbon Alloy Steel Welds, Part I: The Effect of Welding Variables on Microstructure of HY-130 Steel Weldments," *Physical Metallurgy and Failure Phenomena, Proceedings of the Fifth Bolton Landing Conference* (R. J. Christoffel et al., eds.), General Electric Co., Schenectady, NY, 1978, pp. 219-230.

A-19. Hasson, D. F.; Zanis, C. A.; and Anderson, D. R., "Fracture Toughness of HY-130 Steel Weld Metals," *Welding Journal, Welding Research Supplement* , Jun 1984, pp. 197s-202s.

A-20. Read, D. T., "Experimental Results for Fitness-for-Service Assessment of HY-130 Weldments," NBS Report NBSIR 84-1699, Mar 1984.

A-21. Deb, P.; Challenger, K. D.; and Therrien, A. E., "Structure-Properties Correlation of Submerged-Arc and Gas-Metal-Arc Weldments in HY-100 Steel," *Metallurgical Transactions*, Vol. 18A, 1987, pp. 987-999.

APPENDIX B: STATIC FRACTURE EXPERIMENTS

CONTENTS

APPENDIX B

STATIC FRACTURE EXPERIMENTS

INTRODUCTION

The objectives of the static fracture experiments were to derive empirical fracture scaling rules for HY-130 steel weldments loaded quasi-statically and to establish the morphology of the fracture. In this appendix we describe the test geometry and procedure for the static fracture experiments, report the test results, and discuss the fracture scaling rule inferred from those results.

EXPERIMENTAL PROCEDURES

Experimental Configuration and Specimen Geometry

The configuration for the static fracture experiments is illustrated in Figure B-1. A T-shaped specimen is gripped rigidly at the top of the stiffener and loaded in bending symmetrically at the two extremities of the plate. Two 1/2-, four 1/4-, and eight 1/8-scale specimens were manufactured from 41.4-, 12.7-, and 6.35-mm-thick HY-130 steel plates. The dimensions of the specimens can be inferred from Figure B-1, and a series of untested specimens is shown in Figure B-2. Because of material availability and limitations in the loading capability of our mechanical testing system, width B of the specimens was not scaled exactly (50.8, 88.9, and 152.4 mm for 1/8-, 1/4-, and 1/2-scale, respectively). The specimens were gas tungsten arc-welded (GTAW) using 1.63-mm-diameter 100S weld wire and the welding parameters given in Table B-1.

The static fracture experiments were performed under displacement control in a 500-kN servohydraulic machine using a specially designed test fixture. Figure B-3 shows the test arrangement for a 1/2-scale specimen. Similar arrangements--with the fixtures suspended at the set of holes shown at the center of the triangular plate in Figure B-3--were used when testing the 1/4- and 1/8-scale specimens.
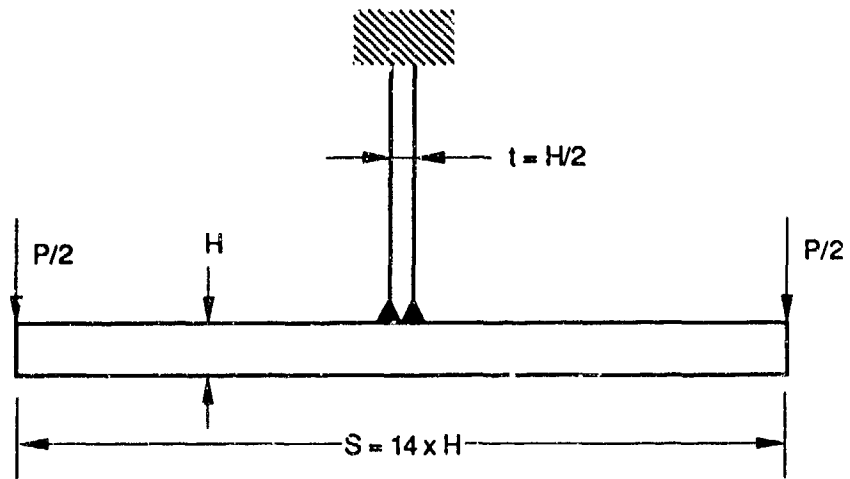
SCALE	H (mm)	WIDTH B (mm)
1/8	6.35	50.8
1/4	12.7	88.9
1/2	25.4	152.4

RA-M-2612-13A

Figure B-1.   Configuration for static fracture experiments.

Figure B-2.   1/8-, 1/4-, and 1/2-Scale HY-130 steel static fracture specimens instrumented with strain gages.
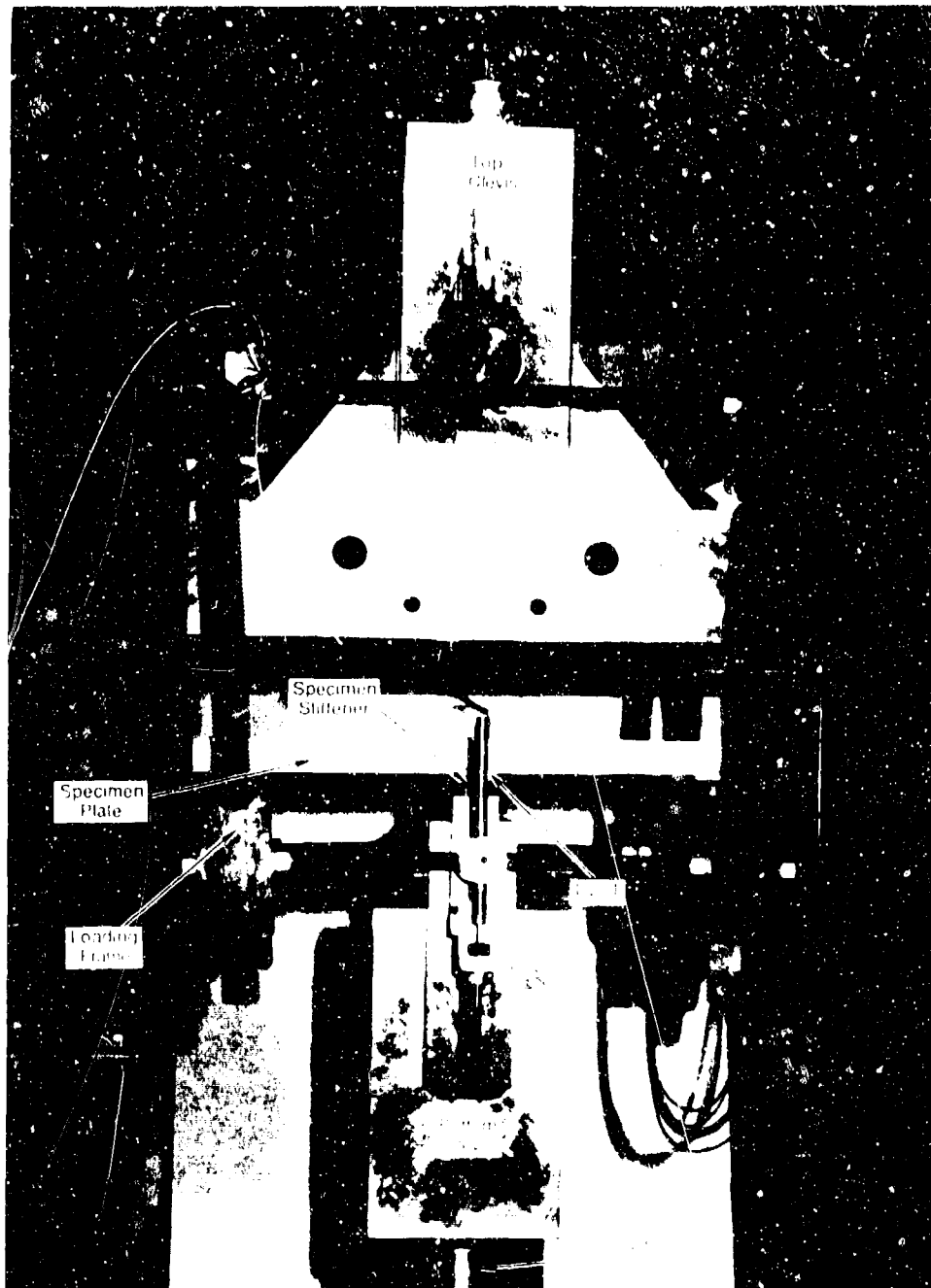
RP 2612 33

Figure B 3   Experimental arrangement for the 1.2 scale static fracture experiments

TABLE B-1. WELDING CONDITIONS FOR STATIC FRACTURE SPECIMENS
(100S WELD WIRE)

Specimen Scale	1/8	1/4	1/2
Weld wire diameter	1.5 mm	1.5 mm	1.5 mm
Amperage	150-160 A	150-165 A	190-200 A
Voltage	18-19 V	18-20 V	26-28 V
Protective environment	Argon	Argon	Argon
Preheat temperature	65°C	69-95°C	95°C
Interpass temperature	65-120°C	65-120°C	95-120°C
Number of passes	1 Sealer + 2 each side	Spec. 0: 1 sealer + 5 each side Spec 1: 1 sealer + 3 each side Specs. 2 + 3: 1 sealer + 4 each side	1 Sealer + 8 each side

Instrumentation

During each static fracture experiment, we measured the applied load, the machine ram displacement, and the specimen center line deflection using a linearly variable differential transformer (LVDT) mounted between the specimen stiffener and the loading frame (Figure B-3). We also performed acoustic emission measurements to detect the point of crack initiation. One specimen of each scale was instrumented with strain gages to verify the uniformity of bending strains across the specimen plate and to assess the effect of welding distortions. The locations of the strain gages are shown in Figure B-2. One gage was mounted on each side of the specimen stiffener to measure its tensile and bending deformation; three gages were mounted longitudinally on the specimen plate, one at the center and two at the edges, to measure the bending strains; and a fourth gage was mounted in the width direction at the center of the specimen plate to measure the transverse strain. The gages were mounted at analogous locations (i.e., scaled locations in each specimen scale). The sizes of the stiffener gages and the two longitudinal gages at the plate edge were scaled with the specimen size. The transverse and longitudinal gages at the plate center were the same size for all experiments. The welding distortion of the specimen was assessed semiquantitatively before each experiment by tracing the specimen contour.

Data Reduction

The objective of the static fracture experiments was to establish the load and load-deflection point at which fracture occurred in the three specimen sizes. For reasons that will become obvious

later, we focused our study on crack initiation. Therefore, an important aspect of the experiments was the detection of fracture onset in the welded joint. As discussed below, fracture always began on either side of the stiffener in the heat-affected zone of the specimen plate and the crack propagated through the plate, more or less parallel to the short transverse direction (Figures B-4 and B-15). We applied two complementary methods to identify fracture initiation.

In the first method we monitored the change in the acoustic emission signal as a function of applied specimen displacement. The second method is illustrated in Figure B-4 and relies on posttest measurements of the deformed specimen shape. Before crack initiation, the specimen deformation was symmetrical with respect to the stiffener plane. However, once fracture began on one side of the weldment, deformation of the opposite side stopped and all specimen deformation was concentrated in the region of the crack. The angle α_{PHP} on the uncracked side at the end of the experiment represents the specimen's plastic deformation to the point of crack initiation. If the specimen elastic compliance C_{SP} is known (from load-displacement measurement during the experiment), the total deflection at crack initiation, henceforth termed plastic hinge displacement d_{PH}, can then easily be estimated from posttest specimen deformation measurements using simple geometric considerations:

$$d_{PH} = d_{PHP} + d_{PHE} = S/2 \, \sin(\alpha_{PHP}) + C_{SP} \, F_{PH} \qquad (B\text{-}1)$$

where d_{PHP} and d_{PHE} are the plastic and elastic components of the plastic hinge displacement, respectively, and F_{PH} is the load at the onset of fracture. Because, as will be shown below, fracture began well after a fully plastic hinge developed at the toe of the weldment, F_{PH} can be approximated by the maximum load (or fully plastic load) measured during the experiment. Alternatively, we can use an iterative process. d_{PH} is estimated first using the yield load; then the corresponding F_{PH} is obtained from the load displacement curve, and d_{PH} is recalculated. The process is repeated until an acceptable convergence is reached.

The asymmetrical nature of the deformation beyond the point of crack initiation makes it difficult to interpret the load displacement records or to use unloading compliance methods to monitor crack extension, which is why we focused on crack initiation for the static experiments. We monitored the load and the displacement during crack propagation only to obtain the total energy and plastic energy inputs for extending the crack to the final arrested length.
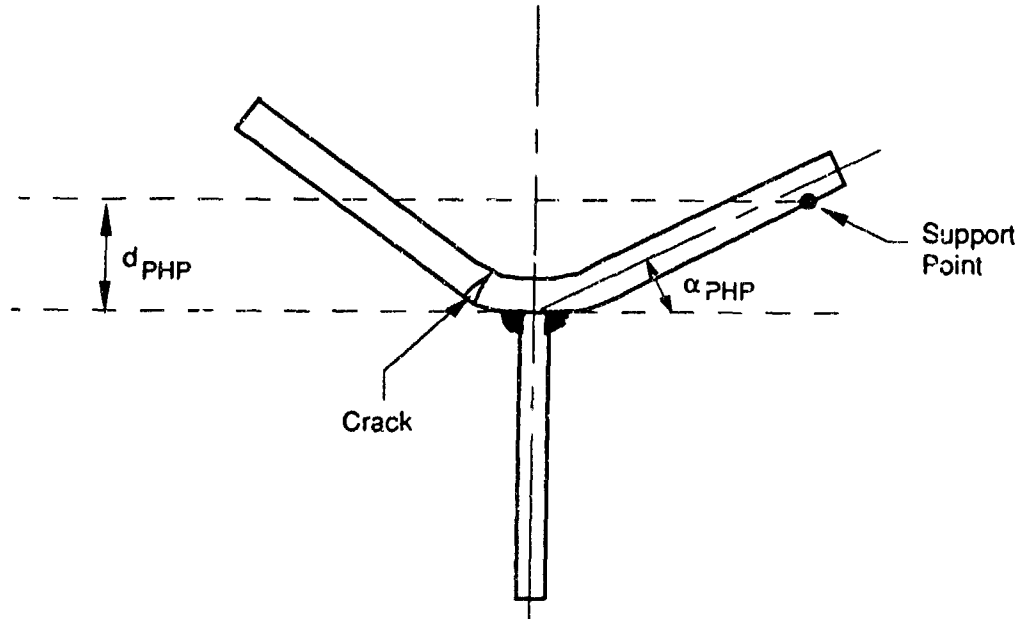
RA-M-2612-82

Figure B-4.   Definition of plastic component of plastic hinge
displacement, d_{PHP}.

To compare the experimental results for the various specimen scales, we normalized them as follows. The load data were multiplied by the factor

$$\alpha_{load} = \frac{S}{\sigma_Y B H^2} \quad \text{(B-2)}$$

where S is the specimen span between supports, σ_Y is the yield strength, B is the specimen width, and H is the specimen thickness (Figure B-1). The specimen displacement data were normalized simply by dividing by the specimen thickness H. The energy inputs were normalized by the factor

$$\alpha_{energy} = \frac{S}{\sigma_Y B H^3} \quad \text{(B-3)}$$

After the experiments, selected specimens were cross-sectioned, polished, and etched for metallographic observations. The crack path and final crack length were determined from these observations.

EXPERIMENTAL RESULTS

Load-Displacement Curves

The normalized load-displacement curves for all 14 experiments are shown in Figures B-5 through B-7. In the 1/2-scale test, HY-130 WSTB2-1, the loading fixture interfered with the specimen deflection toward the end of the experiment, slightly reducing the effective span of the specimen and causing an upward inflection in that part of the load-displacement curve immediately preceding the load drop associated with fracture (Figure B-7a).During all the experiments, the onset of fracture was clearly detectable with acoustic emission. A typical acoustic emission record (the voltage proportional to the event count during a sampling time) is shown in Figure B-8 superimposed on the corresponding load-displacement record for the corresponding 1/4-scale experiment. Early in the experiment, a relatively high acoustic emission was recorded because the specimen was positioning itself in the loading fixture. A long quiet period followed the initial noisy phase. Finally, crack initiation and extension were associated with a sudden sustained burst of the acoustic emission signal. The displacement corresponding to crack initiation, as indicated by the acoustic emission signal, d_{AE}, was obtained for each experiment from a plot similar to that in Figure B-8. We also determined the displacement at initiation, d_{PH}, as indicated by the plastic hinge displacement method.
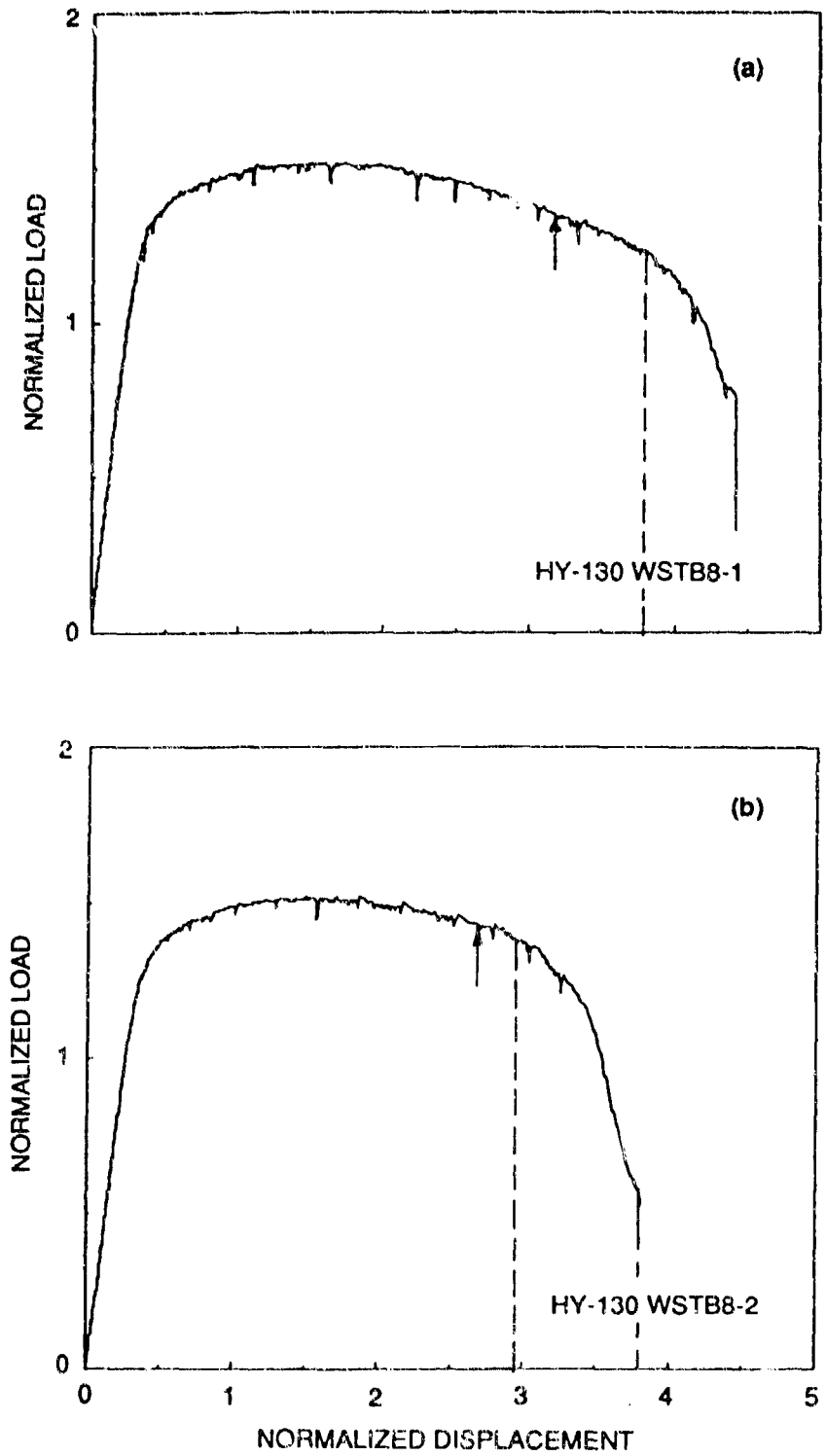
Figure B-5.   Load deflection curves for 1/8-scale experiments.

Figure B-5.   Load deflection curves for 1/8-scale experiments (continued).
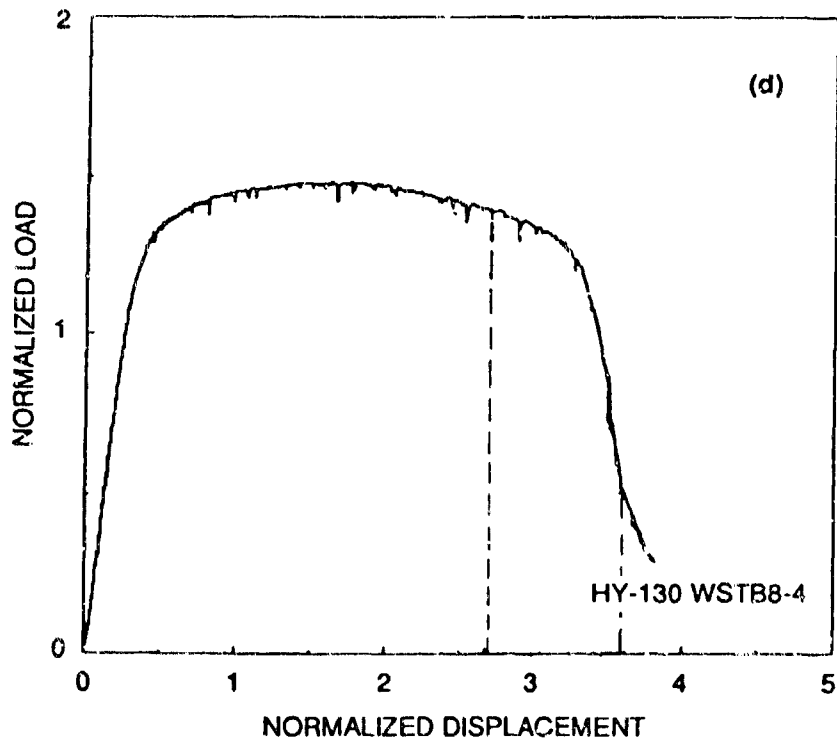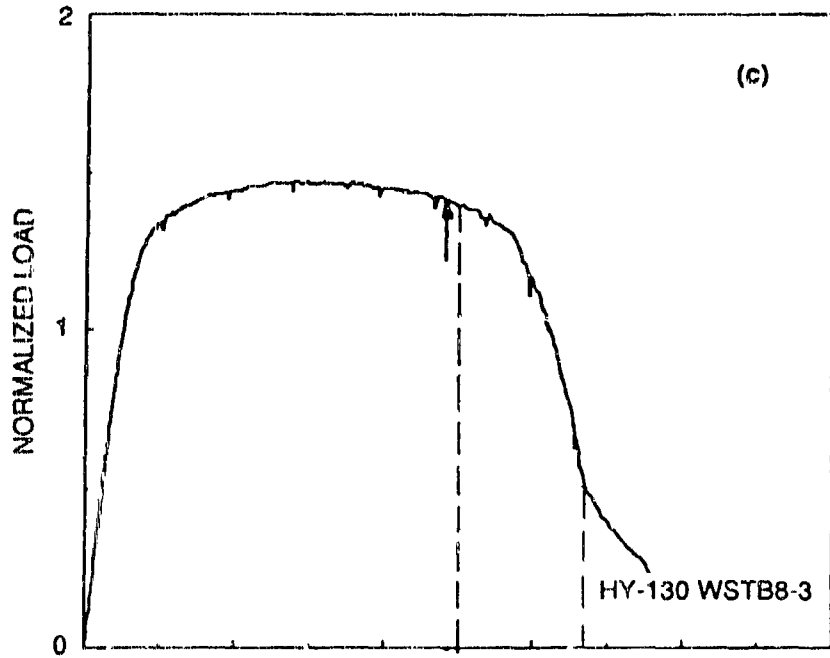
Figure B-5.   Load deflection curves for 1/8-scale experiments (continued)
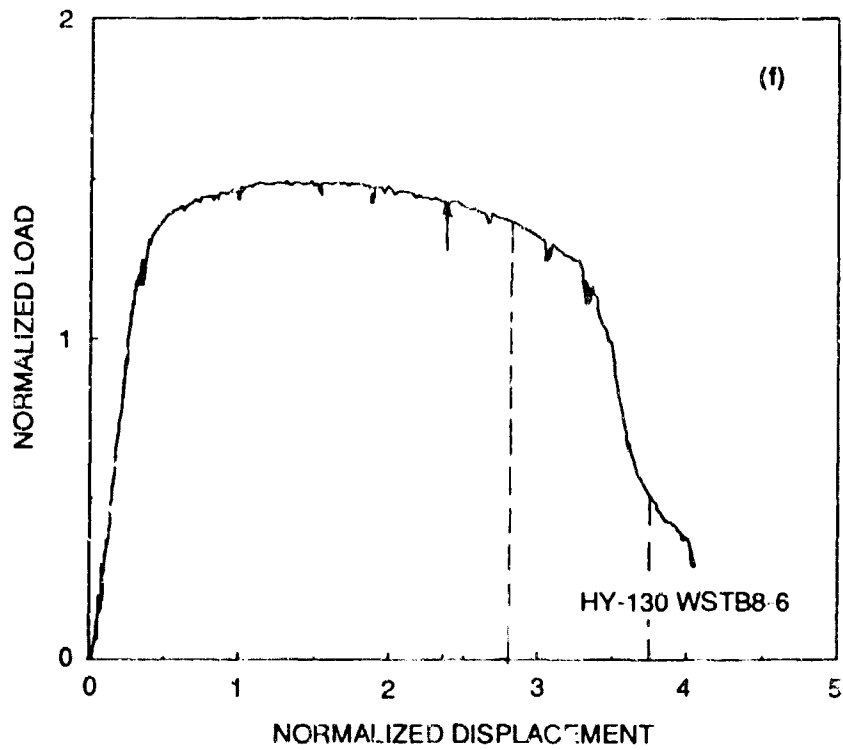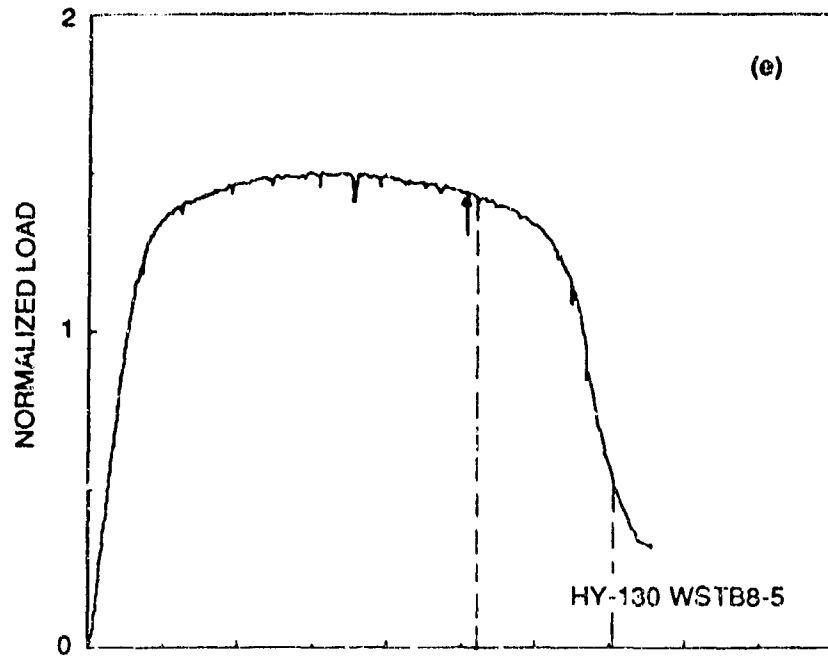
RA-2612-85
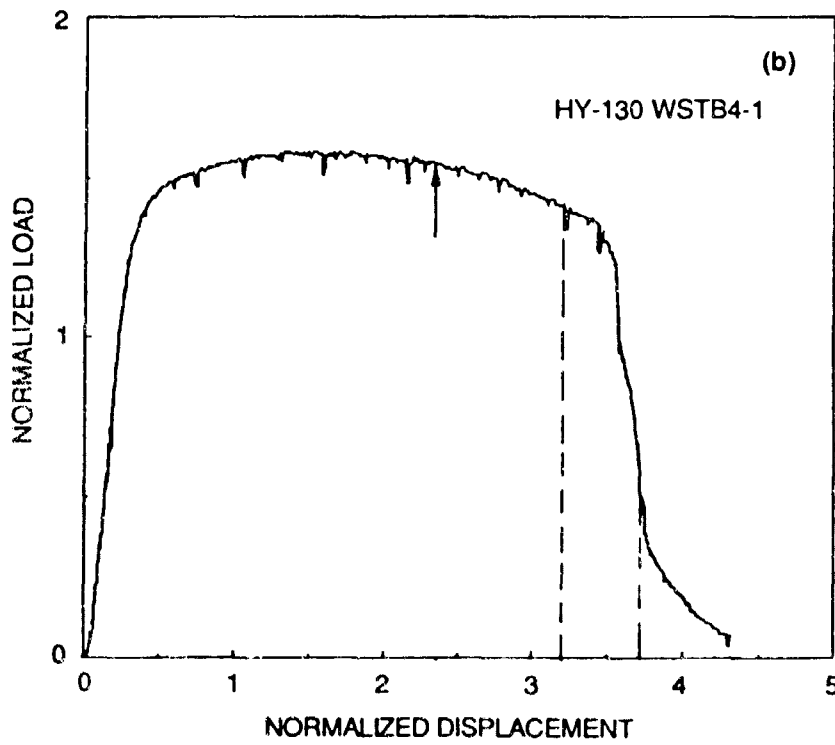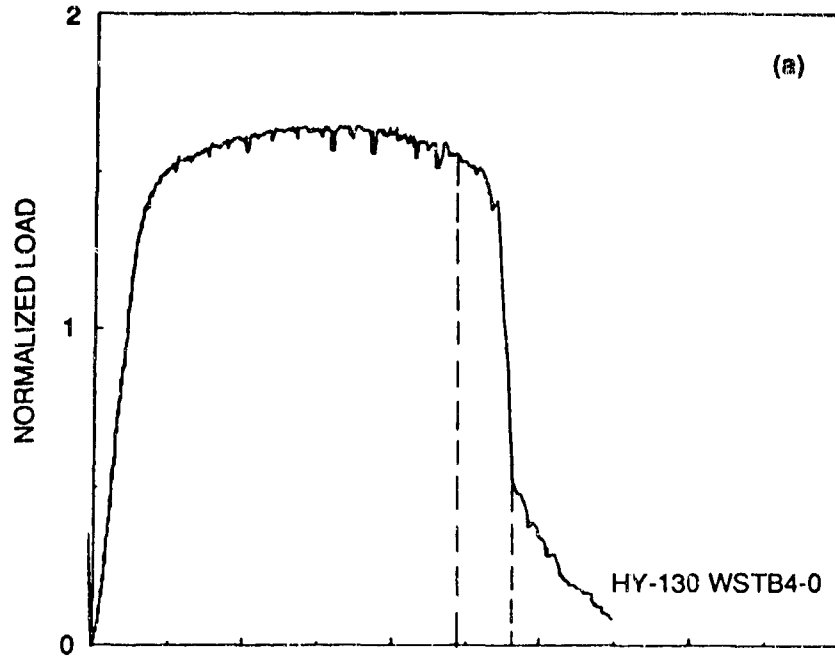
Figure B-5.   Load deflection curves for 1/8-scale experiments (concluded).

Figure B-6.   Load deflection curves for 1/4-scale experiments.
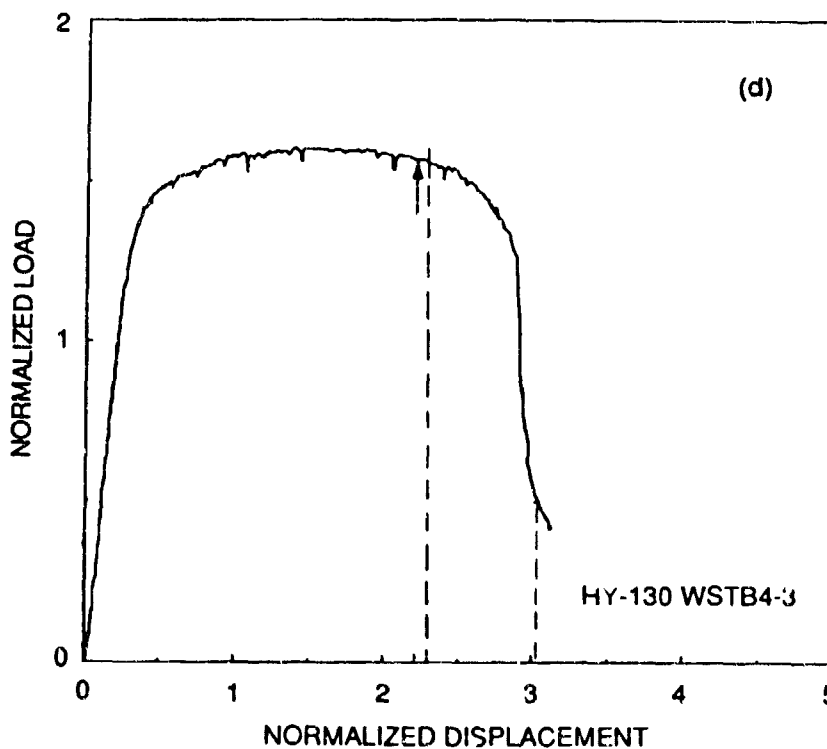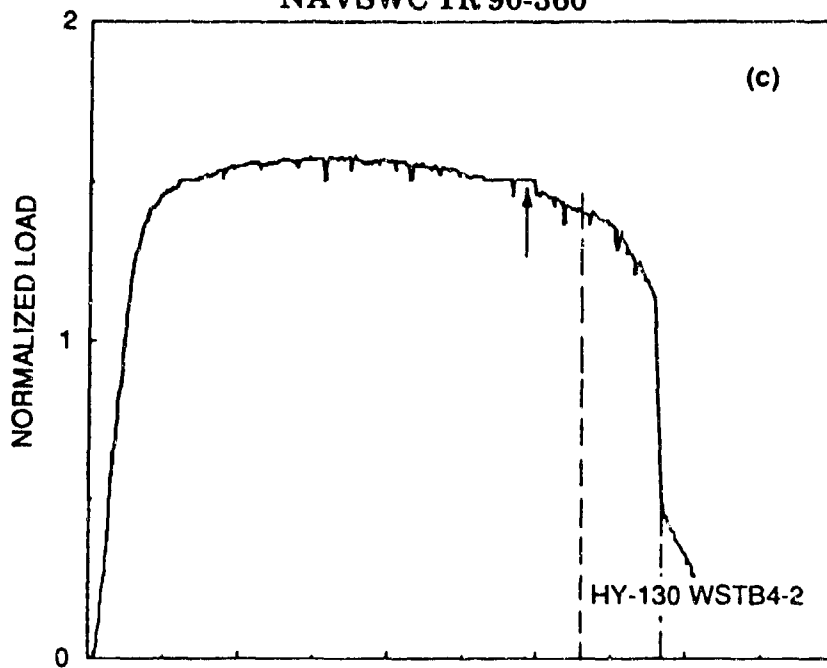
Figure B-6.   Load deflection curves for 1/4-Scale experiments (concluded).
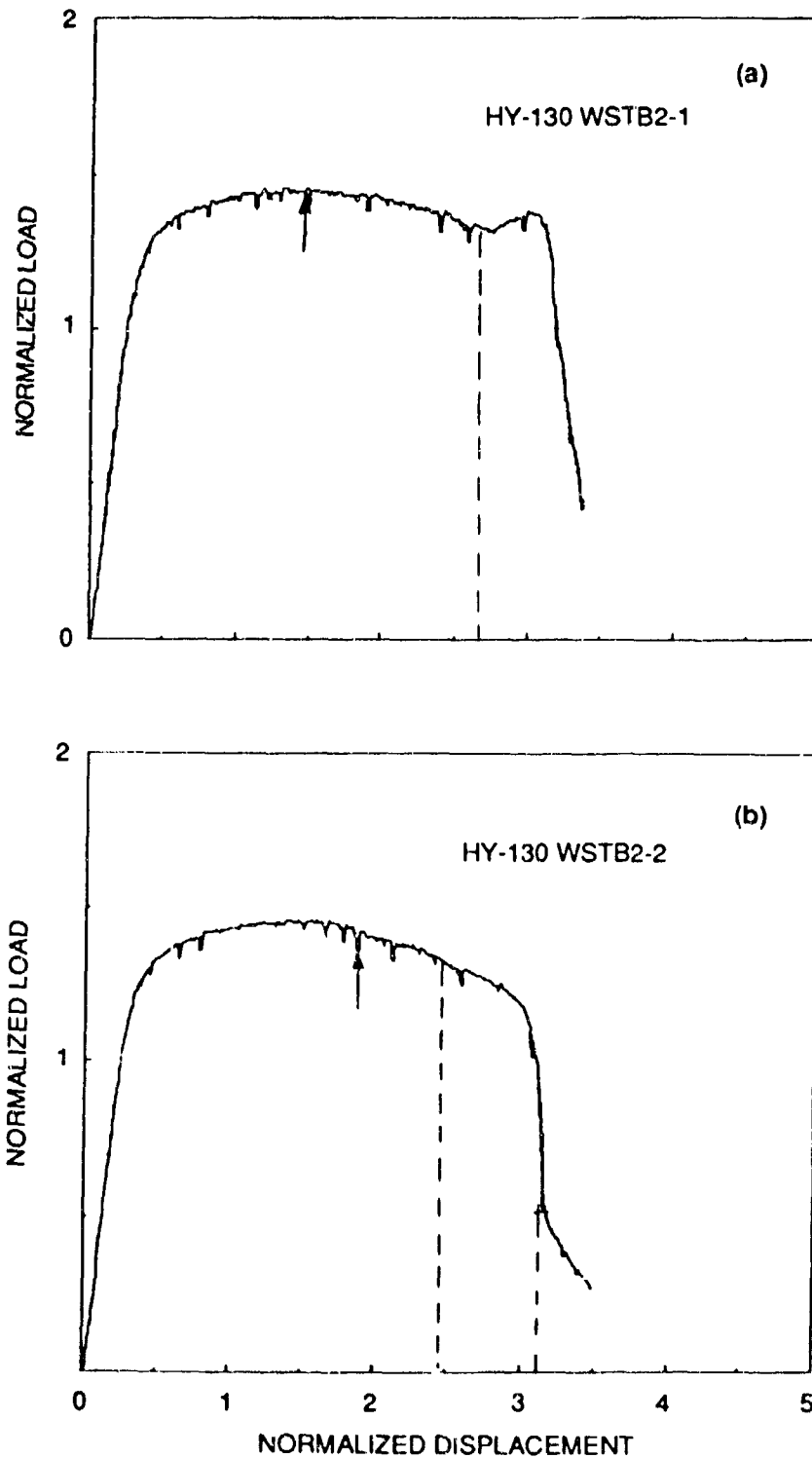
Figure B-7.   Load deflection curves for 1/2-scale experiments.
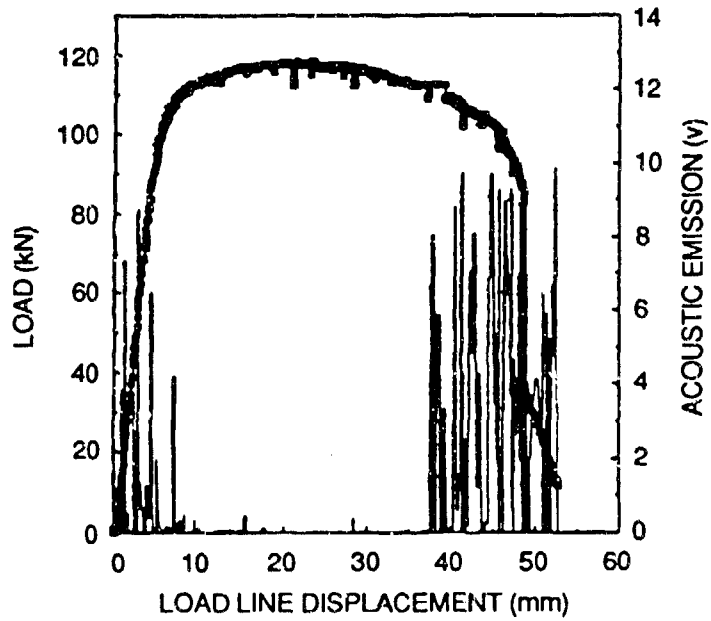
RA-2612-90

Figure B-8.   Acoustic emission record as a function of specimen
displacement superimposed on the corresponding
load-displacement curve to indicate point of crack
initiation d_{AE} (1/4-scale experiment).

The correlation between the displacements at fracture initiation determined by acoustic emission, d_{AE}, and by the plastic hinge displacement method, d_{PH}, is shown in Figure B-9 for the three scales studied. Figure B-9 indicates that acoustic emission always detects the onset of fracture earlier (i.e., at smaller imposed specimen displacements) than the plastic hinge displacement method. In later discussions, the d_{PH} value will be used as the displacement value at crack initiation. In Figures B-5 through B-7, we indicate d_{PH} by a vertical dashed line and d_{AE} by a vertical arrow.

In all the experiments, the load increased to a maximum value and then gradually decreased with deformation until d_{PH} was reached. Beyond d_{PH} the decrease in load or softening, accelerated rapidly as the crack propagated into the plate. The initial softening from the point of maximum load to d_{PH} was not related to fracture but rather was caused by the specimen's great deformation and the resulting shift in its point of contact with the rollers. This geometric softening mechanism was demonstrated by finite element analysis (see Appendix D).

The results of the static fracture experiments are compared in Figure B-10, which plots the normalized load deflection curve of the specimens with the largest and smallest energy absorption for each of the three scales. Also plotted in Figure B-10 are the average displacements d_{PH} at which macroscopic crack extension began for each specimen scale, along with the range of scatter in the experimental data.

Seven of the eight 1/8-scale experiments were spread between the two left 1/8-scale curves in Figure B-9. One 1/8-scale specimen fractured at a much larger displacement than in all the other experiments (HY-130 WSTB8-1). Therefore, the load-deflection curve from that experiment represents the reference load-displacement curve for an unfractured specimen with which all the other load-deflection curves can be compared. The displacement at which the load-displacement curve begins to deviate from the reference curve is then another indication of the displacement at crack initiation. Estimates of the point of crack initiation based on this third method agree well with the predictions of the plastic hinge method.

In the four 1/4-scale experiments, two tests generated almost identical load-deflection curves with low displacement at crack initiation, and the other two tests had almost identical curves with high displacement. These two extremes are indicated in Figure B-10. The two 1/2-scale experiments produced almost identical results (except for the specimen-fixture interference in one test), so only one curve is shown.

RA-2612-91
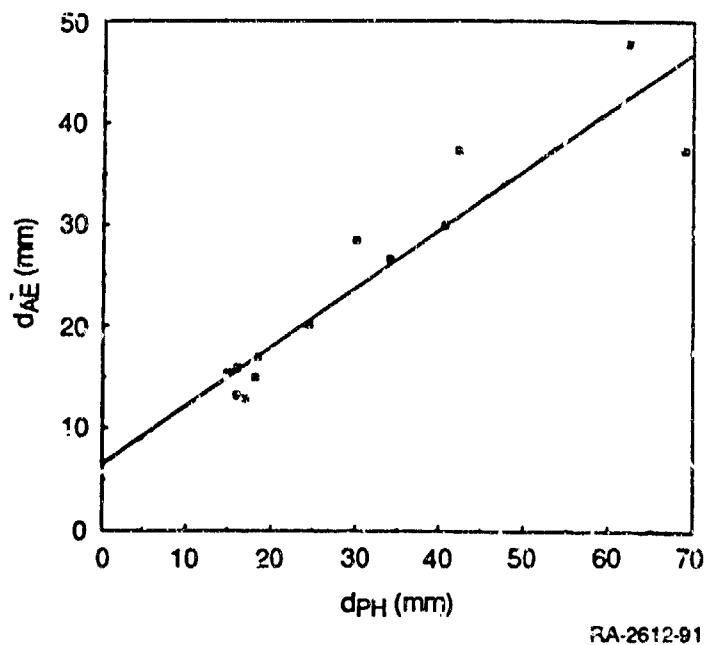
Figure B-9.   Plot of d_{AE} versus d_{PH}.
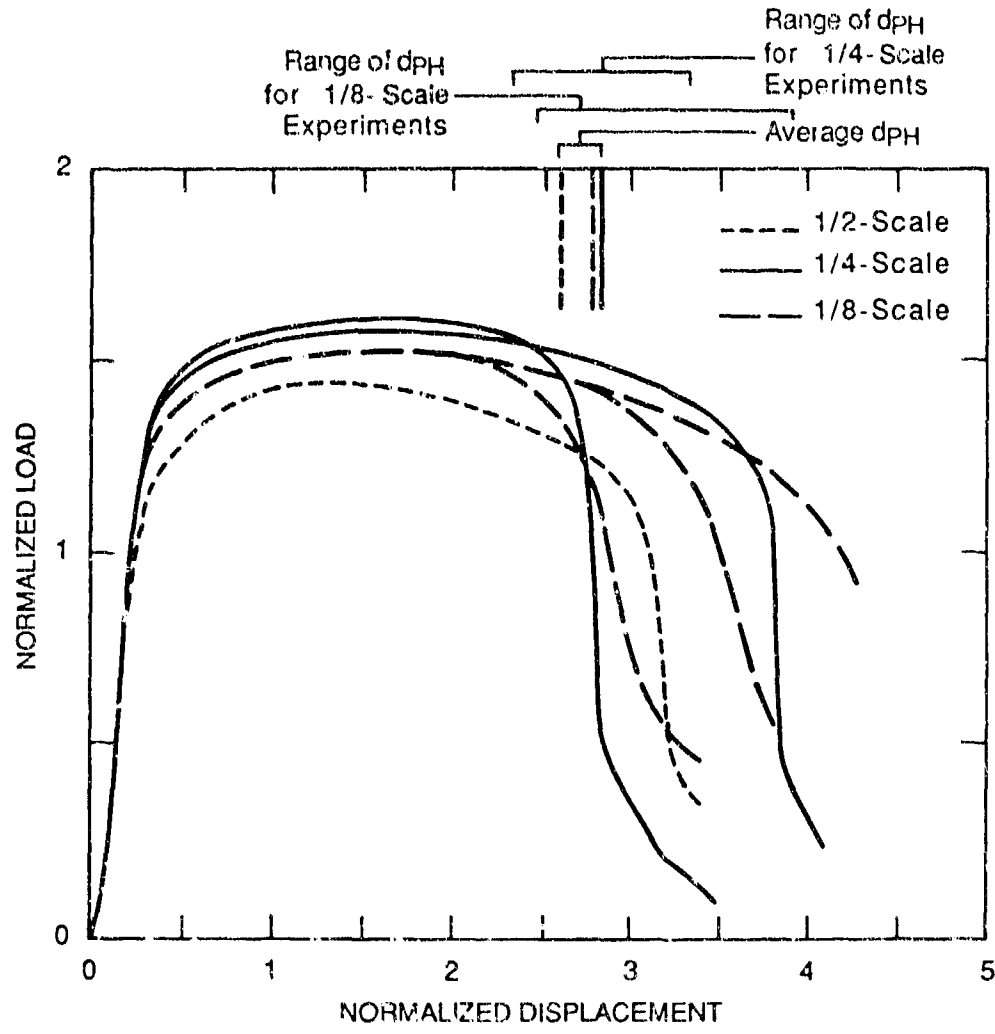
Figure B-10. Summary and comparison of results of the static fracture experiments.

From Figures B-5 through B-7 and B-10, we observed that in all the experiments fracture began well into the fully plastic domain. The average displacements at fracture initiation for each of the three scales are similar, and the differences are well within the observed scatter. Figure B-10 also reveals some differences in the overall shape of the normalized load-displacement curves. This is particularly true for the 1/2-scale curve, which falls 10 percent below the 1/4- and 1/8-scale curves. This difference in limit load is surprising, because from continuum mechanics considerations we expect the load-deflection curve for geometrically scaled specimens also to scale geometrically. Comparing the normalized elastic stiffnesses for the three specimen scales [normalized by $4EB(H/S)^3$], we also notice that the 1/2-scale specimens are significantly less stiff (up to 16%) than the specimens of the other two scales. Again, this observation is contrary to the anticipated scaling behavior.

Plastic Energy Dissipation

The normalized plastic energy dissipated during the static experiments is plotted in Figure B-11 for the three scales tested. It increases almost linearly with applied displacement to the point of crack initiation. The differences in slope among the three scales are due to differences in the limit load values discussed above. The observed differences in the displacements at crack initiation result in somewhat more important differences in the energy dissipation, on the order of 25 percent of the total energy dissipated. However, these differences are of the same magnitude as the scatter for the 1/8- and 1/4-scale experiments.

We also evaluated the plastic energy dissipated during crack extension. Without reliable crack growth measurements, we evaluated the energy dissipated from the point of crack initiation to the point where the applied load was reduced by crack growth to a normalized value of 0.5 under fixed displacement conditions. For all three scales, the normalized energy dissipation during the crack growth phase defined above was about 0.8-1, which represents about 20-25 percent of the total energy dissipated during the test.

Strain Distributions

The strain measurements in the stiffener for each specimen scale are shown in Figure B-12 as a function of the normalized specimen displacement. This figure plots the average of the sum of the strains on opposite sides of the stiffener, which represents the tensile strain (and is proportional to the applied load), and the difference, which represents the bending strain. As expected, the tensile strains are consistent with the load measurement and show similar differences in the maximum amplitude as a function of specimen scale.
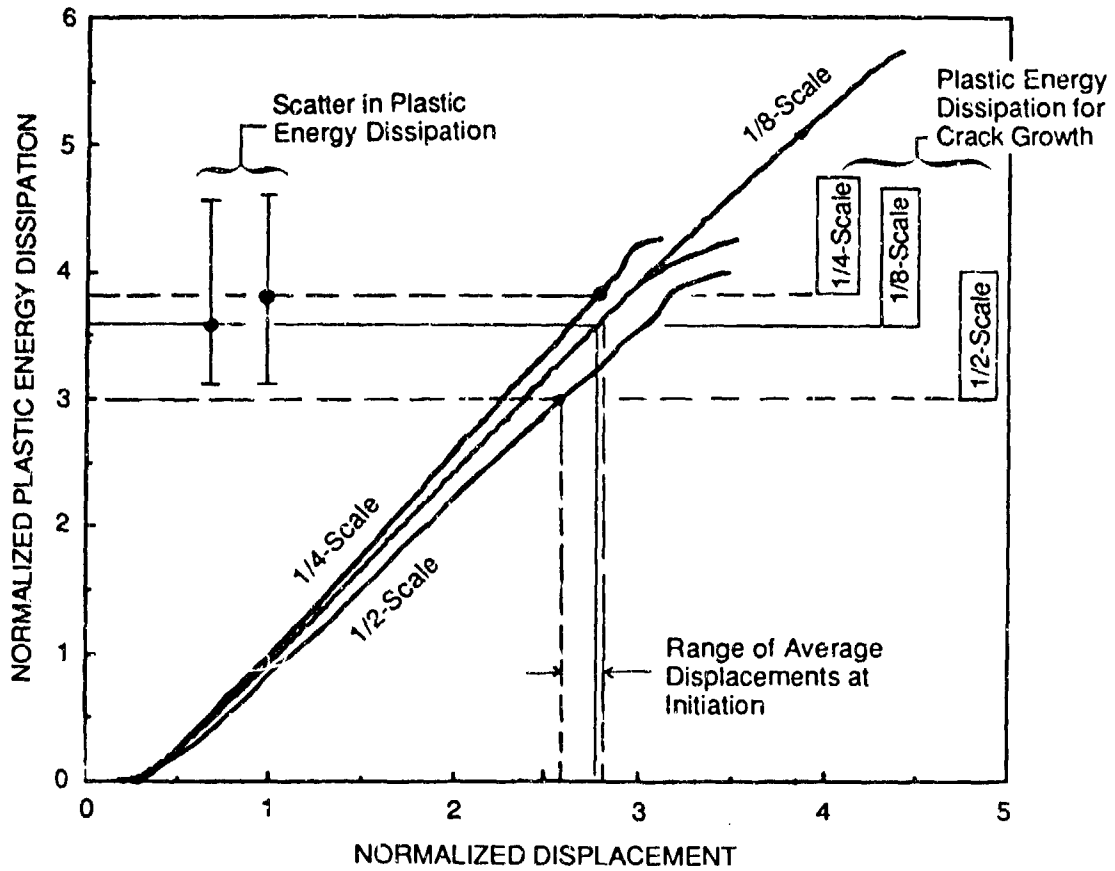
Figure B-11. Normalized plastic energy dissipation in static fracture experiments.
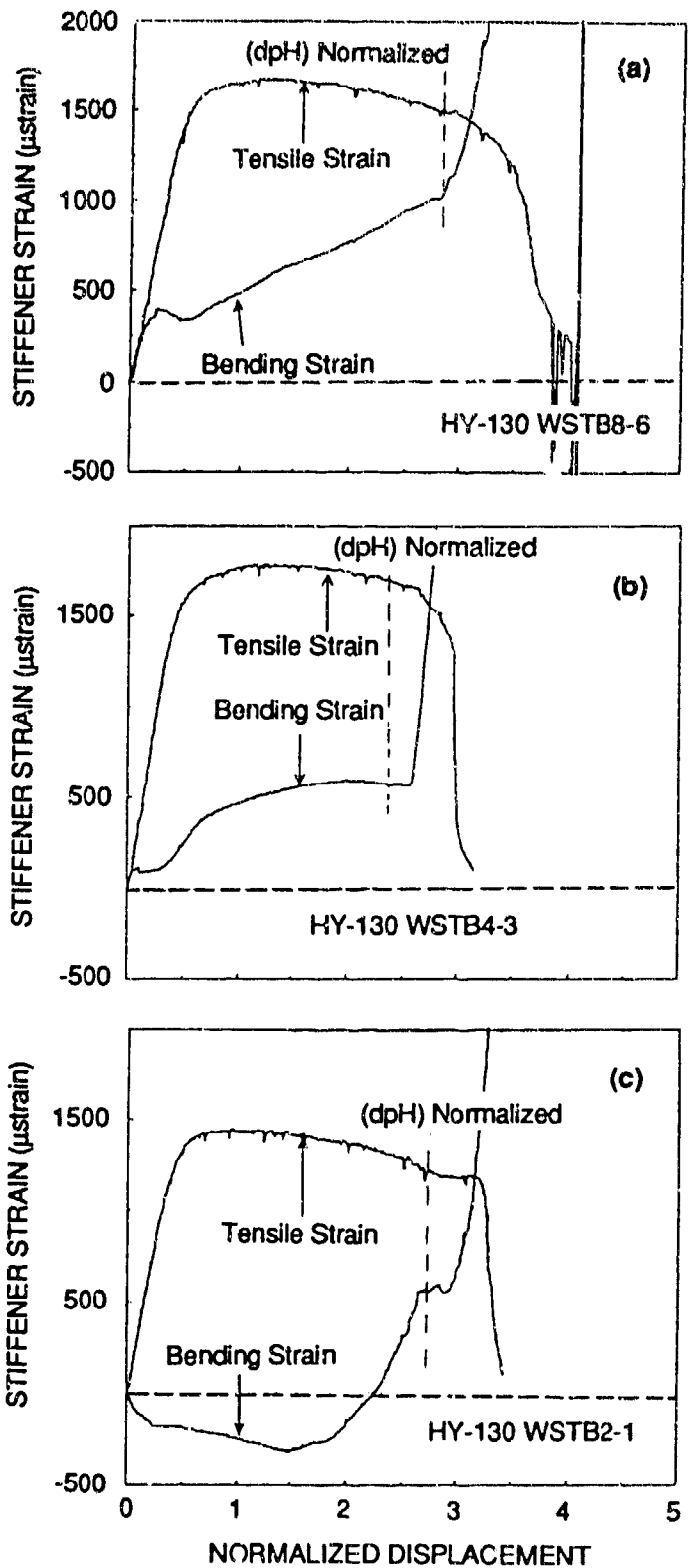
Figure B-12. Stiffener tensile and bending strains.

Figure B-12 also shows that significant bending strains developed in the stiffener and varied nonlinearly with displacement during most of the experiments. The variation in bending strain was quite different in the three specimen scales during most of the experiment but showed a similar rapid increase toward the end. We believe that the bending of the stiffener was a consequence of the small specimen warpage, which caused the specimen to rotate around the weldment axis. The great increase in stiffener bending strain at the end of the test was associated with fracture initiation, and the displacement at which it started, agrees very well with the plastic hinge displacement.

Longitudinal strain measurements across the plate width demonstrate that, despite specimen warpage, the plate bending was uniform. This uniformity is illustrated in Figure B-13, which plots for each specimen scale the two strain measurements showing the greatest difference as a function of normalized specimen displacement. Here again, the displacement at which the longitudinal bending strain in the plate reached a maximum agrees very well with the plastic hinge displacement, giving us confidence in our ability to detect crack initiation.

The transverse strain measurements at the mid-width position on the top of the specimen plate are shown in Figure B-14, which indicates that although a state of plane strain might be anticipated at that location, significant transverse compressive strains were nevertheless induced during the experiment. Figure B-14 also shows that the transverse strain increased with increasing specimen scale. Transverse strains resulted from the rotation around the longitudinal direction of planes normal to the plate width direction. This rotation was induced by the great bending strains in the longitudinal direction. Therefore, strictly plane strain conditions are never achieved at the top of the specimen plate, although they may still prevail on average across the plate thickness. Indeed, finite element simulations, (see Appendix D) demonstrate that the load-deflection curve, calculated on the assumption of plane strain conditions, accurately predicts the experimentally measured curve.

Fractographic Observations

Figure B-15 shows cross sections through fractured weldments of 1/8-, 1/4-, and 1/2-scale, respectively. The overall appearance and crack shapes are similar for all three scales. A crack begins in the HAZ. After a few millimeters of extension, the propagation path changes rather abruptly and the crack extends farther in a direction more or less parallel to the plate normal. More detailed observations reveal scale-dependent differences in the crack initiation sites in the HAZ. In the 1/8-scale specimens, cracks began at the toe of the weld metal and cut across the HAZ before turning into the base metal of the specimen plate (Figure B-15a). In the 1/2-scale specimen, cracks
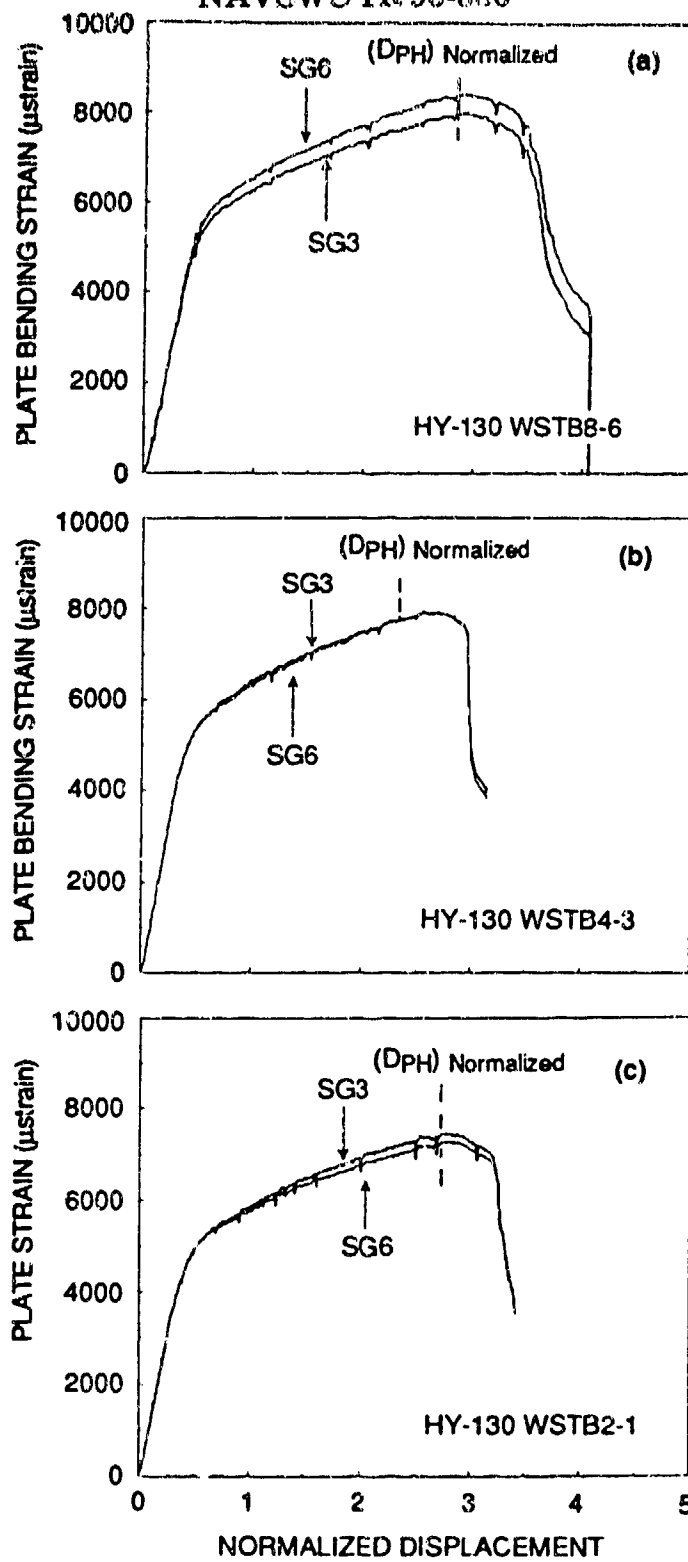
Figure B-13. Plate longitudinal bending strains.
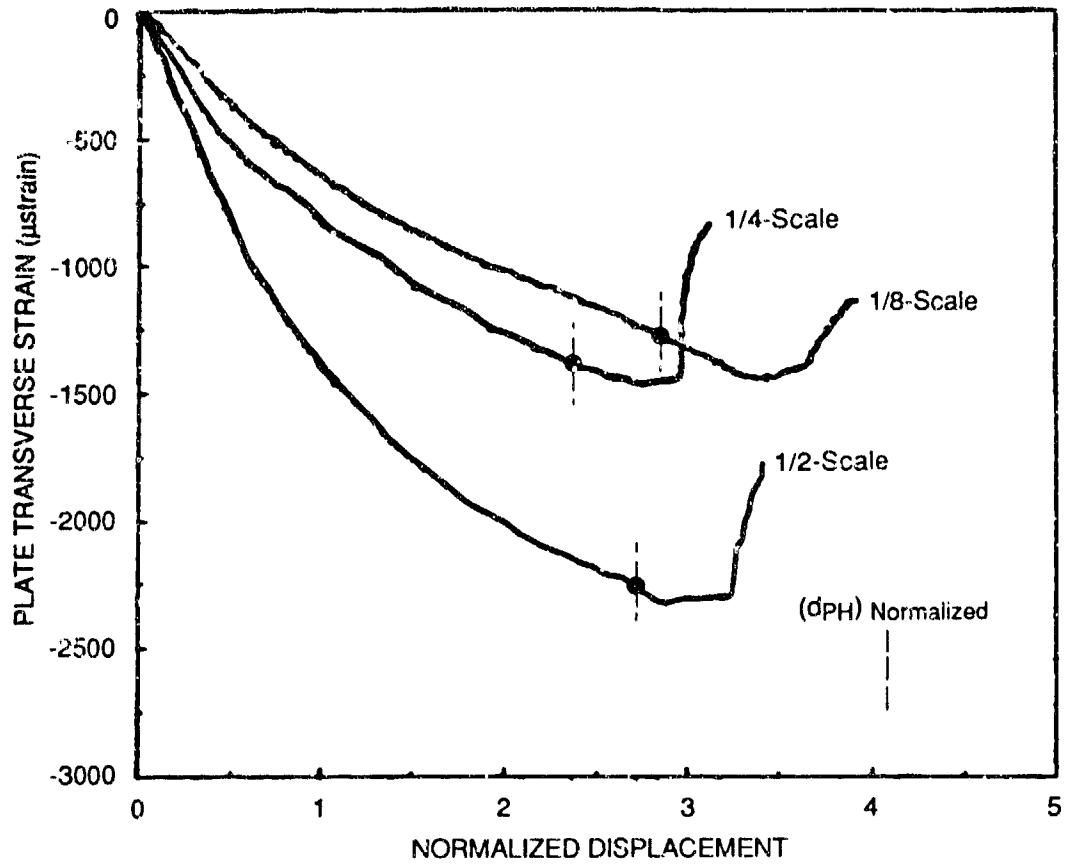
Figure B-14. Plate transverse strain.

1/8-Scale

1/4-Scale

1/2-Scale

(a)

Stiffener

Weld Metal

Initial Crack

Heat-Affected Zone

Plate

(b)

Stiffener

Weld Metal

Initial Crack

Heat-Affected Zone
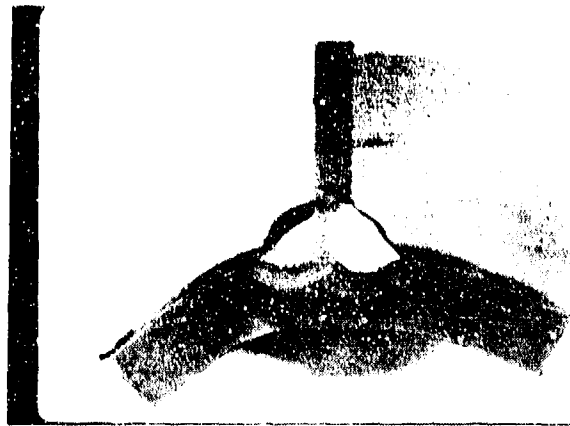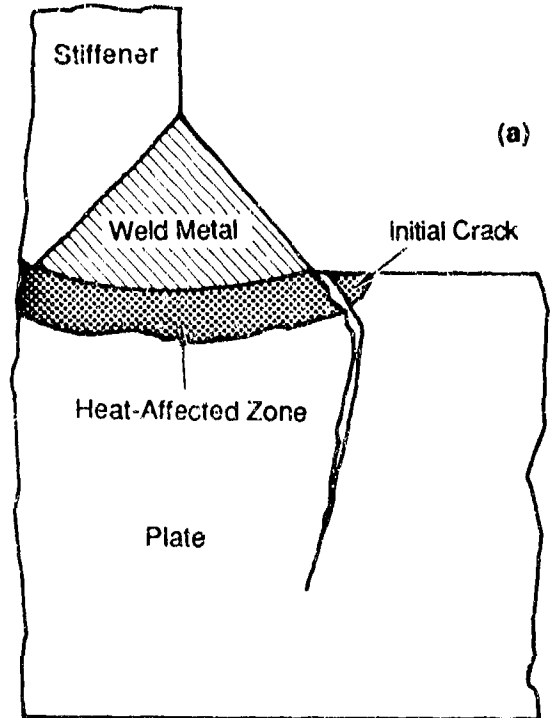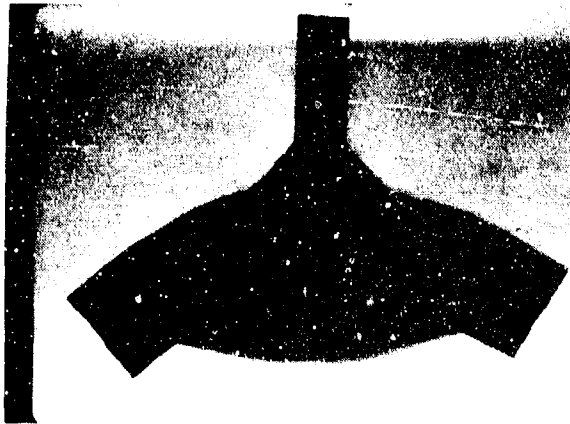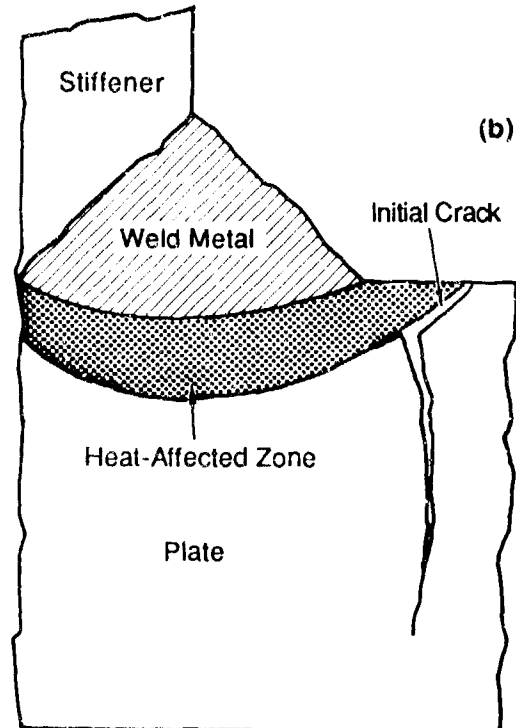
Plate

RP-2612-36

Figure B-15.   Cross section of statically fractured specimens showing crack path.

began at the HAZ/base metal interface at the top of the specimen plate (Figure B-15b); they propagated along the interface for a few millimeters and then also turned into the base metal. In the 1/4-scale specimens, both types of initiation sites were observed, alternating for collinear crack segments along the specimen width.

A reconstruction of the crack profiles using metallographic cross sections indicates that after propagating across the HAZ or along the HAZ/base metal boundary, the first crack stopped and blunted before restarting and propagating into the base metal. This behavior is illustrated in Figure B-16, where the crack shown in the cross section of Figure B-16a has been partly closed in Figure B-16b to reveal the blunting that occurred at the HAZ/base metal interface.

In the 1/8-scale specimens, the amount of blunting, as measured by the crack opening displacement, appears to correlate with the plastic hinge displacement d_{PH} (Table B-2). This correlation suggests that the scatter in the fracture initiation results may be due to variations in the HAZ properties. Unfortunately, a similar correlation does not extend to the other specimen scales, and no clear-cut conclusion can be drawn from these data at present. Nevertheless, the data in Table B-2 may prove useful in assessing the fracture resistance of the HAZ/base metal interface to provide input for the weldment fracture model.

TABLE B-2. CRACK OPENING DISPLACEMENT DATA FOR ARRESTED CRACK
AT HAZ/BM INTERFACE

Specimen HY-130 No.	Crack Opening Displacement, 0.1 mm Behind Crack Tip (µm)	Normalized Plastic Hinge Displacement
WSTB8-1	210-220	3.86
WSTB8-2	125	2.91
WSTB8-4	60-70	2.68
WSTB8-8	<10	2.52
WSTB4-0	200	2.68
WSTB4-2	60-70	3.31
WSTB2-2	460-470	2.46

DISCUSSION

Before discussing the scaling rule for the fracture of HY-130 steel weldments suggested by the results of the static fracture experiments, we will focus on four individual aspects of the results and their impact on our overall conclusions: (1) detecting crack initiation, (2) the effect of warpage and the implication of the strain measurement results, (3) the discrepancy in the fully plastic load values, and (4) the scatter in the data.

RP-2612-35

Figure B-16. Reconstruction of arrested crack in 1/8-scale specimen showing blunting of the crack tip and crack opening displacement.

Detecting Crack Initiation

We used two methods to establish fracture initiation in the experiments: acoustic emission measurements and the plastic hinge displacement method. Figure B-9 indicates that acoustic emission always detects the onset of fracture earlier than the plastic hinge displacement method. This finding is not surprising, because acoustic emission records the stress waves emitted by the formation of individual microfractures, whereas the plastic hinge displacement is associated with the formation of a macroscopic crack on one side of the weld joint, which results in termination of the deformation on the other side. Therefore, we interpret the acoustic emission signal as indicative of the onset of microscopic fracture, whereas plastic hinge displacement indicates the onset of macroscopic fracture associated with measurable reductions in structural stiffness. Because we are concerned with structural rather than microstructural failure, we adopted the plastic hinge displacement definition of crack initiation.

The consistency of the correlation between the acoustic emission and plastic hinge displacement methods demonstrates that we have a good method of identifying fracture initiation in our experiments. Another verification of the method is provided by the measurements of strains from the instrumented specimens. In a previous section we showed that characteristic changes in the strain records, which can be explained in terms of the effect of crack initiation, occur at a displacement that is in good agreement with d_{PH}. Comparing the normalized load-displacement curves with the reference curve obtained from experiment HY-130 WSTB8-1 provides a third verification. Here again, the displacement at which the load-displacement curve begins to deviate from the reference curve is in good agreement with d_{PH}.

By comparing d_{PH} with displacement values obtained by the strain or reference curve method, we estimate that the uncertainty in the normalized displacement at the point of fracture initiation is approximately ± 0.15, or ± 5 percent. Therefore, we conclude that our determination of the point of fracture initiation is reliable. The uncertainty is much smaller than the scatter in the data.

Effect of Specimen Warpage and Implications of Strain Measurement Results

The longitudinal strain measurements performed on three specimen plates (Figure B-13) indicate that specimen warpage does not significantly affect the uniformity of the bending moment across the specimen plate. On the other hand, we measured bending strains in the stiffener that suggested some asymmetry in the specimen loading. An estimate, based on the measured bending strains, indicates that the moment in the stiffener never exceeds about 1 percent of the total moment applied to the weldment. Therefore, slight asymmetry in loading, which may be caused by specimen warpage or asymmetry in the weld geometry or the loading fixture, does not significantly influence the results.

The transverse strain measurements (Figure B-14) demonstrate that, despite the great width of our specimens, a state of plane strain was not achieved at the top surface of the specimen plate. As might be expected, comparing the 1/8-, 1/4-, and 1/2-scale data shows that the transverse strains were reduced by a (relative) increase in specimen thickness. The lack of plane strain conditions in the specimen may somewhat impair our ability to model the weldment fracture. However, the strain measurements were performed about halfway between the weldment and the load application point; the weldment region was significantly more constrained because of the stiffener. Therefore, we expect a state of stress closer to plane strain at the fracture initiation point than at the location of the transverse strain gage.

Discrepancy in Stiffness and Fully Plastic Load Values

Figure B-10 indicates a significant difference falling below a reasonable scatter range in the elastic stiffness, the yield load, and the fully plastic load for the 1/2-scale specimens compared with loads for the other two scales. This difference is disturbing, because from continuum mechanics considerations we expect identical normalized load-displacement curves from geometrically scaled specimens.

Comparing the longitudinal strains measured on the plate surface, which are a direct measure of the plastic hinge moment, indicates that the difference in fully plastic load measured by the load cell reflects an actual difference in the plastic hinge moment and is not due to geometric effects introduced, say, by differences in the sizes of loading fixtures. Effects associated with nongeometric scaling of the specimens and differences in the flow properties of the material used to fabricate the various specimen sizes may explain the differences in plastic hinge moment. Geometric effects may also explain the difference in normalized stiffness.

In characterizing the weldments, we noticed that the 1/2-scale weldment was relatively smaller than the others (see Appendix A). From statics considerations we estimated that this size difference could result in a decrease in stiffness and fully plastic load of up to 4 percent. However, finite element simulations of the size differences reported in Appendix D did not reveal appreciable differences in yield and fully plastic loads. Another more important parameter not scaled was the specimen width. As we mentioned above, the width has a marked influence on the transverse strain measured on the specimen, suggesting a loss of constraint as the relative width of the specimen is decreased.

Because a loss of constraint is also associated with a reduction in the fully plastic load, the thickness differences could explain the observed fully plastic load differences. Departure of the experimental conditions from the plane strain assumption could also explain the observed

difference in normalized elastic stiffness. However, finite element simulations indicate that the load-deflection curve calculated using a plane strain assumption accurately predicts the 1/8- and 1/4-scale load-deflection curves. Furthermore, if the thickness differences influenced the stiffness and the fully plastic load, we would anticipate a consistent ranking of the normalized stiffness and fully plastic load level in the 1/2-, 1/4-, and 1/8-scale specimens (the relative width of the plate steadily decreased with specimen scale in our experiments), but no such ranking was actually observed. The 1/4-scale tests had the highest normalized stiffness and fully plastic load, and the 1/2-scale tests had the lowest, with the 1/8-scale tests in the middle. Therefore, the difference (in normalized thickness) of the three specimen scales alone is an unlikely cause of the discrepancy in the stiffness and fully plastic load.

Differences in flow properties owing to different material sources cannot fully explain the difference in yield and fully plastic loads, because the curves were scaled by the yield stress and no difference in flow stress greater than 4 percent was measured between the thicker and thinner plates from which specimens were made. (These differences were accounted for when plotting Figures B-7 and B-10.)

On the basis of these considerations and in the absence of more definitive answers, we conclude that the differences between the normalized stiffnesses and the normalized fully plastic loads probably result from the combined influence of the differences in specimen thickness and weldment size, and slight differences in the flow properties, possibly affecting only the weldment region (see the hardness maps in Figures A-14 and A-15 in Appendix A).

Because of the differences in fully plastic loads, some caution will be necessary when deriving the scaling rules for fracture. If, on the one hand, the load differences are associated with differences in relative size and yield and flow properties associated with the weldment region only, then they represent a scaling effect in themselves. If, on the other hand, the load differences are due to thickness-induced constraint differences, then the state of stress in the crack initiation region would be different. That event in turn would have implications for crack initiation conditions, because ductile fracture initiation is known to depend on the state of stress. In that respect, the 1/2-scale specimens would experience a less severe state of stress than the 1/4- or 1/8-scale specimens, so they would appear more resistant to fracture initiation than if their normalized thickness were equal to that of the 1/8-scale specimens.

Scatter in the Data

Aside from the differences in the fully plastic loads, which are not statistical, we also observed a significant scatter in the displacement values at the onset of crack initiation. On the

basis of the available, statistically sparse data, it appears that the scatter increases with decreasing specimen size, a trend often observed in fracture toughness or strength testing of materials to which a weakest-link theory of strength can be applied. The scatter in the values of d_{PH} amounts to more than ± 25 percent of the average value for the 1/8-scale specimens. Comparable scatter is observed in the energy dissipation data.

The demonstrated reliability of the fracture initiation detection method shows that experimental uncertainties do not contribute significantly to the scatter in the results. Rather, the scatter is due to the intrinsic scatter in the geometric and material properties of the weldments. Finite element analysis of weldments with different weld bead geometries (see Appendix D) reveals that geometric variations could account for up to 25 percent of the scatter in the displacement value at fracture initiation.

Variability in the strength and fracture properties of the weldment is more difficult to assess. Our approach has been to perform simulations using the weldment model discussed in Appendix D. At present we have not accumulated enough information to make a conclusive statement about the impact of weldment properties on the scatter in the fracture results. More simulations and possibly more detailed experimental characterization of the weldment properties will be needed.

Weldment fracture is often affected by residual stresses induced by the welding process. However, we do not believe that residual stresses have a significant influence on fracture in HY-130 steel weldments, because fracture occurs after these weldments have undergone great plastic deformation, completely redistributing the residual stress field.

Empirical Scaling Rule

Before deriving an empirical scaling rule for the fracture of HY-130 steel T-weldments on the basis of results of the static fracture experiments, we must emphasize at least four limitations that may restrict the rule's validity: (1) The results of the static fracture experiments show considerable scatter. (2) The fracture data base is statistically scarce, particularly for the 1/2-scale experiments, for which only two tests were performed. (3) The lower fully plastic load for the 1/2-scale specimens, if caused by a thickness-related constraint effect, may have influenced the fracture behavior, making the specimens appear tougher than if their relative width had been equal to that of the 1/8-scale specimens. Similarly, if strength differences in the weldment region are responsible for the lower fully plastic load in the 1/2-scale experiments, we also expect a slight effect on the fracture behavior because of the influence of the local flow strength on the stress triaxiality. In the

following discussion we assume that such a constraint effect is not significant. (4) We obtained experimental data for only three scales, so we have no verification of the behavior at a scale of 1/1.

Bearing in mind these four limitations, the results of the static fracture experiments suggest that fracture initiation in HY-130 steel welded T-weldments follows geometric scaling. This means that the normalized displacement and plastic energy dissipation at fracture initiation will be the same for every specimen scale. This conclusion is justified on the basis of our data if we consider that the differences in the average d_{PH} and plastic energy dissipation for the three specimen scales fall well within the scatter for each of the scales (except for the 1/2-scale plastic energy dissipation, because of the lower fully plastic load).

Comparing the increase in displacement and the energy dissipated in reducing the normalized load to 0.5 during crack extension further suggests that few scale-induced differences will occur during the crack propagation phase, particularly when the displacement increment and the energy absorbed during crack propagation are compared with the total displacement and total fracture energy, respectively. An elastoplastic fracture analysis of crack extension in bend specimens of three different scales confirms this conclusion (see Appendix D).

The conclusion that fracture in HY-130 steel T-weldments follows replica scaling can be rationalized on the basis of two arguments. First, the experimental results show that the fracture experiments were dominated by plastic deformation. Hence, the energy dissipated in actually damaging and eventually fracturing the material is small compared with the overall plastic dissipation. Therefore, scale-induced differences in the fracture energy are likely to be even smaller and will be difficult to observe given the scatter in the results. This argument is consistent with an analysis of fracture scaling under rigid perfectly plastic conditions presented by Atkins,[B-1] which shows that when the structural plastic energy dissipation is large compared with the fracture energy, fracture processes will approximately obey geometric scaling.

The second argument invokes a local fracture criterion to demonstrate that crack initiation in the bulk of the material (i.e., in material in which no preexisting macrocrack is present) or at blunt notches should follow geometric scaling. Consider a local fracture criterion consisting of two conditions. The first, which can be termed the continuum condition, requires that a critical combination of stress and strain be reached in the material. The second, termed the microstructural condition, requires that the critical combination be satisfied over a critical distance related to a characteristic microstructural dimension. This type of criterion has often been discussed in the literature, for both cleavage fracture[B-2,B-3] and ductile void growth fracture.[B-3,B-4]

When the criterion is applied to fracture at a blunt notch, the microstructural condition is always satisfied because the area of elevated stress and strain in the notch region extends over great

distances compared with the characteristic microstructural dimension. In this situation, fracture is controlled only by a high enough combination of stresses and strains (the continuum condition), and the fracture criterion no longer contains a nonscalable material length parameter. Therefore, the criterion predicts that fracture initiation at a blunt notch or stress concentration will follow geometric scaling. This situation may be considered equivalent to crack initiation at a welded T-joint containing no large defects and provides a rationale for our experimental observations that, in first approximation, fracture initiation follows replica scaling.

On the other hand, the situation is reversed in the case of fracture from a preexisting sharp crack, where high stresses and strains are always encountered. However, they prevail only over a limited distance in the crack tip region, which is comparable to the characteristic microstructural dimension. In this situation the continuum condition is always met, and fracture is controlled by the microstructural condition of extending the high stress and strain field over a large enough volume. The fracture criterion now contains a nonscalable length parameter, the characteristic microstructural dimension, and therefore fracture from a sharp crack will not follow geometric scaling. This is the situation that would prevail in the welded T-joint once a sharp crack has begun, and so we expect non-geometric scaling effects during the crack growth phase of fracture. However, as noted above, these effects may be slight in comparison with the scatter in the data and the effect of overall plastic deformation, so they will be difficult to identify.

More experimental verification of the proposed scaling rule is desirable, in particular to resolve the uncertainty about the fully plastic load in the 1/2-scale experiments. Simulations of the type described in Appendix D using the weldment fracture model will also provide more accurate estimates of possible nonscaling effects during crack extension or of nonscaling caused by differences in material properties in welds of different sizes.

SUMMARY AND CONCLUSIONS

We developed a static test to establish the morphology of fracture in HY-130 steel T-weldments. In particular we demonstrated that the beginning of a macroscopic crack can be determined reliably and unambiguously. Fracture of 1/8-, 1/4- and 1/2-scale weldments showed essentially the same morphology. On the basis of the experimental results, we conclude that, in first approximation, the load displacement at fracture initiation in specimens of different scales is governed by geometric scaling. Moreover, the normalized total energy dissipated during crack extension is essentially the same for all three specimen scales investigated. We therefore conclude that, in first approximation, geometric scaling may also govern the conditions for crack propagation.

REFERENCES

B-1. Atkins, A. G., "Scaling in Combined Plastic Flow and Fracture," *Journal of Mechanical Sciences*, Vol. 30, 1988, pp. 173-191.

B-2. Ritchie, R. O.; Knott, J. F.; and Rice, J. R., "On the Relationship Between Critical Tensile Stress and Fracture Toughness in Mild Steel," *Journal of the Mechanics and Physics of Solids*, Vol. 21, 1973, pp. 395-410.

B-3. Ritchie, R. O.; Server, W. L.; and Wulleart, R. A., "Critical Fracture Stress and Fracture Strain Models for Prediction of Lower and Upper Shelf Toughness in Nuclear Pressure Vessel Steels," *Metallurgical Transaction A*, Vol. 10A, 1979, pp. 1557-1570.

B-4. Mudry, F., "Methodology and Applications of Local Criteria for Prediction of Ductile Tearing," *Elastic-Plastic Fracture Mechanics* (L. H. Larson, ed.), ECSC, EEC, EAEC, Brussels and Luxembourg, Belgium, 1985, pp. 263-283.

APPENDIX C: DYNAMIC FRACTURE EXPERIMENTS

CONTENTS

APPENDIX C

DYNAMIC FRACTURE EXPERIMENTS

INTRODUCTION

The dynamic fracture experiments were performed to verify that the empirical scaling rule derived on the basis of the static fracture experiments is also valid under dynamic loading conditions and for a specimen configuration more accurately simulating the ring-stiffened cylinder configuration of interest to the Naval Surface Warfare Center (NAVSWC). This appendix first describes the test configuration, the instrumentation, and the method of analyzing the experiments. We then present the results of ten dynamic fracture experiments (six 1/4- and four 1/8-scale) and discuss the scaling rule inferred from these results.

EXPERIMENTAL PROCEDURE

Experimental Configuration and Specimen Geometry

In the dynamic fracture experiments we achieved high strain rates by loading the specimen with sheet explosive. This method built on the experience previously gained at David Taylor Research Center with a modified explosive tear test.[C-1,C-2] The test configuration was based on an original design proposed by Mr. W. W. McDonald (NAVSWC, White Oak Laboratory) and Dr. D. W. Nicholson (NAVSWC consultant, Stevens Institute of Technology, Hoboken, NJ). The specimen for the dynamic fracture experiments consisted of a slotted base plate with two symmetrically positioned welded stiffeners (Figure C-1a). The dimensions for a 1/4-scale specimen are indicated i. Figure C-1b. The schematic of the loading arrangement is shown in Figure C-2a and a 1/4-scale specimen mounted in the loading fixture is shown in Figure C-2b. Each stiffener was rigidly attached to an independent E-shaped yoke with a cover plate and shoulder bolts. The specimen plate was bolted to a steel die, which in turn was rigidly attached to a base plate. The two yokes also rested on the base plate and surrounded the specimen plate and the die. The yokes could be tilted, and their position relative to each other and to the specimen could be independently adjusted in three directions.
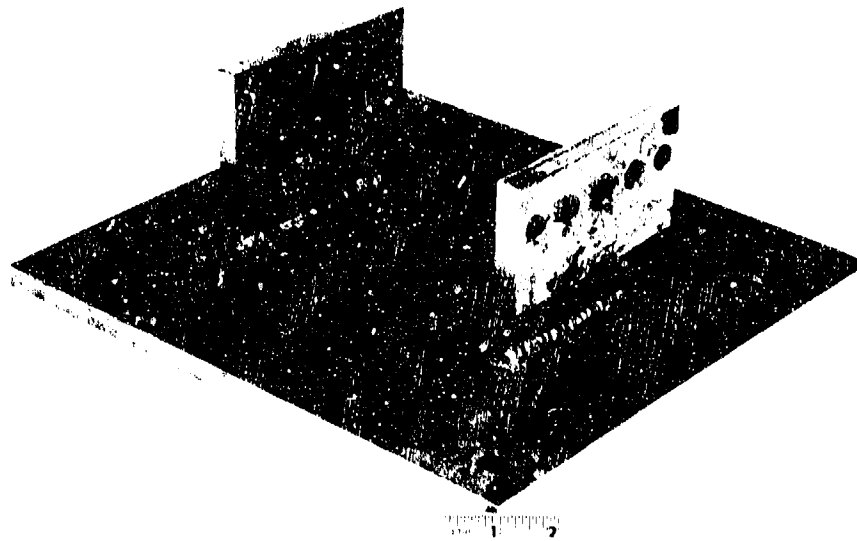
(a) 1/4-Scale specimen
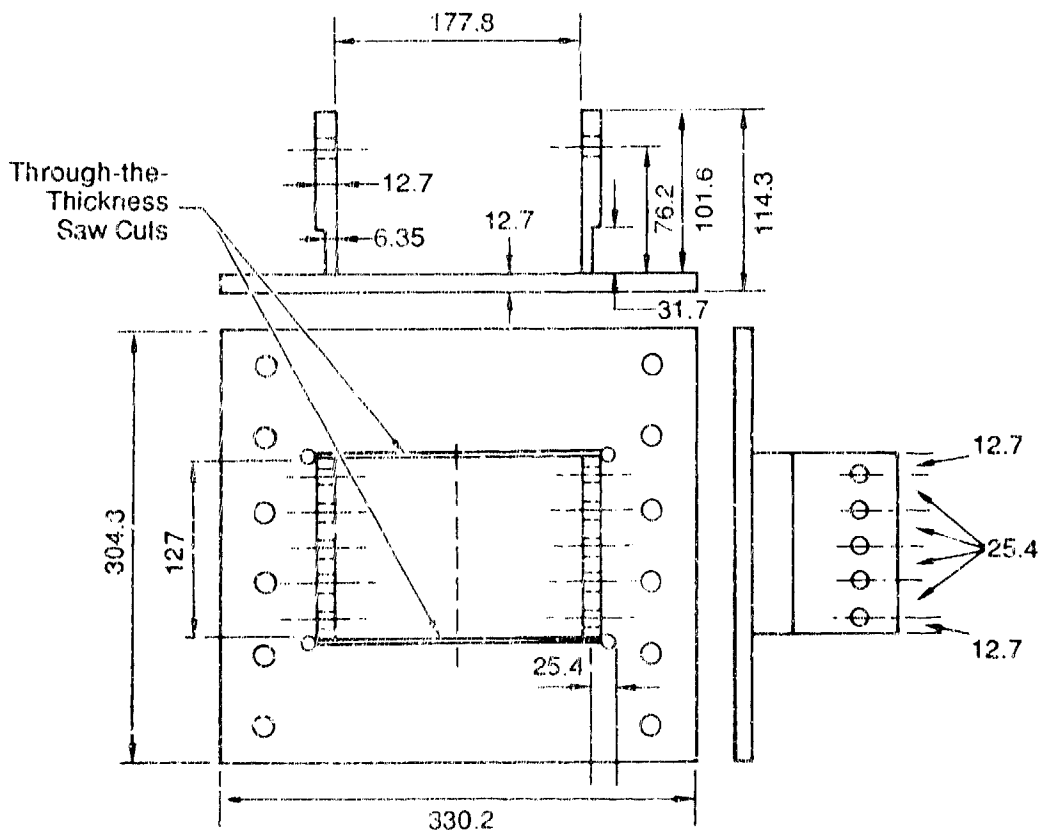
(b) Dimensions (in mm) of 1/4-scale specimen

RP-2612-7A

Figure C-1. Specimen for dynamic fracture experiments.
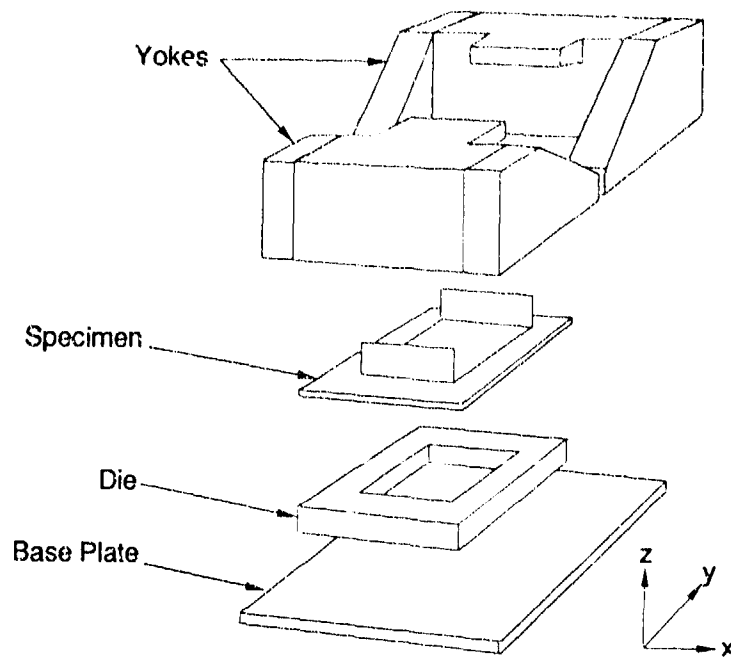
(a) Schematic of fixture
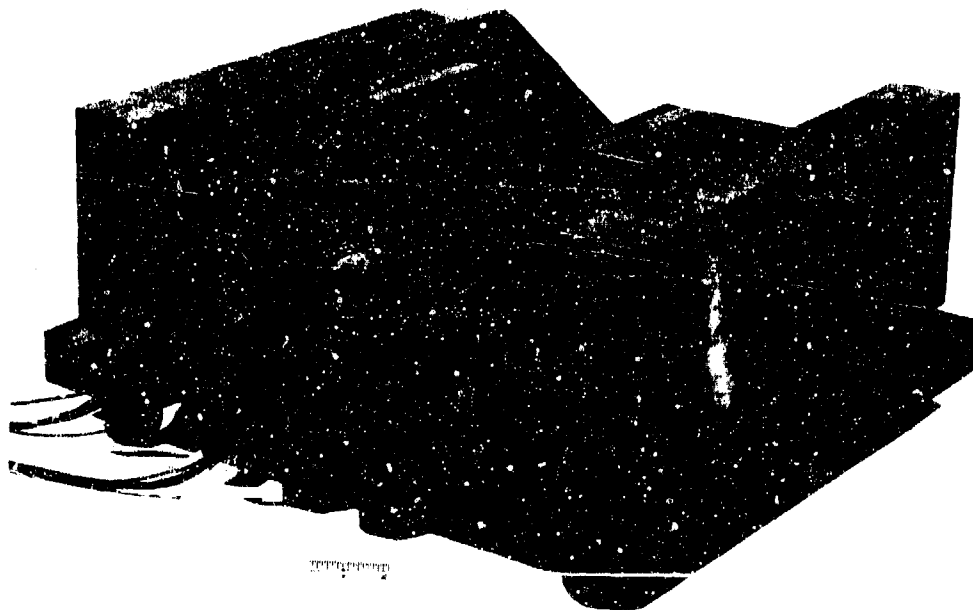
(b) Specimen-fixture assembly for 1/4-scale experiments

RP-2612-8A

Figure C-2.   Loading fixture for dynamic fracture experiments.

This freedom of adjustment was achieved by supporting each yoke with four adjustable jack-bolts and locking the yoke in position with three tie-bolts. The holes in the base plate for the tie-bolts had enough clearance to permit tilting and some translation of the yoke in the base plane. This design allowed precise adjustment of the yokes to accommodate any specimen distortion, particularly that of the stiffener caused by welding. In turn, accommodating welding distortions prevented prestressing the specimen during installation in the test fixture and permitted uniform loading of the stiffener during the test.

In the experiment, the center of the specimen plate between the two slots was loaded with strips of sheet explosive backed by blocks of polymethymethacrylate (PMMA), which increased the impulse delivered to the plate for a given explosive sheet thickness. The charge design and the details of the arrangement used in the experiments are discussed below. With this test arrangement, only the center portion of the specimen plate was significantly deformed during the experiments, whereas the portion supported by the die acted as a reaction frame, inducing membrane stresses in the plate. Membrane stresses represented a major difference in the loading mode of the dynamic fracture specimens compared with that of the static fracture specimens.

We constructed fixtures to load specimens corresponding to 1/4- and 1/8-scale of the full-scale structural element of interest. We also fabricated six 1/4- and four 1/8-scale specimens. Table C-1 summarizes the welding parameters used to fabricate the dynamic fracture specimens.

The 1/4-scale specimens were used to establish the loading conditions needed for fracture initiation and full fracture of the plate and to verify the reproducibility of the test conditions. The 1/8- and 1/4-scale dynamic fracture experiments confirmed the scaling rule derived from the static fracture experiments.

TABLE C-1. WELDING CONDITIONS FOR DYNAMIC FRACTURE EXPERIMENTS
(GTAW PROCESS, 100S WELD WIRE)

Specimen Scale	1/8	1/4
Weld wire diameter	1.5 mm	1.5 mm
Amperage	150-160 A	150-165 A
Voltage	18-19 V	18-20 V
Protective environment	argon	argon
Preheat temperature	65°C	69-90°C
Interpass temperature	65-120°C	65-120°C
Number of passes	1 sealer + 2 each side	1 sealer + 3 each side, alternating side of deposition

Explosive Charge Design

To achieve appropriate loading of the dynamic fracture specimens using sheet explosive, we performed a series of numerical simulations and a preliminary explosive test.

To guide our choice of sheet explosive thickness and tamping material, we performed one-dimensional calculations using the SRI PUFF 8 code.[*][C-3] Another objective of these calculations was to demonstrate that solid tamper materials could adequately simulate the effect of water overburden in underwater explosions and that, for the sake of convenience, solid tampers could be substituted for water in the explosive fracture experiments.

We performed three calculations simulating a 12.7-mm-thick steel plate loaded by detonating a 5.08-mm-thick sheet of explosive with 50.8-mm-thick tamping. The specific energy for the explosive was 5.8 MJ/kg and the density 1.0 kg/m^3. The tamping material was water, PMMA, or steel. We also performed two simulations with prescribed boundary conditions at the surface of the explosive to obtain limits on the achievable impulse; in one simulation we prescribed a free boundary condition (an approximation for air as tamping material) to obtain a lower limit, and in the other case we prescribed a rigid boundary condition to obtain an upper limit. Because we used an approximate equation of state for the explosive gases, the results of the simulations should be considered approximate estimates, which can be used to evaluate ratios of impulses and velocities, rather than absolute values.

The results of the simulations are summarized in Figure C-3, which plots the particle velocity history at mid-thickness in the specimen steel plate. The impulse delivered to the plate at any given time was proportional to the velocity in Figure C-3. After about 60 μs, the plate velocity remained essentially constant for all cases, and a velocity equal to 80 percent or more of the final velocity--and hence the total impulse--was already imparted to the plate after 20 μs. This observation suggests that instantaneously imposing an initial velocity to the specimen plate may be a reasonable approximation in simulations of the dynamic experiments.

Figure C-3 also shows that tamping with water, PMMA, or steel increased the total delivered impulse by factors of 7, 9, or 16, respectively, over the value achievable with air. The increase was controlled by the density of the tamping material and by the wave speed. The maximum achievable impulse (rigid boundary condition) was about 22 times that for air. The impulse value obtained with PMMA was comparable to that obtained with water, so PMMA can be used in our experiments as a practical simulant for water. Finally, the simulations indicated that plate velocities of several hundred meters per second could be expected in the explosive experiments.

---

[*]PUFF 8 is a Lagrangian finite difference computer program for calculating one-dimensional stress wave propagation through solid, liquid, gaseous, and porous materials.
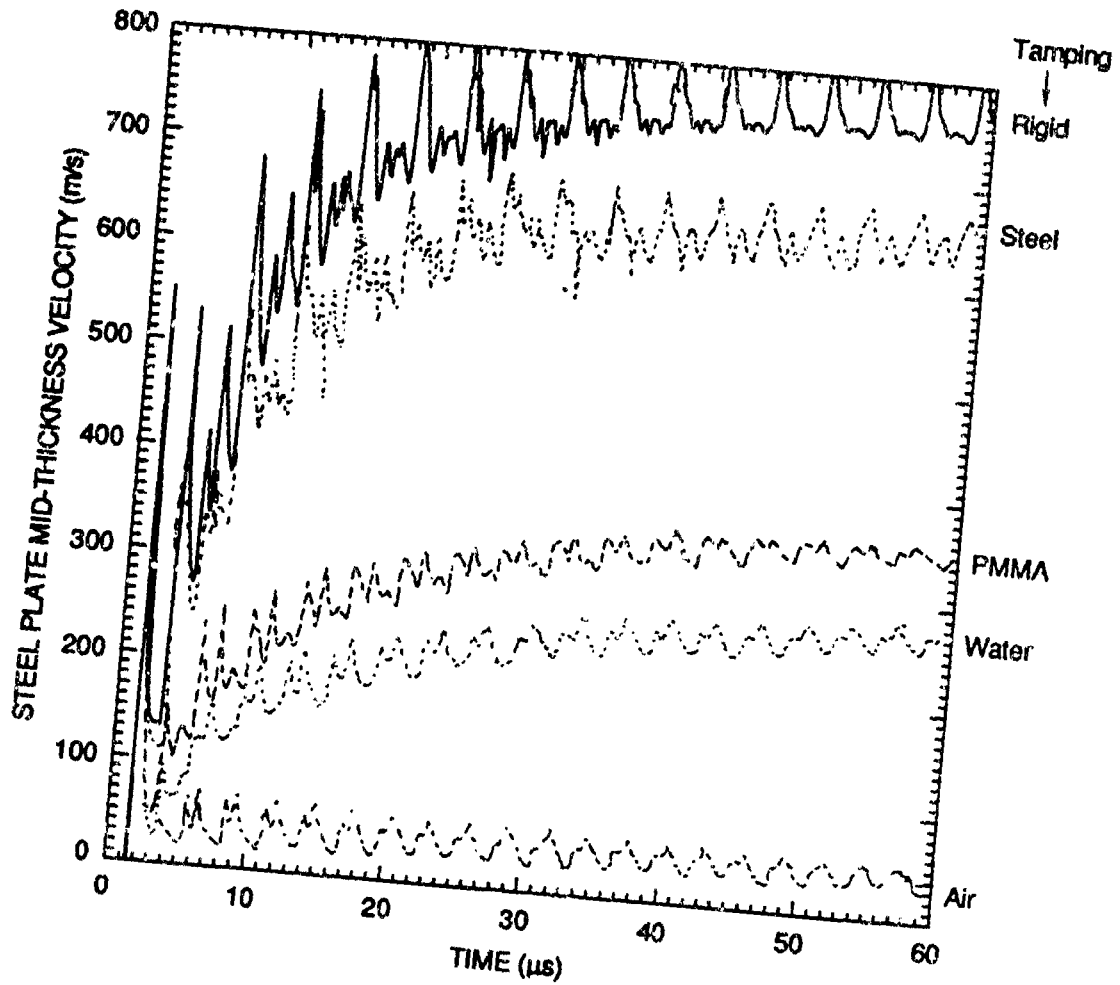
Figure C-3.   Effect of different tamping materials on the mid-thickness velocity
of a steel plate loaded by tamped sheet explosive.
One-dimensional finite difference simulation; steel plate thickness:
12.7 mm, sheet explosive thickness: 5.08 mm, tamping material
thickness: 50.8 mm, sheet explosive specific energy: 5.8 MJ/kg, sheet
explosive density: 1000 kg/m³.

RA-2612-97

As a complement to the simulations, we performed a preliminary explosive test to verify that no spalling would occur when the steel plate was loaded directly in contact with the sheet explosive without intermediate tamping material and to demonstrate that no plate shearing would occur at the edge of the explosive sheet. We loaded a plate of HY-130 steel, 152.4 by 50.8 by 12.7 mm thick with a sheet of DuPont Detasheet® D, 101.6 by 50.8 by 2.54 mm thick tamped with two cubes of mild steel with a 50.8-mm edge length. After the experiment we sectioned the HY-130 steel plate, polished it, and inspected it for spall and shear damage in the zone immediately beneath the explosive. Careful examination revealed no material damage.

On the basis of the simulation and experimental results, we concluded that sheet explosive in direct contact with the specimen plate and tamped with PMMA provides adequate dynamic loading of the specimen to simulate, in first approximation, loads applied to ring-stiffened structures by underwater explosions.

The actual charge configuration used in the 1/4-scale experiments is shown in Figure C-4. Dimensions for the 1/8-scale experiments were scaled exactly. Only a central region of the plate, 101.6 x 127 mm, was explosively loaded. A horizontal sheet of explosive, tamped by two 50.82- x 127-mm blocks of PMMA, was started along the specimen's axis of symmetry by a vertical line generator, itself started by a strip of Detasheet® and a detonator. With this arrangement, the explosive was started uniformly along the specimen width, and the detonation swept symmetrically on both sides of the center line toward the stiffeners. In all the experiments we used Detasheet® C explosive, except for test HY-130 WE4-1, in which we used Detasheet® D. We switched to Detasheet® C because it is the explosive routinely used at NAVSWC. Detasheet® C contains only 70 percent pentaerythriotol tetranitrate (PETN) while Detasheet® D contains 75 percent. The properties of these explosives are listed in Table C-2.

TABLE C-2. PROPERTIES OF SHEET EXPLOSIVES

Explosive Type	Detasheet® C	Detasheet® D
Composition	70% PETN, 30% inert binder	75% PETN, 25% inert binder
Specific energy, E_0 (MJ/kg)	3.40	3.64
Density, r (kg/m^3)	1500	1450

We obtained the specific energy value E_0 for Detasheet® C from the value for Detasheet® D, applying a simple rule of mixture:

$$E_0[\text{Detasheet}^® \text{ C}] = (0.70/0.75)E_0[\text{Detasheet}^® \text{ D}]$$
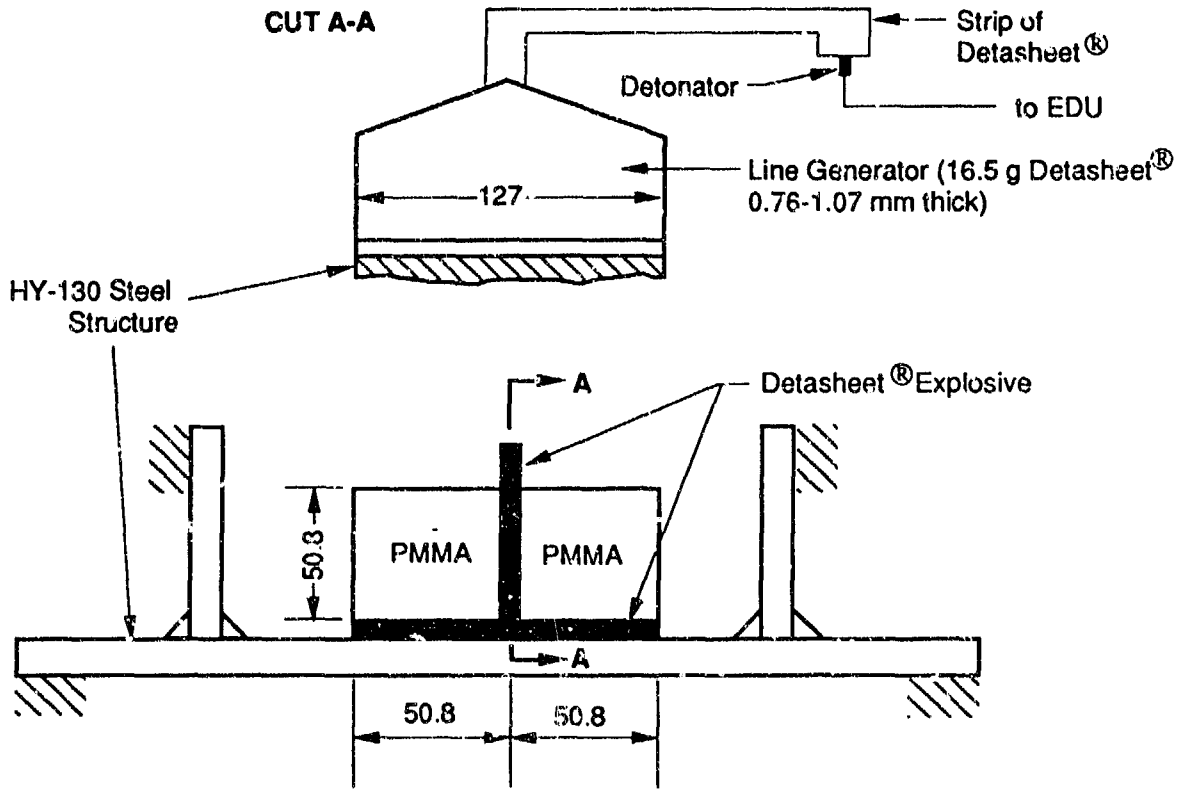
RA-M-2612-08

Figure C-4. Explosive charge configuration for dynamic fracture experiments.
Dimensions (mm) for 1/4-scale experiment shown.

We controlled the amount of deformation induced in each experiment by changing the thickness of the sheet explosive.

Instrumentation

The purpose of the instrumentation for the dynamic fracture experiments was to provide (1) data to characterize the loading applied to the specimen, which could serve as input for numerical simulations; and (2) indications of fracture onset in the specimen.

The instrumentation consisted of sets of contact pins to measure the deflection history at the plate center, piezo pins to detect the onset of crack initiation, and, in the first three 1/4-scale experiments, strain gages. The objective of the strain history measurements was to obtain experimental data for later validation of numerical simulations of the experiments, to provide an estimate of the strain rates, and possibly to indicate the time at which fracture began or completely severed the plate from the rest of the specimen.

Figure C-5a shows a schematic of the contact pins used to measure plate deflection histories. One or two sets of four looped copper strips were mounted in a staggered arrangement on a polycarbonate base. The sets of pins were then mounted beneath the specimen, along the center line, with their axis parallel to the stiffener axis (Figure C-6). The height differences between the apex of each loop as well as the clearance between the bottom of the plate and the top of the highest loop were carefully measured before the experiments.

During the experiment, a rectangular voltage pulse was generated every time the deforming plate contacted one of the staggered pins, a recording of the time of contact. Because we knew the distance between each pin, we could easily measure the deflection history of the specimen's center line from the contact time. As shall be seen below, this method yielded very satisfying and reliable results. The details of the deflection history that could be measured depended on and clearly increased with the number of contact pins.

A piezo pin consists of a brass rod on which a small piezoelectric quartz crystal is mounted. Two pins were mounted beneath the specimen at the level of the two weldments (Figure C-6). The idea behind using the piezo pins was that when a crack began at the toe of the stiffener weld and completely penetrated the plate, the plate would move rapidly downward and strike the piezo pin. Upon impact a large piezoelectric voltage pulse would be induced, indicating the approximate time at which full fracture of the plate occurred. This method required several adjustments of the pin orientation before it gave reasonable indications of the time of fracture in the only 1/8-scale experiment in which complete fracture occurred.
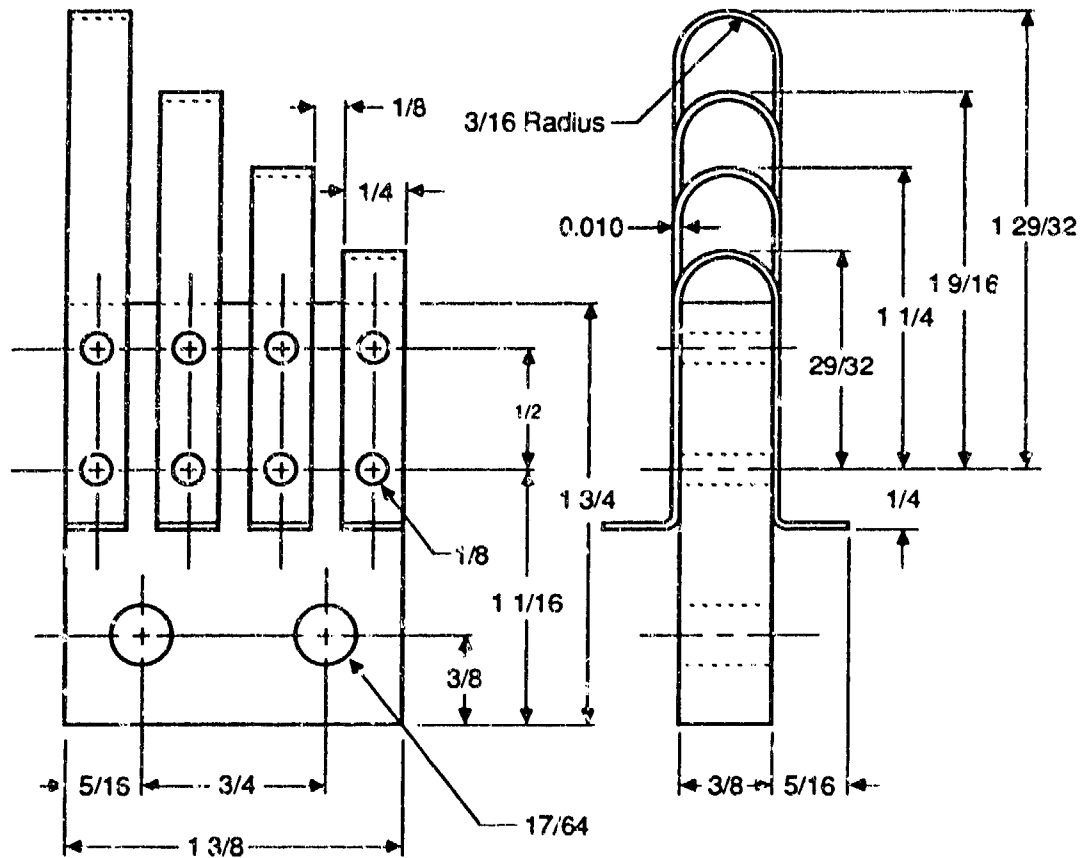
Dimensions in inches
1 in. = 25.4 mm

Materials:
Body-Phenolic/Delrin/Plexiglas
Strips-Copper/Brass

RA-2612-90

Figure C-5.   Contact pins used to measure the deflection history of the
specimen center line (set of four staggered contact pins).

The first three 1/4-scale experiments were instrumented with strain gages: eight gages in test HY-130 WE4-1 and six in tests WE4-2 and -3. The position of the gages for the latter two experiments is indicated in Figure C-6. Four gages were mounted on the stiffeners and two at the bottom of the plate near the weldments. For test WE4-1, two more gages, facing gages 3 and 6 in Figure C-6, were mounted on the top of the plate. We tried to protect the gages from the effects of the explosive blast by covering them with rubber pads and steel shims. We were also careful to minimize the size of the lead solder joints with the gage contact pads. Unfortunately, despite these precautions, the strain gages produced poor records and were abandoned in later experiments.

Data Reduction Procedure

The dynamic fracture experiments were analyzed in two steps. First we analyzed the raw data from the contact pin to get an estimate of the plate center displacement history and the initial velocity V_0; then we analyzed the available strain gage and piezo pin data. The raw deflection history data were then reanalyzed to improve the accuracy and consistency of the results and of the estimates of the initial velocity.

Reducing of Raw Data. The principal piece of data analyzed in the experiments was the deflection history record for the plate center, obtained from the contact pins. From the measured pin-plate spacing and the contact time for the different pins, we obtained the discrete points (up to eight) of the deflection history. By fitting a polynomial through these raw data points and differentiating, we could then estimate the initial velocity V_0 at the plate center. We found that a second-order polynomial fit most of the data points with a good degree of accuracy (see Results section).

In some cases, individual contact times yielded data points of the displacement history that deviated significantly from the general trend, indicating an erroneous contact, possibly caused by the ionized explosive gases or flying debris. This deviation was more prevalent for contact times late in the experiment. These obviously erroneous data points were eliminated from the data set used for fitting the displacement history curves. As a result, there is an uncertainty about the late times deflection history predicted by the second-order polynomial fit to the raw displacement history data. This uncertainty applies particularly to the predicted maximum plate center deflection $(d_{max})_{raw\ fit}$ and the time $(t_{max})_{raw\ fit}$ at which that deflection was reached.

After the experiments, we inspected the specimens to establish whether fracture began and measured the final plastic deflection at the center to the specimen plate, which often did not agree with the maximum deflection predicted by the polynomial fit to the raw data. Therefore, we used the plate center plastic deflection measured after the experiment to improve the polynomial fit of the
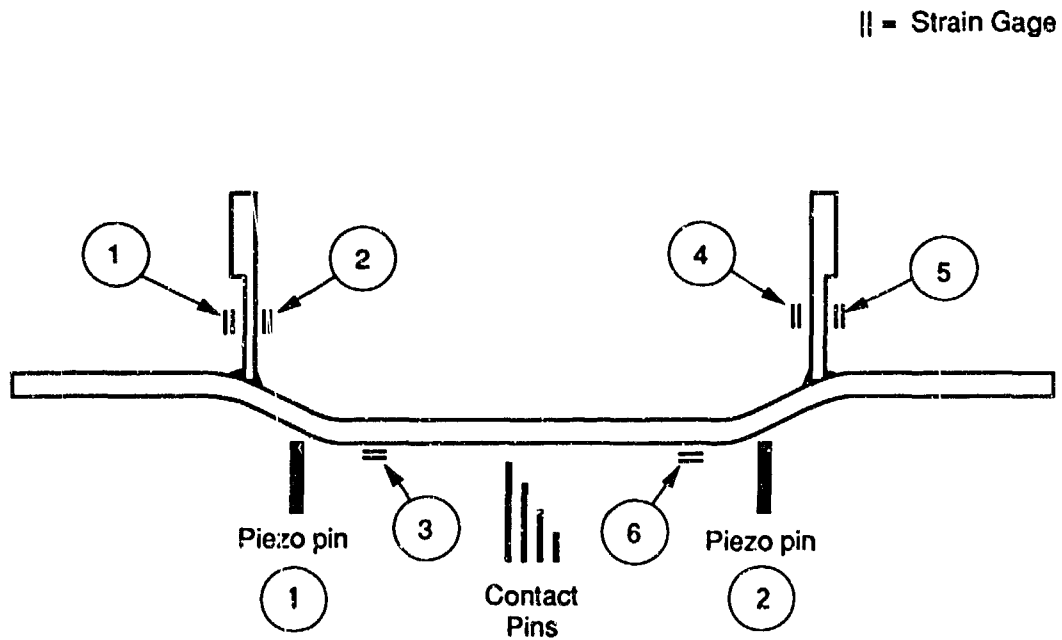
Figure C-6.   Position of instrumentation for dynamic fracture experiments.
The contact pins have been rotated 90 degrees for clarity.

experimental deflection history and to obtain more consistent velocity data. For specimens that fractured completely, we measured the center deflection from a reconstruction of the specimen.

In an approach analogous to that used in evaluating the static fracture experiments, we interpreted the posttest deflection values of the partially or completely fractured specimens as the deflection "at fracture." However, the precise stage of fracture corresponding to these deflections is not known. Strain gage records, when available, were analyzed to evaluate the type and level of deformation in the specimen, but little useful information was obtained from this analysis.

Normalizing Procedure. In the dynamic fracture experiments described here, we independently varied the specimen scale (1/4- and 1/8-scale), the specific explosive energy (Detasheet® D and C) and thickness (1-3 mm), and the tamping material thickness (25.4 and 50.8 mm). Eventually we will also vary the material tested (HY-130 steel, titanium alloys).

To analyze the structural (continuum) response of the specimens in a meaningful way, we had to normalize the experimental results to account for the differences in size, explosive specific energy and thickness, tamping material density and thickness, and specimen material properties. A normalization procedure that appears to account correctly for the parameter variations can be derived in the following way.

First, we consider the shape of the center deflection histories for the explosively loaded specimens and assume that no fracture occurred. Let the maximal deflection at the plate center line be d_{max} and the time at which this deflection is reached be t_{max}, as illustrated in Figure C-7a. We propose to normalize the experimental results using d_{max} and t_{max}. As mentioned above and demonstrated in the next section, a second-order polynomial provides a good fit to the experimental data, suggesting that (1) a simple rigid-perfectly plastic hinge model can appropriately describe the motion of the plate center line, and (2) the plate center line undergoes uniform deceleration until d_{max} is reached. We use these two assumptions to express d_{max} and t_{max} as functions of specimen yield strength σ_y, density ρ_p, length L_p, thickness h_p, and initial plate velocity V_0. Then, assuming the simple model of Figure C-7b and equating the initial kinetic energy of the plate to the work done in the plastic hinge yield the expressions for d_{max}

$$d_{max} \sim \frac{L_p^2\, \rho_p}{h_p\, \sigma_y} V_0^2 \qquad \text{(C-1)}$$

Similarly, the angular momentum equation yields the expression for t_{max}:

$$t_{max} \sim \frac{L_p^2\, \rho_p}{h_p\, \sigma_y} V_0 \qquad \text{(C-2)}$$
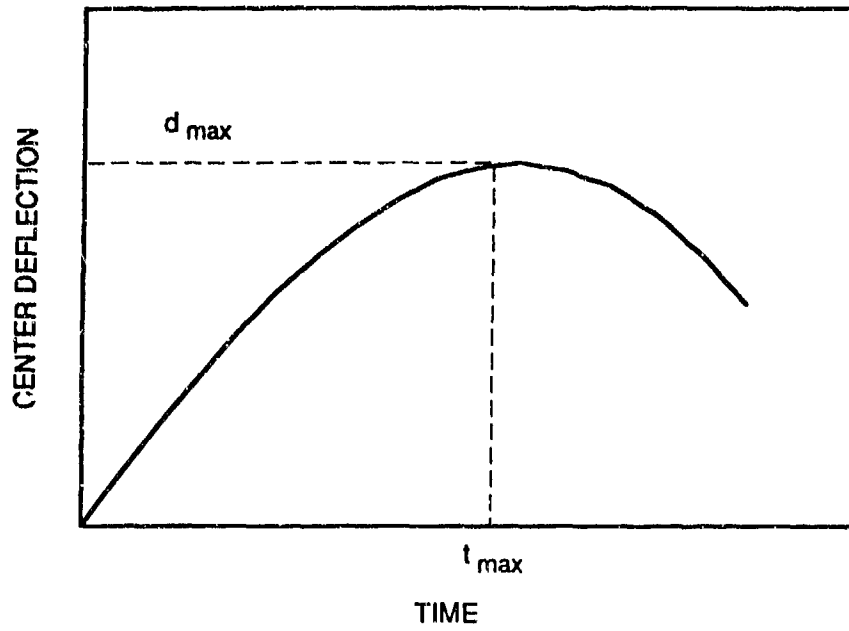
(a) Definition of t_{max} and d_{max}
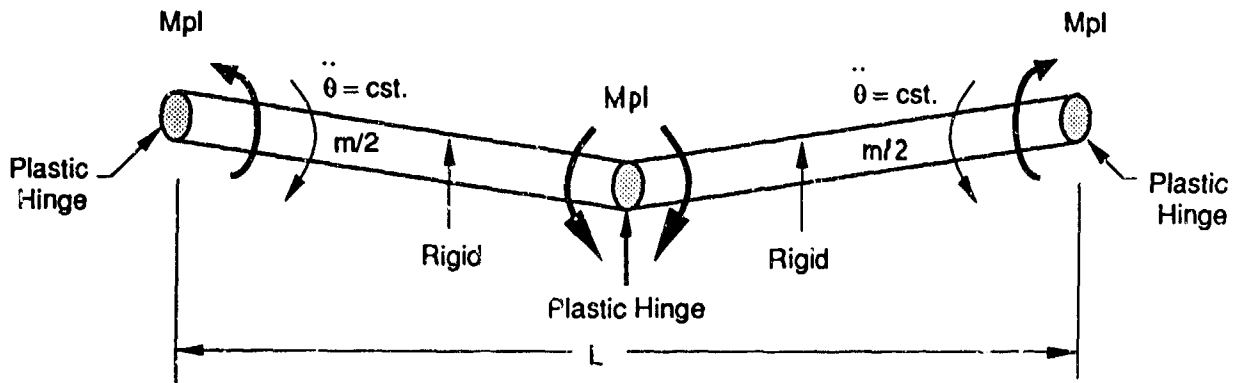
(b) Plastic hinge model of specimen

RM-2612-30

Figure C-7. Normalization analysis.

The groups of parameters on the right-hand side of Equations (C-1) and (C-2) represent the appropriate expressions for normalizing the experimental deflections and the times, respectively.

The next step is to express the initial velocity V_0 as a function of the explosive specific energy E_0, density ρ_e, and thickness h_e and of the tamping material density ρ_t and thickness h_t. This relationship can be obtained from a simple approximate analysis[4] and is given by

$$V_0 = \alpha\sqrt{2E_0}\left[\cfrac{3}{1 + 3\cfrac{h_p\rho_p}{h_e\rho_e} - \left(\cfrac{2\cfrac{h_p\rho_p}{h_e\rho_e} + 1}{2\cfrac{h_t\rho_t}{h_e\rho_e} + 1}\right) + \left(1 + 3\cfrac{h_t\rho_t}{h_e\rho_e}\right)\left(\cfrac{2\cfrac{h_p\rho_p}{h_e\rho_e} + 1}{2\cfrac{h_t\rho_t}{h_e\rho_e} + 1}\right)^2}\right]^{1/2}$$

(C-3)

In Equation (C-3), α is an undetermined coefficient relating the proportion of the specific energy converted to kinetic energy of the plate to the total specific energy of the explosive. We later determined the value of α by fitting Equation (C-3) to the experimentally determined initial velocities.

Combining Equation (C-3) with the right-hand side of Equations (C-1) and (C-2) yields normalizing quantities for the experimental deflection and time, respectively, that include the influence of size, specimen material properties, and explosive and tamping material characteristics. This normalization procedure was used when comparing the structural responses of the specimens.

From Equations (C-1) through (C-3) we can draw other conclusions regarding the dependence of the initial plate center velocity and the maximum plate center deflection on test parameters. A plot of Equation (C-3) suggests that V_0 varies with the square root of the explosive thickness. This idea is illustrated in Figure C-8, which plots V_0 for the geometric and material parameters corresponding to our experiments with Detasheet® C and D and for a value of α of 0.645. The resulting curve is fitted almost exactly by the equation

$$V_0 = 453.28\,(h_e/h_p)^{1/2}$$

(C-4)

Therefore, combining Equations (C-1) and (C-4) also suggests that the maximum plate center deflection normalized by the specimen plate thickness should vary linearly with the explosive thickness normalized by the plate thickness. Experimental evidence for this conclusion will be

RA-2612-100
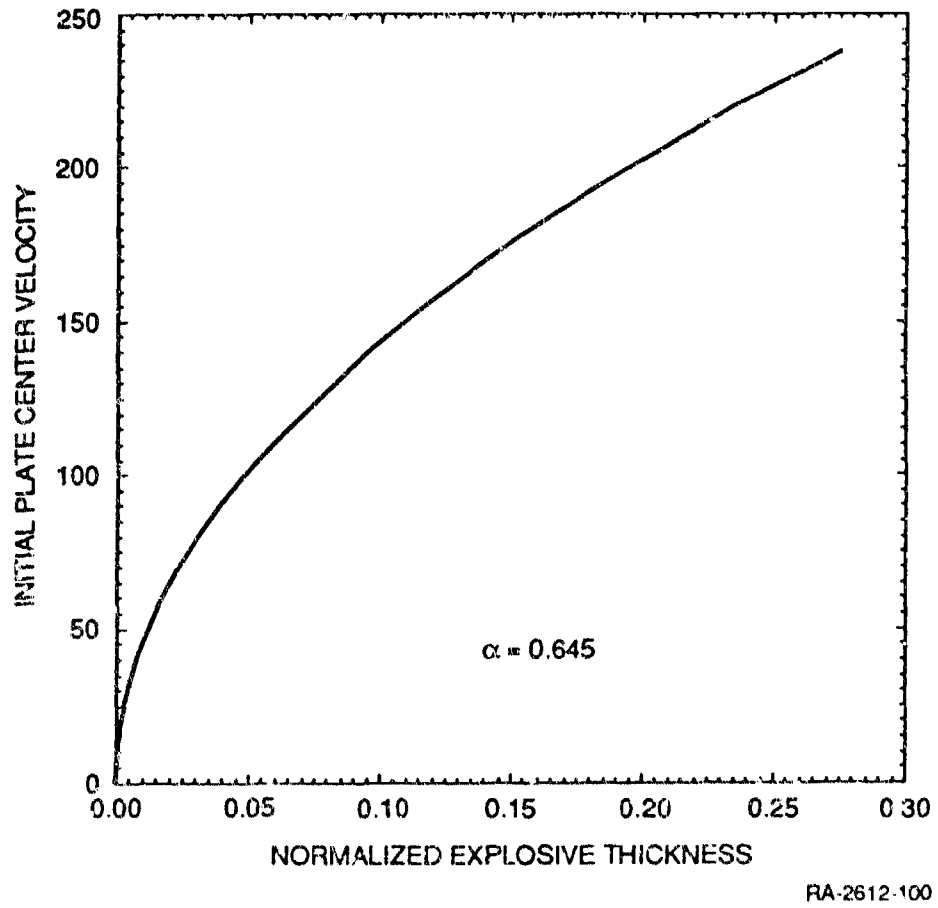
Figure C-8.   Initial plate center velocity versus normalized explosive thickness relation predicted by Equation (C-3).

presented in the next section, and we use the linear relationship between explosive thickness and maximum center plate deflection in an improved analysis of the deflection history data.

To derive fracture scaling rules, we simply normalize the explosive thickness and the deflections by the specimen plate thickness.

Improved Data Reduction Procedure. As will become apparent from the experimental results, the maximum deflection predicted by the second-order polynomial fit to the raw experimental deflection history data does not agree with the estimate of the maximum deflection based on posttest measurements of the specimens. To remove this inconsistency and to improve the accuracy of the initial velocity data derived from the polynomial fits, we include the final deflection of the specimen (measured after the test) in data used to fit the second-order polynomial. The procedure involved the following steps.

1. We estimated the maximum plate center deflections reached during the experiments $(d_{max})_{exp}$ by combining the final plate center deflections measured after the experiments with an estimate of the elastic springback of the plate obtained from a two-dimensional dynamic finite element analysis of the explosive experiments (see below and Appendix D). Here, only the experiments with incipient or no fracture were considered.

2. We generated a linear regression for the normalized maximum deflection as a function of normalized explosive thickness from the $(d_{max})_{exp}/h_p$-h_e/h_p experimental data. On the basis of this linear regression, we estimated the maximum deflection that the fractured specimens would have experienced if fracture had not occurred.

3. For each experiment, we performed a new second-order polynomial fit to the raw experimental data augmented by the point consisting of $(d_{max})_{exp}$ and $(t_{max})_{raw \ fit}$, where $(t_{max})_{raw \ fit}$ represents the time of maximum deflection predicted by the polynomial fit to the raw data.

4. From the polynomial fit to the augmented data set we calculated a new time of maximum deflection $(t_{max})_{fit \ 1}$ and compared it with $(t_{max})_{raw \ fit}$. If the difference between the two maximum times exceeded 5 percent, we performed another polynomial fit to the raw data augmented by the point $(d_{max})_{exp}$, $(t_{max})_{fit \ 1}$. This iterative procedure was repeated until the difference between the times of maximum deflection calculated from successive polynomial fits was less than 5 percent. In general, two iterations were enough.

5. We checked the consistency of the deflection histories generated by the improved data reduction procedure, then compared the deflection histories for specimens loaded with increasingly thicker sheet explosive and verified that they yielded increasingly higher initial velocity and larger maximum deflection, consistent with Equations (C-1) through (C-4). To further verify the consistency of the experimental data with the normalization analysis, we evaluated the parameter α in Equation (C-3) by plotting V_0 as predicted by Equation (C-3), with $\alpha = 1$ versus the value obtained from the experiments, and performing a linear regression. We then compared the predictions of Equation (C-3) with the fitted value of α for the initial velocity as a function of explosive thickness with the experimental data. Although this comparison was not an

independent check (we had already fitted α to the experimental data), it ensured consistency among the data reduction procedure, the normalization analysis, and the experimental data.

6. The last step of the data reduction procedure consisted of normalizing the experimental data and plotting the normalized deflection histories for all the experiments.

In the Experimental Results section we present for each experiment the raw experimental data and the results after improved data reduction.

Finite Element Simulation of Experiments. We performed two-dimensional dynamic finite element analysis of the dynamic fracture experiments to evaluate the elastic springback deflection at the plate center in experiments in which no complete fracture occurred and to obtain the strains and strain rates in the weldment region. The results of these calculations are discussed in more detail in Appendix D. Here it suffices to mention that the maximum strain rates in the weldment region were on the order of several thousands per second.

EXPERIMENTAL RESULTS

The results of the dynamic fracture experiments are summarized in Table C-3 and Figure C-9. Table C-3 lists for each experiment the initial velocities from the raw data fit and the improved data reduction procedure, the final plate center plastic deflection, the maximum plate center deflection, and the corresponding instrumentation and loading conditions. As previously discussed, the maximum plate center deflection of the specimen was estimated by adding the elastic component of the deflection, calculated in a dynamic finite element simulation of the experiment (see Appendix D), to the final plate center plastic deflection measured after the experiment.

The initial velocities listed in Table C-3 were determined by differentiating second-order polynomials fitted to either the raw experimental deflection history data or the augmented experimental data set (after the improved data reduction procedure).

Figure C-9a plots the deflection histories for the 1/4-scale experiments, along with limit curves (dashed lines) defining the conditions for fracture initiation and complete fracture. Figure C-9b plots the corresponding data for the 1/8-scale experiments. Below we present the results of each experiment individually, including photographs of the final specimen deformation and the plate center deflection history. The figures showing the plate center deflection history also compare the polynomial fit to the raw data only and that to the augmented data set with posttest measurements of the maximum deflection.
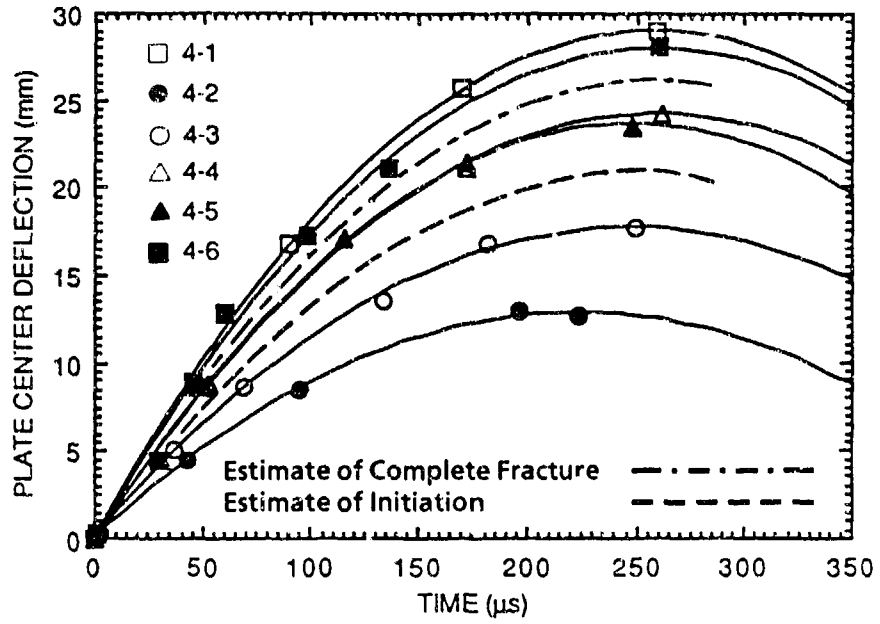
(a) 1/4-Scale experiments
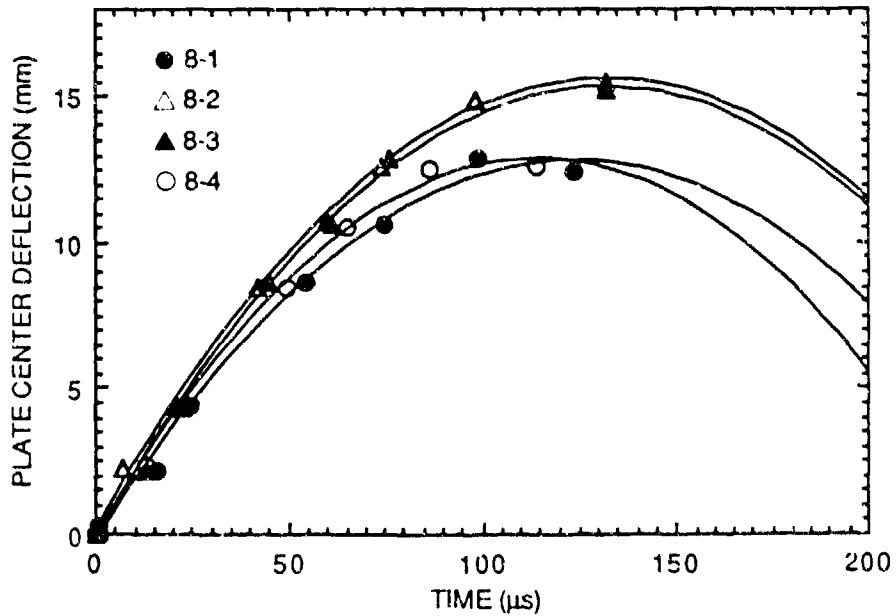
(b) 1/8-Scale experiments

RA-2612-101

Figure C-9.   Deflection histories for 1/4- and 1/8-scale experiments.

TABLE C-3. RESULTS OF DYNAMIC FRACTURE EXPERIMENTS

HY-130 Experiment No.	Explosive Thickness (mm)	Explosive Type	Initial Velocity, Raw Data Fit (m/s)	Initial Velocity, Improved Data Reduction (m/s)	Final Plastic Plate Center Deflection (mm)	Maximum Plate Center Deflection (mm)	Instrumentation	Comment
WE4-1	2.87 or 3.05 equivalent	D C	221	226	22.0[a]	28.9[b]	8 SG, 4 CP	Fracture through on side only; stiffener broke on other side
WE4-2	1.38	C	111	115	9.8	12.6	6 SG, 8 CP, 2 PP	No fracture
WE4-3	1.63	C	138	142	15.2	17.6	6 SG, 8 CP, 2 PP	No fracture
WE4-4	2.54	C	188	187	22.1	24.2	8 CP, 2 PP	Partial fracture
WE4-5	2.54	C	185	192	21.4	23.5	8 CP, 2 PP	Partial fracture
WE4-6	2.98	C	225	216	26.3[a]	28.0[b]	8 CP, 2 PP	Fracture through both sides
WE8-1	1.36	C	189	211	11.4	12.5	8 CP, 2 PP	No fracture, plate anchoring bolt deformation
WE8-2	1.65	C	210	235	14.2	15.2	8 CP, 2 PP	Incipient fracture, plate anchoring bolt fracture
WE8-3	1.65	C	226	234	13.5	15.5[b]	8 CP, 2 PP	Complete fracture
WE8-4	1.36	C	206	227	11.6	12.6	8 CP, 2 PP	Partial fracture

[a] Reconstructed.
[b] Pseudodeflection from linear fit of experimental data.

1/4-Scale Dynamic Fracture Experiments

The first three 1/4-scale experiments served mainly to test the instrumentation and to bracket the explosive thicknesses needed to cause incipient or complete specimen fracture. The last three tests yielded useful fracture data and established their reproducibility.

WE4-1. Specimen HY-130 WE4-1 was instrumented with eight strain gages (four gages on the stiffener and four gages on the plate; see Figure C-6) and four contact pins to measure the plate's deflection history. The specimen was loaded with a sheet of 2.87-mm-thick Detasheet® D explosive tamped with two PMMA blocks. Our choice of explosive thickness was based on the results of the static fracture experiments and the one-dimensional calculations.

Fractures occurred at three locations during the experiment. The plate was completely severed by a crack that began at the toe of one of the stiffener-plate welds; another crack propagated partly through the plate at the other stiffener-plate weld, and the stiffener sheared off at a 45-degree angle to its tensile axis (Figure C-10). The important fractographic observation from this test was that the mode of fracture at the toe of the stiffener-plate weld was the same as that observed in the static experiments and in explosive loading of large-scale ring-stiffened structures.

Figure C-11 summarizes the records obtained during the experiment. The velocity pins performed satisfactorily, as indicated by the well-defined rectangular pulses shown in the time record. The front edge of the rectangular pulses marks the time during which the bottom of the plate was in contact with the pin. From analyzing of the velocity pin data, we obtained the plate center deflection history shown as a solid curve in Figure C-12. From the improved polynomial fit, we calculated an initial plate center velocity of 224.5 m/s.

From a posttest reconstruction of the plate we estimated that full plate fracture occurred at a plastic deflection of 22 mm at the specimen center line. The total deflection after adding the elastic component was 24.1 mm. Introducing this value in Figure C-12, we see that the last dynamically measured experimental point was recorded after fracture and is therefore questionable.

Four of the eight strain gages (gages 2, 3, 7 and 8) produced a record that lasted about 40 μs. At that time all four records showed a transient value. Because the final plastic plate deflection indicates a fracture time of about 150 μs, it is unlikely that this transient was associated with fracture. Rather, it was probably due to gage failure (gages 2, 3, and 8) or to a great increase in strain, possibly associated with stiffener bending (gage 7). The other gages failed less than 20 μs into the experiments; therefore, little useful information was gained from the strain gage records.
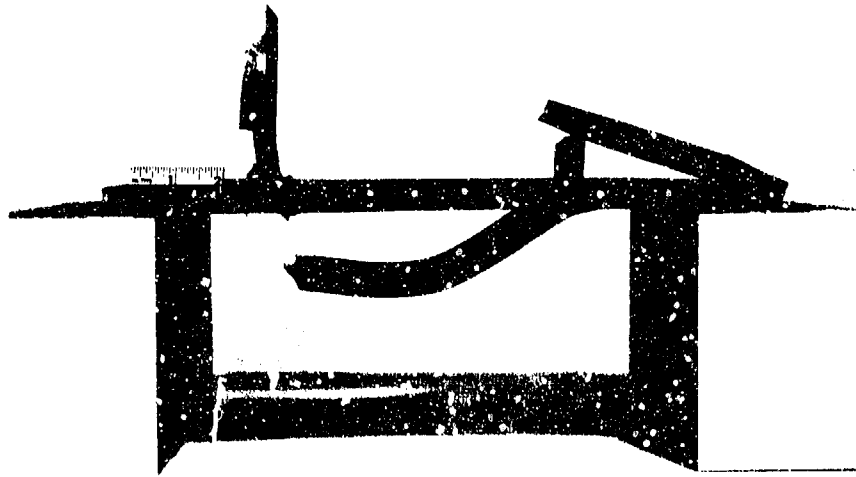
(a) Overall view
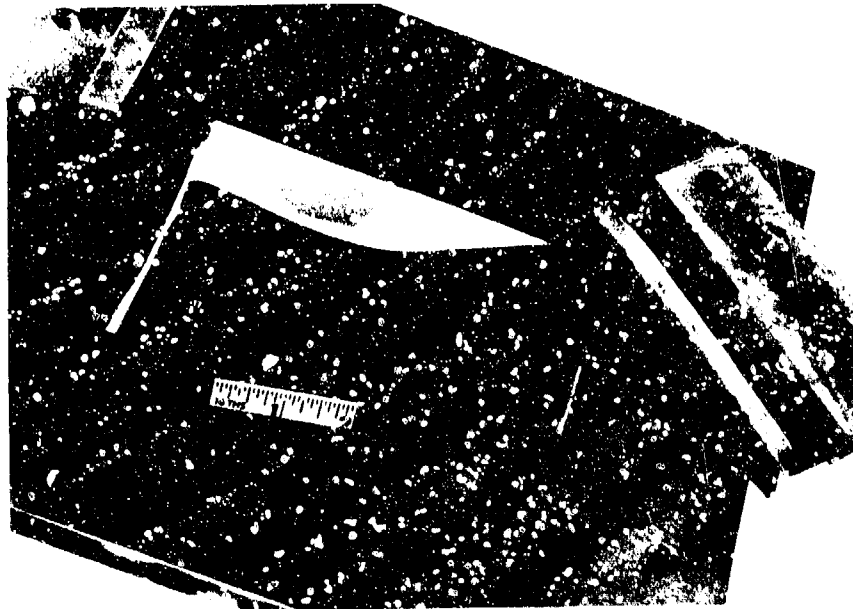
(b) Detail view of fracture region

RP-2612-102

Figure C-10. Posttest specimen deformation for experiment HY-130 WE4-1.
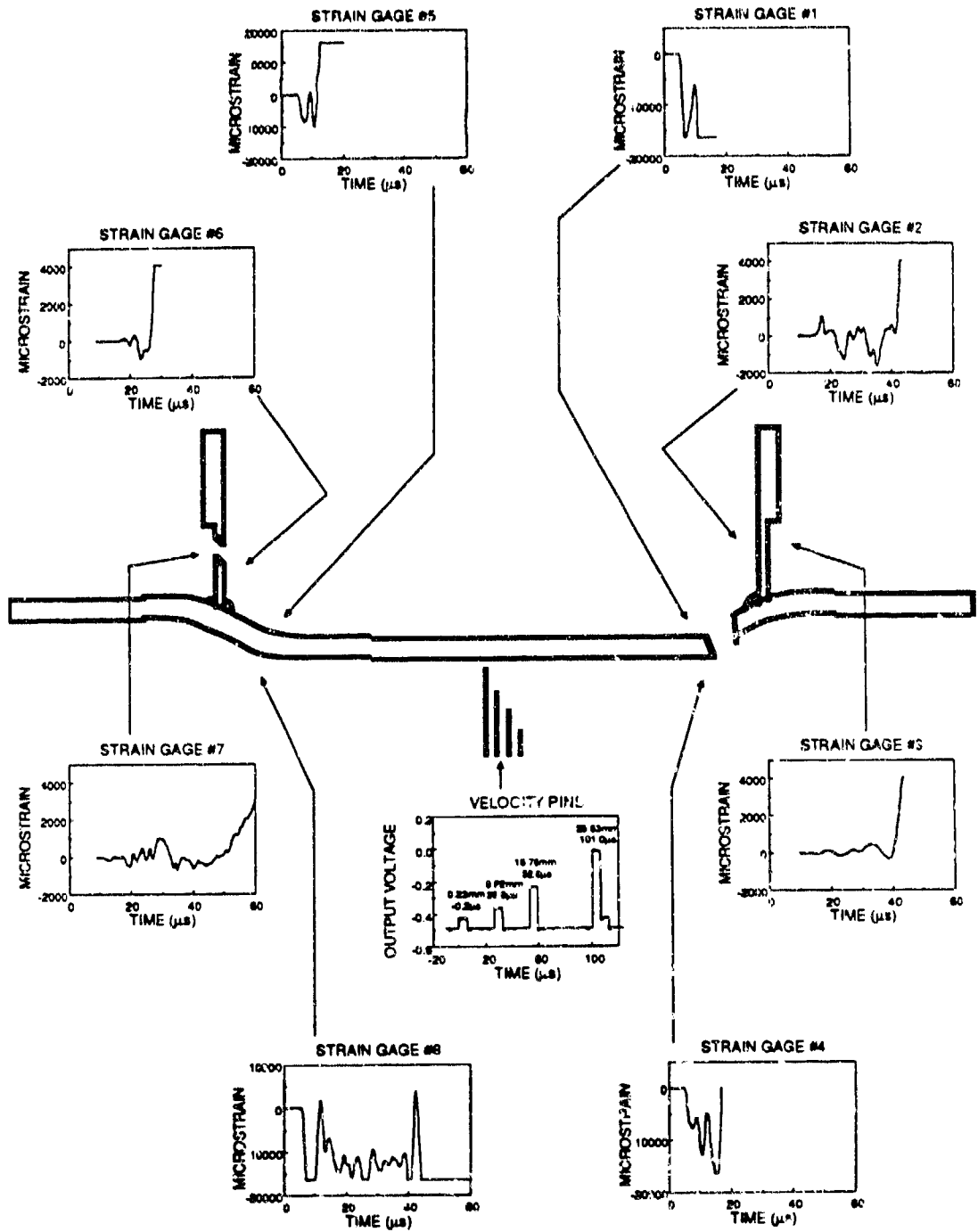
Figure C-11. Summary of records for experiment HY-130 WE4-1.

RA-2612-103
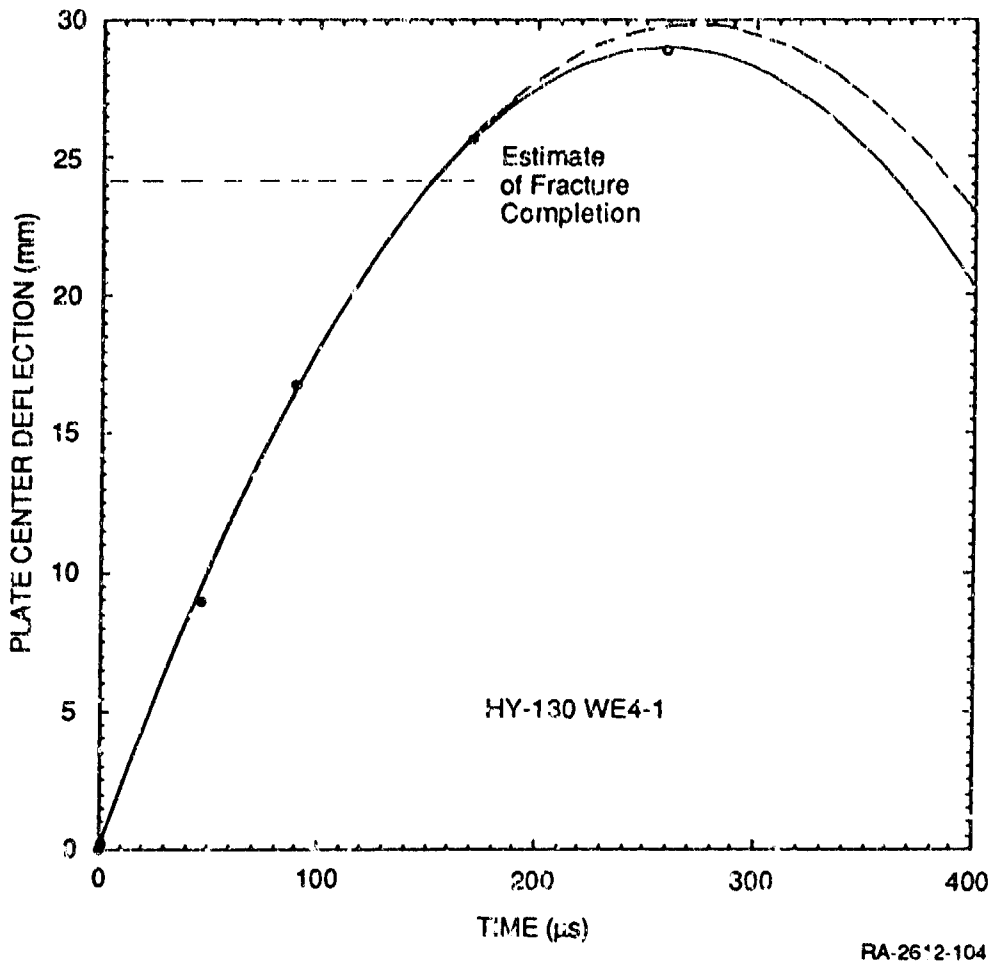
Figure C-12. Plate center deflection history for experiment HY-130 WE4-1.

In summary, test HY-130 WE4-1 yielded the following main results:

- We demonstrated that the test design was sound and that the desired type of fracture was produced.

- We evaluated the dynamic instrumentation. In particular, we showed that useful deformation history information can be obtained with simple contact pins and, on the other hand, that strain gages may not survive long enough to yield meaningful information.

- An upper limit for the explosive charge needed to cause fracture was established to be 2.9 mm of Detasheet® D.

WE4-2 and -3. The purpose of these experiments was to estimate the charge needed to start and only partly propagate a crack through the specimen plate. The specimens were loaded with 1.09- and 1.63-mm-thick Detasheet® C, respectively. Both specimens were instrumented with six strain gages and two sets of contact pins, for a total of eight pins and two piezo pins. The locations of the gages were the same as those in test HY-130 WE4-1, except that the two gages at the top of the plate were omitted (Figure C-6). In an attempt to improve the performance of the strain gages, we protected them with more rubber pads and steel shims.

Because of the small explosive charge, neither specimen fractured during the experiments. The posttest deformation of the two specimens is compared in Figure C-13. The plate center deflection histories for the experiments are shown in Figure C-14. The estimated initial velocities for specimens HY-130 WE4-2 and -3 were 114.6 and 142.3 m/s, respectively. The resulting final plastic deflections were 9.8 and 15.2 mm, respectively, and the maximum deflections were approximately 12.6 and 17.6 mm. During the posttest inspection of the specimens, we noticed that the frame part of the plate was bowed and that the plate deflected significantly (1-2 mm) immediately beneath the stiffeners. Because the specimens did not fracture, the piezo pins did not produce any meaningful signal during the experiments.

Of the total of 12 strain gages fielded in the two experiments, only three, all on the stiffener exteriors, yielded strain records exceeding 50 µs. All the other gages failed early in the experiments. Figure C-15 shows the three successful strain records obtained. Figures C-15a and c show strain histories at identical center locations on the stiffener exterior in tests HY-130 WE4-2 and -3, respectively. The overall strain histories were similar during the first 200 µs or so, although they differed in the details of the recorded oscillations. At later times, even the overall aspect of the two curves differed.

(a) HY-130 WE4-2
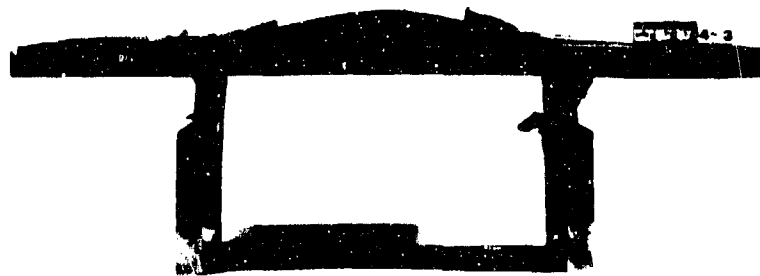
(b) HY-130 WE4-3

RP-2612-105

Figure C-13. Comparison of posttest specimen deformation for experiments
HY-130 WE4-2 and -3.
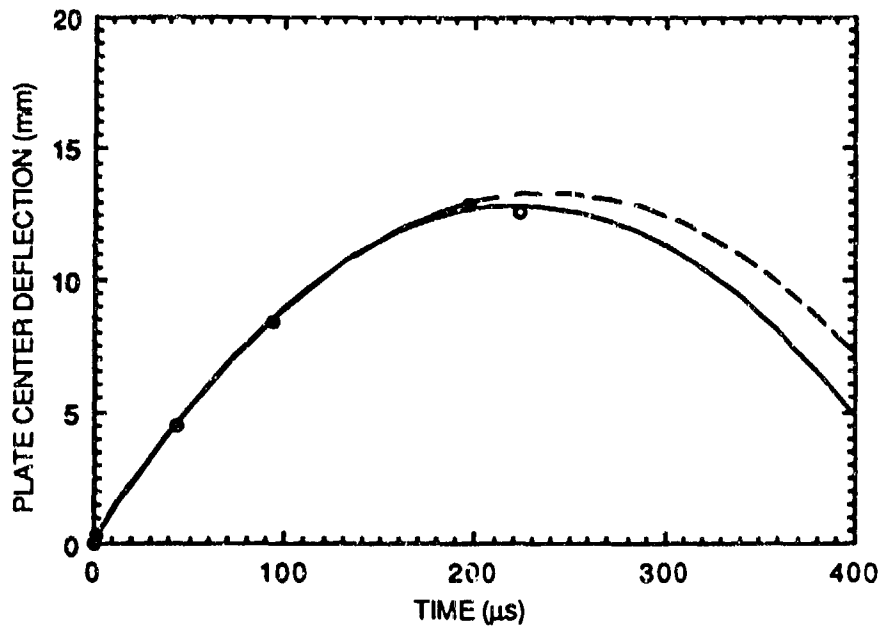
(a) HY-130 WE4-2
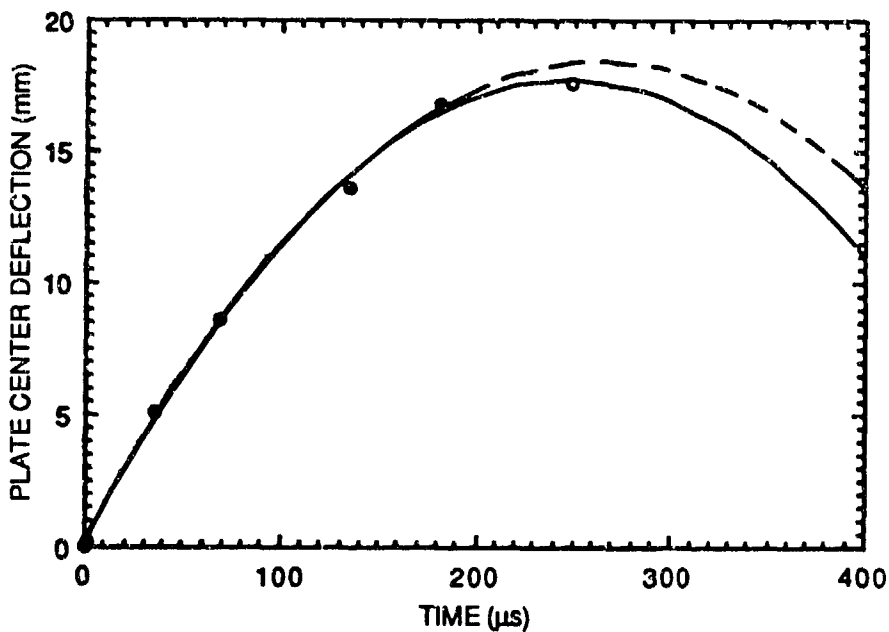
(b) HY-130 WE4-3

RA-2612-106

Figure C-14. Plate center deflection histories for experiments HY-130 WE4-2 and -3.
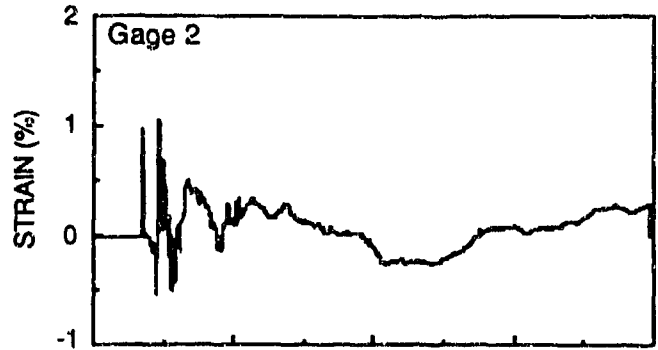
(a) Experiment HY-130 WE4-2
at center
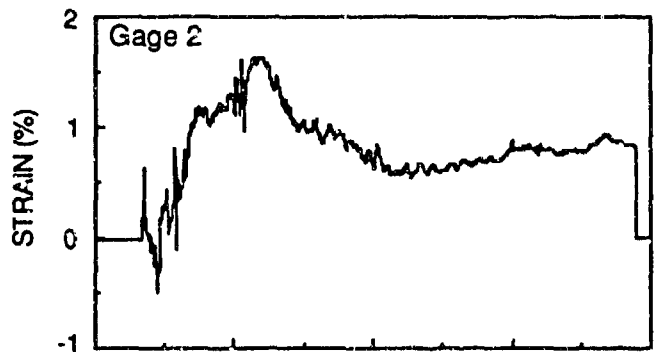
(b) Experiment HY-130 WE4-3 stiffener 1,
4 mm above center
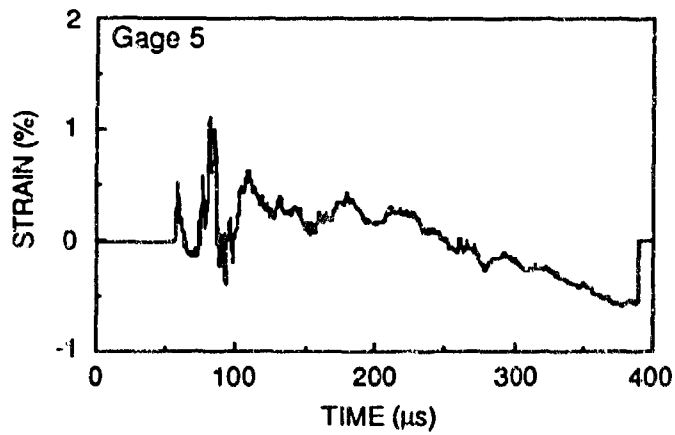
(c) Experiment HY-130 WE4-3 stiffener 2,
at center

RA-2612-24

Figure C-15. Useful histories recorded on stiffener exterior
during explosive experiments.

Strains well above the uniaxial yield strain of about 0.4 percent were reached during the earlier part of the experiments. Figure C-15b shows the strain history for the second stiffener in specimen HY-130 WE4-3. The vertical position of the gage from which this record was obtained was about 4 mm higher than that of the gage from which the record in Figure C-15c was obtained. Comparing the two strain histories indicates that the difference in position resulted in great differences in the strain histories. This difference was caused by the development of a plastic hinge in the stiffener; the strain history in Figure C-15b was measured closer to the plastic hinge than that in Figure C-15c.

Figure C-16 shows the early strain history recorded with two strain gages positioned at opposite locations on the inside and outside of the same stiffener in test HY-130 WE4-3. In first approximation, the two histories are symmetrical with respect to the time axis, implying that at the beginning of the experiment, the stiffener was loaded mainly in bending.

Besides providing some strain gage information on specimen deformation, tests HY-130 WE4-2 and -3 yielded deflection information that combined with the deflection at fracture estimated from test WE4-1, helped us to bracket the loading conditions needed to cause partial fracture in the next two experiments.

WE4-4 and -5. We selected Detasheet® C thickness for tests HY-130 WE4-4 and -5 to induce partial fracture in the specimens, both of which were tested with the same charge thickness of 2.54 mm to demonstrate the reproducibility of the results and instrumented with only contact pins and piezo pins.

As we anticipated from the previous test results, cracks began in each experiment, and we observed partial penetration of the plate at the root of both stiffener welds. The posttest deformation of the specimens (Figure C-17a), the extent of cracking (Figure C-17b), the deflection histories (Figure C-18), and the initial plate center velocities (187.1 and 192 m/s, respectively) were almost identical for these two experiments. The good reproducibility of the results is demonstrated in Figure C-17, which compares the deformed specimens after the experiments. The final plastic deflections of the plate centers were 22.1 and 21.4 mm, respectively, and the maximum deflections were 24.2 and 23.5 mm. Because the plates did not fracture completely, the piezo pins did not produce a record.

From tests HY-130 WE4-4 and -5, we obtained the following results:

- We established the Detasheet® C explosive thickness (2.54 mm) and hence the initial plate velocity ($\approx$190 m/s) needed to induce partial plate fracture .

- The deflection of the plate center at fracture was $\approx$24 mm.
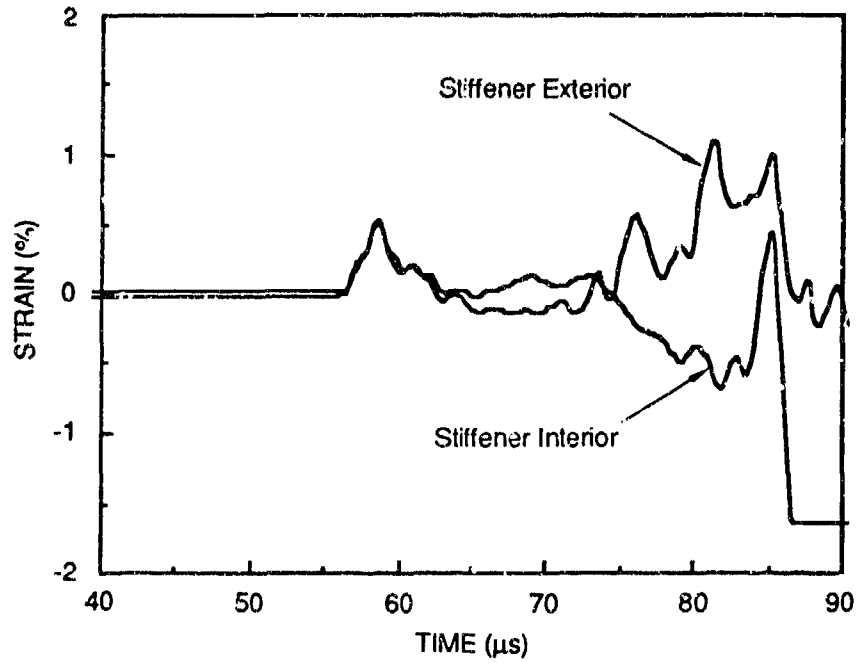
Figure C-16.   Comparison of early strain histories on interior and exterior of stiffener in experiment HY-130 WE4-3.

HY130WE4-4
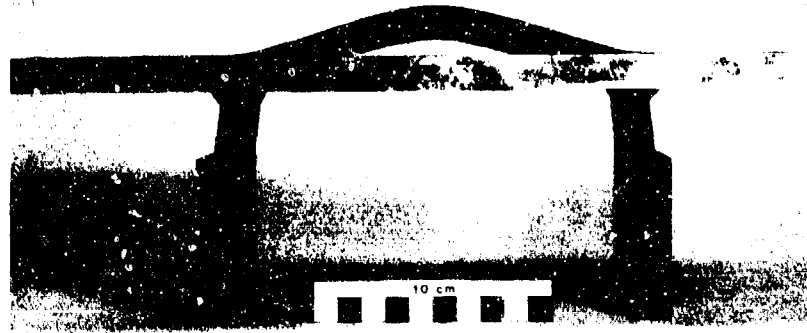
HY130WE4-5
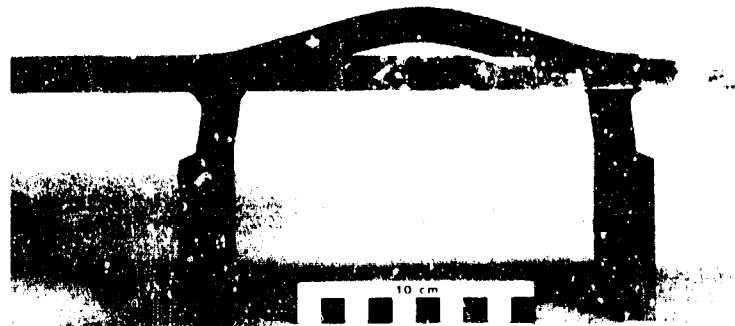
(a) Overall view

RP-2612-107

Figure C-17. Comparison of posttest specimen deformation and fracture for
experiments HY-130 WE4-4 and -5.

HY130WE4-4
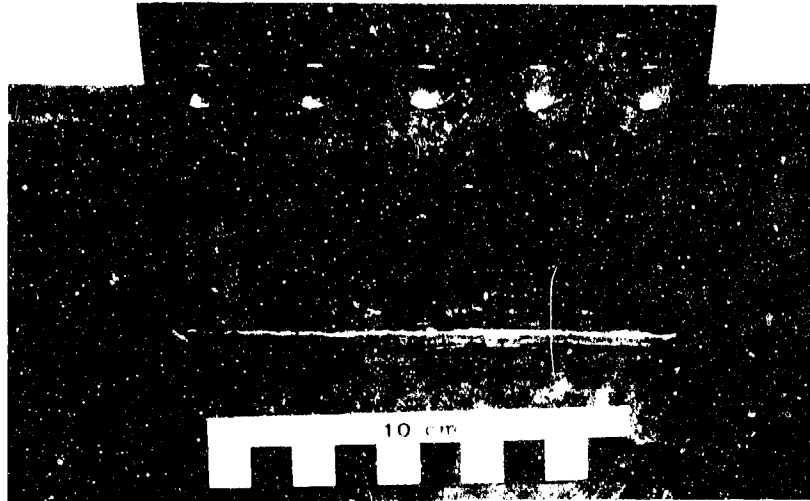
HY130WE4-5
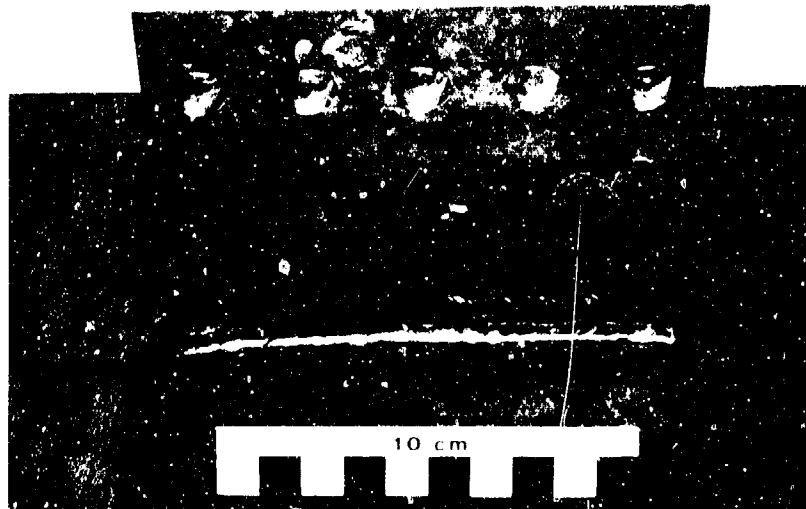
(b) Detail view of fracture region

RP 2612 108

Figure C-17. Comparison of posttest specimen deformation and fracture for experiments HY-130 WE-4-4 and 5 (concluded).
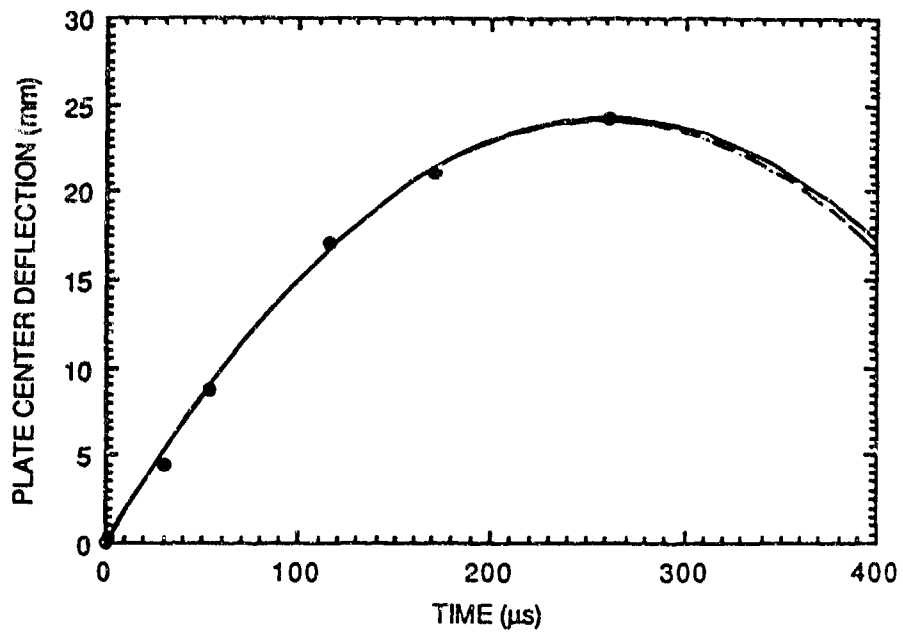
(a) HY-130 WE4-4
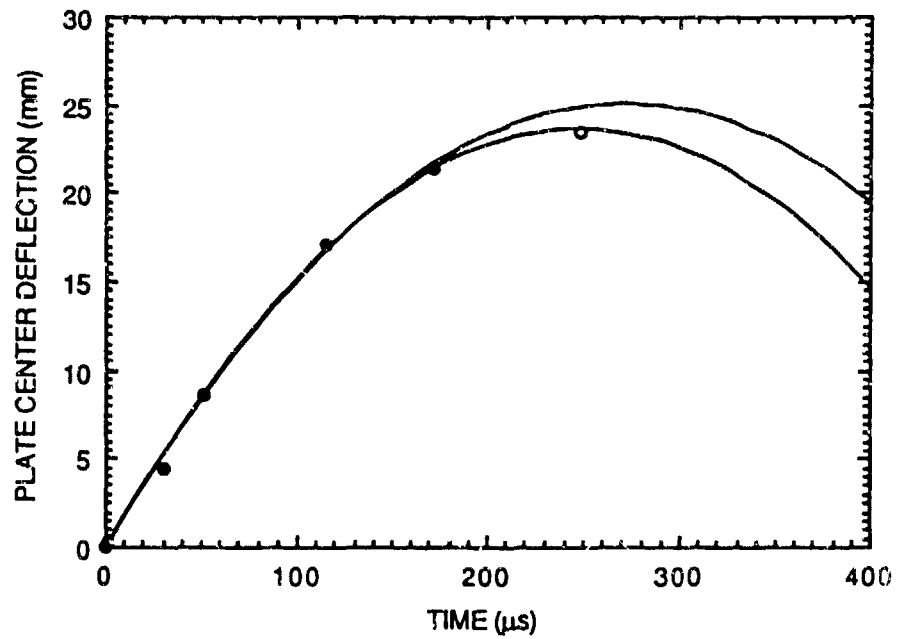
(b) HY-130 WE4-5

RA-2612-109

Figure C-18.   Plate center deflection histories for experiments HY-130 WE4-4 and -5.

- We demonstrated that the dynamic fracture results are reproducible and that we have good control of the experimental conditions.

<u>WE4-6</u>. In test HY-130 WE4-6, we chose the Detasheet® C explosive thickness of 2.98 mm to cause complete specimen fracture. Therefore, this test was a verification of the results obtained in test WE4-1.

The anticipated fracture behavior was indeed observed in this specimen, which fractured completely at both weldment locations (Figure C-19). The plate center deflection history is shown in Figure C-20. The estimated initial velocity was 216.3 m/s. By matching the two pieces of the specimen after the test, we estimated that the maximum permanent deflection at the plate center was 26.3 mm and the maximum deflection at fracture was 28.5 mm. This deflection is very close to the value of the maximum deflection in Figure C-20, suggesting that the plate had just enough kinetic energy to drive the cracks through the thickness.

In test HY-130 WE4-6, the piezo pins failed to indicate the time of complete fracture because of inappropriate positioning with respect to the strongly deflected plate. To resolve this problem, we adopted a tilted position for the pins in the 1/8-scale experiments.

From test HY-130 WE4-6, we obtained the following results:

- We established the Detasheet® C explosive thickness (2.98 mm) and hence the initial plate velocity ($\approx$220 m/s) needed to induce complete plate fracture.

- The plate center deflection at fracture was $\approx$28.5 mm.

- The results of the test are in good agreement with the results of test HY-130 WE4-1.

1/8-Scale Dynamic Fracture Experiments

We performed four 1/8-scale dynamic fracture experiments. The first two were invalidated by loading fixture deformation problems encountered during the experiments. The last two established the conditions for inducing partial and complete fracture in the 1/8-scale. This information, compared with the corresponding data from the 1/4-scale experiments, provided the scaling rules for fracture under dynamic loading conditions.

<u>WE8-1 and -2</u>. Tests HY-130 WE8-1 and -2 were instrumented with eight contact pins and two piezo pins. The explosive charge thickness for test WE8-1 was 1.36 mm (i.e., almost exactly half the thickness needed to produce the scaled loading conditions for tests WE4-4 and -5). Therefore, we expected that these loading conditions would result in partial plate fracture near the weldment. However, although this scaled explosive charge resulted in significant specimen deformation, it did not induce fracture.
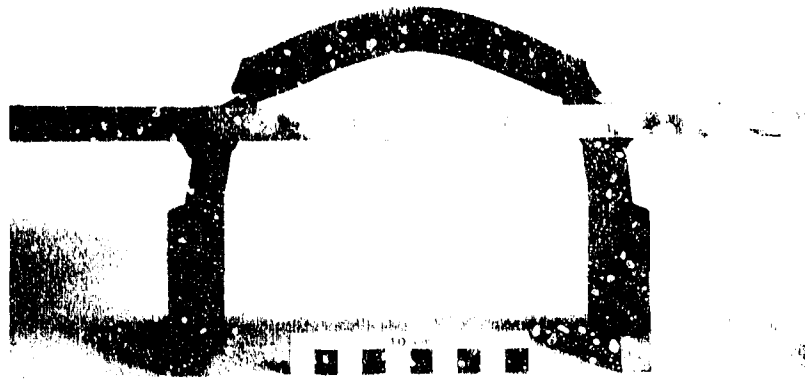
(a) Overall view
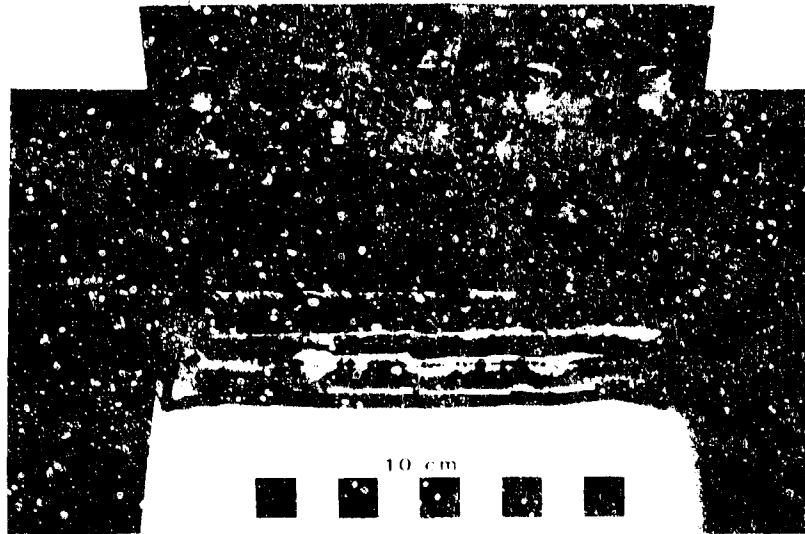
(b) Detail view of fracture region.

RP-2612-110

Figure C-19. Posttest specimen deformation for experiment HY-130 WE4-6.
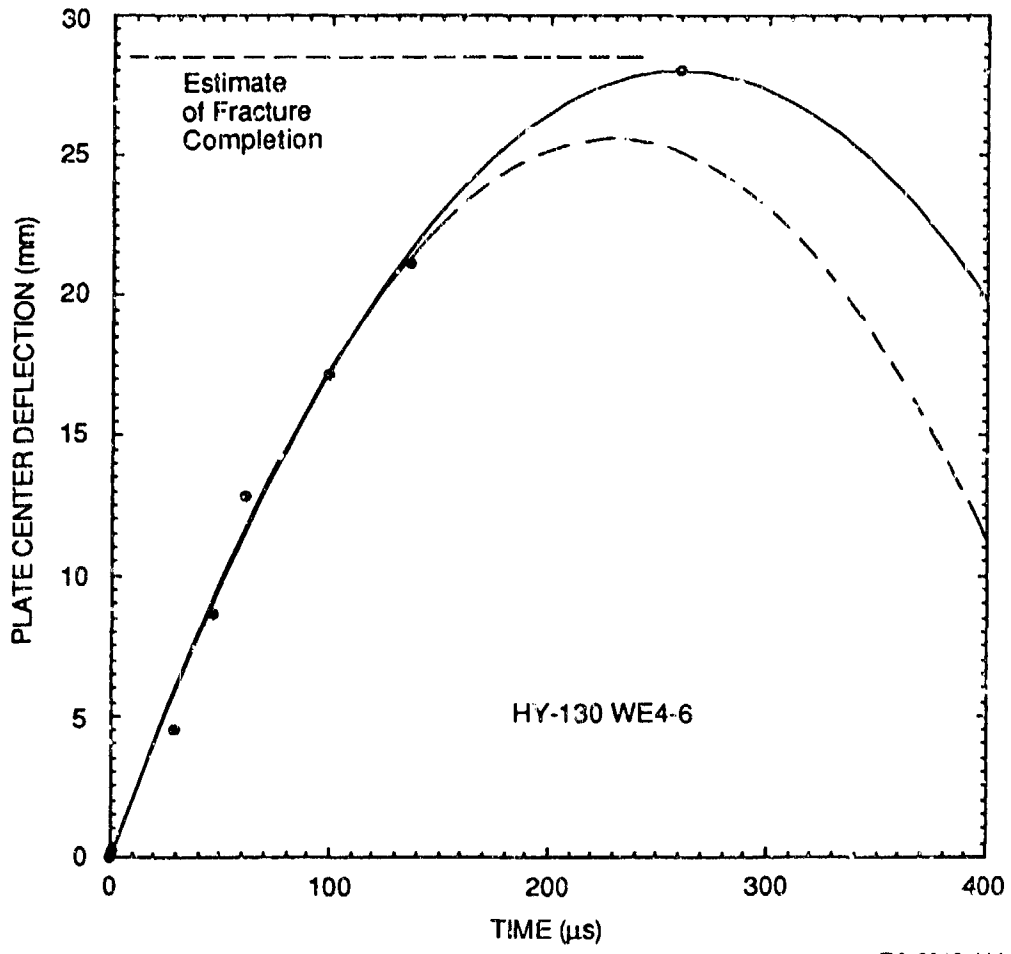
Figure C-20. Plate center deflection history for experiment HY-130 WE4-6.

Figure C-21a shows the deformed specimen after the experiment. The plate center deflection history for test HY-130 WE8-1 is shown in Figure C-22a. The initial velocity was 210.5 m/s, slightly higher than that of tests WE4-4 and -5. The permanent deflection was 11.4 mm, and the maximum was 12.45 mm, consistent with those of tests WE4-4 and -5.

Because no fracture was produced in test HY-130 WE8-1, we increased the charge thickness for test WE8-2 to 1.65 mm. This significantly larger charge, compared with those of tests WE4-4 through -6, produced only limited incipient cracking in one weldment.

Figures C-21b and c show the deformed specimen after the experiment. The plate center deflection history for test HY-130 WE8-2 is shown in Figure C-22b. The initial velocity was 234.5 m/s, somewhat higher than that for test WE4-6. The permanent deflection was 14.2 mm, and the maximum was 15.2 mm.

We could explain the difference in the fracture behavior of the 1/8-scale specimens HY-130 WE8-1 and -2, compared with the 1/4-scale results, in terms of deformations and fractures sustained by the loading fixture during the experiments. Posttest inspection revealed that clamping regions of the specimens were more deformed than corresponding regions in the 1/4-scale experiments. The nature and magnitude of these deformations are illustrated in Figure C-23. The 1/8-scale specimens were more deformed than the 1/4-scale because the 1/8-scale bolts used to clamp the specimens to the die were weaker than the 1/4-scale bolts and therefore were more readily deformed and sheared. Several bolts actually fractured during test WE8-2.

As a result of the weaker clamping of the base plate in the 1/8-scale experiments, the membrane stresses induced in the specimen were lower at a given plate deflection. Thus, the loading in the weldment region was less severe, and larger deflections were required to induce incipient damage in the specimen. To alleviate this problem, we rebuilt the yokes of the loading fixture from stronger hardened 4340 steel, and in the next experiments we used stronger, larger diameter bolts to clamp the specimen base plate to the support die.

Although they did not produce useful data to establish a scaling rule for dynamic fracture of HY-130 steel weldments, tests WE8-1 and -2 clearly illustrated the significant influence of the clamping conditions and resulting membrane stresses on weldment fracture.

WE8-3. Test HY-130 WE8-3 was performed with the modified loading fixture, which guaranteed better constraint of the plate membrane deformation. The specimen was instrumented with eight contact pins and two inclined piezo pins. We loaded the specimen with 1.65-mm-thick Detasheet® C, the same thickness as that used for specimen WE8-2 and in about 11 percent more than half the explosive thickness that produced complete fracture in the 1/4-scale specimen WE4-6.
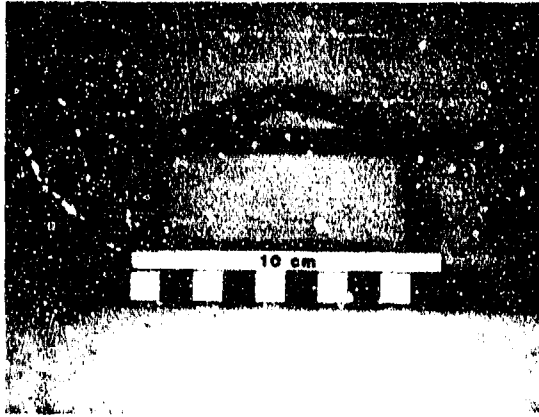
(a) HY-130 WE8-1, overall
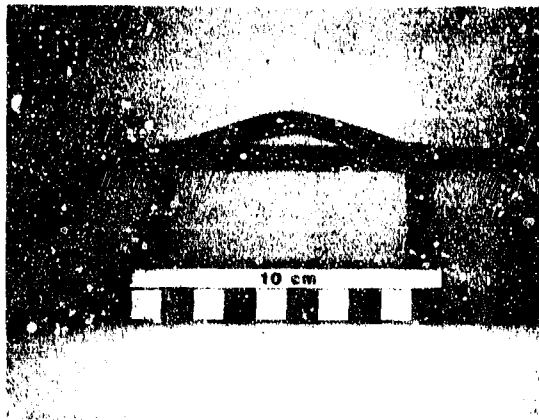
(b) HY-130 WE8-2, overall
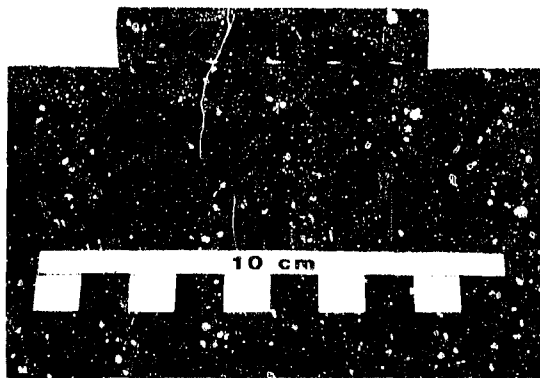
(c) HY-130 WE8-2, detail

RP-2612-112

Figure C-21.   Posttest specimen deformation
for experiments HY-130 WE8-1
and -2.

(a) HY-130 WE8-1
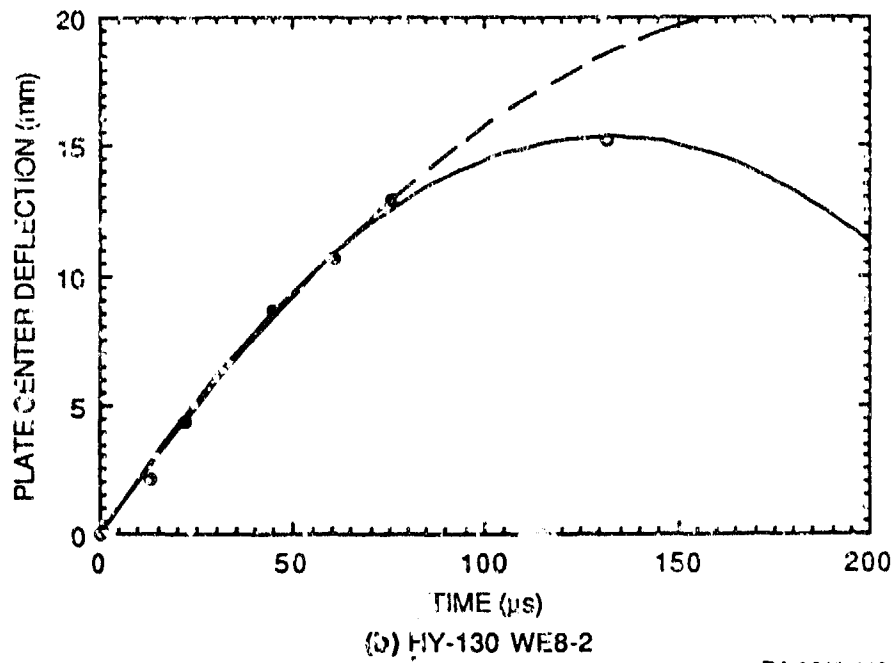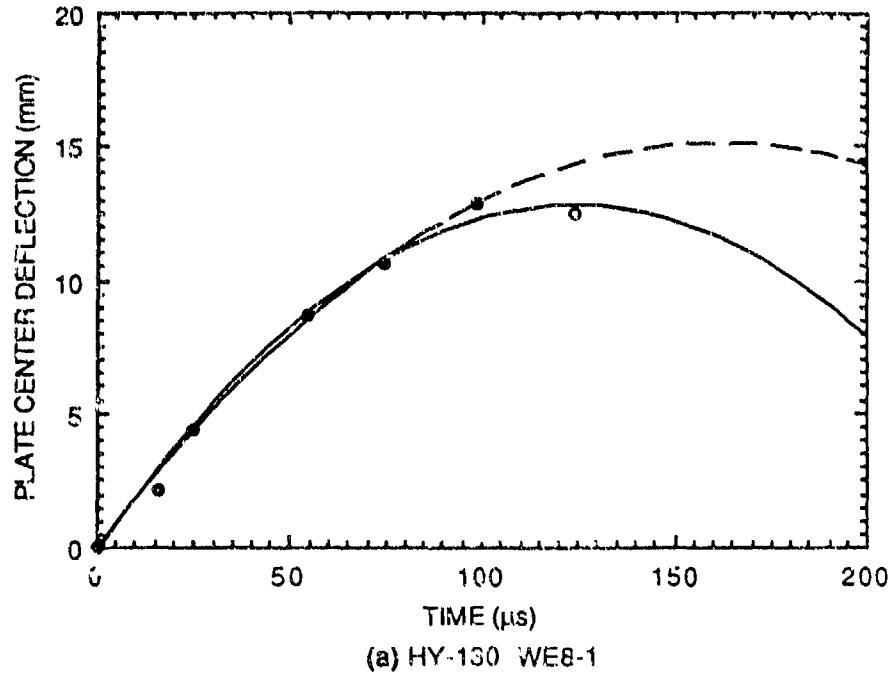
(b) HY-130 WE8-2

RA-2612-113

Figure C-22.   Plate center deflection histories for experiments
HY-130 WE8-1 and -2.
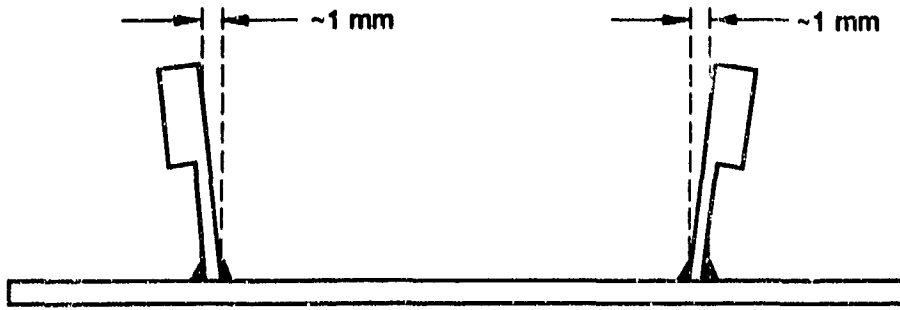
(a) Side view
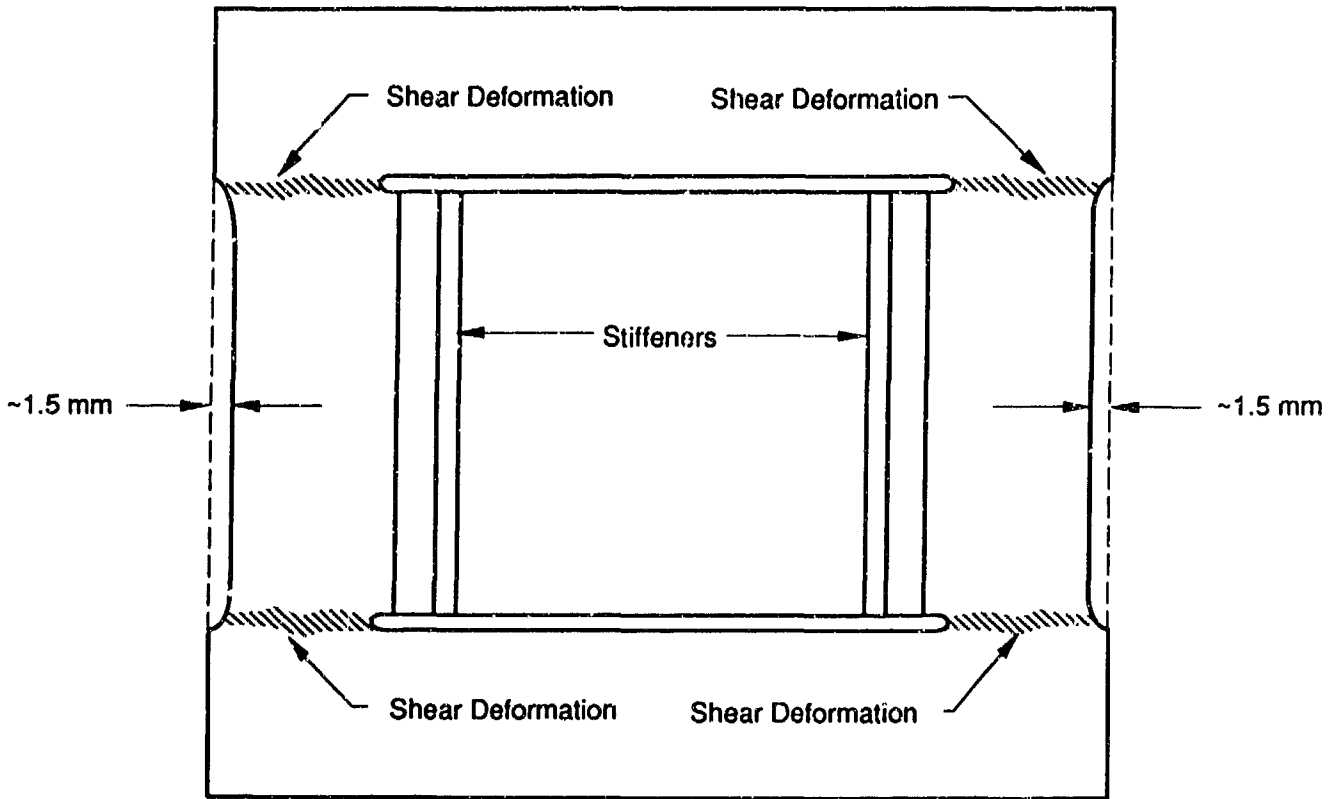
(b) Top

RM-2612-29

Figure C-23. Schematic of uncontrolled deformations in specimen HY-130W E8-2.

This experiment induced complete fracture at both stiffener weldments. Figure C-24 shows the specimen after the experiment. The center plate deflection history for specimen HY-130 WE8-3 is shown in Figure C-25. The initial velocity was 234.2 m/s, and the reconstructed plastic deflection after the experiment was 13.5 mm, almost exactly half the value from the corresponding 1/4-scale test WE4-6. The corresponding total deflection was 14.3 mm.

The time of contact of the specimen plate with the piezo pins indicated that complete fracture occurred between 66 and 89 μs and at a center plate deflection between 11.5 and 14.5 mm. This latter value was consistent with the estimate of the deflection at fracture based on posttest measurements.

From test HY-130 WE8-3 we obtained the following significant results:

- With the proper loading fixture strength, we demonstrated that an explosive charge scaled from a 1/4-scale experiment in which complete fracture occurred also induces complete fracture in the 1/8-scale experiment.

- The reconstructed maximum deflection of the fractured 1/8-scale specimen plate normalized by the plate thickness was almost equal to the normalized deflection reconstructed for the corresponding fractured 1/4-scale specimen HY-130 WE4-6.

WE8-4. Test HY-130 WE8-4 was also performed with the modified loading fixture. The specimen was instrumented with eight contact pins and two inclined piezo pins and loaded with 1.36-mm-thick Detasheet® C. This thickness was the same as that used for specimen WE8-1 and about 7 percent more than half the explosive thickness that produced partial fracture in the 1/4-scale specimens WE4-4 and -5.

In this experiment, partial fracture was induced at the root of both stiffeners. Figure C-26 shows the specimen after the experiment. The plate center deflection history is shown in Figure C-27 and is similar to that for test HY-130 WE8-1. The initial velocity was 227.4 m/s, which seems high compared with that for test WE8-1. The measured plastic deflection after the experiment was 11.6 mm, and the maximum was 12.6 mm, only slightly higher than half the value from the corresponding 1/4-scale tests WE4-4 and -5.

From test HY-130 WE8-4 we obtained the following significant results:

- With the proper loading fixture strength, we demonstrated that an explosive charge scaled from a 1/4-scale experiment in which partial fracture occurred also induces partial fracture in a 1/8-scale experiment.

- The maximum deflection of the partially fractured 1/8-scale specimen plate normalized by the plate thickness was almost equal to the normalized deflection reconstructed for the corresponding fractured 1/4-scale specimens HY-130 WE4-4 and -5.
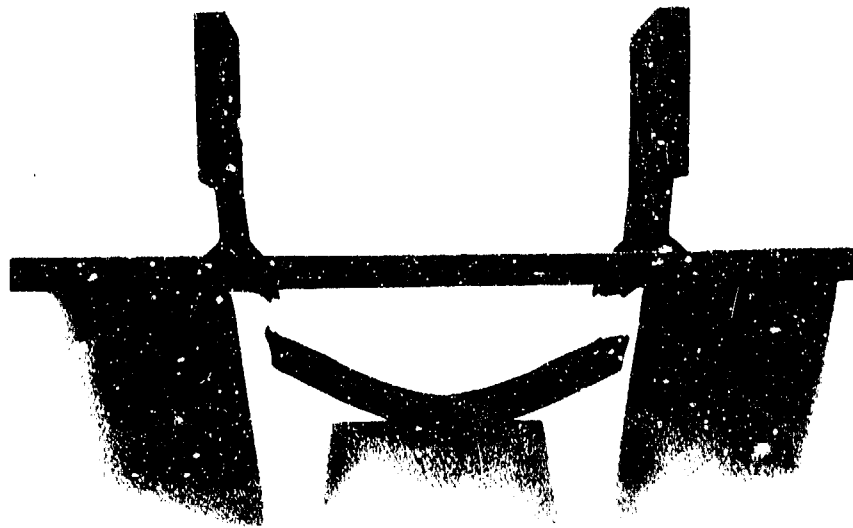
(a) Overall view
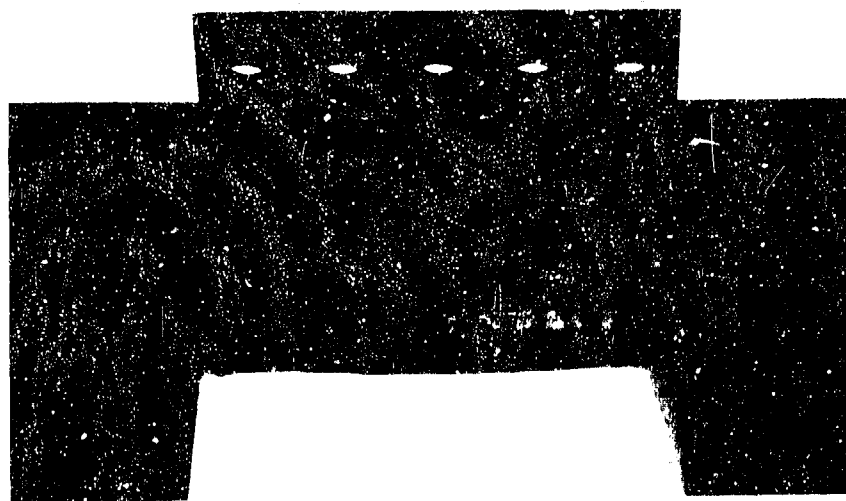
(b) Detail view of fracture region

RP-2612-114

Figure C-24.   Posttest specimen deformation for experiment HY-130 WE8-3.
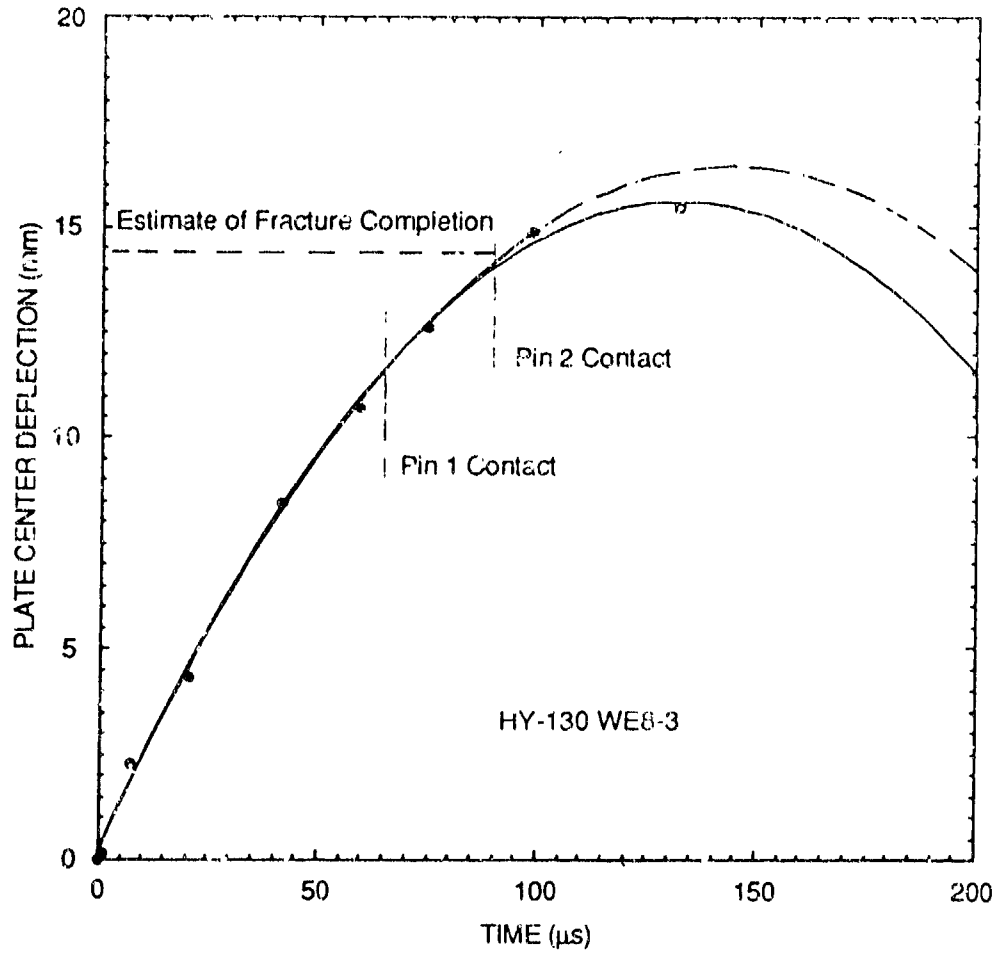
Figure C-25. Plate center deflection history for experiment HY-130 WE8-3.

RA- 2612-115
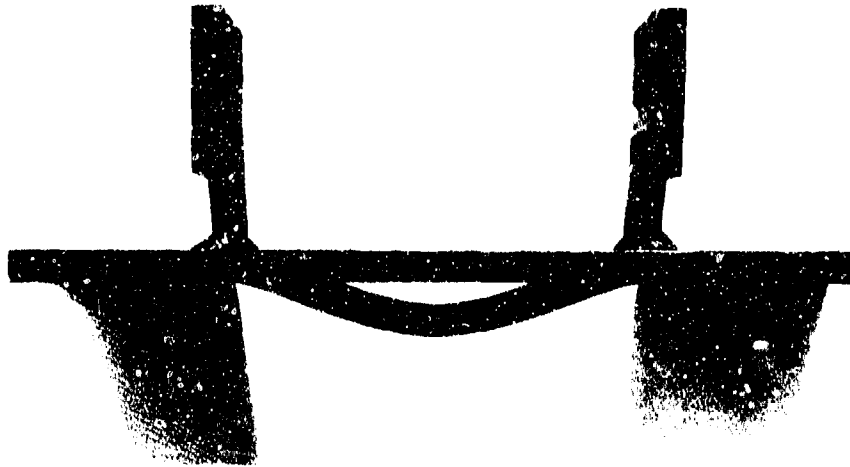
(a) Overall view

(b) Detail view of fracture region

RP-2612-116

Figure C-26. Posttest specimen deformation for experiment HY-130 WE8-4.

RA-2612-117
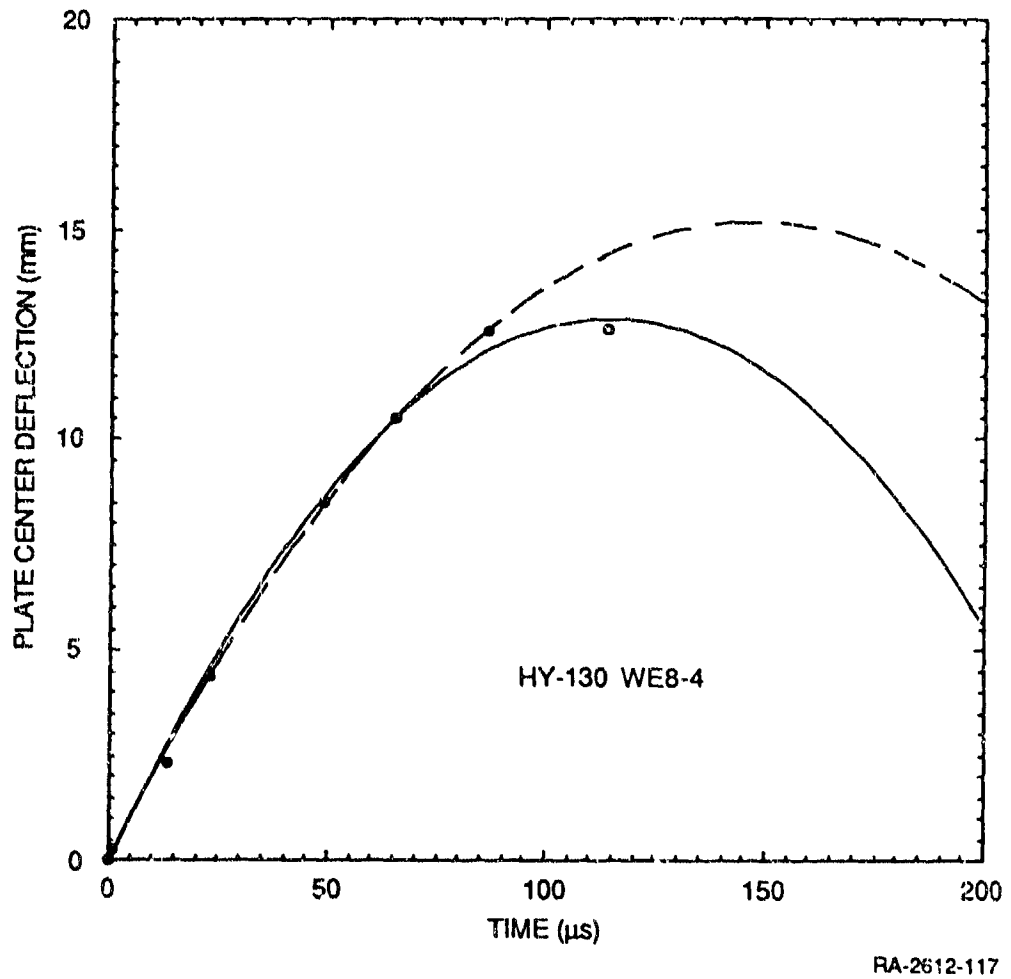
Figure C-27. Plate center deflection history for experiment HY-130 WE8-4.

Normalized Results

We used the normalization parameters defined in Equations (C-1) through (C-3) to normalize the results of the dynamic fracture experiments. In Equation (C-3) we used a value of $\alpha = 0.645$ determined from the plot of the experimental V_0 versus V_0 predicted by Equation (C-3), with a value of $\alpha = 1.0$. The regression is shown in Figure C-28 and indicates a reasonably linear fit of the relationship between experimental and theoretical V_0.

The normalized plate center deflection histories for all dynamic fracture experiments on HY-130 steel weldments are shown in Figure C-29. Figure C-29a shows the data normalized using the experimentally determined initial plate center velocity in Equations (C-1) and (C-2). Because the time normalization depends on V_0 and the deflection normalization depends on V_0^2, the normalized deflection histories will be significantly affected by errors in estimating the initial plate center velocity.

In an attempt to eliminate the uncertainty in the value of the initial velocity, we also normalized the data using V_0 calculated from Equation (C-3) with $\alpha = 0.645$. This approach is equivalent to normalizing the data directly by the explosive thickness, which is the variable we control directly in the experiments. The results of this second normalization are shown in Figure C-29b. Normalizing with V_0 from Equation (C-3) yielded significantly smoother normalized data. In Figure C-29, we have included curve fits to the normalized data for experiments HY-130 WE4-2, -3, and -4 and WE8-2.

From Figure C-29 we made the following observations. The normalized deflection histories for all the experiments collapsed on the same curve for early times, whereas the histories for experiments with different initial velocities tended to diverge at later times. The normalization with V_0 calculated from Equation (C-3) (Figure C-29b) suggests that the normalized data could fall into two sets. The first set contains tests HY-130 WE4-2 and -3, which were performed at the two lowest velocities. We fitted a single curve to the normalized data from these two experiments (upper curve in Figure 9 of the report), although it was not clear whether a single curve fit was appropriate. The second set contains all the other experiments, which were performed at higher initial plate center velocities. All the data points for this set appear to group around a single curve (lower curve in Figure 9 of the report) given by the equation

$$d_{NORM} = -2.4734 \times 10^{-4} + 0.99973\, t_{NORM} - 8.8745\, (t_{NORM})^2 \tag{C-5}$$

The implications of these observations for understanding the specimen's structural response are discussed in the next section.
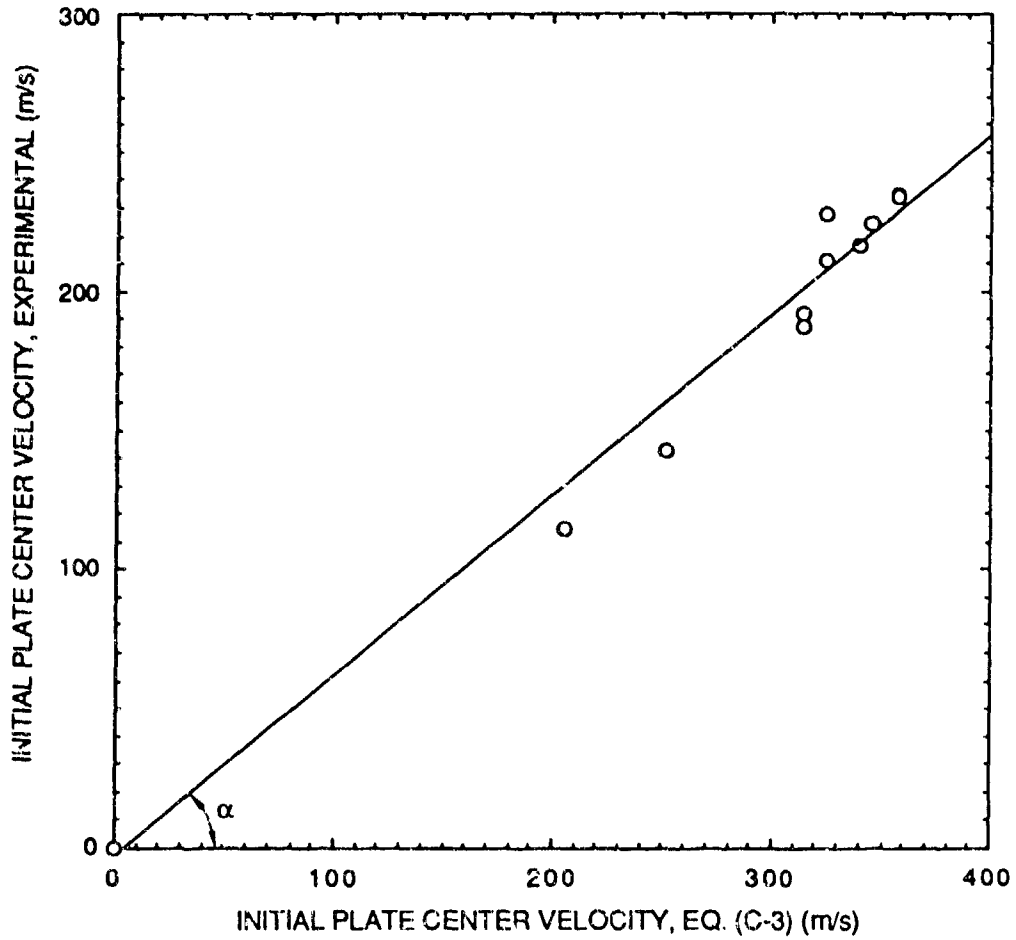
RA-2612-118

Figure C-28. Estimation of parameter α from the predicted and measured values of V_0.

(a) Experimentally determined V_0

HY-130 WE
□ 4-1
◆ 4-2 (Fit)
● 4-3 (Fit)
△ 4-4 (Fit)
▲ 4-5
■ 4-6
● 8-1
+ 8-2 (Fit)
× 8-3
○ 8-4

(b) V_0 from Equation (C-3) with $\alpha = 0.645$
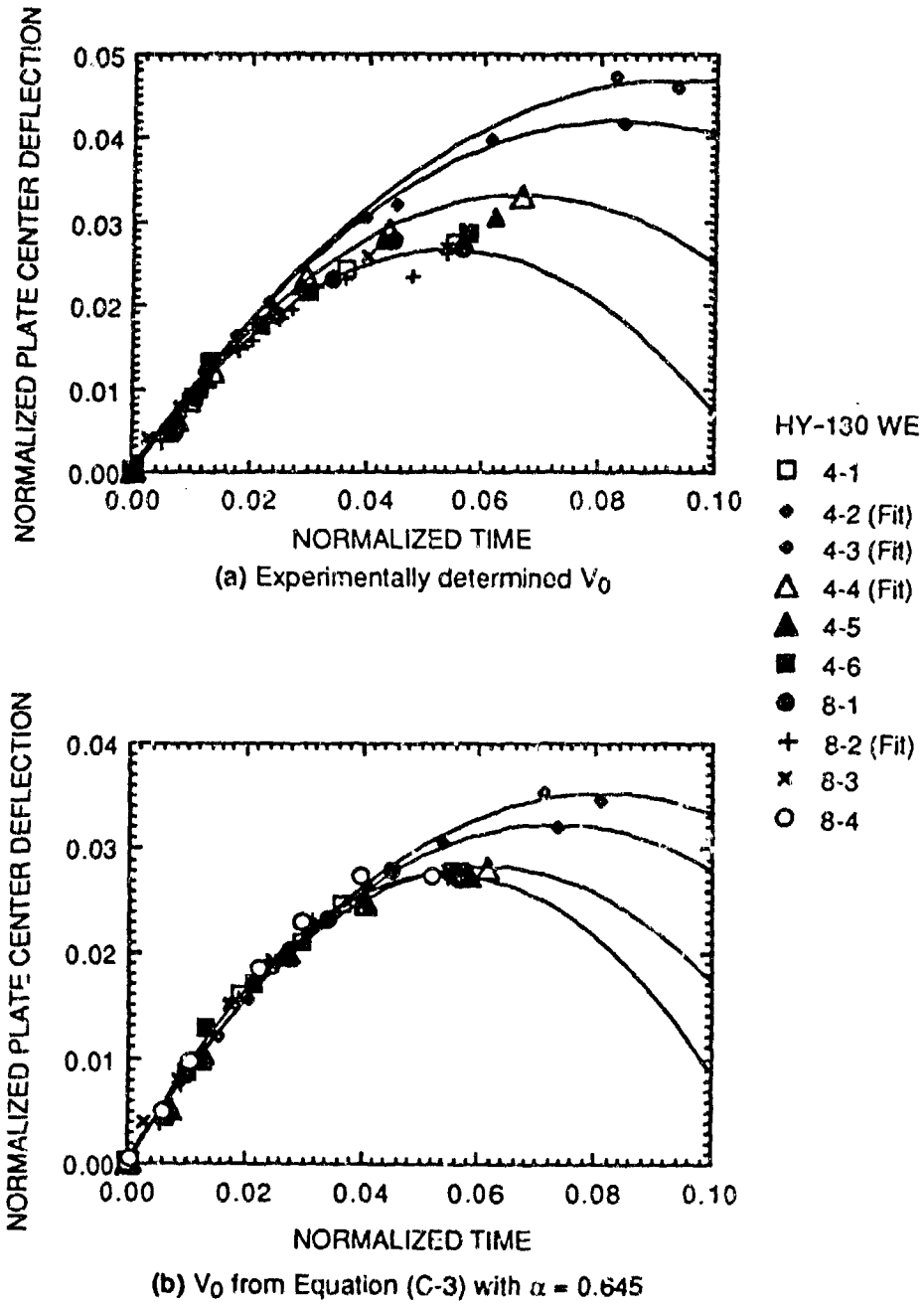
RA-2612-119

Figure C-29. Normalized plate center deflection histories for all dynamic fracture experiments on HY-130 steel weldments.

C-48

DISCUSSION

The discussion in this section first focuses on the analysis method for the dynamic fracture experiments and on how accurate and reproducible the results are. We then discuss the implication of the results for scaling HY-130 steel weldments under dynamic loading conditions.

Test Analyses

Assessment of the Improved Data Reduction Procedure. The purpose of the improved data reduction procedure was to improve the consistency of the deflection histories and to guarantee that the maximum specimen deflection predicted by the polynomial fit to the experimental data matched the deflection values obtained by posttest measurements of the specimen.

Comparing the deflection histories for the raw and corrected data demonstrates that a monotonic ranking of initial velocities, deflection histories, and maximum deflections with explosive thickness was achieved with the improved data reduction procedure. This monotonic ranking was not achieved when plotting the raw data. Significant improvements were introduced in the deflection histories for test HY-130 WE4-6 and the 1/8-scale experiments. The latter were affected more by the improved data reduction procedure, suggesting that the deflection measurements were less reliable in those experiments. This observation is not surprising, because the deflections were two times smaller than those in the 1/4-scale experiments, whereas the accuracy of the measurements remained the same because the measurement system was the same.

The improved data reduction procedure relies on the posttest measurement of the permanent deflection and on an estimate of the elastic deflection obtained from finite element simulations. In three cases (tests HY-130 WE4-2, WE3-1, and WE8-4) the posttest maximum deflection estimates fell slightly below the maximum deflection measured in the experiment. This discrepancy may be due to the uncertainty either of the experimental measurements or in estimating the elastic component of the deflection with the finite element analysis, which analysis may underestimate the actual elastic component of the deflection (see Appendix D).[*]

Consistency of Experimental Results and Test Analysis. We based our improved reduction procedure for the experimental data on the analysis and assumptions underlying Equations (C-1) through (C-3). It is therefore important to verify that the results of the experiments are indeed consistent with the analysis and assumptions. The normalized maximum plate center deflections measured in experiments with either no fracture or only partial fracture are plotted in Figure C-30 as a function of the normalized explosive thickness, along with a linear fit to the experimental data.

---

[*]For example, the boundary conditions assumed in the simulations were probably more rigid than those actually prevailing at the specimen plate and stiffener edges.
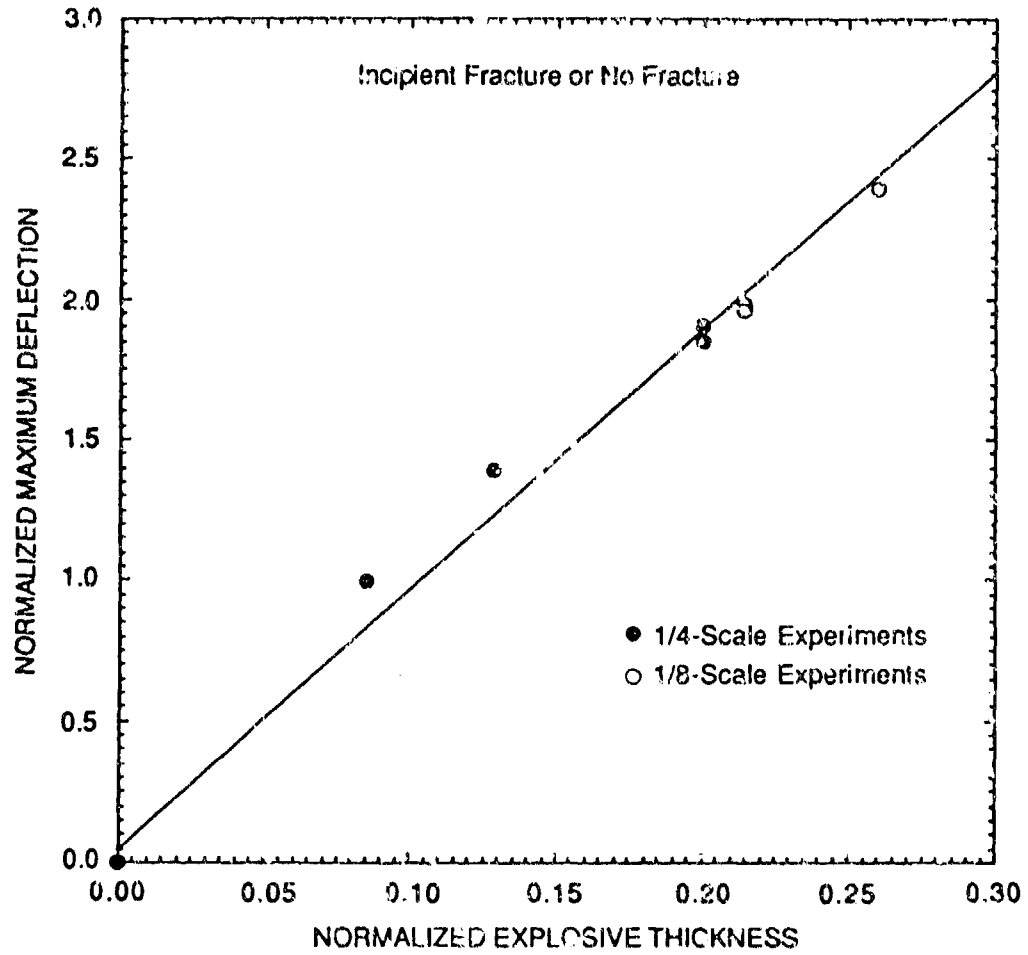
Figure C-30. Normalized experimental maximum center plate deflection as a function of normalized explosive thickness (normalization by specimen plate thickness).

We normalized explosive thickness and deflection by the specimen plate thickness. The figure shows that overall, the predicted linear relationship between maximum center plate deflection and explosive thickness is well borne out by the experimental data. However, the experiments performed with the smallest explosive thicknesses (tests HY-130 WE4-2 and -3) have about 20 percent higher measured maximum deflections than predicted by the linear fit.

Figure C-31 plots the experimental initial plate center velocity as a function of the normalized explosive thickness, along with the parabolic curve predicted by Equation (C-3), with $\alpha = 0.645$. Overall, the experimental data agree well with the predicted velocity, with a maximum deviation of no more than 13.3 percent (Table C-4)

Although the comparisons of predicted and measured data are not a completely independent verification of the correctness of the analysis (e.g., α was evaluated using the experimental data), they nevertheless demonstrate the consistency of the analysis and the experimental results.

Accuracy of Initial Velocity Estimates. The initial plate center velocity is an essential experimental parameter, because we use this velocity to prescribe the initial conditions in finite element simulations of the dynamic fracture experiments. Therefore, it is important to obtain an estimate of the uncertainty of the values of the initial velocities.

We applied three approaches in evaluating the uncertainties in the measured velocities. In the first, we compared the measured and predicted velocities and used the difference as an estimate of the uncertainty in the initial velocity values. As discussed above, this difference was smaller than ≈ 14 percent in all the experiments. In the second approach, we compared the velocity estimates obtained from the polynomial fits to (1) the raw experimental data and (2) the corrected data (columns 4 and 5 in Table C-3). Taking this difference as an estimate of the uncertainty in the initial velocity, we conclude that the initial velocities are measured to better than ≈ 12 percent.

TABLE C-4. COMPARISON OF PREDICTED AND MEASURED INITIAL PLATE CENTER VELOCITIES

HY-130 Specimen No.	V_0 from Eq. (C-3) (m/s)	V_0 Experimental (m/s)	% Deviation from Eq. (C-3)
WE4-1	223.1	224.5	-0.7
WE4-2	132.2	114.6	13.3
WE4-3	162.2	142.3	12.2
WE4-4	202.7	187.1	7.7
WE4-5	202.7	192.0	5.2
WE4-6	219.6	216.3	1.5
WE8-1	209.8	210.5	-0.3
WE8-2	231.1	234.9	-1.7
WE8-3	231.1	234.2	-1.3
WE8-4	209.8	227.4	-8.4
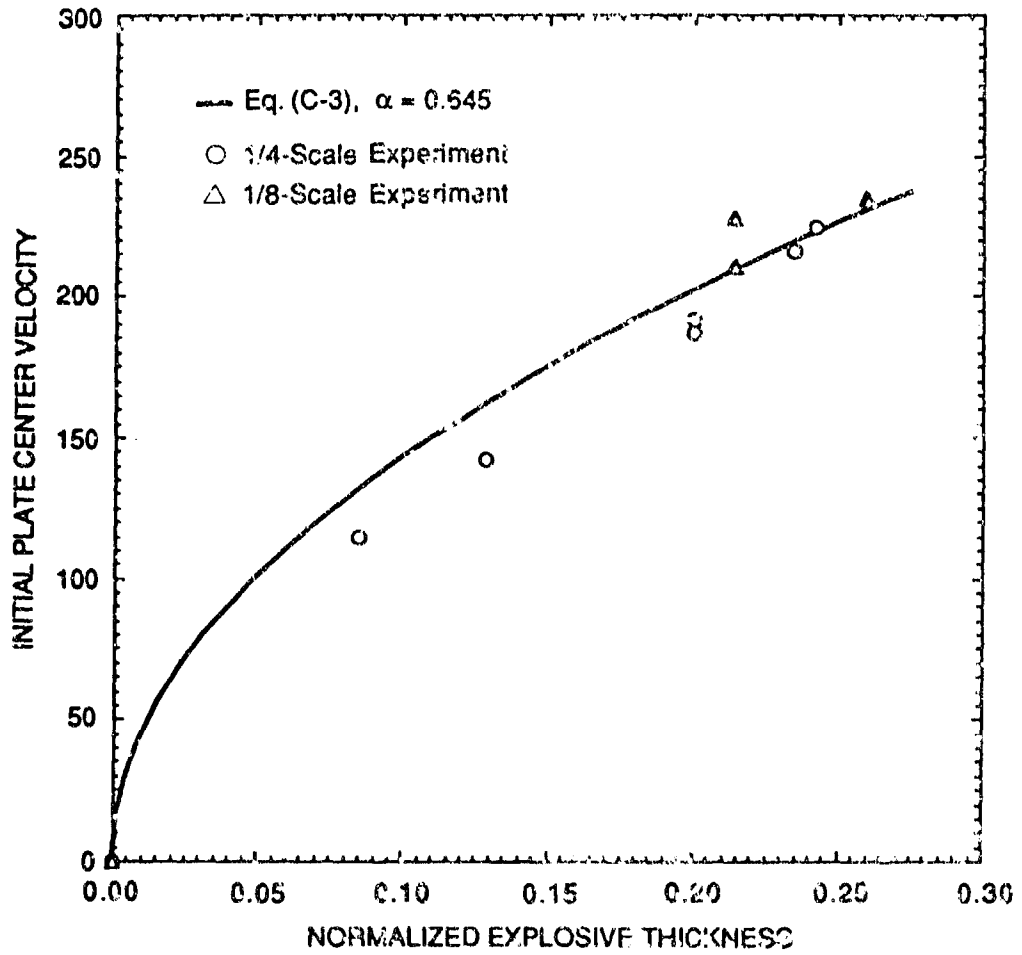
RA-2612-121

Figure C-31. Comparison of predicted and measured initial plate center
velocity dependence on the normalized explosive thickness.

A third and probably better estimate of the uncertainty in initial velocity can be obtained by comparing the initial velocity for two experiments performed with the same thickness of sheet explosive. We can perform this comparison for tests HY-130 WE4-4 and -5, WE8-1 and -4, and WE8-2 and -3. The difference in velocities for each set of experiments is smaller than 8 percent. Therefore, assuming that differences in initial velocity can be attributed entirely to measurement errors and not to, say, differences in explosive yield or plate material properties, we estimate that the initial velocities are measured to within 8 percent.

On the basis of this estimate, we conclude that the measurement accuracy on the initial velocity is on the order of ±10 percent or better.

Reproducibility of Experiments and Effect of Experimental Setup on Fracture Initiation. In the preceding discussion, we showed that for a given explosive thickness and specimen scale, the initial plate center velocities were quite reproducible. Furthermore, tests HY-130 WE4-4 and -5 demonstrate that the specimen deformation and fracture can be faithfully reproduced from test to test. The results of tests WE8-1 and -4 and WE8-2 and -3 indicate that the plate center deflection histories are also quite reproducible, although the attachment conditions and the deformation of the plate edges were different.

The loading arrangement can have a profound influence on fracture onset, if not on the overall specimen deformation, and we will need to control them with considerable care in future experiments. A more quantitative evaluation of these loading fixture effects could be fairly easily obtained by performing more dynamic finite element simulations in which some degree of compliance is introduced in the plate and stiffener clamping and attachment regions.

Specimen Deformation Response. A good understanding of the specimen deformation response is important in evaluating the fracture behavior of weldments and planning new experiments. The normalized center plate deflection histories in Figure C-29 suggest that a single normalized curve may describe at least the early part of the specimen deformation history. For later times the situation is less clear, because we observe at least two groupings of the curves and we must consider several possibilities.

First, it is possible that for each explosive thickness (or, equivalently, for each initial plate center velocity) there is a different deformation mode and hence a different normalized plate center deflection history. According to this interpretation and considering the set of data normalized using the experimental initial velocity, all the normalized deflection histories would still be well represented by second-order polynomials, but the normalized maximum deflections would decrease with increasing initial velocity.

Alternatively, only two deformation modes may be active in the specimens, one for low initial velocities (tests HY-130 WE4-2 and -3) and one for high initial velocities (all the other experiments). These two deformation modes might correspond to one regime--at low initial velocities and for small resulting maximum deflections--where the deceleration of the plate motion is effected predominantly by the bending moments, and to a second regime--at higher initial velocities--where the membrane stresses would be mainly responsible for slowing down the plate motion. This interpretation would account for the agreement of all the curves at small normalized times, because the early deformation would be controlled mainly by the bending of the plate.

A third possibility is that the difference in the normalized deflection histories for experiments HY-130 WE4-2 and -3 was due to differences in experimental conditions, such as the clamping arrangement of the specimen plate and stiffener. Indeed, measurements of the deformation of the specimens tested in these two experiments indicated that the plate immediately under the stiffener deflected significantly more (≈ 1 mm) than in other experiments (compare Figures C-13 and C-17a). This deflection under the stiffeners suggests that they were not as rigidly attached to the yokes as in the other experiments.

The finite element simulations of the dynamic fracture experiments (Appendix D) suggest that the first of these three interpretation may be the correct one. However, more work is needed to clarify this point. We recommend more detailed posttest measurements of the plate deformations and additional finite element simulations of the experiments in which we vary the boundary conditions for the specimen. More experiments with initial velocities lower than 150 m/s may also provide some clarification.

<u>Overall Evaluation of Dynamic Fracture Experiments</u>. In analyzing and evaluating the dynamic fracture experiments, we took a somewhat simplistic "one-dimensional" approach, focusing on the measurement of the plate center deflection. The preceding considerations and the finite element simulations described in Appendix D indicate that this approach provides a good description of the experiments, although we still need to clarify some uncertainties about the details of the specimen deformation. In particular, we measured the plate center initial velocity to within 10 percent or better. Our ability to measure the initial plate center velocity reliably is an important result because we used this measured velocity as initial condition for the finite element simulations of the experiments (see Appendix D). Moreover, the normalized deflection histories can guide selection of the proper loading conditions for future experiments with other materials or with different scales and specimen thicknesses.

Fracture Scaling Rule

To derive fracture scaling rules from the results of the dynamic experiments we need to define the fracture events we want to consider and the loading and deformation parameters that lead to these events.

The dynamic nature of these experiments made monitoring the crack initiation and the extension phase much more difficult than during the static experiments. Therefore, we chose to bracket the explosive thickness needed to produce incipient fracture on the one hand and complete fracture on the other. We then defined the loading conditions in terms of explosive thickness or of initial plate center velocity, V_0. We relied primarily on post-test observations to estimate the deflection at which fracture initiated.

In evaluating the fracture scaling rule, we compared the conditions needed to produce partial fracture in tests HY-130 WE4-4 and -5 to those conditions in test HY-130 WE8-4; similarly, we compared the conditions to produce complete fracture in tests WE4-1 and, more important, WE4-6 to those in test WE8-3. The fracture-controlling parameters for these experiments are compared in Table C-5. The explosive thickness and the deflection "at fracture" were normalized by the specimen plate thickness. The deflection "at fracture" was obtained from the posttest measurements by adding an estimate of the elastic component of the deflection.

TABLE C-5. FRACTURE CONTROLLING PARAMETERS FOR EXPERIMENTS
WITH INCIPIENT OR COMPLETE FRACTURE

HY-130 Specimen No.	Normalized Explosive Thickness	Experimental Initial Velocity (m/s)	Normalized Deflection "at Fracture"	Extent of Fracture
WE4-4	0.2000	187.1	1.90	Partial
WE4-5	0.2000	192	1.85	Partial
WE8-4	0.2142	227.4 (?)	1.98	Partial
WE4-1	0.2421	224.5	1.90	Complete
WE4-6	0.2346	216.3	2.24	Complete
WE8-3	0.2598	234.2	2.25	Complete

With our current understanding of the experiments, it is not possible to establish exactly to what event in the fracture process the deflection "at fracture" corresponds. Comparing the deflections for specimens in which partial and complete fracture occurred suggests that the plate center continues to be plastically deformed even after a crack begins in the weldment region. Therefore, we cannot identify the reconstructed deflection "at fracture" as that at the beginning of a

macrocrack in the plate that would freeze deformation elsewhere, as we did in analyzing the static fracture experiments.

The fracture-controlling parameters are further compared in Figure C-32, which plots the normalized maximum deflection achieved at the plate center as a function of the normalized explosive thickness. In this figure we also delineated, using the experimental results, domains corresponding to partial and complete fracture, respectively. The results in Table C-5 and Figure C-32 indicate that in first approximation and on the basis of the sparse available data, dynamic fracture of the 1/8- and 1/4-scale HY-130 steel T-weldments followed replica scaling. Therefore, the conclusions drawn from the static fracture experiments are substantiated by the dynamic fracture results, although loading rates and conditions were vastly different.

More experiments to provide verification of this conclusion are desirable, because the results for partial and complete fracture of the 1/8-scale experiments fall slightly to the right of the 1/4-scale experiments and could indicate a small scaling effect if more data were available.

<u>Comparing Deflection at Fracture for Dynamic and Static Fracture Experiments</u>. In the static fracture experiments, fracture began at a normalized plate deflection of about 2.5. Table C-5 shows that an upper-limit normalized deflection for the beginning of dynamic fracture is approximately 1.9 for a specimen half span comparable to that in the static experiments. The difference in deflection is probably due to two factors: (1) the difference in loading mode (bending and shear only in the static experiments; and bending, shear, and tension in the dynamic experiments), and (2) a difference of many orders of magnitude in loading rate. Considering our experience in tests HY-130 WE8-1 and -2, we believe that the former factor is more important in reducing the deflection at fracture. This conclusion is supported by the results of preliminary finite element simulations of the dynamic fracture experiments, which indicate that despite the large difference in loading rate, estimates of the fracture strains in the weld toe region are consistent with the fracture strains in the static fracture experiments.

CONCLUSIONS

The results of the dynamic fracture experiments and their analysis demonstrate that we have developed a reliable testing procedure for investigating the dynamic fracture of T-weldments. We can measure the initial specimen plate center velocity to within 10 percent or better. This information provides adequate initial conditions for a faithful finite element simulation of the experiments.
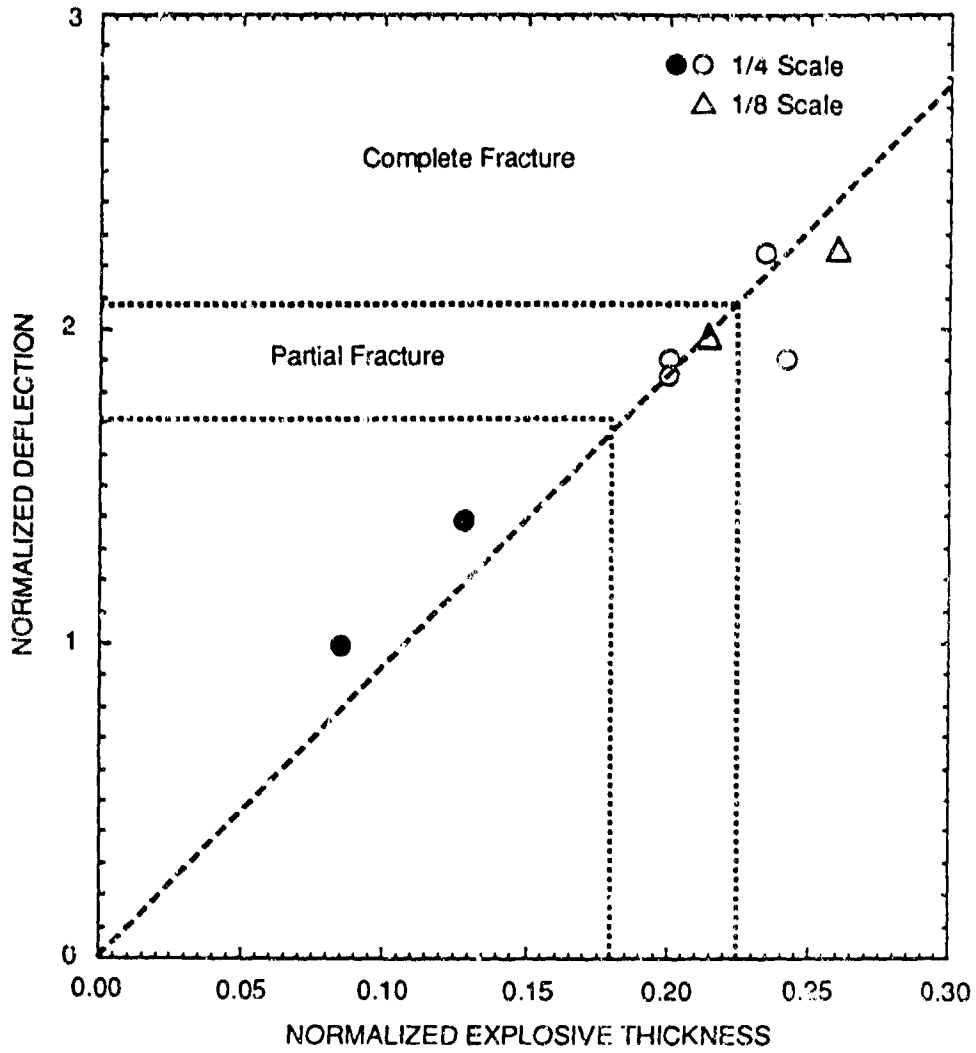
RA-2612-146

Figure C-32. Fracture envelope for HY-130 steel weldments established on
the basis of the dynamic fracture experiments.

(Dashed straight line represents predicted maximum deflection in the
absence of fracture.)

We also gained a good understanding of the specimen structural response. In particular we established the dependence of the initial plate center velocity, the maximum deflection on test parameters such as explosive type and thickness, and specimen and tamping material properties and dimensions.

With the dynamic fracture test procedure we established with good reliability the range of explosive thicknesses (or initial velocities) needed to induce partial or complete fracture. We demonstrated that the fracture mode produced in the experiments is similar to that observed in the static fracture experiments and in corresponding large-scale structures. More important, we demonstrated that, in first approximation, fracture of 1/8- and 1/4-scale HY-130 steel weldments under dynamic loading follows replica scaling.

REFERENCES

C-1. Rasmussen, E. A., "Development of a Simplified Method to Simulate Pressure Hull Response to Dynamic Loading," *David Taylor Naval Ship Research and Development Center Report*, Bethesda, MD, Aug 1984.

C-2. Dally, J. W. and Gifford, L. N., "A Simple Method to Assess the Stability of Shallow Cracks in Submarine Hulls," *David Taylor Research Center Report*, DTRC-SSPD-89-172-23, Bethesda, Feb 1989.

C-3. Seaman, L., "SRI PUFF 8 Computer Program for One-Dimensional Stress Wave Propagation," *SRI International Final Report*, Volume II, prepared for U.S. Army Ballistic Research Laboratory, Contract No. DAAK11-77-C-0083, SRI Project 6802, Menlo Park, CA, Aug 1978.

C-4. Abrahamson, G. R., "Explosively Induced Impulses," Internal Report No. 009-62, Stanford Research Institute, 1962.

APPENDIX D: MODELING HY-130 STEEL WELDMENT FRACTURE AND FINITE ELEMENT SIMULATIONS

CONTENTS

APPENDIX D

MODELING HY-130 STEEL WELDMENT FRACTURE AND FINITE ELEMENT SIMULATIONS

INTRODUCTION

This appendix describes the analytical work performed in support of the weldment fracture experiments and focused primarily on developing and implementing a weldment model capable of simulating the fractures observed during the experimental part of the program. We also performed finite element simulations of the dynamic fracture experiments to evaluate the structural response of the specimen and to calculate the deformation, strain, and strain rates in the weldment during the experiment. Finally we performed a static elastoplastic analysis of crack growth in HY-130 steel specimens to estimate the magnitude of nonscaling effects during crack growth and to compare the energy needed to extend the crack with that needed for nucleation.

The objectives and intended applications of the weldment model are

- To guide the interpretation of the fracture experiments by providing the stress and strain distributions in the regions where fracture occurred.

- To provide a more quantitative evaluation of the crack growth phase of fracture and the nonscaling effects potentially associated with crack growth.

- To provide a theoretical justification and rationale for the empirical scaling rules derived from the experimental results. A theoretical interpretation of the experimental results is an essential step in the safe application of the empirical scaling law to full-scale weldments not experimentally investigated in the present program.

- To serve as a basis for generalizing the empirical scaling rules to weldments prepared by welding processes other than the GTAW process used in this investigation, which may have different fracture properties.

- To guide the choice of an appropriate severity parameter to describe critical fracture conditions in the Naval Surface Warfare Center (NAVSWC) statistical fracture model.

- To provide a tool for investigating statistical effects on weldment fracture.

- To aid the design of scale-model experiments using specimens with machined rather than welded stiffeners, in which geometric scaling of the stiffener-plate joint fracture is enforced by introducing appropriate stress concentrations.

The weldment fracture model developed in this program consists of three parts: (1) a geometric and strength model of the weldment representing the various regions and strength gradients observed in the weld characterization task using metallographic cross section (see Appendix A); (2) a local fracture model that predicts when a small deformed, stressed volume of weldment material fails and loses its strength; and (3) a finite element discretization of the weldment incorporating the other two models. In this study, we used the implicit finite element code NIKE2D[D-1] and the explicit finite element code DYNA2D[D-2] for simulation of the static and dynamic fracture experiments.

The objectives of the modeling effort are quite ambitious, and significant developments are still needed to provide the desired degree of confidence in the weldment fracture model. Nonetheless, it will be shown below that the model has been developed enough to demonstrate clearly its promising capabilities and usefulness. In the following sections we discuss each part of the model and present the results of initial simulations, with and without the local fracture model of the weldment fracture experiments.

WELDMENT FRACTURE MODEL

Model of Weldment Geometry and Strength

We based our model of the weldment geometry on the metallographic observations reported in Appendix A (see Figures A-14 through A-16).

The investigation of trial 1/8-, 1/4-, and 1/2-scale GTAW weldments indicates that the width of the resulting heat-affected zone (HAZ) is more or less constant and independent of weldment scale. The weld bead in the 1/2-scale weld is proportionally smaller than that in the 1/8- or 1/4-scale weldments. The hardness maps also indicate a significant strength gradient across the weldments. The HAZ and the weld metal (WM) have a strength up to 20 percent higher and lower, respectively, than the base metal (BM). The gradient in hardness, and therefore in strength, tends to increase with decreasing weldment scale.

Guided by these experimental observations, we propose the simple model for the weldment illustrated in Figure D-1. We divided the weldment into three regions: the WM, the HAZ, and the BM. We assumed simple shapes for each weldment region and symmetry around the stiffener axis. We characterized the geometry and dimensions of each region with the parameters indicated in Figure D-1. In particular, we kept t_{HAZ}, the thickness of the HAZ constant, consistent with the metallographic observations. This constant t_{HAZ} is a nonscaling parameter that may introduce nonscaling effects in simulations of the weldment fracture. The height, H_{WM}, and the angle θ, of
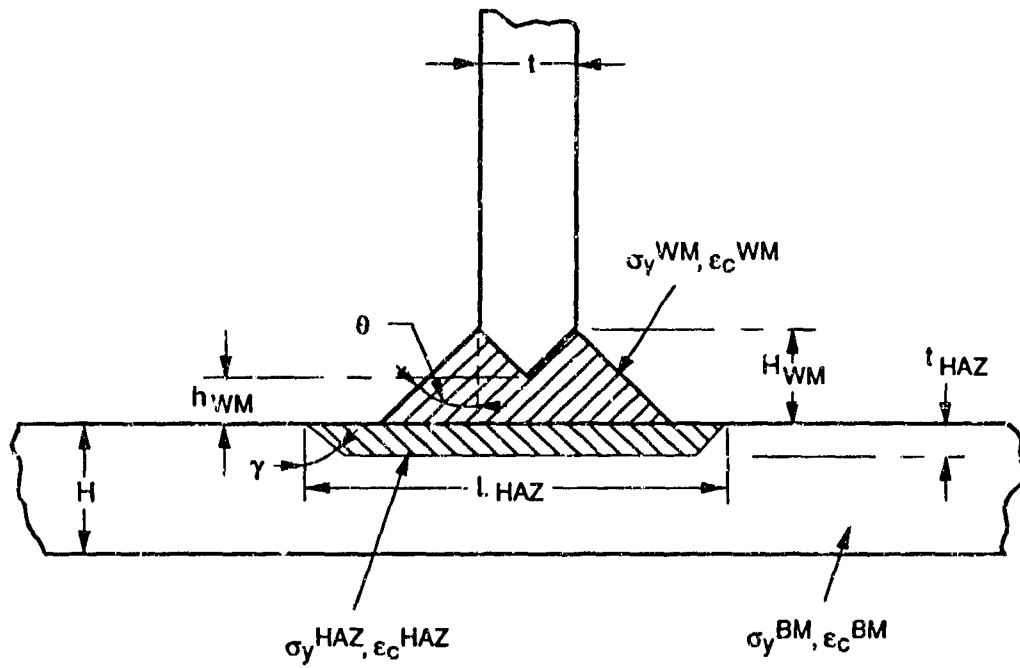
RA-M-2612-122

Figure D-1.   Model of weldment geometry and strength.

the weld bead, are two other important parameters that can be varied to reflect observed differences in the weld bead geometry, among specimens of either the same scale or different scales.

Different material properties can then be assigned to each of the three material regions. In first approximation, we assumed homogeneous and isotropic material properties within each region. However, it would be relatively easy to subdivide each region into smaller zones to introduce gradients in material properties within each zone and hence model more closely the actual weldments.[D-3] We assigned to the HAZ a stress-strain curve equal to that of the BM multiplied by a factor of 1.2. Similarly, we assigned to the WM a stress-strain curve equal to that of the BM multiplied by a factor of 0.8. We also varied the fracture properties of the weldment regions by changing parameters in the local fracture model, as discussed below.

Local Fracture Model

A sound weldment does not, in principle, contain a single large macroscopic crack. Therefore, fracture mechanics theories such as linear elastic fracture mechanics (LEFM), based on the stress-intensity factor concept, and elastoplastic fracture mechanics (EPFM), based on the J-integral concept, are not suitable for making fracture predictions in weldments. Rather, one must resort to material damage models or to so-called local fracture models.[D-4-D-7] In this research program, we adopted what is probably the simplest local fracture criterion still adequate to perform simulations of the fracture experiments

Fractographic studies have established that in the temperature range corresponding to the structural applications pertinent to this investigation, HY-130 steel fails microscopically by the nucleation, growth, and coalescence of voids (see Appendix A). This mechanism is also often called microscopically ductile fracture. A detailed review of the mechanisms governing the kinetics of microvoid nucleation, growth, and coalescence is beyond the scope of this report. It suffices to mention that at low strain rates, the rate of void growth is controlled by the plastic strain and is also strongly dependent on the state of stress, as measured by the ratio of mean stress, σ_{mean}, to effective stress, σ_{eff}.[*] On the basis of these observations, several ductile fracture criteria have been proposed.[D-8,D-9,D-11,D-12]

Here, we selected a formulation of the ductile fracture criterion proposed by Mudry[D-7] on the basis of observations by MacKenzie et al.[D-10] According to this formulation, failure of a material element of a characteristic size R_{MIC} occurs once the element has accumulated a critical

---

[*]At high strain rates (on the order of 1000 s^{-1} or more), voids grow predominantly by a stress-controlled viscous mechanism, and the model presented here may need to be modified.[D-5]

plastic strain, which is a function of the state of stress experienced by the element during straining. Mathematically, fracture of the element occurs when

$$D = \int \frac{d\varepsilon_{eq}^{P}}{\varepsilon_{c}(\sigma_{mean}/\sigma_{eq})} = 1 \quad \text{over } R_{MIC} \tag{D-1}$$

where D can be regarded as a normalized damage parameter, ε_{eq}^{P} is the equivalent plastic strain, and $\varepsilon_{c}(\sigma_{mean}/\sigma_{eq})$ is the critical failure strain for a given strain triaxiality $\sigma_{mean}/\sigma_{eq}$.

We can easily show that Equation (D-1) is consistent with the theoretical analysis of void growth and with other associated fracture criteria. Rice and Tracey[9] showed that the growth of spherical cavities in an infinite body is given by

$$\frac{dR}{R} = \alpha \exp\left(\frac{3}{2} \frac{\sigma_{mean}}{\sigma_{eq}}\right) d\varepsilon_{eq}^{P} \tag{D-2}$$

where R is the current radius of the cavity and α is a numerical constant.[*]

If we assume that void coalescence occurs at a critical value of the normalized void size $(R/R^{*})_{c}$, then Equation (D-2) is associated with the following fracture criterion:

$$Ln\left(\frac{R}{R^{*}}\right)_{c} = \int \alpha \exp\left(\frac{3}{2} \frac{\sigma_{mean}}{\sigma_{eq}}\right) d\varepsilon_{eq}^{P} \tag{D-3}$$

By defining the critical fracture strain $\varepsilon_{c}(\sigma_{mean}/\sigma_{eq})$ as

$$\varepsilon_{c}(\sigma_{mean},\sigma_{eq}) = \frac{Ln(R/R^{*})_{c}}{\alpha \exp\left(\frac{3}{2} \frac{\sigma_{mean}}{\sigma_{eq}}\right)} \tag{D-4}$$

we can recast Equation (D-3) in the same form as Equation (D-1).

We obtain a similar result using a ductile fracture model developed by Curran et al.[D-5] Their fracture criterion is based on attaining of a critical void volume, and with the simplest form of the criterion, fracture occurs in a material element when

---

[*]The exact form of Equation (D-2) is only valid for perfect plasticity, but it gives a rather good estimate of void growth in ferritic steels.[D-9]

$$\frac{\Delta v_c}{8\pi N_0 R_0^3} = \int 2.5 \frac{\sigma_{mean}}{\sigma_{eq}} d\epsilon_{eq}^p \tag{D-5}$$

where Δv_c is the critical void volume fraction increase above the initial void volume fraction, R_0 is the center of the activated void nucleating defect size distribution and N_0 is the number of initial defects per unit volume. Again, by defining the critical fracture strain $\epsilon_c(\sigma_{mean}/\sigma_{eq})$ as

$$\epsilon_c(\sigma_{mean}/\sigma_{eq}) = \frac{8\pi N_0 R_0^3}{\Delta v_c \frac{\sigma_{mean}}{\sigma_{eq}}} \tag{D-6}$$

we can recast Equation (D-5) in the form of Equation (D-1).

The key to practical applications of Equation (D-1) is to be able to measure $\epsilon_c(\sigma_{mean}/\sigma_{eq})$ experimentally. Typically this is done by performing tensile tests on notched round bars with different notch radii to vary the degree of triaxiality and to measure the effective strain at fracture.[D-10] To use this method, we must assume that the triaxiality remains constant during the experiment, which is not strictly true. Alternative approaches involve directly measuring $\ln(R/R^*)_c$[D-13] or $(\Delta v)_c$.[D-5]

The local fracture criterion expressed in Equation (D-1) is attractive for our problem because of its simplicity and, more important, because the critical failure data as a function of stress triaxiality have already been measured for HY-130 steel by MacKenzie et al.[D-10]

Specifying a characteristic material element size R_{MIC} is essential for applying the fracture criterion to situations involving steep stress and strain gradients, such as a sharp fatigue crack. Because of the strain singularity at a crack tip, the condition expressed by Equation (D-1) is satisfied for any applied load, and fracture would always be predicted unless Equation (D-1) is met over a certain distance in front of the crack, rather than at a point. Physically, the condition involving R_{MIC} can be rationalized by arguing that at least one void ahead of the crack must grow and coalesce with the tip to produce a crack growth increment. Therefore, a critical strain must act over a distance at least equal to the spacing of the void nucleating inclusions. This argument also provides an interpretation of the length parameter R_{MIC} in terms of microstructural quantities.

Because the ductile criterion we adopted contains a nonscalable microstructural length parameter, R_{MIC}, the criterion implies non replica scaling effects for fracture. These effects are discussed in detail by Giovanola[D-14] and are consistent with predictions of linear elastic and elastoplastic fracture mechanics.

Material Parameters for Local Fracture Criterion and Finite Element Implementation

Material Parameters. To apply the local fracture criterion expressed in Equation (D-1), we need the experimental failure curve $\varepsilon_c(\sigma_{mean}/\sigma_{eq})$ and the length parameter R_{MIC} for the HAZ and BM regions of the weldment. No data are needed for the WM region, because fractographic observations demonstrate that no crack propagates through this zone.

As we pointed out above, the fracture strain data are already available for HY-130 steel in both the longitudinal and transverse orientations (see Figure A-6 in Appendix A) and we demonstrated experimentally that they are relevant to our material. Without data for the HAZ, we applied the curve for the BM to the HAZ. We shifted the failure curve for the BM, as shown in Figure D-2, to reflect the decreased ductility of the HAZ. The amount of the shift is one of the adjustable parameters and was estimated from a finite element simulation of the static experiments discussed below.

Finite Element Formulation of the Local Fracture Criterion. A finite element formulation of the local fracture criterion was implemented in the finite element code NIKE2D.[D-1] The fracture criterion was developed by modifying an existing material model in NIKE2D: elastoplastic with isotropic/kinematic hardening (material type 3). In this model, postyield response is input by specifying effective stress, σ_{eff}, as a function of effective plastic strain, ε^p_{eff}.
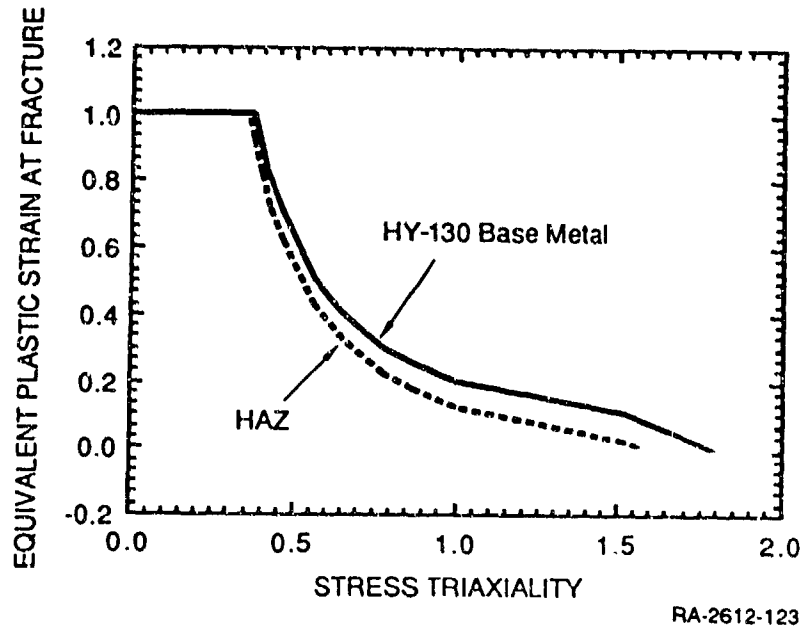
RA-2612-123

Figure D-2. Critical equivalent plastic strain versus stress triaxiality ratio $\sigma_{mean}/\sigma_{eq}$ for HY-130 BM and HAZ.

$$d = \exp[a(1 - D)]$$

RA-2612-124
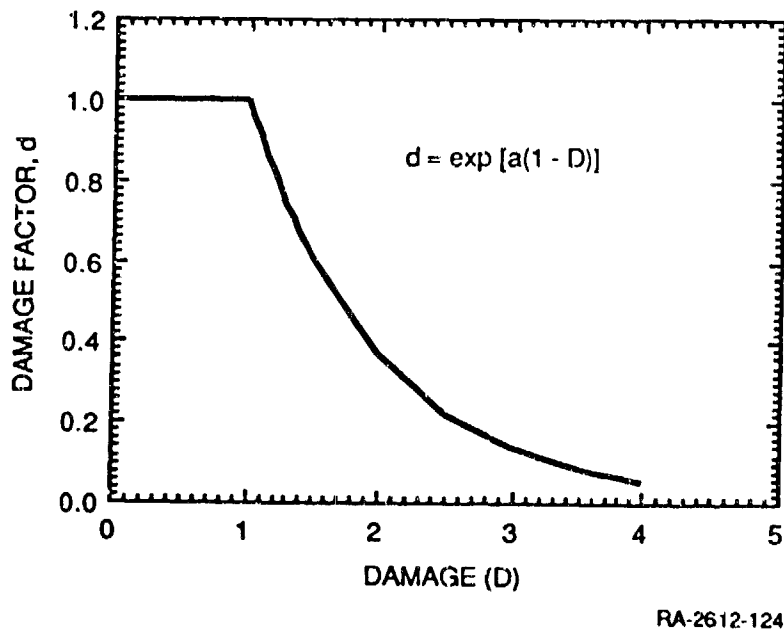
Figure D-3. Strain-softening curve assumed for failing material element.

One important aspect of implementing the local fracture model in a finite element code is how we simulate element failure once the fracture condition has been achieved. In contrast to a more rigorous model (e.g., the Gurson model[D-15] for porous ductile materials), the damage in our model is not, strictly speaking, coupled to the constitutive equation of the material. In other words, damage is not a state variable for our constitutive model. Rather, once the condition expressed by Equation (D-1) is reached in an element, we reduce the strength and mean stress of this element to zero by multiplying strength and mean stress by a damage function d. The choice of the function is based more on considerations of stability of the numerical scheme and simplicity than on those of the physical process of void-induced softening.

The form of d as a function of damage, D, is shown in Figure D-3. For values of D less than 1, d equals 1, and the effective stress-effective strain curve is used as input. For values of D greater than 1, the effective stress and mean stresses are reduced by the damage factor given by

$$d = \exp[a(1-D)] \tag{D-7}$$

where a is a constant that determines how quickly σ_{eff} decays with increasing values of D. Thus, the choice of the unloading path for the element is quite arbitrary and can be adjusted to achieve better numerical stability when simulating crack extension.

The damage parameter D is a function of effective plastic strain and triaxiality of the loading, $\sigma_{mean}/\sigma_{eq}$. In the finite element formulation, damage is accumulated in discrete increments. During each loading step, the increment in damage is calculated by normalizing the increment in effective plastic strain, $\Delta\varepsilon^p_{eff}$, by the value of $\varepsilon_c(\sigma_{mean}/\sigma_{eq})$ corresponding to the given value of $\sigma_{mean}/\sigma_{eq}$. The function $\varepsilon_c(\sigma_{mean}/\sigma_{eq})$, based on the experimental data of MacKenzie et al.[D-10] is shown in Figure D-2, and is given by

$$\varepsilon_c = 0.2(\sigma_{mean}/\sigma_{eq})^{-1.65} - \varepsilon_s \tag{D-8}$$

for values of $\sigma_{mean}/\sigma_{eq}$ between 0 and 1.5. For values of $\sigma_{mean}/\sigma_{eq}$ between 1.5 and 1.8, a range for which no experimental data are available, ε_c varies linearly between the value given by Equation (D-8) for $\sigma_{mean}/\sigma_{eq} = 1.5$ and 0.01. For values of $\sigma_{mean}/\sigma_{eq}$ greater than 1.8, ε_c remains equal to 0.01. For values of $\sigma_{mean}/\sigma_{eq}$ smaller than zero (predominantly compressive loading), we assume that no damage is accumulated. In Equation (D-8), ε_s is a specified shift in the critical strain curve accounting for variations in material properties (e.g., embrittlement in the heat-affected zone). To avoid numerical complications, we imposed minimum and maximum values on ε_c of 0.01 and 1.0. Damage is accumulated using this algorithm until D reaches the
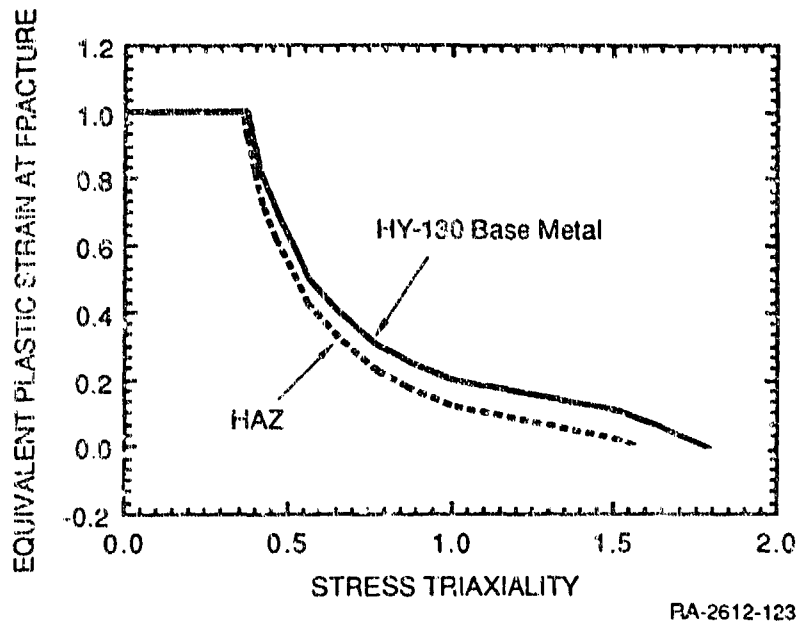
Figure D-2. Critical equivalent plastic strain versus stress triaxiality ratio $\sigma_{mean}/\sigma_{eq}$ for HY-130 BM and HAZ.
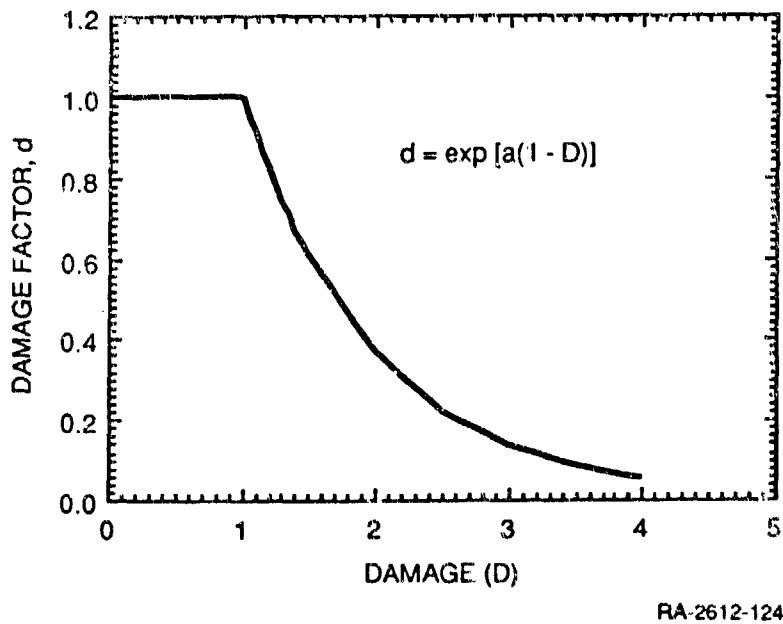

Figure D-3. Strain-softening curve assumed for failing material element.

value of 1. At that time the value for critical strain, ε_{c1}, is stored. Later increments in damage are calculated by normalizing the increment in plastic strain by ε_{c1}.

In using the ductile local fracture criterion in finite element simulations of the weldment fracture experiments, we specify the critical distance R_{MIC} by specifying the mesh size in the region where cracking is anticipated. The appropriate value of R_{MIC} can be determined by performing a fracture experiment using a specimen with a sharp precrack. The fracture experiment is then simulated with the finite element code and the local fracture criterion, and the mesh size (and R_{MIC}) is adjusted to match the experimental results. Mudry[D-7] points out that for pressure vessel steels, a value of R_{MIC} = 0.2 mm has yielded good simulation results. Guided by this experience and to avoid more testing and simulations, we assumed a value of R_{MIC} = 0.4 mm in the preliminary simulations discussed below.

Limitations and Applications of Weldment Fracture Model

In this research program we adopted what is probably the simplest local fracture criterion to model ductile fracture. Furthermore, except for a few verifying tensile experiments, we did not evaluate the model's material parameters. Rather, we relied on experience, data from the literature, and some guided engineering estimates for choosing the material parameters.

In particular, the choice of a value for R_{MIC} was quite arbitrary and, for our preliminary simulations, somewhat coarse. Moreover, the functional form of the damage factor d, was not based on a physical modeling of the geometric softening associated with void growth in the matrix material. Rather, we selected the damage factor functional form to represent a full strength/no strength behavior of the damaged material, while at the same time not compromising the stability of the numerical simulation. Finally, the geometric and strength model of the weldment is also rather simple because no gradual strength gradients were introduced in any of the three zones.

Nevertheless, the simulation results, shown below, indicate that even in its present somewhat rudimentary form, the weldment model can generate useful results in parametric studies of weldment fracture. In particular, the model can provide a quantitative estimate of the nonscaling effects introduced by non-scaling length parameters, such as the width of the heat-affected zone or the microstructural length parameter R_{MIC}.

One possible limitation of the current model is that it may not be applicable to the dynamic fracture experiments. Finite element simulations of the dynamic fracture experiments discussed below indicated that the strain rates in the weld toe region reach several thousands per second and they are likely to be even higher at the tip of the growing crack. At those strain rates, the ductile growth of voids may no longer be only strain-controlled but may also include a stress-driven

viscous growth contribution.[D-5] Therefore, a modification to the model may be needed to reflect the difference in void growth mechanisms at high loading rates.

FINITE ELEMENT SIMULATIONS OF FRACTURE EXPERIMENTS

Finite Element Simulations of Static Fracture Experiments Without Local Fracture Model

Objectives. The objectives of this series of finite element calculations, which do not include the local fracture model, were (1) to investigate the influence of strength and geometric variations in the weldment on the load displacement curve and on the stress and strain distributions in the weld region, (2) to estimate the critical failure strain in the heat affected zone for later use in conjunction with the local fracture model, and (3) to evaluate the effect of large specimen deformations on the load deflection curve recorded in the experiment (geometric softening).

Finite Element Model. We performed the finite element simulations of the static experiments with the NIKE2D code[D-1] using a plane strain formulation and quadrilateral isoparametric elements. A typical mesh used for studying the effects of weldment geometry and strength on the stress and strain fields is shown in Figure D-4. In simulations in which we assigned different material properties to the HAZ and the WM, the mesh configuration (HAZ relative size) modeled a 1/4-scale specimen. Only half the specimen is represented in Figure D-4. The center line of the specimen is a symmetry line, and the top of the stiffener is constrained in both the y and z directions. We imposed a displacement at the node corresponding to the contact point with the support roller.

For all cases analyzed, we performed elastoplastic simulations using one or more of the four stress-strain curves shown in Figure D-5, depending on the simulation.

Effect of Variations in Weld Geometry. We performed simulations in which we varied the weld bead angle θ with respect to the stiffener axis and the weld bead height H_{WM}. The four geometric cases considered are illustrated in Figure D-6. Case 1 represents the baseline case, Case 2 the proportionally smaller bead height in the 1/2-scale specimens, and Cases 3 and 4 two extremes in observed variations in bead angle.

Typical contours of equivalent plastic strain and mean stress obtained in the simulations (for geometric case 1 and the stress-strain curve Base Metal 2 in Figure D-5) are plotted in Figure D-7. The results in Figure D-7 illustrate that the maximum equivalent plastic strain and the maximum mean stress both occur at the same location in the HAZ--at the specimen surface near the toe of the weld bead--consistent with the location of fracture initiation in the experiments.
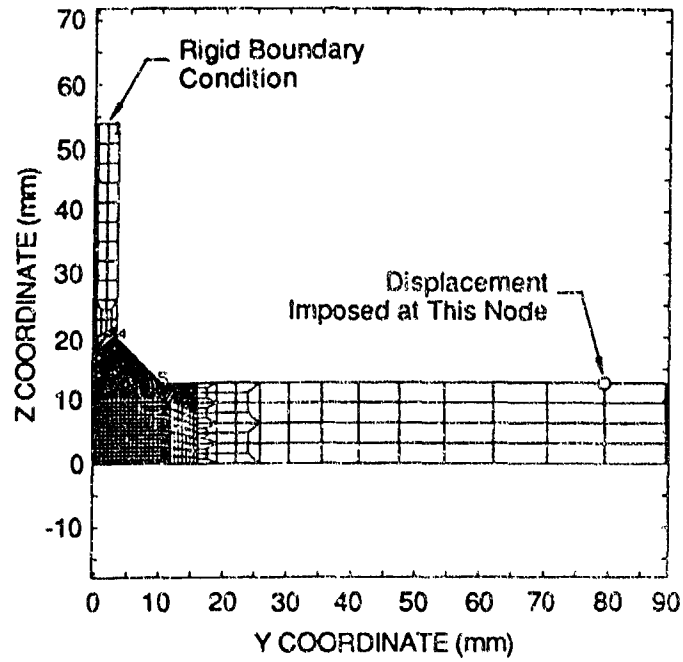
(a) Complete mesh simulating half the specimen
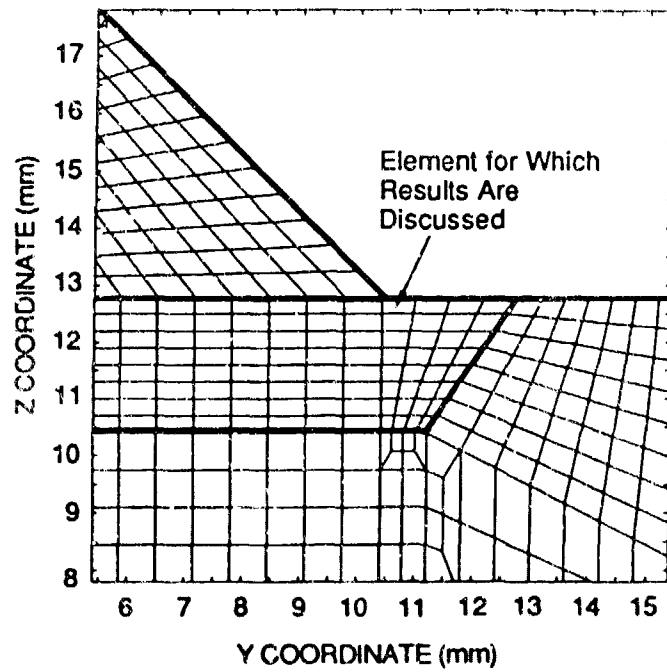
(b) Detail of the weld region

RA-2612-39A

Figure D-4. Typical finite element mesh for simulating static experiments (investigation of geometry and strength effect).
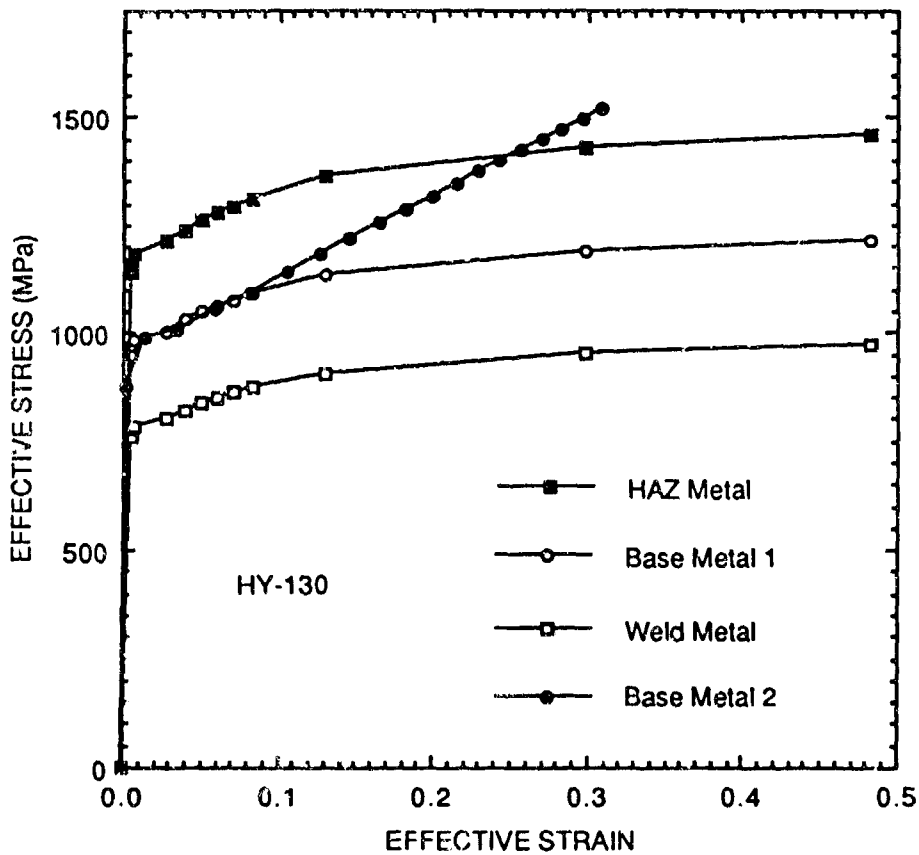
Figure D-5. Stress-strain curves used in the finite element simulations of the static fracture experiments.

Case No.	Bead Angle	Bead Height H$_{WM}$ (mm)
1	45	7.2
2	45	4.2
3	30	7.2
4	60	4.2
5	45	7.2
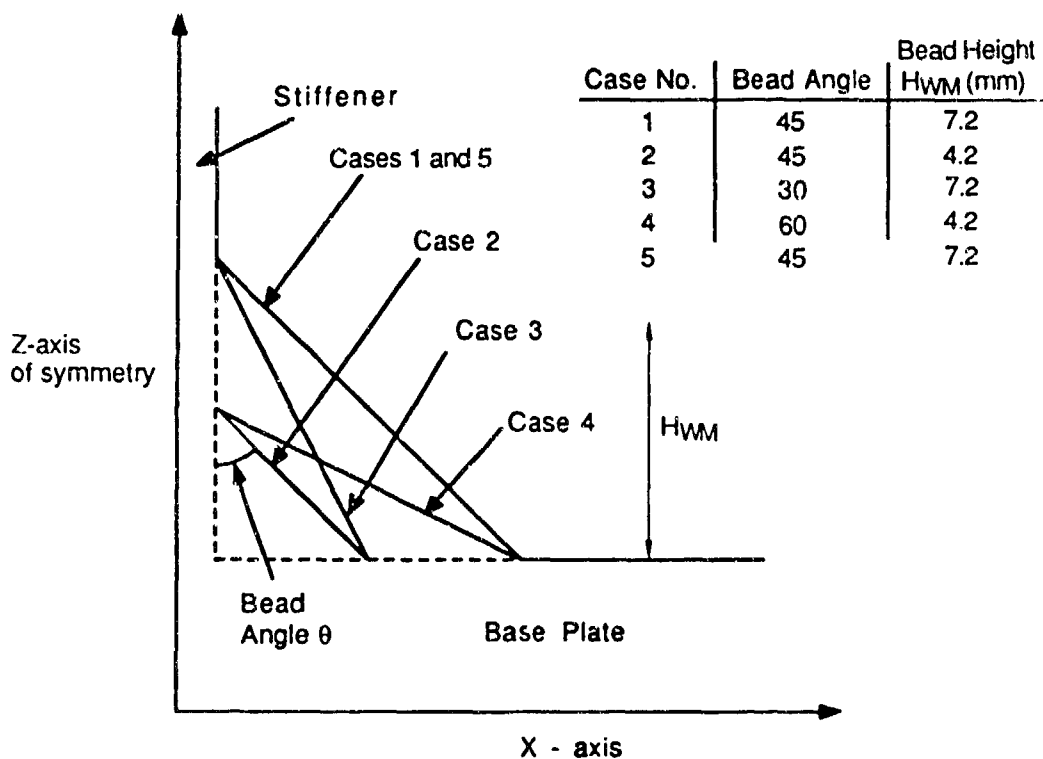
RA-2612-47A

Figure D-6. Variations in weldment geometry investigated in finite
element simulations.

Cases 1 and 5 differ only in the stress-stain curves used.
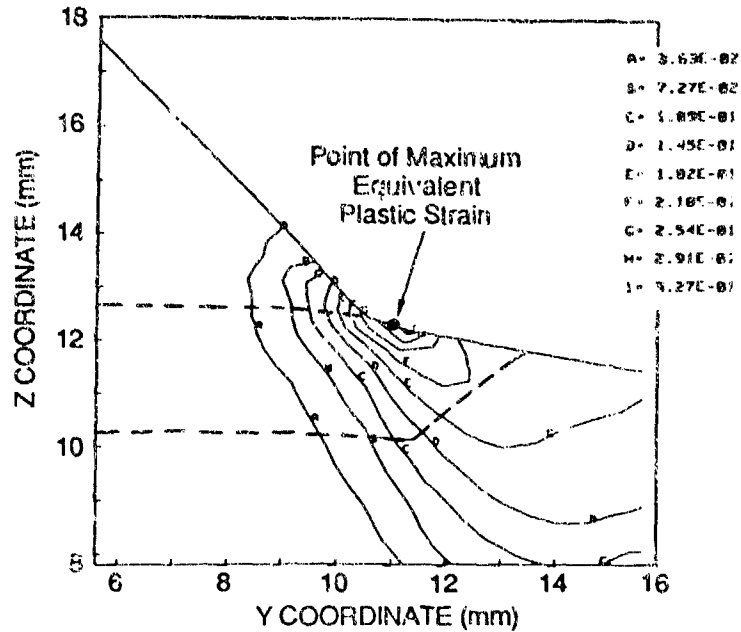
(a) Contours of equivalent plastic strain
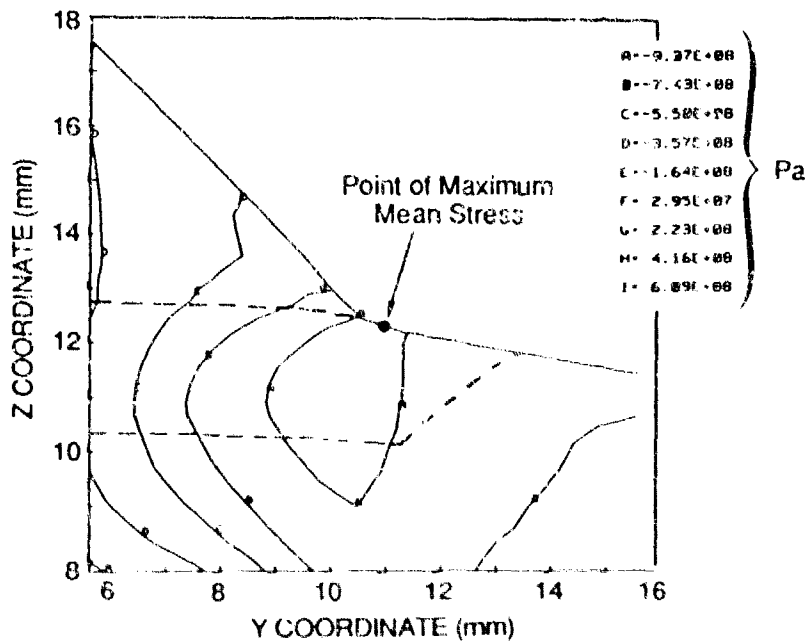
(b) Contour of mean stress

RA-2612-40A

Figure D-7. Typical contour of equivalent plastic strain and mean stress
obtained with the finite element simulation.

Geometrical Case 1, Base metal 2 stress-strain curve.

The results of the calculations for Cases 1 through 4, with the stress-strain curve labeled "Base Metal 1" in Figure D-5 for all three weldment regions, are compared in Figures D-8 through D-10. Figures D-8 and D-9 plot the mean stress and the effective plastic strain in the surface element at the toe of the weld bead as a function of the imposed displacement. Nonnegligible differences in the effective plastic strain and mean stress histories, arise with changes in geometry.

These differences are further illustrated in Figure D-10, which plots the ratio of mean to equivalent stress as a function of effective plastic strain. The strain/mean stress curve is important because, as discussed above, the mechanism of ductile fracture in HY-130 steel is a function of both the imposed plastic strain and the level of triaxial stress. With a view toward evaluating the material parameter for the local fracture model, we also plotted the measured mean stress/failure strain envelope for HY-130 steel in the LT and ST orientations.[D-10] There is a clear influence of the bead geometry on the strain/mean stress curve, with the grouping of the results suggesting that the height of the weld bead rather than the bead angle controls the curve shift.

We can use Figures D-8 through D-10 to assess the effect of geometric variations in the weldment regions on the fracture test results by assuming that the failure envelope for HY-130 steel in the LT direction applies to the material at the toe of the weld in the base plate HAZ. We estimate the failure strain for the various weldment geometries from the intersections of the failure envelope with the calculated strain/mean stress curves in Figure D-10.[*] We then determine the corresponding displacements at crack initiation from Figure D-9.

With this procedure, we find that variations in geometry may induce differences of up to 25 percent in the displacement at the onset of fracture in the element at the toe of the weld. A weldment with a proportionally smaller weld bead appears to experience less severe plastic loading conditions. This observation may explain some of the scatter in the experimental fracture displacement data for the static experiments. On the other hand, we did not observe any measurable change in the level of the yield and fully plastic loads because of the weld geometry differences in the simulations.

Effect of Weldment Strength Gradient. The effect of the strength gradient was investigated by comparing the simulations labeled "Case 1" and "Case 5." Both cases had the same weldment geometry (Figure D-6). For Case 1, we performed the simulation using the Base Metal 1 stress-strain curve for the whole weldment region. For Case 5, the HAZ was assigned the stress-strain

---

[*]This failure criterion is slightly different from that expressed by Equation (D-1) and from the implementation of that equation in the finite element code: The triaxiality ratio $\sigma_{mean}/\sigma_{eq}$ is assumed constant.
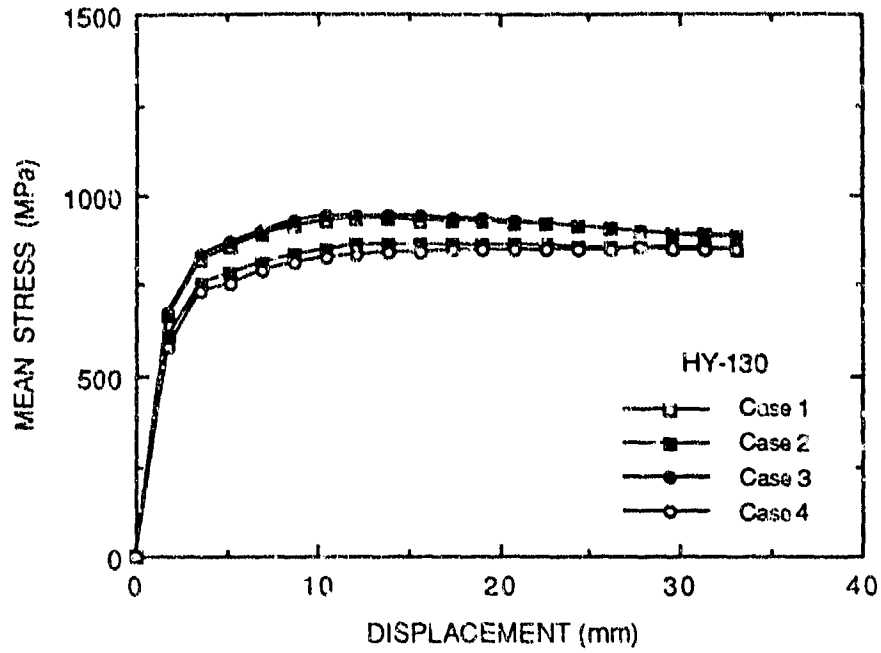
RA-2612-58A

Figure D-8.   Mean stress as a function of specimen displacement for base plate HAZ element immediately at the toe of the weld bead for Cases 1 through 4.
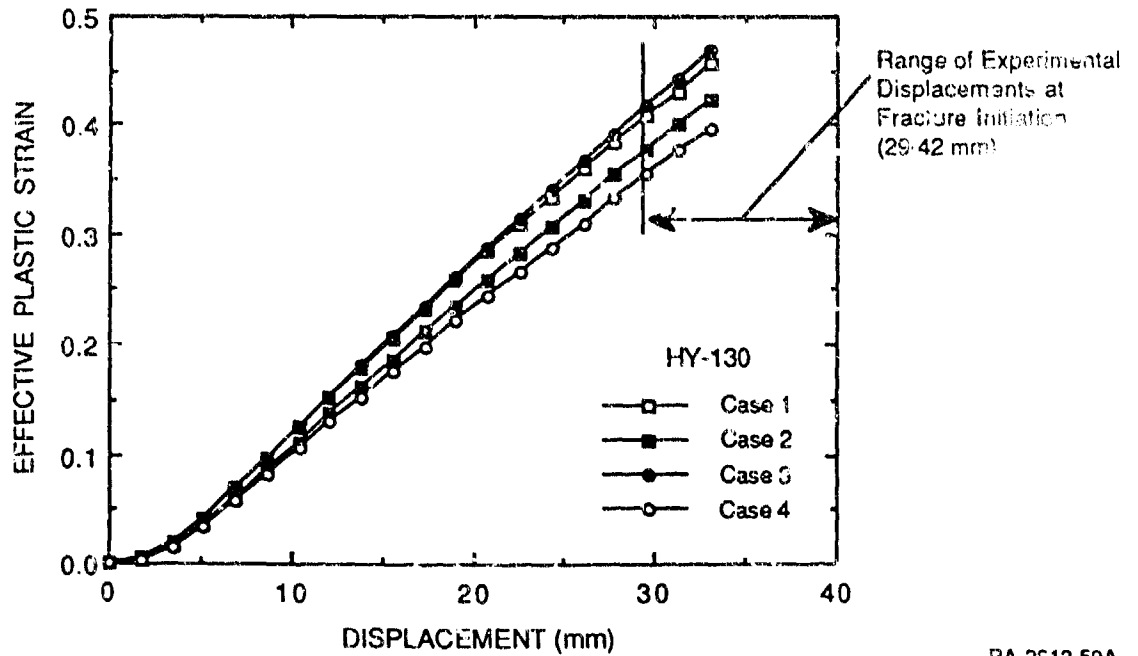
RA-2612-59A

Figure D-9.   Effective plastic strain as a function of specimen displacement for base plate HAZ element immediately at the toe of the weld bead for Cases 1 through 4.
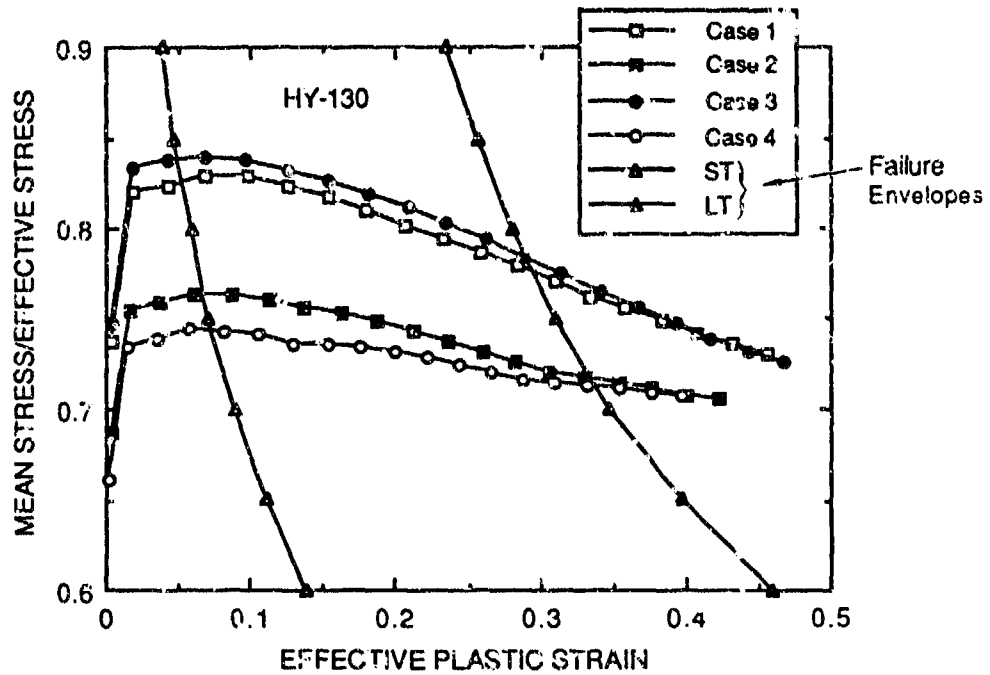
RA-2612-60A

Figure D-10.   Ratio of mean stress to affective stress as a function of effective plastic strain for base plate HAZ element immediately at the toe of the weld bead for Cases 1 through 4.

The strain-mean stress failure envelopes for HY-130 steel in the long transverse (LT) and short tranverse (ST) directions are also plotted.

curve of the base metal shifted up by 20 percent of the yield stress along the stress axis (curve labeled HAZ Metal in Figure D-5), and the weld metal was assigned the stress-strain curve of the base metal shifted down by 20 percent of the yield stress (curve labeled Weld Metal in Figure D-5). These strength differences were based on the maximum hardness differences observed in the weld characterization.

The effect of introducing a strength gradient in the weldment is illustrated in Figures D-11 through D-13, which compare the results of the finite element calculations for Cases 5 and 9.

Like Figures D-8 and D-9, Figures D-11 and D-12 plot the mean stress and the effective plastic strain in the surface element at the toe of the weld bead as a function of the imposed displacement. Figure D-13, like Figure D-10, plots the ratio of mean to equivalent stress as a function of effective plastic strain and the failure curves for HY-130 steel. Decreasing the strength of the weld metal and increasing the strength of the HAZ tends to elevate slightly the mean stress in the element considered (Figure D-11) and to significantly decrease the plastic strain (Figure D-12). Because the effective stress is significantly elevated (20%) in Case 5, the resulting plot of the ratio of mean to equivalent stress as a function of plastic strain for Case 5 is significantly below that for Case 1.

The effect on fracture of a strength differential in the weldment is less straightforward to evaluate than the effect of geometry, because it is likely, on the basis of metallurgical arguments and experience, that a change in strength from region to region is also associated with a change in the failure envelope. If the same failure envelope (e.g., the curve for HY-130 steel in the LT direction) applies for both Cases 1 and 5, then Figures D-12 and D-13 indicate that the HAZ with a higher flow curve would fracture at higher strains and applied displacements. However, if we take the average displacement at the onset of fracture (≈33 mm) and read the corresponding failure strain in Figure D-12, we conclude that the high-strength HAZ fractures at a lower failure strain than the low-strength HAZ, while the degree of triaxiality is essentially the same. Thus, assuming the same displacement at fracture for Cases 1 and 5 implies that the stronger HAZ is more brittle than the softer HAZ, which is more likely than assuming a strength independent failure envelope.

Because the hardness map indicates a significantly higher strength value for the HAZ and lower strength for the weld metal, we believe that Case 5 is more representative of the experimental behavior than Case 1. Using a lower-limit experimental displacement at fracture of about 30 mm for the 1/4-scale fracture experiments. we estimated the failure strain at 0.28 (Figure D-12) and construct the corresponding point in the mean stress-strain diagram (Figure D-13). We then assumed that the failure envelope for the HAZ could be obtained by simply translating that for HY-130 steel in the LT orientation through the failure point for Case 5 corresponding to the
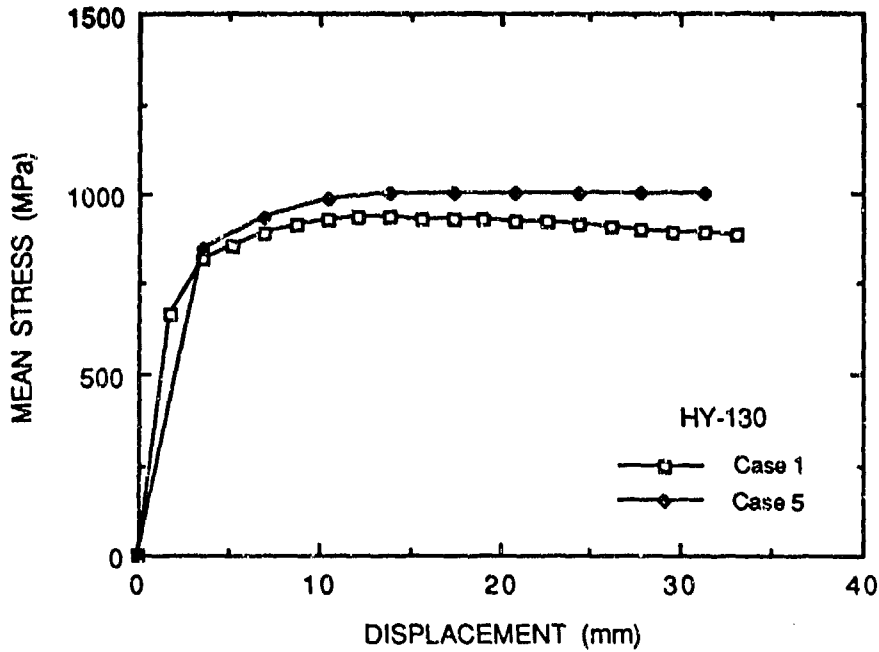
RA-2612-61A

Figure D-11. Comparison of mean stress as a function of specimen displacement for base plate HAZ element immediately at the toe of the weld bead for Cases 1 and 5.
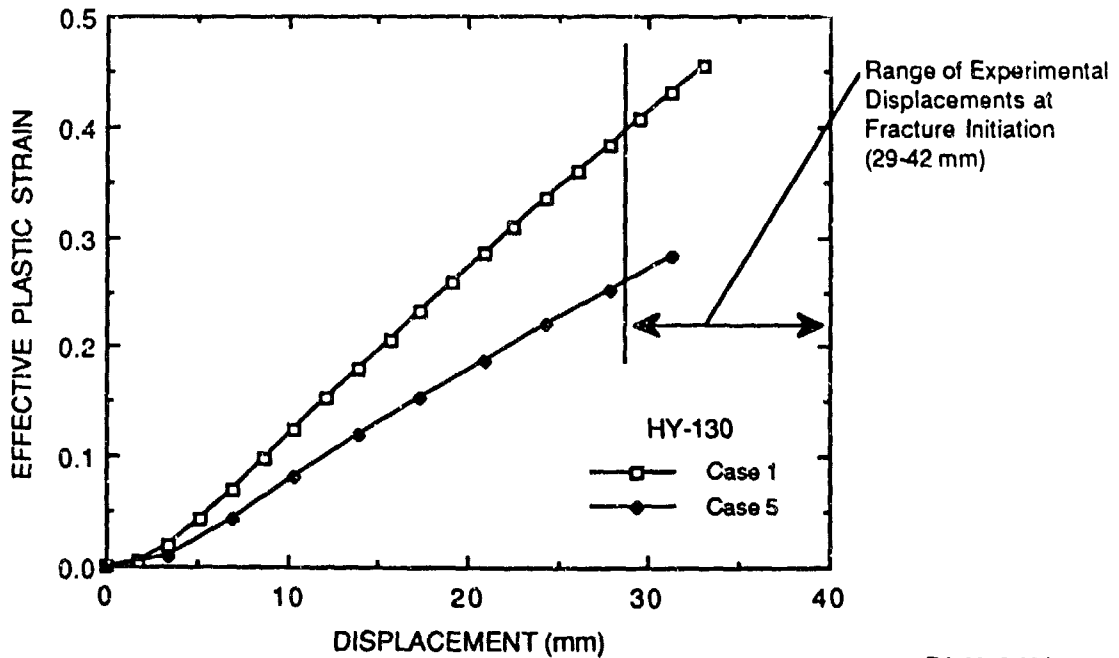
RA-2612-62A

Figure D-12. Comparison of effective plastic strain as a function of specimen displacement for base plate HAZ element immediately at the toe of the weld bead for Cases 1 and 5.
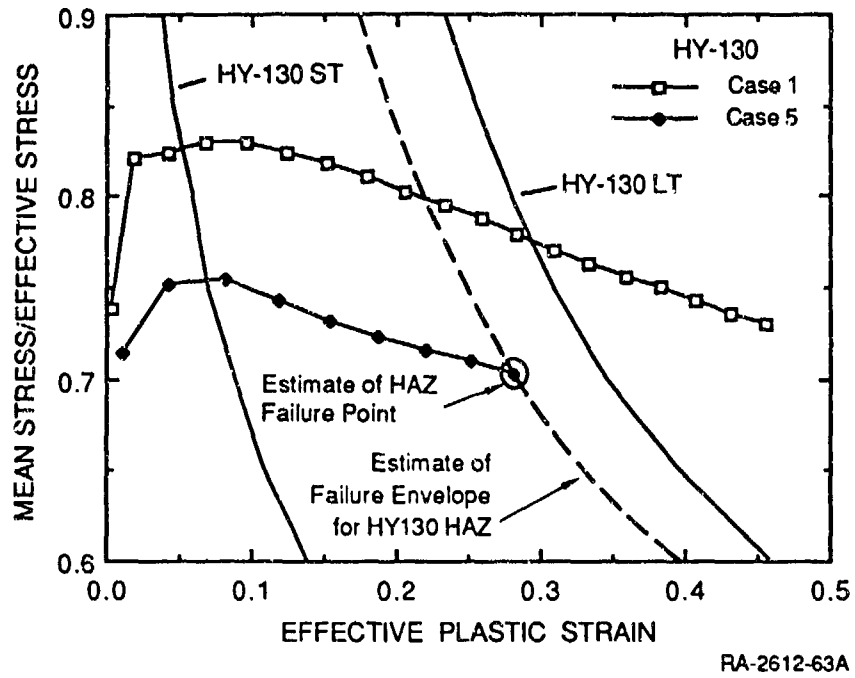
Figure D-13. Ratio of mean stress to effective stress as a function of
effective plastic strain for base plate HAZ element
immediately at the toe of the weld bead for Cases 1 and 5.

experimental conditions. This procedure resulted in the dashed curve in Figure D-13. Without more refined estimates, we used this curve as a failure envelope for the HAZ in simulations using the local fracture criterion.

We also repeated the simulations of Cases 1 through 4, using the flow curve labeled "Base Material 2" in Figure D-5. The objective of these simulations was to investigate the effect of differences in strain hardening on the stress-and-strain distributions at the toe of the weld. A comparison of geometric Case 1 for the two flow curves is presented in Figures D-14 through D-16. For a given geometry and applied displacement, higher mean stresses, lower strains, and a significantly lower strain/mean stress curve are achieved when the hardening of the stress-strain curve is increased. On the basis of the failure curve for HY-130 steel in the LT orientation, we estimated that these differences, resulting from those in the hardening rate, may cause variations in the displacement to failure of 20-30 percent.

Large Deformations and Geometric Softening. In the static experiments, the load was applied to the specimen through contacts that were constrained from moving transversely. During the test, the plate of the specimen deflected very significantly, as illustrated in Figure B-4 of Appendix B. In all the static fracture experiments, the load reached a maximum at a normalized displacement of about 1.5-2.0, then gradually decreased with increasing deflection.

The stress-strain curve for the material hardens moderately after yield, and there is no indication of strain softening. Thus, the decrease in load observed in the experiments must be caused by a combination of specimen cracking and by apparent softening caused by geometric changes of the specimen-loading fixture arrangement associated with large deformations (geometric softening). Geometric softening occurs because the imposed displacement is constrained to move along a fixed vertical line so that the point of displacement application slides transversely along the plate as the deflection increases. This sliding increases the effective moment arm, and a smaller load is needed to cause a given moment (the fully plastic moment) at the weldment. A simple static analysis shows that the load drop associated with geometric softening is proportional to the square of the cosine of the bend angle α (see Figure B-4 in Appendix B).

We performed two finite element simulations to quantify the effect of geometric softening on the specimen response. The mesh for these calculations is shown in Figure D-17a and b. The stress-strain curve labeled "Base Metal 1" was used for all three weldment regions in the two simulations.

For the first calculation, a vertical displacement was imposed at a given point on the plate; this point did not move as the plate deflected (condition 1, Figure D-17c). In the second calculation, the plate displacement was imposed along a vertical line fixed in space, so that the
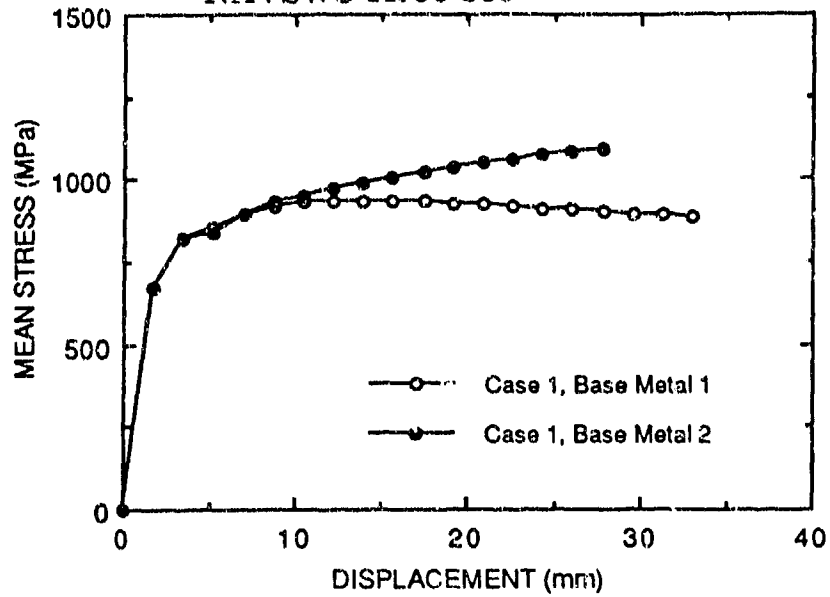
RA-2612-126

Figure D-14. Comparison of mean stress as a function of specimen displacement for base plate HAZ element immediately at the toe of the weld bead for Case 1 with flow curves Base Metal 1 and Base Metal 2.
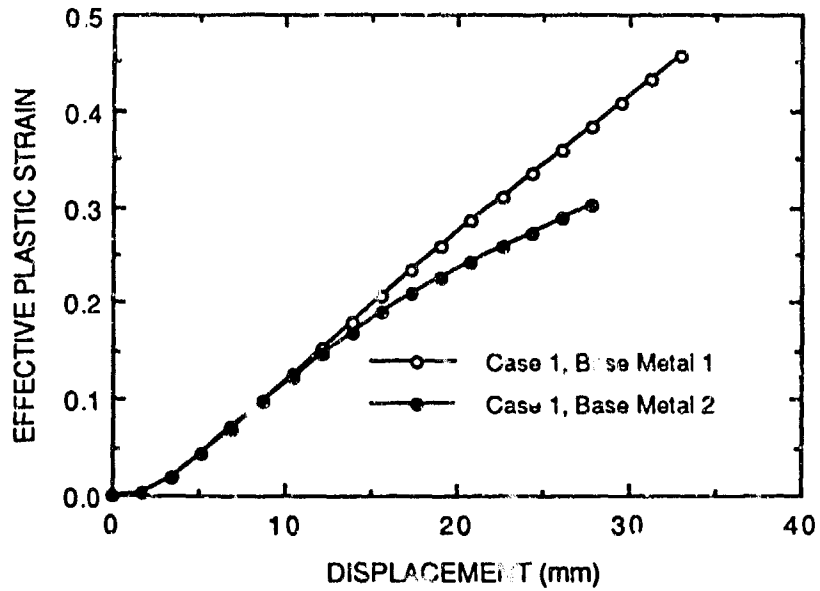
RA-2612-127

Figure D-15. Comparison of effective plastic strain as a function of specimen displacement for base plate HAZ element immediately at the toe of the weld bead for Case 1 with flow curves Base Metal 1 and Base Metal 2.

D-24
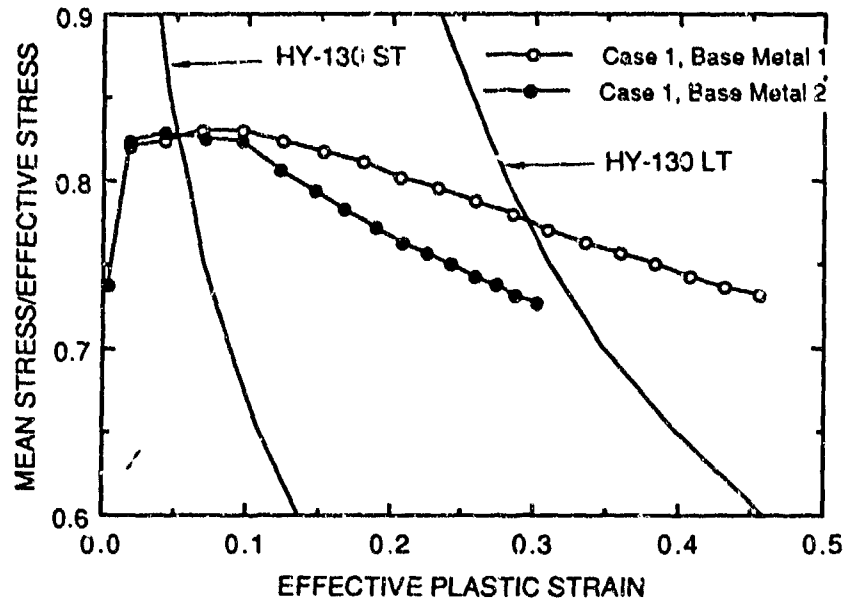
RA-2612-128

Figure D-16. Ratio of mean stress to effective stress as a function of effective plastic strain for base plate HAZ element immediately at the toe of the weld bead for Case 1 with flow curves Base Metal 1 and Base Metal 2.

The strain/mean stress failure envelopes for HY-130 steel in the long transverse (LT) and short transverse (ST) directions are also plotted.
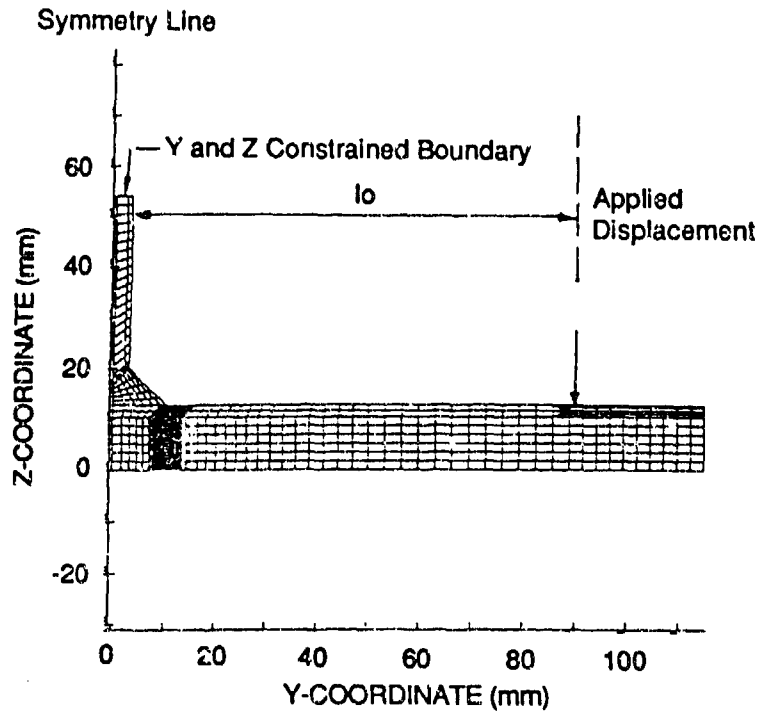
(a) Complete mesh simulating half the specimen
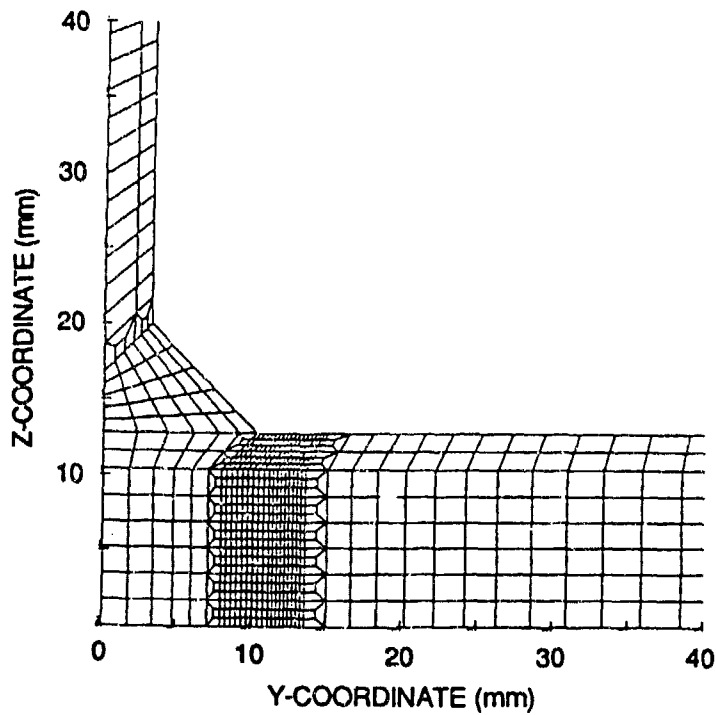
(b) Detail of the weld region

RA-2612-129

Figure D-17. Finite element mesh used for the
investigation of geometric softening
induced by large deformations.

$l < l_0$
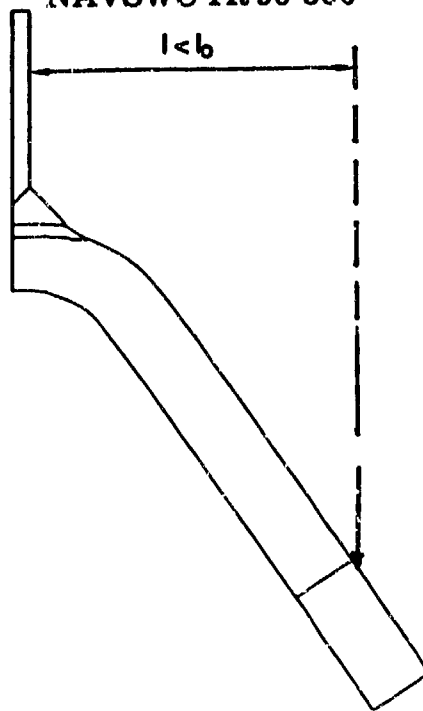
(c) Displacement application point
attached to the plate, condition 1

$l = l_0$
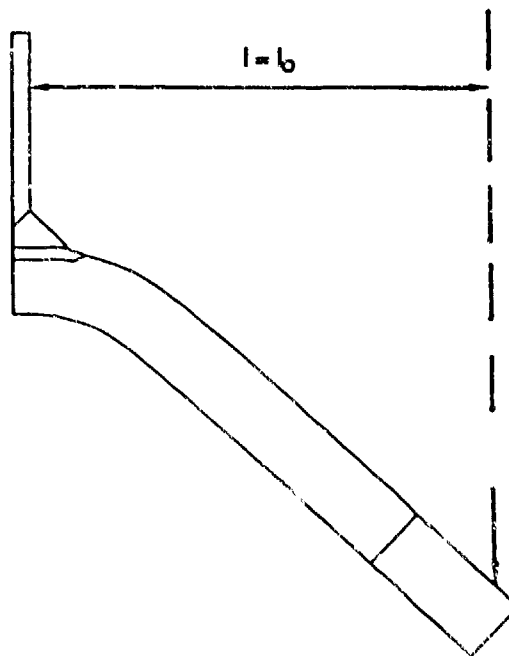
(d) Displacement application point
sliding along the plate, condition 2

RA-2612-147

Figure D-17.   Finite element mesh used for the
Investigation of geometric softening
Induced by large deformations. (concluded)

displacement application point moved transversely as the plate deflected (condition 2, Figure D-17d). The latter situation corresponded to the loading in the experiments. In this calculation we accomplished the second type of boundary condition by introducing a slide line between the displacement application point and the plate. We assumed no friction along the slide line.

Curves for normalized load as a function of normalized deflection for the two conditions are shown in Figure D-18. Both curves show the onset of material yielding near the weld at a deflection of about 0.4. Up to that point the two cases agree closely. However, for deflections greater than 0.5 the two curves differ. Without geometric softening, the load continually increases as the deflection increases. In this case the change in geometry is apparently contributing to the specimen hardening, along with the material constitutive hardening. At a displacement of 1.0 the load is about 1.5, and it gradually increases to 2.0 at a displacement of 4.

In the case with geometric softening, the load reaches a peak of about 1.55 at a displacement of 1.5. Beyond this displacement, the load continually decreases. At a displacement of 4 the load has dropped to about 1.25. The normalized load deflection curves for the two displacement boundary conditions are also compared with the experimental curve for 1/4-scale experiment HY-130 WSTB4-2 in Figure D-18. The curve for condition 2 (geometric softening) agrees very well with the experimental curve. From the comparison, we conclude that much of the specimen softening observed in the experiments can be attributed to geometric effects caused by large deformations.

Discussion and Conclusions. The finite element simulations confirm that, as anticipated on the basis of the experimental observations, the most severe straining of the weldment--and, for that matter, the specimen--occurs at the toe of the weld metal bead in the HAZ. Both the equivalent plastic strain and the stress triaxiality are maximum at that location.

The parametric study, in which we varied the weldment geometry and the strength gradients across the weldment, revealed that variations in these parameters, consistent with the results of the weldment characterization task (see Appendix A) can cause significant differences of 25 percent or more in the specimen displacement at fracture initiation (d_{PH}). This finding provides a possible explanation for the large variations in d_{PH} observed, particularly in the 1/8-scale experiments. Indeed, the weld characterization study revealed the strongest strength gradients in the 1/8-scale specimens. Moreover, because the HAZ is proportionally larger in those specimens than in specimens of the other scales, the fracture behavior of the 1/8-scale weldments will also be more sensitive to geometric variations in the HAZ.

RA-2612-130
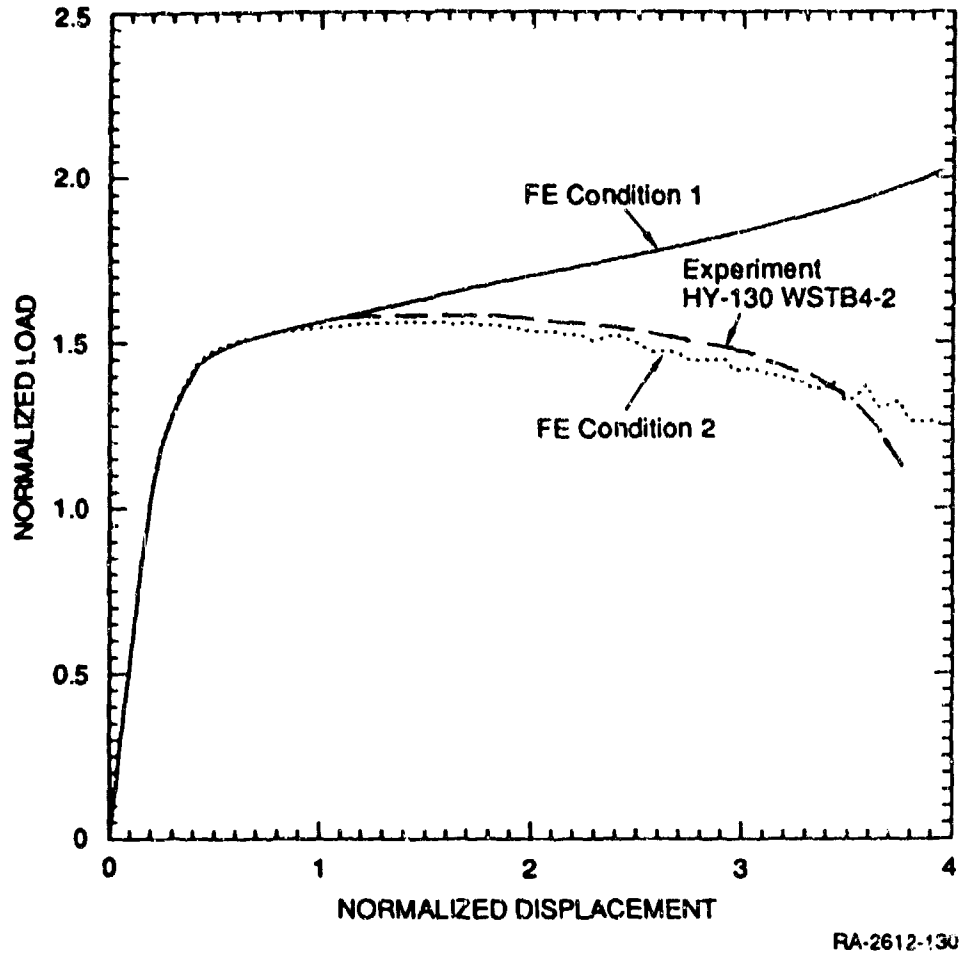
Figure D-18. Comparison of the normalized load-deflection curves for the
finite element simulations with conditions 1 and 2 and with
results of experiment HY-130 WSTB4-2.

From Figures D-12 and D-13, we also conclude that changes in the fracture resistance of the HAZ, as modeled by a shift in the failure envelope $\varepsilon_c(\sigma_{mean}/\sigma_{eq})$, may have an effect similar in magnitude to changes in the weldment geometry and strength gradients.

From a structural viewpoint, a simple static analysis, confirmed by finite element simulations, shows the softening effect caused by large deformations. This geometric softening dominates most of the deformation of the HY-130 steel static fracture specimens and should not be confused with softening introduced by macrocrack nucleation, which occurs only in the last phase of the experiment.

A final remark concerns the comparison of the normalized load-deflection curves obtained from the experiments and from the finite element simulation with the displacement boundary condition 2 (Figure D-18). The good agreement between the two curves demonstrates that although significant transverse strains were measured at the top mid-section of the specimen plate during the experiments (see Appendix B), the fully plastic load for the specimen is predicted correctly assuming plane strain conditions. Therefore, a plane strain assumption is adequate, at least for predicting the specimen's structural response.

Finite Element Simulation of Static Fracture Experiments With Local Fracture Model

Objectives. We performed several preliminary simulations of the 1/4-scale static fracture experiments that included the local ductile fracture model. The general objectives of such simulations have already been discussed in the Introduction to this appendix. The specific objectives of the simulations were to demonstrate the model's capabilities and to investigate how its various parameters affect the simulation of weldment fracture. Here we present the results of only one preliminary simulation to illustrate the model's current capabilities and to point out further developments still needed.

Finite Element Model. We simulated a 1/4-scale welded specimen by introducing the appropriate HAZ-thickness-to-plate-thickness ratio ($t_{HAZ} = 2.4$ mm/H = 12.7 mm). The finite element mesh used for these simulations was the same as that used for investigating geometric softening and is illustrated in Figure D-17. For simplicity in the preliminary simulations, we assumed symmetry along the stiffener axis. In the actual experiments, symmetry is no longer preserved once a crack develops on one side of the stiffener.

We used a 0.4-mm mesh size in the region of anticipated crack extension. The finite element simulation included the support roller and a slide line to account for geometric softening. We applied the same flow curve (labeled "Base Metal 1" in Figure D-5) to all three regions of the weldment and used the HAZ failure curve of Figure D-2 for the HAZ and the HY-130 steel LT

failure curve for the BM region. Once the damage D reached 1, we reduced the material strength and the pressure by multiplying them by the damage factor d given by Equation (D-7), with the coefficient "a" equal to 2.

Simulation Results and Comparison with Experiment. The results of the simulation with the local fracture model are presented in Figures D-19 through D-21. Figure D-19 shows isodamage contours in the weldment region at four levels of applied displacement. Regions within contours with $D \geq 1$ represent regions that fractured. A crack developed at the toe of the weld bead and gradually propagated through the heat-affected zone and into the base metal. This evolution of damage is similar to the fractographic observations of the static fracture specimens (see Figure B-15 in Appendix B). However, the details of the crack path in the simulation are somewhat different from those in the experiment.

Figure D-20 presents calculated contours of effective stress and pressure in the cracked region of the weldment for a normalized displacement of 4. This figure illustrates how deviatoric and mean stresses are relaxed by developing damage in the weldment and fall to zero in the cracked region. Figure D-21 compares the calculated and measured load-displacement curves. The results of the simulation show good qualitative agreement with the experiment. The model seems to predict the beginning of a crack in the heat-affected zone somewhat too early and then to overpredict the fracture resistance of the base metal. The normalized displacement value at which the crack reaches the HAZ/BM interface corresponds well with the value of d_{PH}, which we regard as an indicator of the onset of the first macrocrack.

Discussion and Conclusions. The finite element simulation, including the local fracture model, of a 1/4-scale static fracture experiment demonstrates that the weldment fracture model is capable of simulating the formation of a crack in the HAZ and extending it into the base plate. However, we observed differences between the model predictions and the experimental results with respect to the crack path and to the displacements at which cracking begins and the load starts dropping significantly.

The differences between simulation and experiment are due to several probable factors:

(1) Although we coarsely simulated the differences in fracture properties among the various weldment regions, we did not simulate the strength gradients.

(2) The experimental failure envelope for HY-130 steel does not cover triaxiality ratio greater than 1.2 (see Figure A-6 in Appendix A), and we had to extrapolate to higher values to predict damage ahead of the sharp crack.

(a) d_{NORM} = 2

(b) d_{NORM} = 3

(c) d_{NORM} = 4

(d) d_{NORM} = 5
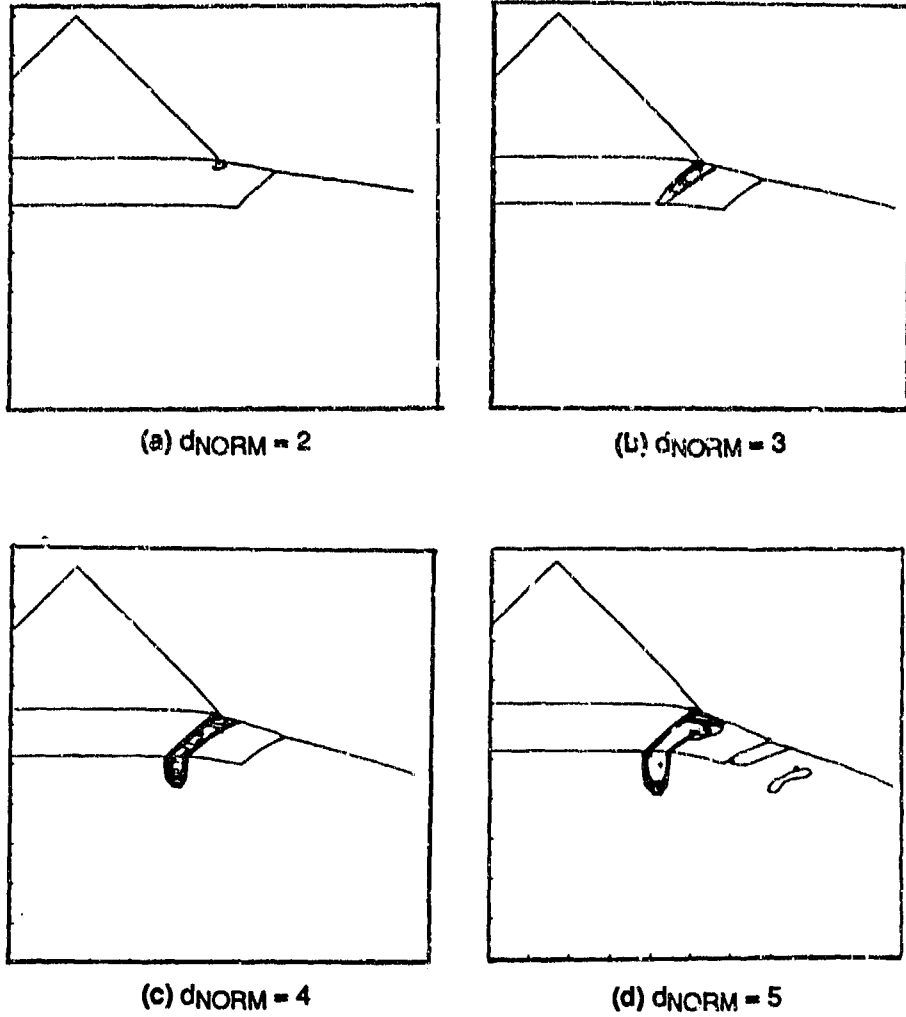
RA-2612-131

Figure D-19.   Contours of damage in a simulated 1/4-scale static fracture
experiment, showing a crack extending through HAZ and into
the specimen plate

(a) Effective stress
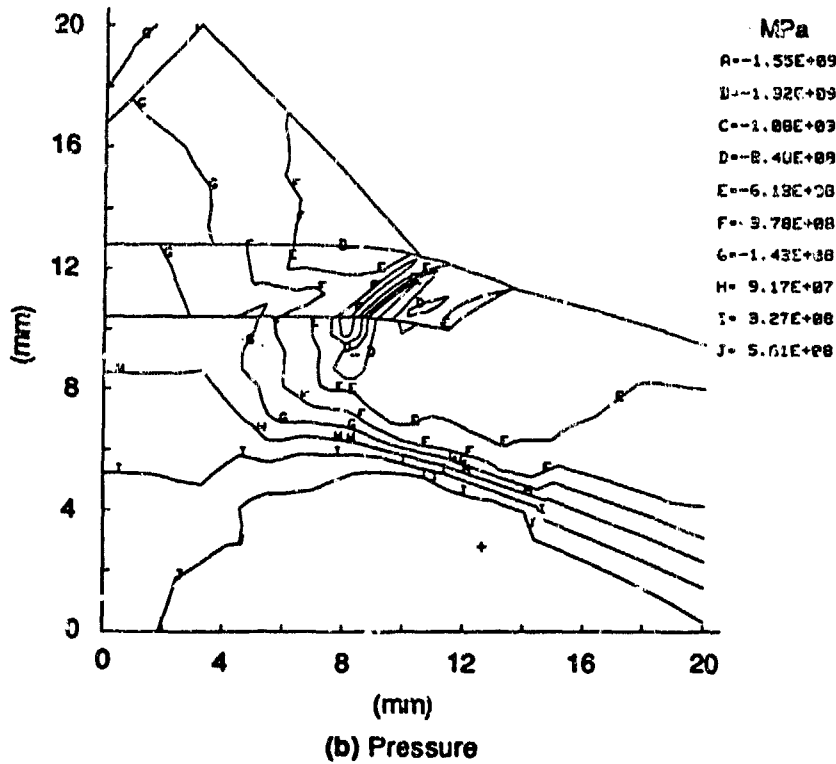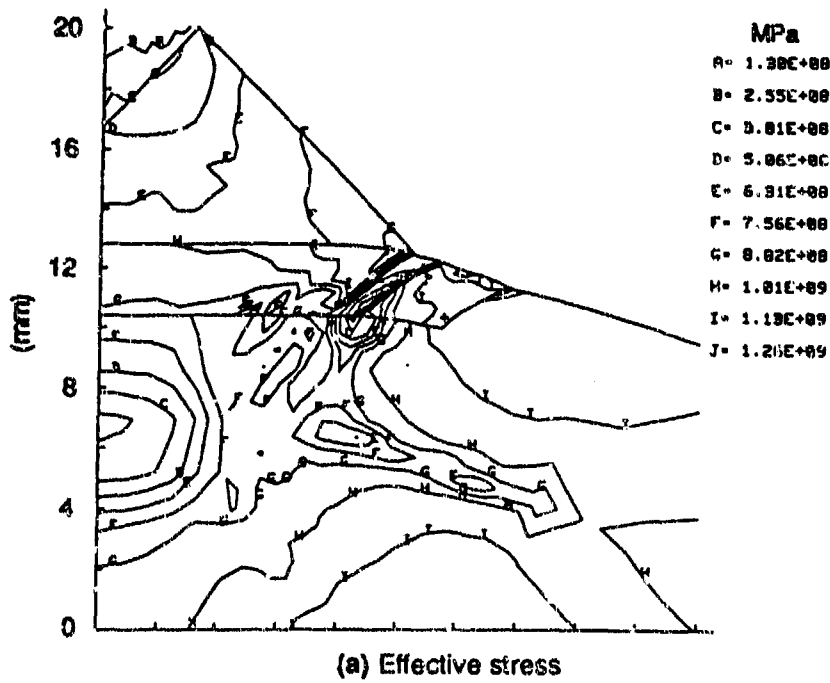
(b) Pressure

RA-2612-132

Figure D-20. Contours of effective stress and pressure in the damage region of the static fracture specimen at a normalized displacement d$_{NORM}$ = 4.
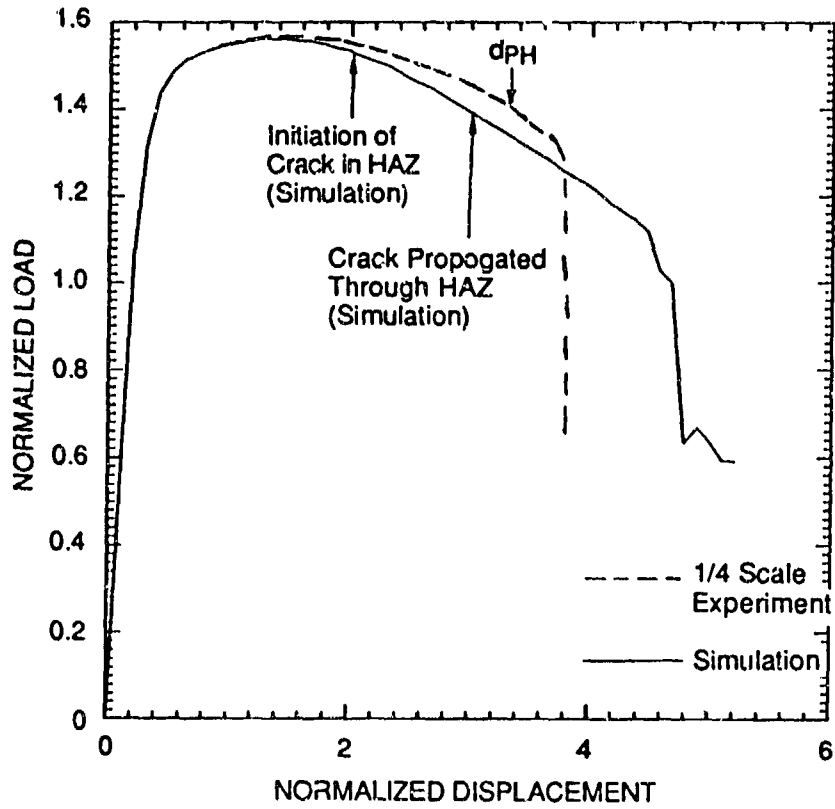
Figure D-21. Comparison of load-deflection curve for experiment HY-130 WE4-2 with calculated curve from finite element simulation with local fracture model.

(3) We used a finite element mesh that was still rather coarse (0.4 mm) and did not reflect the desired characteristic microstructural size of about 0.2 mm. The crack path in the simulation showed the influence of the mesh, because it clearly followed the mesh layout.

(4) Finally, the simulation assumed specimen symmetry along the stiffener axis during the entire fracture process, whereas in the experiment, cracking eliminated symmetry. The difference in symmetry conditions certainly strongly affected the crack propagation phase in the fracture experiment and in the simulation.

If we keep these factors in mind, we believe the fracture simulation results presented here demonstrate the capability of the weldment fracture model developed in this program. The model appears to capture the correct physics of the weldment fracture with only a few adjustable parameters, and we are confident that it will meet its objective. Clearly, more work is desirable before we use the weldment fracture model to evaluate scaling effects or to make fracture predictions. More detailed modeling of the strength distribution in the weldment should be introduced, along with a better definition of the fracture properties for each weldment region. More experimental data for triaxiality ratios greater than 1.2 are needed to model fracture realistically at the tip of a sharp crack. Finally, a finer mesh will help model the crack tip gradients more realistically and allow implementation of a non-scaling microstructural dimension.

Finite Element Simulation of Dynamic Fracture Experiments Without Local Fracture Model

Objectives. The finite element simulations of the dynamic fracture experiments had several objectives:

(1) to demonstrate that the velocity data measured during the experiments provided enough input to model the experiments,

(2) to estimate the strains and strain rates in the weldment region for an initial velocity range comparable to that covered by the experiments,

(3) to compare the dynamic with the static data to determine whether modifications to the local fracture model were necessary for dynamic loading,

(4) to evaluate the specimen response and calculate the elastic components of the maximum center plate deflections for use with the improved experimental data reduction procedure (see Appendix C).

Finite Element Model. The simulations of the dynamic fracture experiments were performed with the DYNA2D two-dimensional finite element code[D-2] using a plane strain formulation and quadrilateral, isoparametric elements. Because of symmetry, we modeled only half the specimen; the undeformed mesh is shown in Figure D-22a. To simulate the specimen's

attachment method in the experiments, we constrained the vertical and horizontal motions of the regions of the plate and the stiffener indicated in Figure D-22a.

To simulate the effect of the sheet explosive, we imposed the initial velocity profile shown in Figure D-22b on the center of the specimen plate. Here we assumed that upon detonation of the explosive, the measured plate center velocity was simultaneously imposed on the plate length covered by the explosive. That assumption was not strictly true, because it takes about 7 μs for the detonation to propagate from the starting line (center line of the specimen) to the opposite edge of the sheet explosive. Moreover, the initial velocity is not reached instantaneously but over a period of about 20-30 μs. However, because detonation and acceleration times are relatively short compared with the total duration of the experiment, the assumption appeared legitimate, in first approximation. The triangular velocity distribution in the plate region closest to the stiffener tries to simulate the effects of the sheet explosive edges, where the detonation pressure is immediately relieved and the impulse imparted to the plate at that location is reduced.

The literature survey presented in Appendix A indicates that the flow properties of HY-130 steel are not rate-sensitive at strain rates up to 10^3 s^{-1}. Therefore, for the simulation of the dynamic experiments, we used the static flow curves for HY-130 steel. We assigned to the base metal and the HAZ the static stress-strain curve labeled Base Metal 1 in Figure D-5 and to the weld metal the curve labeled Weld Metal.

Simulation Results and Comparison with Experiments. The calculated plate center deflection histories from the finite element simulations are shown in Figure D-23. As in the experiments, a second-order polynomial fits the deflection histories well. Table D-1 compares the calculated maximum deflections with the experimentally measured ones and shows that the finite element simulation tends to overestimate the measured deflections by up to 18 percent. The overestimate is larger for the two lower initial velocities.

The calculations also tend to underestimate the time at which the maximum deflection is reached (see Figure C-9 in Appendix C, and Figure D-23). The elastic component of the deflection that we used to correct the final deflections in the improved experimental data analysis procedure in Appendix C was obtained from the calculated final and maximum deflections.

Figure D-24 further compares the normalized displacement histories from the finite element analysis and the experiments. Here we used the normalization procedure described in Appendix C [Equations (C-1) through (C-3)]. The finite element results (Figure D-24a) follow the same trend as the experimental results (Figure D-24b). During the early part of the deflection histories, the data for all velocities fall on more or less on the same curve. Later, curves for different initial velocities fan out from one another, with the difference between curves decreasing with increasing

Y-COORDINATE (mm)

(a) Finite element mesh

(b) Initial velocity distribution
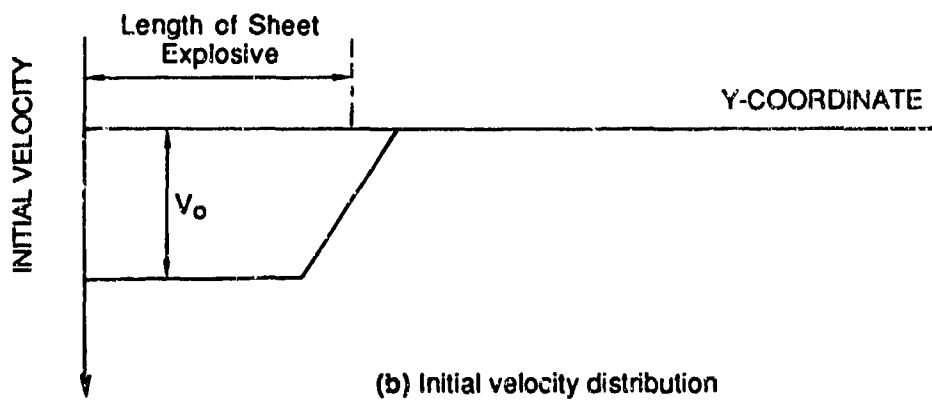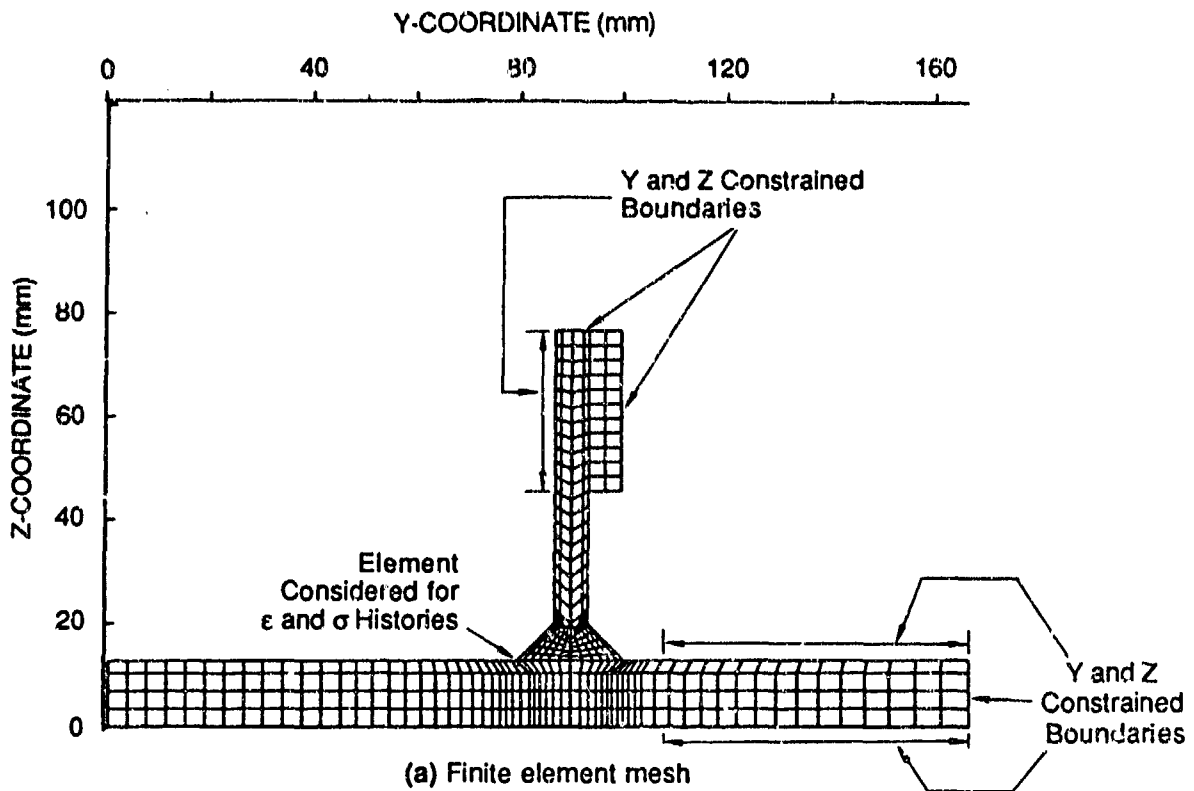
RA-2612-134

Figure D-22.   Finite element model of dynamic fracture experiment.
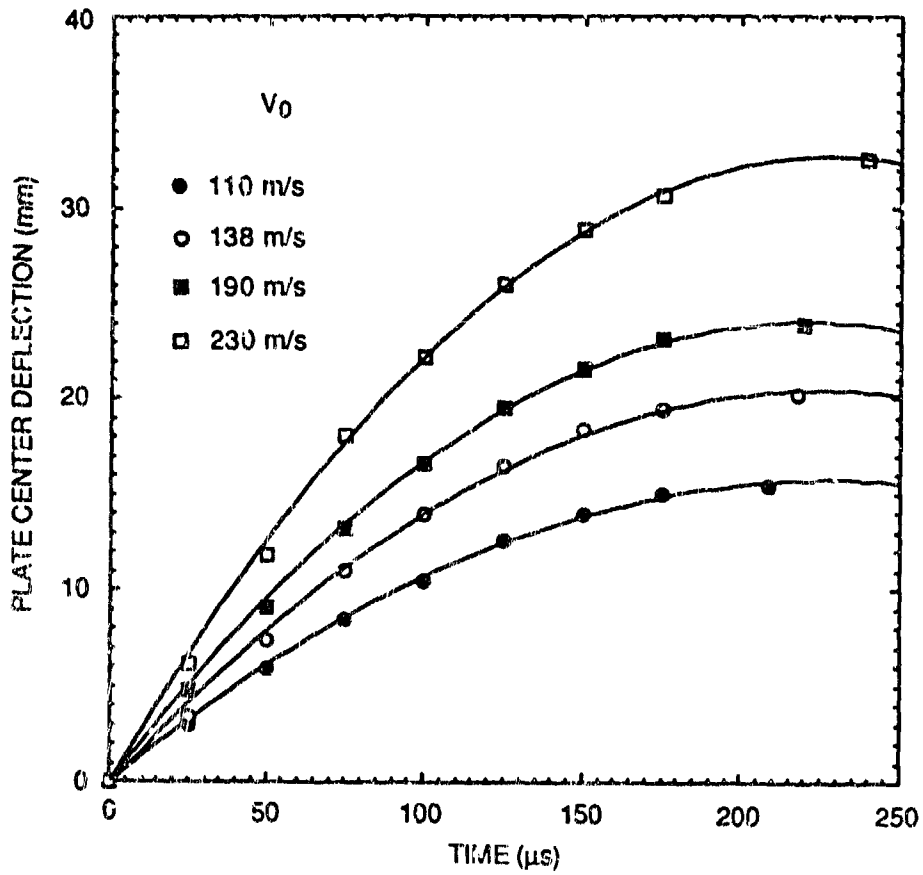
RA-2612-135

Figure D-23. Plate center deflection histories calculated in finite element
simulations of dynamic fracture experiments.

(a) FEM results

(b) Experimental data
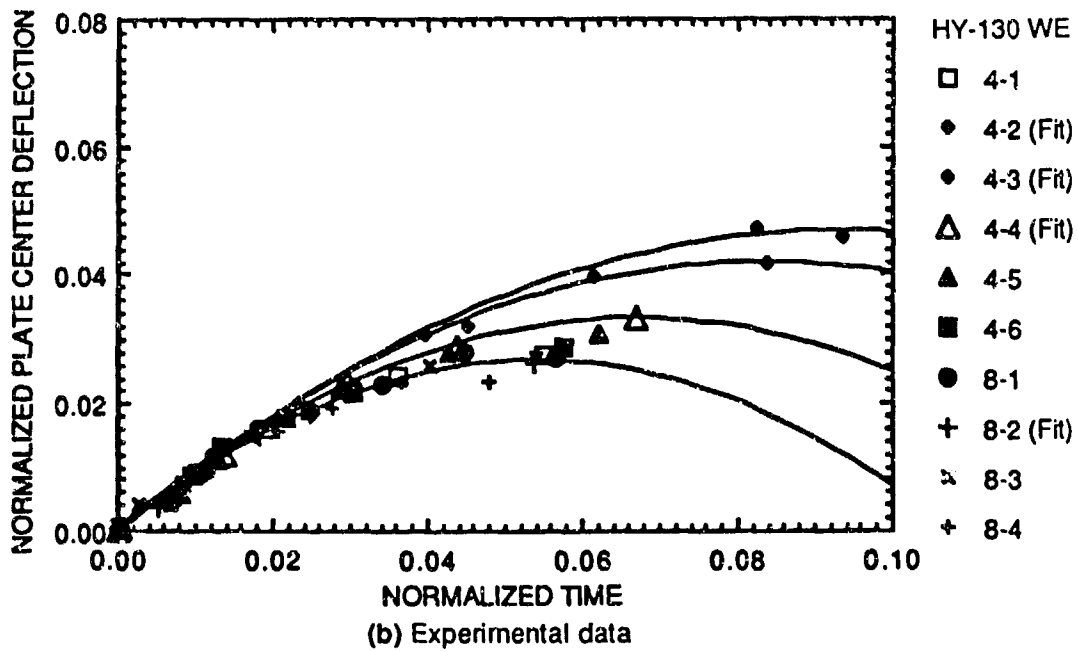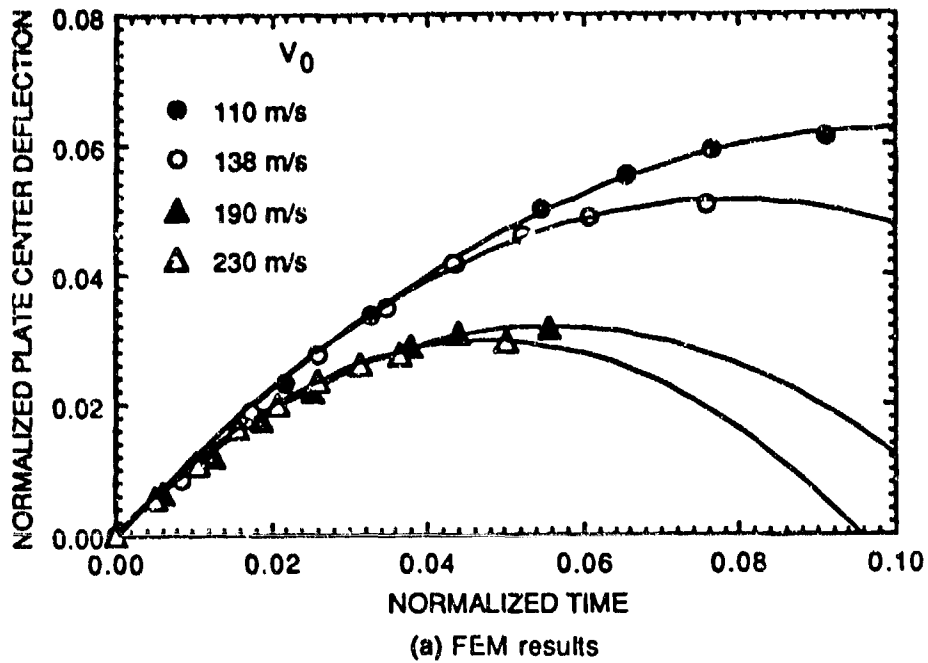
RA-2612-136

Figure D-24.   Comparison of calculated and experimental normalized plate
center deflection histories for dynamic fracture experiments.

initial velocities. This behavior is consistent with the experimental observations and indicates that different deformation modes control the deflection histories, as discussed in Appendix C.

The overall final deformed shape of the specimens measured after the experiments is compared with the calculated shape in Figure D-25. Although the plate underwent many oscillations around the final permanent shape after reaching the maximum deflection, the calculations were terminated before the ringing of the plate had stopped to limit the computational time. Therefore, the calculated and experimental shapes shown in Figure D-25 correspond to slightly different phases of the deformation histories. A measure of the differences is given in Table D-1, which lists the center plate deflections at the time corresponding to the calculated shape of Figure D-25 and compares them with the final calculated and measured plate center deflections.

Overall, the calculated and measured general shapes of the specimens agree well, except for the already mentioned differences in maximum deflections, indicated by Δ in the figure. However, they differ on some of the details of the deformed shapes. Curvatures are more pronounced in the calculations, and no deformation occurs beneath the stiffeners. Moreover, at the higher initial velocities, the calculations show a strain localization developing in the weldment region. A pronounced localization process is not observed in the experiments, probably because there is coupling between strain localization and fracture, with the former accelerating the occurrence of the latter.

The difference in deformation immediately under the stiffener demonstrates the effect of the boundary conditions. In the calculations, the tops of the stiffeners are constrained in the vertical and horizontal directions (Figure D-22); such boundary conditions are difficult to achieve experimentally, and the more compliant stiffener attachment in the experiments allows larger deflections underneath the stiffeners than in the calculations. The observed differences in curvature may be due partly to the differences in the times at which the calculated and experimental shapes are compared (in the calculation the plate is still moving) or to differences in the initial velocity distributions in the simulations and the experiments.

Table D-2 gives a summary of the stress and strain conditions in the weldment region at the location indicated in Figure D-22. Although a more detailed analysis of the data is needed, the results in Table D-2 indicate that the degree of triaxiality in the dynamic fracture experiments is comparable to that in the static experiments. Strain rates in the weldment region increase with increasing initial velocity. Figure D-26 shows typical strain rate histories for initial velocities of 110 m/s and 190 m/s, respectively. Strain rates reach maximum values ranging from about 1800 to 5000 s^{-1} and average values (averaged for one element over the time required to reach the specimen maximum deflection) ranging from 1800 to 2800 s^{-1}.
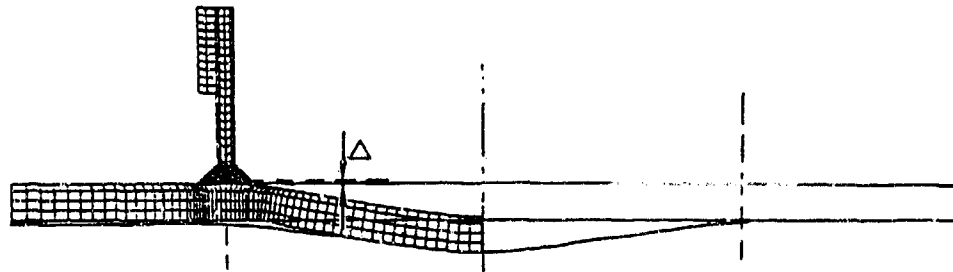
(a) Specimen HY-130 WE4-2, $V_0 \approx 110$ m/s
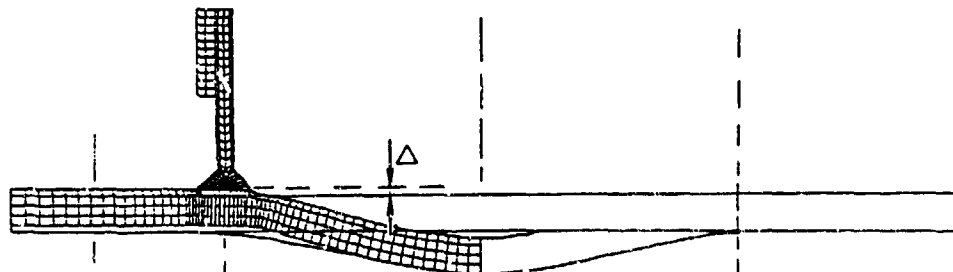
(b) Specimen HY-130 WE4-3, $V_0 \approx 138$ m/s
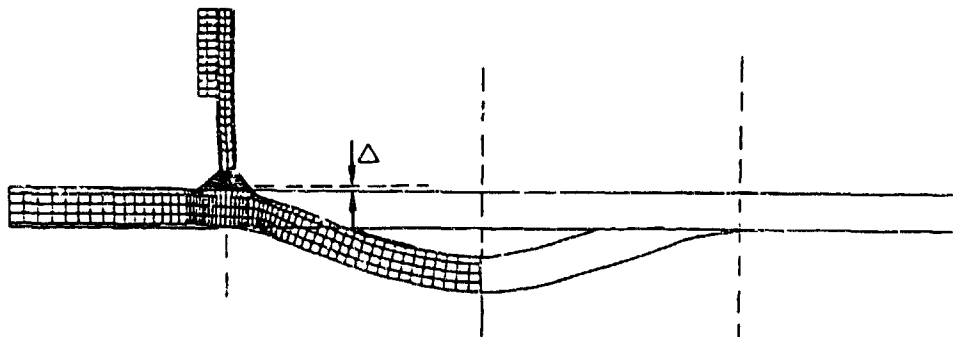
(c) Specimen HY-130 WE4-4, $V_0 \approx 190$ m/s

RA-2612-137

Figure D-25.   Comparison of calculated and measured final specimen shapes.
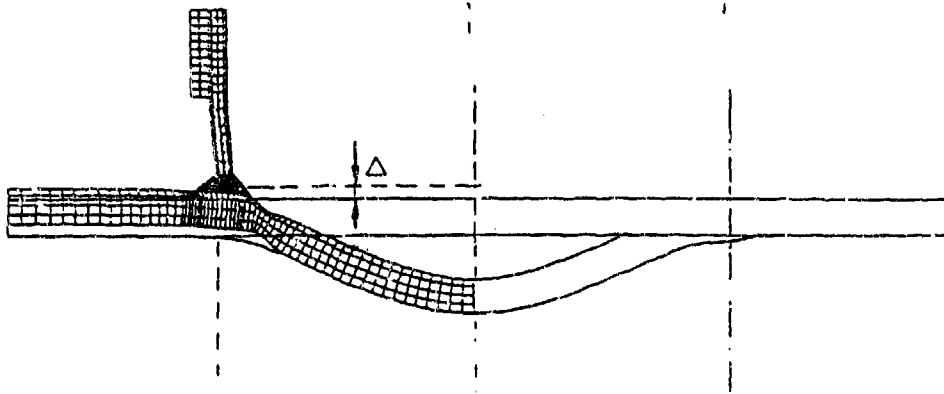
(d) Specimen HY-130 WE3-2, $V_0 \approx 230$ m/s
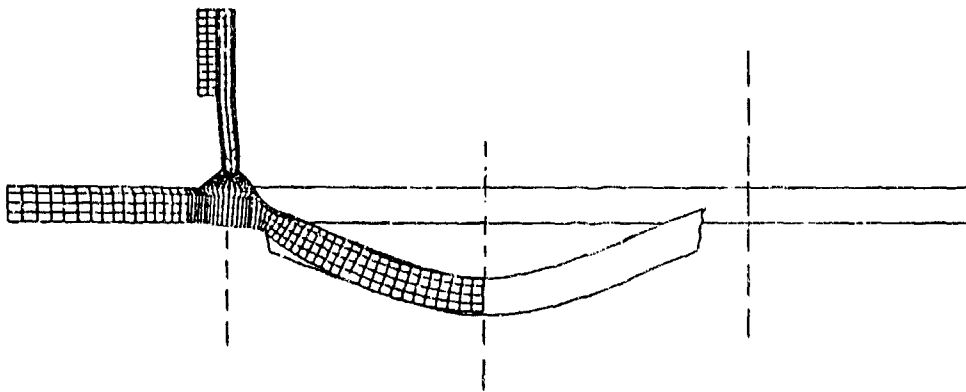
(e) Specimen HY-130 WE4-6, $V_0 \approx 230$ m/s, fractured

RA-2612-138

Figure D-25. Comparison of calculated and measured final specimen shapes (concluded).
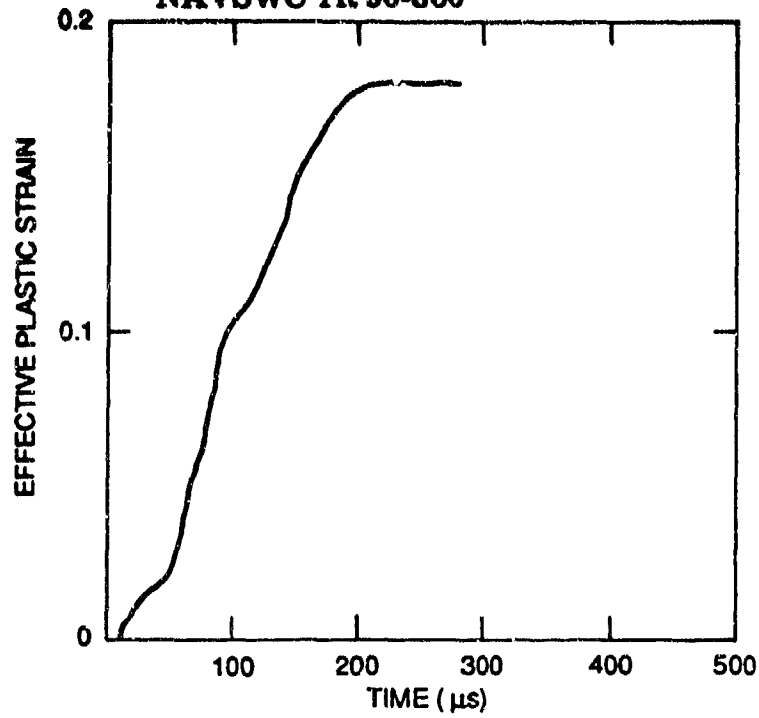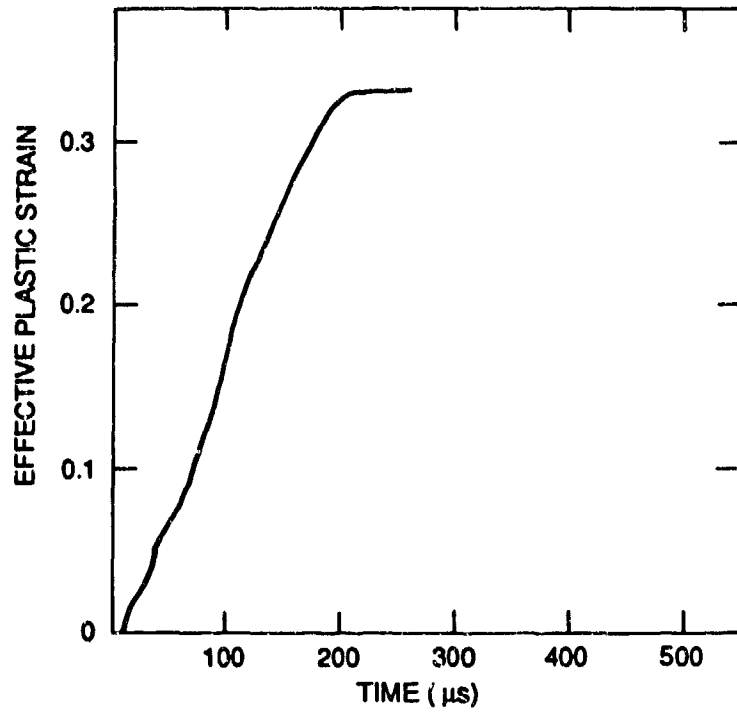
Figure D-26. Strain histories for base plate HAZ element immediately at the toe of the weld bead.
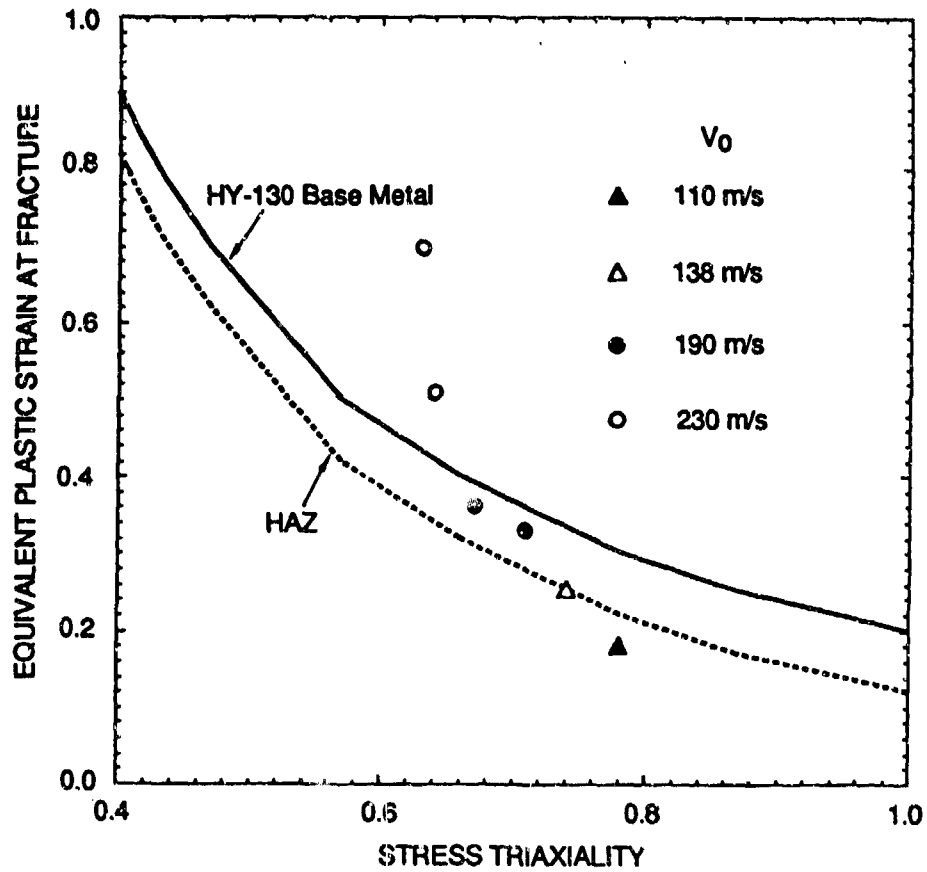
RA-2612-140

Figure D-27. Comparison of calculated maximum strains for base plate HAZ element immediately at the toe of the weld bead with the failure envelope for HY-130 steel.

TABLE D-1. COMPARISON OF CALCULATED AND EXPERIMENTAL MAXIMUM CENTER PLATE DEFLECTIONS

V_0 FE Simulation (m/s)	d_{max} FE Simulation (mm)	d_{final} FE Simulation (mm)	d_{FE} in Fig D-25 (mm)	V_0 Experiment (m/s)	d_{max} Experiment (mm)	d_{final} Experient (mm)	$[(d_{max})FE-(d_{max})exp]/(d_{max})FE$ (%)
110	15.4	12.6	11.1	-	-		
-	-	-	-	115	12.6	9.8	18
138	20.2	17.8	17.4	-	-		
-	-	-	-	142	17.6	15.2	13
190	23.8	21.7	22.9	-	-		
-	-			192	23.5	22.1	1
230	32.5	30.9	31.6	-	-		
-	-			235	30.4	28.4	7

TABLE D-2. STRESS, STRAIN, AND STRAIN RATES IN THE WELDMENT REGION IN DYNAMIC FRACTURE EXPERIMENTS

V_0 (M/S)	$\Sigma_{MEAN}/\Sigma_{EFF}$	$(E^P_{EFF})MAX$	$E_C(\Sigma_{MEAN}/\Sigma_{EFF})$, FROM FIGURE D-2	$(E^P_{EFF})AV$ (S⁻¹)	$(E^P_{EFF})MAX$ (S⁻¹)
110	0.78	0.18	0.22	1100	1800
138	0.74	0.255	0.26	1500	1900
190	0.71	0.33	0.27	1900	2800
	0.67[A]	0.36[A]	0.31[A]		
230	0.64	0.51	0.34	2800	3900
	0.63[A]	0.7[A]	0.28[A]		5000[A]

[A]VALUES FOR PLATE SURFACE HAZ-ELEMENT ADJACENT TO HAZ-BM INTERFACE.

The maximum strain reached in the weldment region also increases with initial velocity. The maximum strains achieved in the HAZ at the top surface of the plate and the failure strains from Figure D-2 are compared in Table D-2 and Figure D-27. For V_0 equal to 110 m/s, the maximum strain is well below the failure strain; for V_0 equal to 138 m/s, the maximum strain is comparable to the failure strain; for V_0 equal to 190 m/s, the maximum strain is about 20 percent higher than the failure strain; and for V_0 equal to 230 m/s, the maximum strain can be more than twice the failure strain.

The maximum strain data are consistent with the experimental observations that show fracture initiation for V_0 between 140 and 190 m/s and complete fracture for V_0 between 190 and 230 m/s; they are also consistent with the fracture strain estimated in the static fracture experiments.

Discussion and Conclusions. The analysis of the dynamic fracture experiments is not complete. We expect to gain more insight into the specimen's structural response by looking at strain histories at various locations along the plate to determine the formation and propagation of plastic hinges. Nevertheless, the current analysis demonstrates that the simulation method gives a good approximation of the actual specimen behavior and that the measurement of the plate center velocity history provides adequate experimental input for the simulations.

Improvements in the model predictions, especially concerning the overall deformed shape of the specimen, can be achieved by adjusting the boundary conditions to reflect the plate and stiffener clamping conditions. This step, an easy modification of the current finite element model, will involve introducing elements with adjustable stiffness at the boundary locations where plate and stiffeners are clamped.

The stress-and-strain fields obtained with the simulations indicate that in spite of the difference in loading mode and strain rate (on the order of several thousands per second in the dynamic experiments), fracture in the dynamic experiments occurs at strain and triaxiality level consistent with those in the static experiments, suggesting that the strain-based ductile fracture criterion applied in one type of experiment may also be applicable in the other. More work will be needed to confirm this conclusion.

ELASTOPLASTIC FRACTURE MECHANICS CALCULATIONS

Introduction

In the static as well as the dynamic fracture experiments, we did not monitor the crack extension behavior in detail. Therefore, we cannot quantify possible non-replica scaling effects associated with crack extension in specimens of different scales, using experimental data alone. To provide at least a rough estimate of the magnitude of the nonscaling effects that can be anticipated during crack extension, we performed an elastoplastic fracture analysis of crack growth in HY-130 steel three-point-bend specimens of different sizes.

Elastoplastic Fracture Mechanics (EPFM) Model and Limitations

In this analysis we applied the J-integral-based engineering EPFM methodology developed by Kumar, et al. under contract from the Electric Power Research Institute.[D-16] In this approach, the crack-driving force is expressed in terms of Rice's path-independent J-integral,[D-17] and the material fracture resistance is expressed in terms of the associated J-resistance curve, which is measured in laboratory experiments on small specimens (see Figure A-8 in Appendix A for the J-resistance curve of HY-130 steel). In the engineering EPFM methodology, the applied J resulting from the loading on the structure is estimated by combining linear elastic solutions and fully plastic deformation plasticity solutions.

To estimate the difference in crack growth behavior with weldment scale during static fracture experiments, we simulated elastoplastic crack growth in three HY-130 steel three-point-bend bars, each with the same initial ratio of crack length over specimen width of 0.5. The geometry of the bend bars corresponds to the standard ASTM E813 specimen.[D-18] The three bars were 6.35, 12.7, and 25.4 mm wide, corresponding to the 1/8-, 1/4-, and 1/2-scale experiments respectively. The stress-strain curve in Figure A-11 and the J-resistance curve in Figure A-8 were used as material models for HY-130 steel in the simulation.

Obviously, modeling weldment fracture with that of three-point-bend bars is a very crude approach, because their geometry and loading are different. Moreover, in the weldment fracture, the initial crack nucleated in the HAZ propagates into material that has already undergone extensive plastic deformation, whereas in the three-point-bend bar simulation, the crack grows into material with only limited plastic deformation. Despite these strong limitations, elastoplastic fracture calculations can provide an order of magnitude estimate of scaling effects during crack growth in HY-130 steel

Results of EPFM Simulations

The results of the EPFM simulation are presented in Figure D-28, which plots the normalized load deflection and crack extension for the three bend specimens. The load was normalized by the parameter

$$\alpha_{load} = \frac{S}{\sigma_Y \, B \, H^2} \tag{D-9}$$

where S, B, and H are the span between supports, the width, and the thickness of the corresponding weldment fracture specimen, respectively, and σ_Y is the yield strength. Here we chose to normalize with the weldment fracture specimen dimensions to facilitate discussion of the
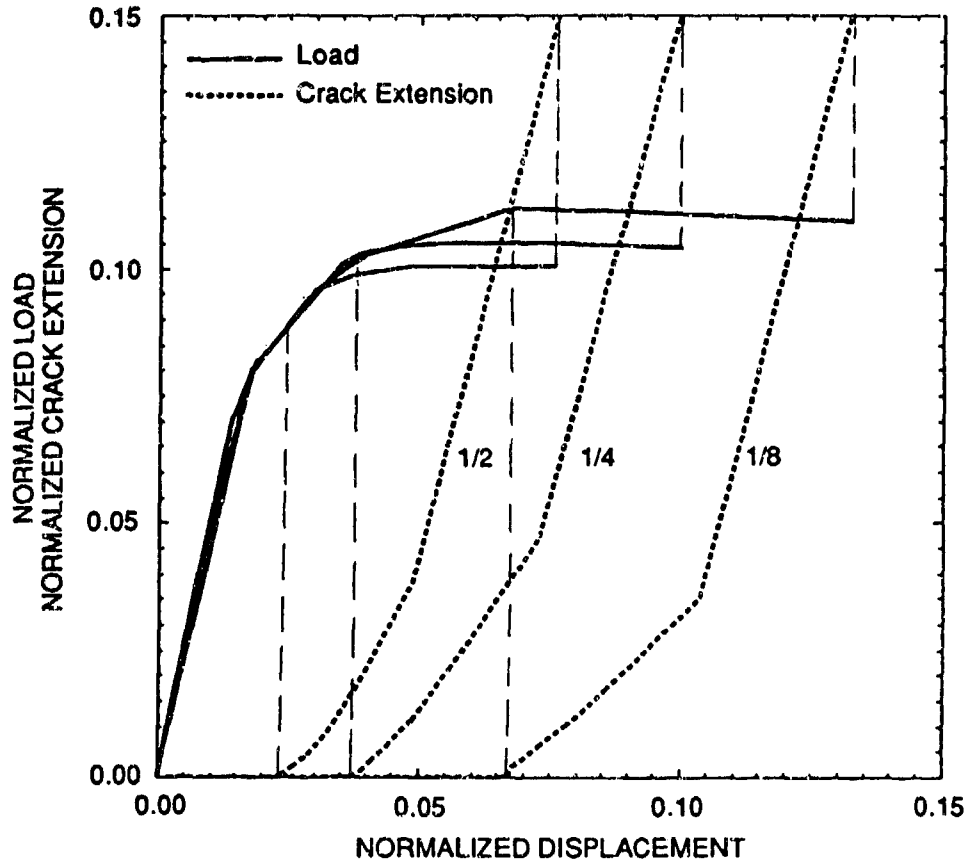
Figure D-28. Normalized results of EPFM analysis of three-point-bend specimens of different sizes.

RA-2612-141

results. This choice does not affect the results, because B and H are the same for the three-point-bend bar and the corresponding weldment specimen, whereas the ratio of the three-point-bend bar span to the weldment specimen span is 2/7. The displacement and the crack extension have been normalized by the specimen width H.

In Figure D-28, we indicated the points of crack initiation for each of the three specimen scales, as well as the points at which each specimen reached the same normalized crack growth increment of 0.15, for a total crack-depth-to-specimen-width ratio of 0.65. We evaluated the scaling effect during crack extension by comparing the increase in displacement and the energy needed to extend the crack by a normalized increment of 0.15. The results are shown in Table D-3.

An increase in scale by a factor of 4 induced differences in the displacement increments and energy dissipations of 17 and 33 percent, respectively.

TABLE D-3. ESTIMATE OF NON-GEOMETRIC SCALING EFFECT DURING 0.15 NORMALIZED CRACK GROWTH IN THREE-POINT-BEND BARS (INITIAL CRACK-DEPTH-TO-SPECIMEN-WIDTH RATIO 0.5, HY-130 STEEL)

	1/8-SCALE	1/4-SCALE	1/2-SCALE	MAXIMUM DIFFERENCE (%)
Normalized displacement Increment	0.062	0.058	0.053	17
Normalized energy dissipation	0.0069	0.006	0.0051	33

Next we compared the normalized displacement increments and energy dissipations to those at the beginning of a macrocrack in the static weldment fracture experiments (see Appendix B).* The comparison revealed that the displacement increment to grow the crack is on the order of only 10 percent of the total displacement at macrocrack initiation. Therefore, non-geometric scaling effects during crack growth induced differences in displacement amounting to only a few percentage points of the total. Similarly, the energy dissipation during crack growth is only a fraction of 1 percent of the total, and the differences introduced by non-geometric scaling effect would be even smaller.

---

*To account for the difference in span between the three-point-bend and the weldment fracture specimens, we multiplied the normalized displacements in Table D-3 by a factor of 3.5.

Discussion and Conclusion

We obtained very crude estimates of non-geometric scaling effects by performing an EPFM analysis of standard three-point-bend specimens. Comparing these estimates with the results of the weldment static fracture experiments indicated that differences in the displacement increments and energy dissipations during crack growth caused by nongeometric scaling amounted to only a few percentage points at most. In view of the great scatter in experimental data, it is doubtful that we could observe the slight differences induced by scaling effects. Therefore, we are justified in concluding in Appendix B that, in first approximation, there does not appear to be a non-geometric scaling effect in the crack growth phase of the weldment static fracture experiments.

CONCLUSIONS

Our modeling effort was aimed at providing a better understanding of the factors affecting the fracture behavior of weldments of different scales by faithfully simulating the structural and fracture response of the test specimens using finite element analysis and a local fracture model.

Although more work is still needed, the results presented here show that our analytical effort has met its objectives. We have demonstrated our ability to simulate faithfully the structural response of the specimens used in both static and dynamic fracture experiments. We have developed a weldment fracture model that incorporates the essential physical parameters governing ductile fracture of weldments and is capable of predicting initiation and growth of cracks in weldments of different sizes. Finite element simulations have provided quantitative information on the critical stress-and-strain conditions for fracture in the dynamic fracture experiments and on the effect on fracture of strength and geometric variations in the weldment region. Through analysis, we have also demonstrated that nonscaling effects during crack growth in HY-130 steel are negligible compared with the data scatter.

The models and analytical methods we have developed can now help to extrapolate the empirical scaling rules derived in the present program to larger, nonexperimentally investigated scales and to define simple fracture characterizing parameters for welded T-joints. With the correct material properties, these methods can easily be extended to analyzing weldment fractures in other alloys, such as the two titanium alloys under investigation in the second phase of the present project.

REFERENCES

D-1. Hallquist, J. O., "NIKE2D: A Vectorized, Implicit, Finite Deformation, Finite Element Code for Analyzing the Static and Dynamic Response of 2-D Solids," Lawrence Livermore Laboratory, UCID-19677, 1983.

D-2. Hallquist, J. O., "User's Manual For DYNA2D: An Explicit Two-Dimensional Hydrodynamic Finite Element Code with Interactive Rezoning," Lawrence Livermore Laboratory, UCID-18756, 1984.

D-3. Matic, P. and Jolles, M. I., "The Influence of Weld Metal Properties, Weld Geometry and Applied Load on Weld System Performance," NRL Memorandum Report 5987, Naval Research Laboratory, Washington, DC 20375-5000, 25 Feb 1988.

D-4. Conference Papers, "International Seminar on Local Approach of Fracture," Jun 3-5, 1986 (J. L. Chaboche et al., eds.), Electricité de France, 77250 Moret-Sur-Loing, France, 1986.

D-5. Curran, D. R.; Seaman, L.; and Shockey, D. A., "Dynamic Failure of Solids," *Physics Reports*, Vol. 147, 1987, pp. 253-388.

D-6. Lemaitre, J., "Local Approach of Fracture," *Engineering Fracture Mechanics*, Vol. 25, 1986, pp. 523-537.

D-7. Mudry, F., "Methodology and Applications of Local Criteria for Prediction of Ductile Tearing," *Elastic-Plastic Fracture Mechanics* (L. H. Larson, ed.), ECSC, EEC, EAEC, Brussels and Luxembourg, Belgium, 1985) pp. 263-283.

D-8. McClintock, F. A., "A Criterion for Ductile Fracture by the Growth of Holes," *Journal of Applied Mechanics*, Vol. 35, 1968, pp. 363-371.

D-9. Rice, J. R. and Tracey, D. M., "On the Ductile Enlargement of Voids in Triaxial Stress Fields," *Journal of the Mechanics and Physics of Solids*, Vol. 17, 1969, pp. 201-217.

D-10. MacKenzie, A. C.; Hancock, J. W.; and Brown, D. K., "On the Influence of State of Stress on Ductile Failure Initiation in High-Strength Steels," *Engineering Fracture Mechanics*, Vol. 9, 1977, pp. 167-188.

D-11. Norris, D. M.; Reaugh, J. E.; Moran, B.; and Quiñones, D. F., "A Plastic-Strain, Mean-Stress Criterion for Ductile Fracture," *Journal of Engineering Material and Technology*, Vol. 100, 1978, pp. 279-286.

D-12. Ritchie, R. O.; Server, W. L.; and Wulleart, R. A., "Critical Fracture Stress and Fracture Strain Models for Prediction of Lower and Upper Shelf Toughness in Nuclear Pressure Vessel Steels," *Metallurgical Transaction A*, Vol. 10A, 1979, pp. 1557-1570.

REFERENCES (Cont.)

D-13. Beremin, F. M., "Study of Fracture Criteria for Ductile Rupture of A508 Steel," in: *Advances in Fracture Research (ICF5)* , (D. François, ed.), Pergamon Press, 1981, pp. 809-816.

D-14. Giovanola, J. H., "The Scaling of Fracture Phenomena," Poulter Laboratory Special Technical Report 001-82, SRI International, Menlo Park, CA 94025, 1982.

D-15. Gurson, A. L., "Continuum Theory of Ductile Rupture by Void Nucleation and Growth Part I: Yield Criteria and Flow Rules for Porous Ductile Materials," *Journal of Engineering Materials and Technology*, Vol. 2, 1977, pp. 2-15.

D-16. Kumar, V.; German, M. D.; and Shih, C. F., "An Engineering Approach for Elastic-Plastic Fracture Analysis," General Electric Company Topical Report to Electric Power Research Institute, Research Project 1237-1, Schenectady, NY, Jul 1981.

D-17. Rice, J. R., "A Path-Independent Integral and the Approximate Analysis of Strain Concentration by Notches and Cracks," *Journal of Applied Mechanics*, Vol. 35, 1968, pp. 379-386.

D-18. ASTM Standard E 813-87, "Standard Test Method for J_{Ic}, a Measure of Fracture Toughness," *ASTM Annual Book of Standard*, Vol. 03.01, American Society for Testing and Materials, Philadelphia, 1987.

DISTRIBUTION

DOD ACTIVITIES (CONUS):	COPIES		COPIES
		SEA-03P4 (A. MANUEL)	1
		PEO-SUB-R (D. DOZIER)	1
DTIC		PEO-SUB-X	1
CAMERON STATION		PMO-350	1
ALEXANDRIA, VA 22304-6145	12	PMO-350T (C. SIEL)	1
		PMO-402 (M. ALPERI)	1
ATTN: ONR-00R (A. J. FAULSTICH)	1	PMO-406 (G. DANIELO)	1
ONR-332 (A. VASUDEVAN)	1	PMO-407 (W. HINCKLEY)	1
ONR-333 (K. LATT)	1	COMMANDER	
ONR-333 (D. HOUSER)	1	NAVAL SEA SYSTEMS COMMAND	
ONR-334 (R. BARSOUM)	1	WASHINGTON, DC 20362-5105	
ONR-334 (G. MAIN)	1		
ONR-334 (R. VOGELSONG)	1	ATTN: TECHNICAL LIBRARY	1
ONR-334 (Y. RAJAPAKSE)	1	6380 (R. BADALIANCE)	1
ONR-334 (G. REMMERS)	1	6380 (T. CHWASTYK)	1
OFFICE OF NAVAL RESEARCH		6380 (P. MATIC)	1
800 N. QUINCY STREET, BCT		COMMANDING OFFICER	
ARLINGTON, VA 22217-5000		NAVAL RESEARCH LABORATORY	
		WASHINGTON, DC 20375	
ATTN: G. KOPCSAK	1		
OUSDRE/TWP-OM		ATTN: TECHNICAL LIBRARY	1
THE PENTAGON		COMMANDING OFFICER	
WASHINGTON, DC 20301		COASTAL SYSTEMS STATION	
		DAHLGREN DIVISION	
ATTN: J. BLOOM	1	NAVAL SURFACE WARFARE CENTER	
OUSDRE/T&E LFTO		PANAMA CITY, FL 32407-5000	
THE PENTAGON			
WASHINGTON, DC 20301		ATTN: TECHNICAL LIBRARY	1
		CODE 65.4 (A. WIGGS)	1
ATTN: R. MENZ	1	CODE 65.4 (N. GIFFORD)	1
USD(A)/DDRE (R/AT/ET)		CODE 65.4 (J. DALLY)	1
STAFF SPECIALIST FOR WEAPONS		CODE 65.4 (J. CARLBERG)	1
TECHNOLOGY		CODE 65.4 (E. RASMUSSEN)	1
THE PENTAGON		CODE 67 (J. W. SYKES)	1
WASHINGTON, DC 20301		CODE 67.1 (C. MILLIGAN)	1
		CODE 67.1 (B. WHANG)	1
ATTN: SEA-03P (A. MALAKHOFF)	1	CODE 67.1 (S. ZILLIACUS)	1
SEA-03P1 (T. W. PACKARD)	1	CODE 67.2 (P. DUDT)	1
SEA-03P2 (R. MCCARTHY)	1	CODE 67.2 (G. WALDO)	1
SEA-03P22 (W. WILL)	1	COMMANDER	
SEA-03P3 (J. SCHELL)	1	CARDEROCK DIVISION	
SEA-03P31 (J. TRAYLOR)	1	NAVAL SURFACE WARFARE CENTER	
SEA-03P3 (R. BOWSER)	1	BETHESDA, MD 20084-5000	
SEA-03P4 (D. NICHOLS)	1		

DISTRIBUTION (Cont.)

	COPIES		COPIES
ATTN: TECHNICAL LIBRARY	1	ATTN: TECHNICAL LIBRARY	1
CODE 69 (R. FUSS)	1	69SG (Y. SHIN)	
DIRECTOR		SUPERINTENDENT	
UNDERWATER EXPLOSIONS		NAVAL POSTGRADUATE SCHOOL	
RESEARCH OFFICE		MONTEREY, CA 93940	
CARDEROCK DIVISION			
NAVAL SURFACE WARFARE CENTER		ATTN: TECHNICAL LIBRARY	1
PORTSMOUTH, VA 23709		PRESIDENT	
		NAVAL WAR COLLEGE	
ATTN: CODE 614 (R. LINK)	1	NEWPORT, RI 02841	
CODE 614 (T. MONTEMARANO)	1		
CODE 615 (M. VASSILAROS)	1	ATTN: CODE 435B	1
OFFICER IN CHARGE		COMMANDER	
CARDEROCK DIVISION DETACHMENT		OPERATIONAL TEST AND EVALUATION	
NAVAL SURFACE WARFARE CENTER		FORCE	
ANNAPOLIS, MD 21402-5067		NORFOLK, VA 23511-6388	
COMMANDER		ATTN: TECHNICAL LIBRARY	1
NAVAL UNDERSEA WARFARE DIVISION		CODE SP (C. MCFARLAND)	1
KEYPORT, WA 98345-0580	1	CODE SPSD (K. GOERING)	1
		CODE SPSD (M. GILTRUD)	1
ATTN: N911	1	CODE SPSD (D. BRUDER)	1
CHIEF OF NAVAL OPERATIONS		DIRECTOR	
NAVY DEPARTMENT		DEFENSE NUCLEAR AGENCY	
WASHINGTON, DC 20350		WASHINGTON, DC 20305	
OASN/RE&S		ATTN: TECHNICAL LIBRARY	1
-SUBS/ASW	1	DIRECTOR	
NAVY DEPARTMENT		ADVANCED RESEARCH PROJECTS	
WASHINGTON, DC 2030	1	AGENCY	
		3701 NORTH FAIRFAX DRIVE	
ATTN: TECHNICAL LIBRARY	1	ARLINGTON, VA 22203-1714	
COMMANDER			
NAVAL AIR WARFARE CENTER		ATTN: PGI-4B (S. HALPERSON)	1
WEAPONS DIVISION		DEFENSE INTELLIGENCE AGENCY	
CHINA LAKE, CA 93555		BOLLING AIR FORCE BASE	
		WASHINGTON, DC 20340-6762	
ATTN: TECHNICAL LIBRARY	1		
COMMANDER		COMMANDER	
NAVAL UNDERSEA WARFARE		NAVAL WEAPONS EVALUATION	
CENTER DIVISION		FACILITY	
NEWPORT, RI 02840-5047		KIRTLAND AIR FORCE BASE	
		ALBUQUERQUE, NM 87117-5669	1
ATTN: TECHNICAL LIBRARY	1		
COMMANDING OFFICER		ATTN: C. FOWLER	1
NAVAL MARITIME INTELLIGENCE		DEFENSE SCIENCE BOARD	
CENTER		THE PENTAGON	
4301 SUITLAND ROAD		WASHINGTON, DC 20301	
WASHINGTON, DC 20390-5140			

DISTRIBUTION (Cont.)

	COPIES		COPIES
ATTN: TECHNICAL LIBRARY U.S. ARMY RESEARCH LAB APG, MD 21005-5066	1	ATTN: 7141 (TECHNICAL LIBRARY) SANDIA NATIONAL LABORATORIES P.O BOX 5800 ALBUQUERQUE, NM 87185	1
ATTN: LIBRARY DIRECTOR DEFENSE RESEARCH AND ENGINEERING WASHINGTON, DC 20305	1	ATTN: TECHNICAL LIBRARY 8746 (D. DAWSON) 8742 (W. KAWAHARA) 8742 (D. BAMMANN)	1 1 1 1
ATTN: T. MATUSKO AIR FORCE OFFICE OF SCIENTIFIC RESEARCH BOLLING AIR FORCE BASE WASHINGTON, DC 20332	1	P.O. BOX 969 SANDIA NATIONAL LABORATORIES LIVERMORE, CA 94551-0969	
NON-DOD ACTIVITIES:		ATTN: L-313 (TECHNICAL LIBRARY) UNIVERSITY OF CALIFORNIA LAWRENCE LIVERMORE NATIONAL LABORATORY P.O. BOX 808	1
ATTN: GIFT AND EXCHANGE LIBRARY OF CONGRESS WASHINGTON, DC 20540	4	LIVERMORE, CA 94550-0427	
ATTN: TECHNICAL LIBRARY INSTITUTE FOR DEFENSE ANALYSES 1801 N. BEAUREGARD ST. ALEXANDRIA, VA 22311	2	ATTN: TECHNICAL LIBRARY THE JOHNS HOPKINS UNIVERSITY APPLIED PHYSICS LABORATORY JOHNS HOPKINS ROAD LAUREL, MD 20723-6099	1
ATTN: S. SHARPE EXECUTIVE DIRECTOR SHIP STRUCTURE COMMITTEE U. S. COAST GUARD (G-MI/R) 2100 SECOND STREET, S. W. WASHINGTON, D. C. 20593-0001	1	ATTN: T. WIERZBICKI M. HOO FATT MASSACHUSETTS INSTITUTE OF TECHNOLOGY OCEAN ENGINEERING DEPT. CAMBRIDGE, MA 02139	1 1
ATTN: R. SIELSKI MARINE LIASON BOARD NATIONAL ACADEMY OF SCIENCES 2101 CONSTITUTION AVE WASHINGTON, D. C. 20418	1	ATTN: F. MCCLINTOCK MASSACHUSETTS INSTITUTE OF TECHNOLOGY MECHANICAL ENGINEERING DEPT. CAMBRIDGE, MA 02139	1
ATTN: TECHNICAL LIBRARY CENTER FOR NAVAL ANALYSES 4401 FORD AVENUE P.O. BOX 16268 ALEXANDRIA, VA 22302-0268	1	ATTN: J. GIOVANOLA SRI INTERNATIONAL POULTER LABORATORY 333 RAVENSWOOD AVE. MENLO PARK, CA 94025	10
ATTN: TECHNICAL LIBRARY LOS ALAMOS NATIONAL LABORATORY P.O. BOX 1663 LOS ALAMOS, NM 87545	1	ATTN: LIBRARY PENNSYLVANIA STATE UNIVERSIT APPLIED RESEARCH LABORATORY P.O. BOX 30 STATE COLLEGE, PA 16804-0030	1

DISTRIBUTION (Cont.)

	COPIES		COPIES
ATTN: D. KOSS	1	4610 (R. BARASH)	1
10 STEIDLE BUILDING		4620 (K. KIDDY)	1
PENNSYLVANIA STATE UNIVERSITY		4620 (H. MAIR)	1
UNIVERSITY PARK, PA 16802		4620 (D. HAN)	1
		4620 (M. MOUSSOUROS)	1
ATTN: A. KUSHNER	1	4620 (J. KOENIG)	1
MECHANICAL ENGINEERING		4620 (W. MCDONALD)	10
SUNY AT STONY BROOK		4630 (G. HARRIS)	1
STONY BROOK, NY 11794-2300		4630 (D. BENDT)	1
		4630 (M. MAIR)	1
ATTN: I. NESTOR	1	8530 (LIBRARY)	1
DIRECTOR, RESEARCH AND CODES		90D (D. PHILLIPS)	1
AMERICAN INSTITUTE OF STEEL		905 (C. DICKINSON)	1
CONSTRUCTION, INC.		9210 (F. ZERILLI)	1
ONE EAST WACKER DRIVE, SUITE 3100		9540 (D. TASSIA)	1
CHICAGO, IL 60601-2001		9540 (P. WALTER)	1

GENERAL DYNAMICS
ELECTRIC BOAT DIVISION
75 EASTERN POINT RD

INTERNAL: (DAHLGREN DIVISION)

	COPIES		COPIES
GROTON, CT 06340-3312	1	E231	2
		E232	3
WEIDLINGER ASSOCIATES		R30 (C. MUELLER)	1
333 SEVENTH AVE		R31 (J. TOENEBOEHN)	1
NEW YORK, NY 10001	1	G05 (J. GOELLER)	1
		G22 (W. HOLT)	1
ATTN: J. GREENHORN	1	G22 (W. MOCK)	1

DRA ST LEONARDS HILL
DUNFERMLINE FIFE KY11 5PW
SCOTLAND, UNITED KINGDOM

	COPIES
ATTN: I. CULLIS	1

DRA FORT HALSTEAD
SEVENOAKS KENT TN14 7BP
ENGLAND, UNITED KINGDOM

	COPIES
ATTN: TAF (M. BORRMANN)	1

IABG
EINSTEINSTRASSE 20
D-85521 OTTOBRUNN GERMANY

INTERNAL: (INDIAN HEAD DIVISION)

	COPIES
PM7 (R. KAVETSKY)	1
40 (W. WASSMANN)	1
40E (E. JOHNSON)	1
4140 (R. GARRETT)	1
420 (L. TAYLOR)	1
4210 (S. VAN DENK)	1
460 (H. HUANG)	1

REPORT DOCUMENTATION PAGE

Public reporting burden for this collection of information is estimated to average 1 hour per response, including the time for reviewing instructions, searching existing data sources, gathering and maintaining the data needed, and completing and reviewing the collection of information. Send comments regarding this burden estimate or any other aspect of this collection of information, including suggestions for reducing this burden, to Washington Headquarters Services, Directorate for Information Operations and Reports, 1215 Jefferson Davis Highway, Suite 1204, Arlington, VA 22202-4302, and to the Office of Management and Budget, Paperwork Reduction Project (0704-0188), Washington, DC 20503

1. AGENCY USE ONLY (Leave blank)	2. REPORT DATE June 1990	3. REPORT TYPE AND DATES COVERED 9/6/86 - 2/28/90

4. TITLE AND SUBTITLE

Investigation of the Fracture Behavior of Scaled HY-130 Steel Weldments

5. FUNDING NUMBERS

N60921-86-C-0253

6. AUTHOR(S)

J. H. Giovanola, R. R. Klopp, J. W. Simons, and A. H. Marchand

7. PERFORMING ORGANIZATION NAME(S) AND ADDRESS(ES)

SRI International/Poulter Laboratory
333 Ravenswood Avenue
Menlo Park, CA 94025-3493

8. PERFORMING ORGANIZATION REPORT NUMBER

9. SPONSORING/MONITORING AGENCY NAME(S) AND ADDRESS(ES)

Naval Surface Warfare Center (R14)
10901 New Hampshire Avenue
Silver Spring, MD 20903-5000

10. SPONSORING/MONITORING AGENCY REPORT NUMBER

NAVSWC TR 90-360

11. SUPPLEMENTARY NOTES

12a. DISTRIBUTION/AVAILABILITY STATEMENT

Approved for public release; distribution is unlimited.

12b. DISTRIBUTION CODE

13. ABSTRACT (Maximum 200 words)

The Naval Surface Warfare Center is developing a statistical model to predict the fracture probability of welded, ring-stiffened naval structures subjected to dynamic loads. In support of this statistical model development, SRI International is conducting a research program aimed at establishing scaling rules for fracture of weldments of different sizes and defining simple parameters to correlate the fracture damage produced in experiments with loading conditions.

This report describes the approach taken to achieve these objectives and the application of this approach to undermatched (100S weld wire) welded T-joints in HY-130 steel. A similar study of Ti alloys weldments will presented in a separate report

14. SUBJECT TERMS

| Fracture | HY-130 Steel | Local Fracture Model |
| Weldments | Scaling Rules | Explosive Loading |

15. NUMBER OF PAGES
236

16. PRICE CODE

17. SECURITY CLASSIFICATION OF REPORT UNCLASSIFIED	18. SECURITY CLASSIFICATION OF THIS PAGE UNCLASSIFIED	19. SECURITY CLASSIFICATION OF ABSTRACT UNCLASSIFIED	20. LIMITATION OF ABSTRACT SAR

GENERAL INSTRUCTIONS FOR COMPLETING SF 298

The Report Documentation Page (RDP) is used in announcing and cataloging reports. It is important that this information be consistent with the rest of the report, particularly the cover and its title page. Instructions for filling in each block of the form follow. It is important to *stay within the lines* to meet *optical scanning requirements*.

Block 1. Agency Use Only (Leave blank).

Block 2. Report Date. Full publication date including day, month, and year, if available (e.g. 1 Jan 88). Must cite at least the year.

Block 3. Type of Report and Dates Covered. State whether report is interim, final, etc. If applicable, enter inclusive report dates (e.g. 10 Jun 87 - 30 Jun 88).

Block 4. Title and Subtitle. A title is taken from the part of the report that provides the most meaningful and complete information. When a report is prepared in more than one volume, repeat the primary title, add volume number, and include subtitle for the specific volume. On classified documents enter the title classification in parentheses.

Block 5. Funding Numbers. To include contract and grant numbers; may include program element number(s), project number(s), task number(s), and work unit number(s). Use the following labels:

```
C   -  Contract      PR   -  Project
G   -  Grant         TA   -  Task
PE  -  Program       WU   -  Work Unit
       Element              Accession No.
```

BLOCK 6. Author(s). Name(s) of person(s) responsible for writing the report, performing the research, or credited with the content of the report. If editor or compiler, this should follow the name(s).

Block 7. Performing Organization Name(s) and Address(es). Self-explanatory.

Block 8. Performing Organization Report Number. Enter the unique alphanumeric report number(s) assigned by the organization performing the report.

Block 9. Sponsoring/Monitoring Agency Name(s) and Address(es). Self-explanatory.

Block 10. Sponsoring/Monitoring Agency Report Number *(If Known)*

Block 11. Supplementary Notes. Enter information not included elsewhere such as: Prepared in cooperation with...; Trans. of...; To be published in.... When a report is revised, include a statement whether the new report supersedes or supplements the older report.

Block 12a. Distribution/Availability Statement. Denotes public availability or limitations. Cite any availability to the public. Enter additional limitations or special markings in all capitals (e.g. NOFORN, REL, ITAR).

```
DOD   -  See DoDD 5230.24, "Distribution
            Statements on Technical Documents."
DOE   -  See authorities.
NASA  -  See Handbook NHB 2200.2
NTIS  -  Leave blank.
```

Block 12b. Distribution Code.

```
DOD   -  Leave blank.
DOE   -  Enter DOE distribution categories
            from the Standard Distribution for
            Unclassified Scientific and Technical
            Reports.
NASA  -  Leave blank.
NTIS  -  Leave blank.
```

Block 13. Abstract. Include a brief *(Maximum 200 words)* factual summary of the most significant information contained in the report.

Block 14. Subject Terms. Keywords or phrases identifying major subjects in the report.

Block 15. Number of Pages. Enter the total number of pages.

Block 16. Price Code. Enter appropriate price code *(NTIS only)*

Blocks 17.-19. Security Classifications. Self-explanatory. Enter U.S. Security Classification in accordance with U.S. Security Regulations (i.e., UNCLASSIFIED). If form contains classified information, stamp classification on the top and bottom of the page.

Block 20. Limitation of Abstract. This block must be completed to assign a limitation to the abstract. Enter either UL (unlimited) or SAR (same as report). An entry in this block is necessary if the abstract is to be limited. If blank, the abstract is assumed to be unlimited.